Secondary Sonic Boom

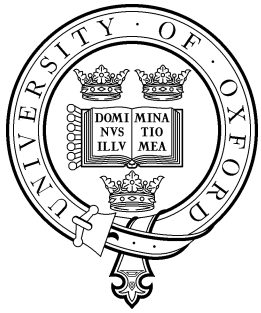

Katerina Kaouri
Somerville College
University of Oxford

A thesis submitted for the degree of
Doctor of Philosophy

Trinity Term 2004

To my sister Marina for who she is.

Acknowledgements

The first place in these acknowledgements belongs to my supervisor Dr David Allwright for all the help and support he has given me throughout the years. He has guided me flawlessly and has always been available to answer all my questions and correct my mistakes with immense clarity, speed and politeness. I am sure that reading my thesis repeatedly was not a fun thing to do, but he did it diligently and efficiently. Furthermore, David and his wife Susan have been very understanding and helpful through difficult personal times; I am grateful for this.

I would also like to thank Dr John Ockendon for the many discussions on sonic boom over the years, and for demonstrating the value of "solving the simplest problem first". His input has been very valuable throughout the course of this work, in particular for the asymptotic methods that were used in this thesis. I would also like to gratefully acknowledge Dr Hilary Ockendon for being a very helpful and efficient College Advisor throughout the years I spent in Oxford.

My friends Angelos, Mauricio and Petros have made life in Somerville fun, and Tereza shared with me great transatlantic conversations in the early hours of the morning (and not only). Also Fasi has been there for me through good and bad times, a constant source of laughs, great conversation (and occasionally good food). Finally, I would like to thank my family for always believing in me and offering me their unconditional love.

I would also like to thank Dr Paul Dellar for helpful suggestions on some parts of this thesis as well as Fortran and CLAWPACK, Nim Arinaminpathy who kindly proofread many parts of this thesis, and Dr Gregory Kozyreff for initiating me to Mathematica, which has indeed proved to be a very useful tool. I would also like to thank Kseniya, John, Reason and Max for making the room DH27 a pleasant place to work, and Nim for keeping up the good spirits on the third floor of Dartington House in the long series of late nights.

The work included in this thesis took place between March 2001 and October 2004 and for its major part it was funded by the Sonic Boom European Research Programme (SOBER). I would also like to gratefully acknowledge discussions with other SOBER participants: Laurent Dallois, Julian Scott and François Coulouvrat. Furthermore, I would like to acknowledge discussions with John Ockendon, Hilary Ockendon, Jon Chapman, and Joe Keller regarding work in Chapter 7.

Finally, I would like to acknowledge a Leventis Foundation Educational Grant and a Somerville Graduate Scholarship.

This thesis aims to resolve some open questions about sonic boom, and particularly secondary sonic boom, which arises from long-range propagation in a non-uniform atmosphere.

We begin with an introduction to sonic boom modelling and outline the current state of research. We then proceed to review standard results of gas dynamics and we prove a new theorem, similar to Kelvin's circulation theorem, but valid in the presence of shocks.

We then present the definitions used in sonic boom theory, in the framework of linear acoustics for stationary and for moving non-uniform media. We present the wavefront patterns and ray patterns for a series of analytical examples for propagation from steadily moving supersonic point sources in stratified media. These examples elucidate many aspects of the long-range propagation of sound and in particular of secondary sonic boom. The formation of *fold caustics* of boomrays is a key feature. The focusing of linear waves and weak shock waves is compared.

Next, in order to address the consistent approximation of sonic boom amplitudes, we consider steady motion of supersonic thin aerofoils and slender axisymmetric bodies in a uniform medium, and we use the method of matched asymptotic expansions (MAE) to give a consistent derivation of Whitham's model for nonlinear effects in primary boom analysis. Since for secondary boom, as for primary, the inclusion of nonlinearities is essential for a correct estimation of the amplitudes, we then study the paradigm problem of a thin aerofoil moving steadily in a weakly stratified medium with a horizontal wind. We again use MAE to calculate approximations of the Euler equations; this results in an inhomogeneous kinematic wave equation.

Returning to the linear acoustics framework, for a point source that accelerates and decelerates through the sound speed in a uniform medium we calculate the wavefield in the *time-domain*. Certain other motions of interest are also illustrated. In the accelerating and in the manoeuvring motions fold caustics that are essentially the same as those from steady motions in stratified atmospheres again arise. We also manage to pinpoint a scenario where a *cusp caustic* of boomrays forms instead. For the accelerating motions the asymptotic analysis of the wavefield reveals the formation of singularities which are incompatible with linear theory; this suggests the re-introduction of nonlinear effects. However, it is a formidable task to solve such a nonlinear problem in two or three dimensions, so we solve a related one-dimensional problem instead. Its solution possesses an unexpectedly rich structure that changes as the strength of nonlinearity varies. In all cases however we find that the singularities of the linear problem are regularised by the nonlinearity.

Contents

List of Figures

Chapter 1

Introduction

1.1 Historical background and research motivation

The general theme of this thesis is the mathematical modelling of sonic boom as generated by supersonic aircraft, and in particular of secondary boom.

After the U.S. military pilot C. Yaeger successfully broke the sound barrier in 1947 theoretical work on supersonic flow suddenly gained new glamour and hands-on applicability. Intense research activities ensued and the U.S., U.K., France and the former Soviet Union all launched SuperSonic Transport (SST) programmes, which led to the production of the first generation of supersonic aircraft.

However, it did not take long to realise that the by-products of supersonic flight were far from pleasant. Sonic boom frequently reached inhabited areas causing many complaints and it was one of the key factors for the cancellation, in 1971, of the U.S. SST programme.

Meanwhile, the British-French Concorde made its maiden flight in 1969, and from 1976 it flew transatlantic flights routinely. Concorde service was terminated in October 2003—its technological success was never questioned but it had never been a highly profitable project.

Figure 1.1: Concorde in a British Airways flight, 2003.

However, it is highly probable that civil supersonic aviation will be reinstated in the future, as the travel market is steadily growing, both for leisure and business purposes. Hence sonic boom research is currently undergoing a renaissance.

The human response to aircraft noise [116] is complicated because of the multitude of factors involved such as previous exposure, geographic location, time of day, socioeconomic status etc[1]. Sonic boom contributes an additional environmental noise impact, specific to supersonic flight. As of 1973, civil supersonic flights are forbidden above land [3]. However, the long-term effects on health of daily exposure to sonic booms are yet to be investigated, and a quantitative measure of acceptability has not been established. It is however commonly accepted that loud and unexpected noises tend to disorient and startle people, and studies indicate that reaction to sonic boom is far more severe than reaction to other types of noise at analogous amplitude levels [79, 114]. Furthermore, there are fears that sonic boom will pose a threat to aquatic life, and to fowl, farm and wild animals [36]. Therefore, the environmental impact of sonic boom needs to be carefully evaluated and precise noise regulations for sonic boom need to be devised. Such regulations could substantially limit the profitability of a new SST or stop its implementation altogether.

For successful mitigation of the annoyance due to sonic boom, a thorough understanding of the generation and propagation of the relevant acoustic waves is required. Such an understanding should lead to new predictions and modifications in aircraft design and operation that would limit the impact of sonic boom. In Section 1.2 we explain what a sonic boom is and classify the different forms in which it is heard at the ground, in Section 1.3 we discuss the current state of sonic boom research, and in Section 1.4 we give an outline of this thesis.

1.2 Sonic boom

A shock-wave pattern is formed around an aircraft when flying at supersonic speed (i.e. faster than sound). Sonic boom is the noise from these shock waves, as heard at the ground. Sonic booms are weak shocks: the typical overpressure at the ground is up to 100 Pa, a shock strength of order 10^{-3} of the atmospheric pressure [126].

For weak shocks nonlinearities can be neglected, to a first approximation, and the disturbance due to the motion of a supersonic aircraft can be thought of as the linear

[1]Sound is recorded in Pa or dB. However there are various metrics that estimate the sound *perceived* by a human ear. Such noise metrics, as formally stated by the U.S. Federal Aviation Administration (see http://www.nonoise.org/library/ane/ane.htm), are the A-Weighted Sound Level (AL), Sound Exposure Level (SEL), Yearly Average Day Night Level (DNL) metric etc.

superposition of small disturbances (i.e. sound waves) spreading out from its successive positions at the speed of sound. In a homogeneous atmosphere, and thinking for simplicity of the aircraft as a point source in two dimensions, these disturbances form circular wavefronts centered at the successive positions of the aircraft, as illustrated in the left schematic of Figure 1.2. The wavefronts overlap and form an envelope, called the *Mach envelope*. In two dimensions the Mach envelope is a wedge, and in three-dimensions it is a cone, called the Mach cone. The semivertical angle of the Mach cone is the Mach angle $\theta_M = \arcsin(1/M)$, where M is the ratio of the source speed to the sound speed and is called the *Mach number*.[2] All the sound is contained in the Mach envelope, and (to a first approximation) the envelope is the location of the sonic boom. Figure 1.2 also illustrates why sonic boom is so startling—there is no precursor. Furthermore, Figure 1.2 illustrates the difference in the wavefront patterns due to a supersonic and a subsonic motion; in the latter case the wavefronts are nested and the sound is radiated in all directions. These two motions are discussed and compared in more detail in Chapter 3.

On the left schematic of Figure 1.2, we also show the "boomrays": these will also be defined in detail in Chapter 3 and are the rays emitted at angle $\theta_B = \arccos(1/M)$ to the direction of motion. The disturbances propagating along boomrays reinforce each other at the observer position and are heard as a single "boom". We can thus alternatively think of the Mach envelope as made of the tips of the boomrays, and the boom as travelling along boomrays. Tracing the boomrays is in fact the standard method to follow the path of the shock wave in sonic boom prediction methods, and underpins the so-called "ray theory approach" to sonic boom.

Depending on the flight and atmospheric conditions, the shock wave formed by supersonic flight can reach the observer on the ground in four forms—primary boom, secondary boom, focused boom, and shadow-zone boom—which we now describe in turn.

1.2.1 Primary boom

The term "primary boom" refers to shock waves leaving the aircraft downwards and propagating directly to the ground. The typical pressure signature at the ground is a double-shock N-wave, characterised by two sudden rises in pressure of $10 - 100\,\mathrm{Pa}$, separated by $0.1 - 0.3\,\mathrm{s}$. (If the r.m.s. pressure in a continuous sound was $10 - 100\,\mathrm{Pa}$, the sound pressure level would be $114 - 134\,\mathrm{dB}$.) An N-wave is illustrated in Figure

[2] Concorde, for example, cruised at Mach 2.

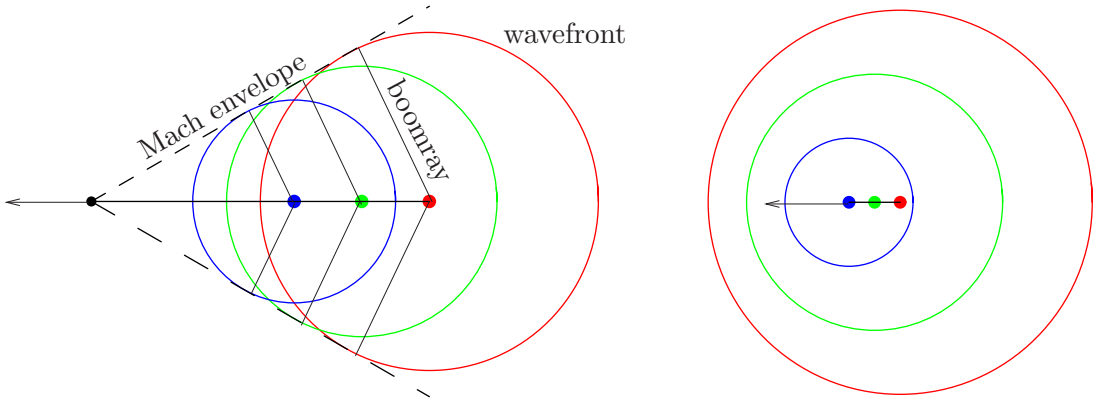

Figure 1.2: The wavefront patterns due to a supersonic motion (left) and due to a subsonic motion (right). In the supersonic case the wavefronts form an envelope but in the subsonic case they are nested.

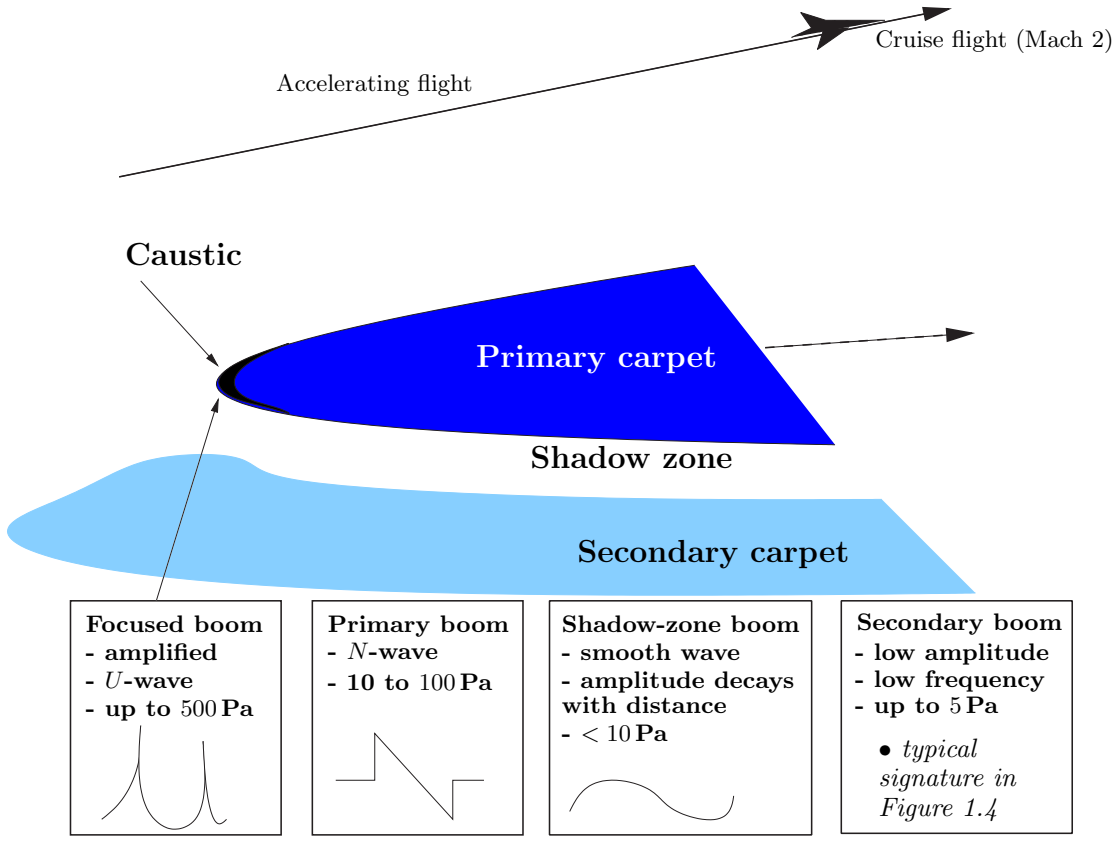

Figure 1.3: Sonic boom carpet and pressure signatures, for an aircraft flying in a straight line and accelerating through the sound speed to a cruise flight with Mach 2. Primary boom is discussed in Section 1.2.1, secondary boom in 1.2.2, focused boom and caustics in 1.2.3, and shadow-zone boom in 1.2.4.

1.3 (second plot from the left). The primary carpet, defined as the area on the ground where primary boom is heard, is a strip of land directly below the aircraft, as also illustrated in Figure 1.3. Primary boom is the most annoying type of boom, and has also been known to cause structural damage [76].

1.2.2 Secondary boom

Secondary Sonic Boom (SSB) or over-the-top boom, is due to shock waves that are returned to the ground by temperature or wind gradients in the atmosphere *above* the aircraft. The presence of SSB was not given due consideration until routine operation of Concorde was established. SSB is less annoying than primary boom but may cause easily observable building vibration and rattling [76]. The evaluation of its community acceptance is still at a very early stage.

Data from supersonic flights show that the primary and secondary booms are very different in nature [104]. SSB is much less intense than primary boom with peak pressures up to about 5 Pa, and lasts up to 1.5 minutes, which is around 100 times the duration of an N-wave. It has lost most of the high-frequency content, and is heard as a low-frequency rumble with occasional thumps. A typical pressure signature for SSB appears in Figure 1.4. We see that most of the pressure signature is within 0.2 Pa, but that there are also two peaks that are at about 5 Pa, and approximately 30 s apart. Such multiple arrivals are typical features of SSB signatures.

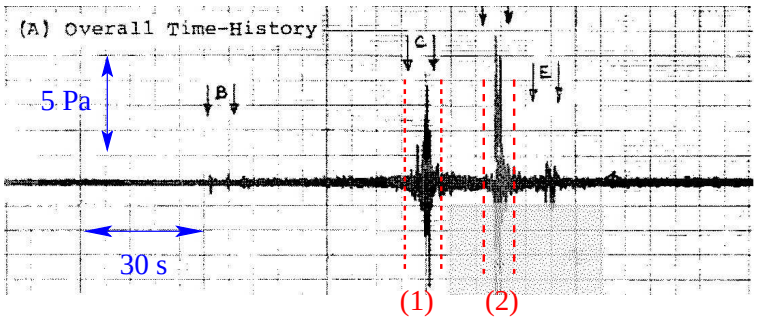

Figure 1.4: A typical pressure-time history of secondary sonic boom, recorded in Malden, New England, during Concorde's approach to JFK airport (British Airways Flight BA-171), on 18-07-1979—from Rickley and Pierce [104], p.71.

The secondary carpet, the area of the ground where secondary boom is heard, is much wider than the primary carpet, sometimes $300 - 1000$ km from the flight path, as illustrated in Figure 1.3. With further propagation, SSB can degrade into

an infrasonic disturbance that can travel thousands of miles under certain weather conditions.

We have to note that the shock waves involved in SSB either propagate upwards from the aircraft, or having propagated downwards they subsequently reverse direction by reflection at the ground. In the former case we have a so-called *direct* secondary boom and in the latter case an *indirect* secondary boom. This is illustrated schematicatically in Figure 1.5.

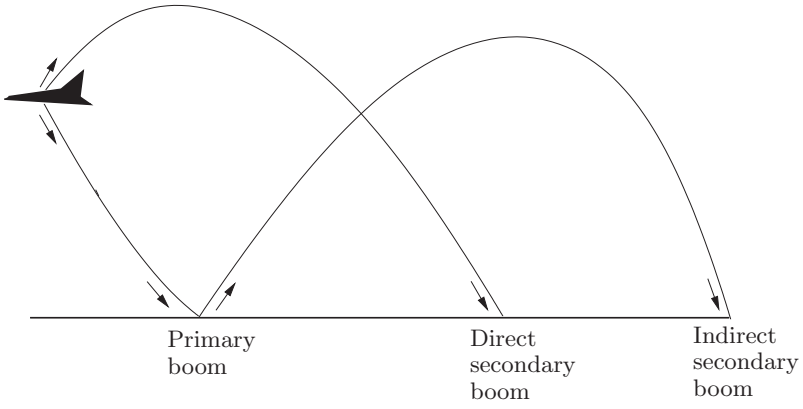

Figure 1.5: A schematic illustrating a direct and an indirect secondary boom.

Furthermore, in a typical stationary atmosphere, SSB can only be generated by reflection from the thermosphere, around or above 100 km altitude; we will call this a *thermospheric* SSB. With wind in the upper atmosphere, SSB may return to the ground from an altitude of about 50 km in the stratosphere, and we will thus call this a *stratospheric* SSB. We shall see this in more detail in Chapter 3 where we discuss a typical atmospheric sound speed profile.

1.2.3 Focused boom

The third type of boom signature that has been recorded [123, 47] is shown in the left-most schematic of Figure 1.3. It is called a U-wave due to its shape. The resulting boom heard at the ground is characterised by peak pressures 2 to 5 times larger than those in a typical N-wave, and it is usually called *focused boom*. This amplification of boom intensity is due to focusing of the shock waves, taking place when the aircraft accelerates (including acceleration through the sound speed). Turns and other manoeuvres may also lead to focusing, but in many cases this can be reduced or avoided by proper selection of the aircraft trajectory.

Similar focusing also occurs in the atmosphere due to the inhomogeneous sound speed. In a stationary stratified atmosphere focusing occurs at some height, in or below the thermosphere, where the boom is reflected downwards.[3] The issue of focusing is therefore relevant to the propagation route by which secondary boom reaches the observer on the ground.

The three focusing scenarios discussed above are geometrically similar, and involve the production of a U-wave. Because of this, and because secondary boom can itself be focused[4], in this thesis we will also give attention to accelerating motions and manoeuvres.

1.2.4 Shadow-zone boom

The gap between the primary and secondary carpets shown in Figure 1.3 occurs because part of the shock wave is trapped in an atmospheric waveguide and never reaches the ground. This will be explained in more detail in Chapter 3.

At the boundary of the primary carpet with the gap region the pressure signature is attenuated and loses its N-wave characteristic due to ground impedance effects and diffraction. A schematic of this fourth type of boom signature is included in Figure 1.3. This boom is usually called the "shadow-zone boom", because it is analogous to the propagation of light by creeping rays over the unlit surface of a curved obstacle [18].

1.3 Current state of sonic boom research

The basic theory of sonic boom has been delineated in [124, 125, 45, 54] and implemented into practical models in [54, 120, 13, 24, 98, 106]. The basic sonic boom theory mainly concerns primary booms from steady level flight. Much of this work was accomplished by the early 1970's, and was largely motivated by the SST effort.

However, secondary boom, focused boom and shadow-zone boom are subjects of continuing investigation. Below we will present the major results for the four types of boom, and outline some of the open questions.

[3] The boomray launched upwards in the plane of flight reflects at the height where the sound speed is equal to the aircraft speed, usually called the *sonic height*; those launched obliquely reflect lower. More details are given in Chapter 3, and illustrated with examples.

[4] Figure 1.3 illustrates only focusing of primary boom, but acceleration may also cause focusing of secondary boom.

1.3.1 Primary boom

The first theoretical results on sonic boom came from the ballistic projectiles community: within sonic boom nomenclature the flow pattern from a projectile is precisely the shock-wave pattern due to a supersonic flight. In 1946 Landau analysed the weak shock waves from a supersonic projectile and predicted an N-wave shape for the pressure signature in the far-field [67] (i.e. at distances large compared with the body dimensions). Soon afterwards, measurements of projectiles confirmed Landau's predictions [35].

In 1952, Whitham wrote a seminal paper for sonic boom research [124]. In this he explained in detail the generation of the flow pattern from a ballistic projectile and made it clear that sonic boom is a steady state phenomenon; it is generated continuously as the aircraft flies supersonically and not only at the moment that the aircraft breaks the sound barrier.

Near the aircraft (near-field), the pressure field is directly dependent on the geometry and the aerodynamics of the vehicle. Supersonic aircraft aerodynamics is most easily computed by linearised supersonic flow theory [50, 39, 70, 126] and it is presented in the normalised form of the so-called Whitham function [124, 126]. More recently, with the advent of increased computing power, CFD methods have been devised to calculate the near-field signature [89, 20, 100], but they are still under development and not in wide use. However, shocks, even when very weak, are inherently nonlinear. According to the linearised supersonic flow theory shock waves travel at the sound speed, but in reality the speed of a shock wave is greater than the sound speed and amplitude-dependent, and it turns out that at large distances from the aircraft the weak nonlinearities have an important cumulative effect [124]. Whitham has shown that nonlinear effects can be easily incorporated by shifting appropriately the characteristics predicted by the linear theory, while still using the amplitudes predicted by the linear solution [124, 125]. This is the famous Whitham's rule. It has been used extensively in sonic boom research (and it is discussed in great detail in Chapter 4).

For a pointed aerofoil or axisymmetric body there are generally two shock waves, one attached to the front (usually called the bow shock) and the other attached to the tail (usually called the tail shock)—see, for instance, [126, 70].

An aircraft is a non-smooth body and in the near-field the shock-wave pattern contains several shock waves, corresponding to the various compressions caused by the detailed shape of the aircraft. However, away from the aircraft the shock wave pattern distorts and steepens, and in the far-field it coalesces into only a bow and a tail

shock, as in the case of a simpler, smooth body. Records from flight tests substantiate this since the N-wave signatures for various aircraft of similar size and weight are essentially the same [76]. In this thesis we will study the paradigm problems of a pointed aerofoil and a slender body—work on more complicated body shapes appears in [50, 52, 74, 122, 125, 38].

Figure 1.6 displays a schematic of the coalescence of the near-field shock waves, that leads to the N-wave in the far-field. At the bow shock the local pressure p increases rapidly by amount Δp above the atmospheric pressure; Δp is usually called the overpressure. There is a slow expansion phase between the bow shock and the tail shock until the pressure is a certain amount below the atmospheric pressure, and at the tail shock the atmospheric pressure is recovered rapidly. Generally, the overpressure and the recovery pressure are of similar size. The N-wave moves with the aircraft; it is detected once at a specific observation point on the ground. If the

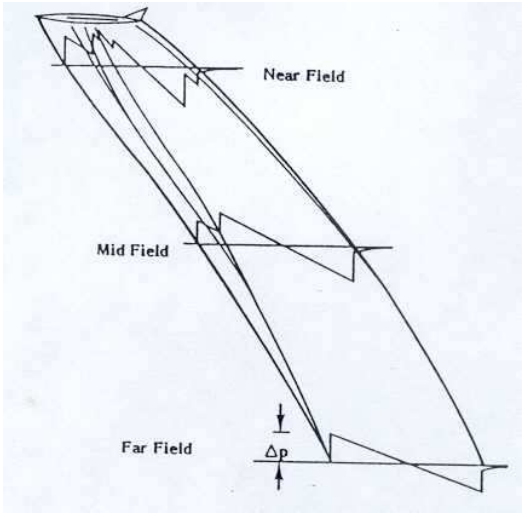

Figure 1.6: Schematic of the far-field wave pattern from a supersonic aircraft, in a frame moving with the aircraft—from [76].

time difference between these two rapid compressions is small, as for a bullet, the two compressions are not separately audible and the ear detects a single explosive sound. However for longer bodies, or an aircraft high enough in the atmosphere, a double boom may be heard. Note that as the ear responds only to sounds above a certain frequency, it only perceives the rapid compressions and not the slow expansion phase.

Furthermore, atmospheric variation below the aircraft also needs to be taken into account for primary boom propagation. In an inhomogeneous medium the boomrays refract away from regions of higher sound speed. This refraction problem is analysed

using Geometrical Acoustics (GA) in non-uniform media [17, 65]. GA is generally a good approximation since the wavelength is much smaller than the length-scale of propagation involved, and also the length-scale of atmospheric variation. Blokhintsev in [17] established the GA theory for monochromatic waves in a non-uniform, moving medium, and Keller showed in [65] that this theory also applies to weak shock waves.

Based on these theoretical results the following procedure has been widely used in the prediction of primary sonic boom: the Whitham function is obtained for the particular aircraft geometry, usually using linearised supersonic flow theory. Then at a certain distance from the aircraft (which depends on its size, shape and speed), the boomrays are launched using pressure values from the Whitham function. The boomrays are then traced, with Whitham's rule being applied to account for the nonlinearities.

The codes [54, 120, 13, 106, 24, 98] generally implement the prediction method outlined in the previous paragraph, and have been used to predict primary boom carpets and signatures successfully. We note that each of these codes has its own capabilities and limitations depending on the task in hand at the time; the review [99] by Plotkin contains a brief overview of the sonic boom codes that were available in 2002, together with a discussion of their relative merits and disadvantages.

Some open questions in primary boom research concern propagation through turbulence in the lower atmosphere [30, 93, 13, 96, 95], absorption and dispersion due to viscosity and non-equilibrium (relaxation) effects [101, 83, 115, 12, 60, 49, 62], underwater penetration [117], and so on—these however are not within the scope of this thesis and we will not discuss them further.

1.3.2 Secondary boom

A complete theoretical understanding of secondary boom is yet to be acquired. SSB involves propagation over long distances and it is thus quite likely that many effects that can be safely neglected in primary boom studies need to be taken into account.

Rogers and Gardner in [108] concluded that attenuation in the atmosphere leads to a thermospheric SSB of insignificant amplitude. On the other hand, in [33], Donn presented measurements of SSB traces and he interpreted them as stratospheric and thermospheric SSBs being of similar amplitude but with the latter having lower-frequency content. Furthermore, boomray tracing was used in [104], based on real meteorological data and Concorde flight conditions, to predict signal arrivals within

20 s of those recorded (no amplitude calculations were undertaken however).[5] Additionally, the report [48] is a helpful summary of the state of knowledge of SSB in 1995, and some information is also found in the sonic boom review papers [76] and [99].

Below we list the major open questions, prior to the SOBER programme, and outline which of them are addressed in this thesis:

- Focusing is an important aspect of an accurate prediction of SSB, as outlined in Section 1.2.3 above. Preliminary work on this appears in [55, 91, 41]. Further results appear in this thesis, especially in Chapter 3, and are outlined in Section 1.4.

- We have also discussed how nonlinear effects are important in determining the far-field signature for a primary boom. The inclusion of nonlinearities in SSB propagation is also an interesting open problem. In Chapter 5 we develop a paradigm model where such nonlinearities are incorporated in a consistent manner. Other related work is in [55, 91, 108, 111, 7].

- The influence of the Coriolis effect on sound propagation in the atmosphere has been studied by [110] and further reviewed by the author within the SOBER programme [63]. It was found that for a propagation range of even 1000 km, the Coriolis effect is insignificant. This was to be expected as the timescale of SSB propagation is much smaller than a day.

- The effect of the earth's curvature is insignificant for short-range propagation over the earth's surface but can become important in the kind of long-range propagation involved in SSB. It has also been studied within the SOBER programme by the author [63]. It was concluded that over long ranges these effects are important, but that they can be nevertheless easily incorporated in a "flat-earth" boomray tracing code to first order, by appropriately modifying the sound speed profile with a linear correction.

- The low amplitudes involved in SSB and the long-wavetrain nature of the signature indicate that dissipation and dispersion due to viscosity and relaxation effects are likely to be important. These effects on SSB have not been studied in this thesis, but have been studied within the SOBER programme [7].

[5] It was subsequently concluded by the U.S Department of Transportation that SSB affected inhabited areas in New England, and Concorde was requested to decelerate to subsonic speeds further away from the coast.

- Three-dimensional wind or temperature inhomogeneities, such as atmospheric gravity waves, may also be a reason for the multiple arrivals observed in the SSB signature. These effects have been studied within the SOBER programme. Also, small-scale inhomogeneities created near the ground by turbulence may be important for explaining the nature of the SSB signatures. To our knowledge, these effects have not been studied as yet.

In SSB propagation many widely separated length-scales are involved and one should be very careful before developing a numerical procedure for SSB prediction. While the propagation distance is 300 to 1000 km, the scale of atmospheric variations is about 10 times smaller and the aircraft length 1000 times smaller still. Consequently, any numerical procedure would have to be able to deal with these multiple scales. Furthermore, focusing in the upper layers of the atmosphere corresponds to a transition from a hyperbolic model to an elliptic one, and this also needs careful numerical treatment.

Only three codes exist for prediction of SSB. The TRAPS code [119] is a reformulation of the primary boom code [54] that can also cater for upward-launched boomrays. It is successful in predicting *where* SSB reaches the ground but it gives too large amplitudes. To resolve this discrepancy, the ZEPHYRUS code [106] was subsequently written; its most important feature is the incorporation of air absorption effects and it indeed predicts lower values for the overpressures. However, ZEPHYRUS is much more computer intensive than TRAPS. More recently, as part of the SOBER programme a third code was constructed [31, 7]; this code includes nonlinearity, absorption and relaxation effects by various chemical species and uses real meteorological data—it supersedes both TRAPS and ZEPHYRUS as it predicts, in reasonable computing time, results that agree well with SSB observations. The thumps are interpreted as due to multipath arrivals due to direct and indirect SSB, and the rumbling noise as an effect of atmospheric gravity waves. The conclusion in [108] that amplitudes of stratospheric SSBs are larger than amplitudes of thermospheric SSBs seems to now be supported by the results in [31, 7].

1.3.3 Focused boom

Focused boom is a topic of great interest in sonic boom research and there is a large literature on it [59, 9, 10, 25, 11, 27]. Some details will be given here, and a more elaborate discussion is given in Chapters 3, 6 and 7.

The focusing in almost any flight condition leads to a smooth envelope of boomrays, a *fold caustic* in the terminology of catastrophe theory [15]. Higher-order focusing, such as that indicated by a cusped envelope of boomrays, a *cusp caustic* in terms of catastrophe theory (and geometrically similar to the famous coffee-cup caustic) is much rarer. Furthermore, perfect lens-like focusing is unlikely to occur [76].

GA predicts an infinite amplitude at caustics. For linear monochromatic waves the amplitude near a fold caustic is determined using the well-established Geometrical Theory of Diffraction [66, 19, 75], which re-introduces diffraction to first order in an appropriately defined Diffraction Boundary Layer (DBL) in the neighbourhood of the caustic. This leads to a linear Tricomi equation.

In the focusing of *weak* shock waves, for an N-wave incident on a fold caustic the linear Tricomi equation gives rise to a reflected wave which is a U-wave with infinite peaks [109]. Such singularities are an unphysical result. The established modelling approach for eliminating these singularities is to combine diffraction effects with nonlinear effects. This procedure leads to a so-called nonlinear Tricomi equation, first derived by Guiraud in [45] and subsequently re-derived in various scenarios in [53, 91, 41, 59, 109]. The solution of the latter equation for an N-wave incident on the caustic yields a U-wave with *finite* peaks [27], in good agreement with the laboratory-scale experiments described in [118, 77].

However, the elimination of the singularities of the linear theory, by introducing nonlinear effects, is a debated issue and the work in Chapter 7 is intended to shed more light on this.

The theory for a cusp caustic is much less well developed; related work is in [92, 29, 28, 25]. The most complete work is by Coulouvrat in [25] where he derives a KZ equation for prediction of the amplitude near a cusp caustic.

1.3.4 Shadow-zone boom

Some theoretical results exist (see [88, 26]) that cater for diffraction effects and ground impedance in sonic boom propagation into the shadow zone but generally little attention has been paid to this aspect of sonic boom propagation.

1.4 Thesis outline

In Chapter 2 we give a brief exposition of gas dynamics and discuss the Euler equations and the Rankine-Hugoniot conditions for a flow with shocks. In this connection, we also prove a new circulation theorem, analogous to Kelvin's circulation theorem, which

is valid for a flow with shocks [8]. In Chapter 4 this theorem allows us to rigorously justify the use of potential flow after a shock is crossed.

In Chapter 3 we linearise the equations of gas dynamics and we present an exposition of Linear Acoustics, in the context of modelling long-range sound propagation, and in particular SSB propagation. (The paradigm situation of a point source is considered.) We carefully outline the connection between the theory of characteristics and GA, which is not always clear in the sonic boom literature. The propagation of thermospheric SSBs is discussed and elucidated with analytical examples of sound propagation in certain model stratified atmospheres. In particular the gap between the primary and secondary carpet, shown in Figure 1.3, is explained with the use of a three-dimensional realistic analytical example and compared with numerical calculations in a real atmosphere.

Special attention is drawn to focusing of the shock waves at the sonic height, which gives rise to a SSB. A general discussion of focusing is included and connected with the focusing observed in our analytical examples, and similarities and differences between focusing of ordinary rays and boomrays are outlined. The linear equations involved are of mixed type: in the two-dimensional case they are hyperbolic below the sonic height and elliptic above. The boom reflects off the sonic height, the Mach envelope having the local shape of a Tricomi cusp. We discuss and illustrate how this Tricomi cusp corresponds to the formation of a fold caustic of boomrays.

In Chapter 4 we use the method of Matched Asymptotic Expansions (MAE) to derive systematically Whitham's rule. We consider thin aerofoils and slender axisymmetric bodies in steady supersonic motion in a uniform, stationary atmosphere. The starting point is the nonlinear potential equation, derived exactly from the Euler equations under the assumption of potential flow. The full equation, to leading order, is approximated in the inner region of the MAE by a linear wave equation, and in the outer region by a nonlinear Kinematic Wave Equation (KWE). An explicit N-wave signature is derived as a solution of the latter KWE, which is exact for a symmetric aerofoil with parabolic shape, and asymptotic for any thin or slender shape in two or three dimensions.

Chapter 5 extends the MAE method of Chapter 4 to the scenario of a thin, two-dimensional aerofoil moving supersonically in a weakly stratified medium with a horizontal wind. This is a paradigm problem for SSB propagation. We start from the full Euler equations, as the assumption of potential flow is abandoned due to vorticity production. Near the aerofoil, in the inner region of the MAE, the wavefield is determined by a linear wave equation to leading order. About 10 aerofoil lengths away

(the middle-region) nonlinear effects become important and the KWE of Chapter 4 arises then at leading order. Moreover, at about 100 aerofoil lengths away we identify a third region, where stratification and nonlinear effects are equally important—and we call this the outer region. The leading-order equation in the outer region is again a KWE, but one that has non-constant coefficients. Our MAE procedure breaks down at the sonic height but below the sonic height it predicts a remarkably simple expression for the amplitude variation.

In Chapter 6 we use a simple approximation method to determine analytically the amplitude near the Mach envelope in various unsteady motions of interest in sonic boom research. For uniform acceleration through the sound speed, in two dimensions the Mach envelope has Tricomi cusps, which are geometrically the same as the cusps at the sonic height in Chapter 3. A qualitative change in the geometry of the Mach envelope occurs when the shock wave passes through a Tricomi cusp and this is carefully illustrated. We find that the wavefield possesses singularities that violate the assumption of small disturbances underlying the linear theory. This suggests that nonlinear effects or dissipation mechanisms have to be re-introduced. In three dimensions, for the same accelerating motion, the Mach envelope is just a conical generalisation of the Mach envelope curve in two dimensions but we find that the wavefield is qualitatively different, due to the difference between the two-dimensional and three-dimensional Riemann functions. Furthermore, for uniform deceleration through the sound speed the Mach envelope is very different from that of the accelerating motion: it does not have a Tricomi cusp and focusing is much less prominent.

The results of Chapter 6 for accelerating motions motivate us to investigate in Chapter 7 the effect of nonlinearity on the sonic singularity that appears in the linear theory when a point force accelerates through the sound speed. As it is a formidable task to solve the relevant nonlinear problem in two or three dimensions, what we have been able to do is to solve a related one-dimensional nonlinear problem, which when linearised yields a sonic singularity, which is similar to that in the higher-dimensional problems. (The results of this chapter have been published in [64].) We present a mainly analytical solution, and we show that introducing nonlinearities of any strength, however small, leads to elimination of the sonic singularity. It still remains an interesting open question whether the introduction of nonlinearity regularises the singularities in two or three dimensions.

Finally, in Chapter 8 we summarise our conclusions and discuss open problems.

Chapter 2

Gas Dynamics

In this chapter we present the equations of gas dynamics, and explain under which assumptions they simplify into the Euler equations, coupled with some appropriate Rankine-Hugoniot conditions. In this connection, we also prove a new circulation theorem, closely related to Kelvin's circulation theorem, Bjerknes' theorem and Crocco's theorem, but one that is valid in the presence of shocks. The latter theorem will be used in Chapter 4 for rigorously justifying the use of potential flow after a shock is crossed.

2.1 The equations of motion

The differential equations of motion for a compressible, simple fluid are

$$\frac{\partial \rho}{\partial t} + \frac{\partial}{\partial x_j}(\rho u_j) = 0, \tag{2.1}$$

$$\frac{\partial}{\partial t}(\rho u_i) + \frac{\partial}{\partial x_j}(\rho u_i u_j - \sigma_{ji}) - \rho F_i = 0, \tag{2.2}$$

$$\frac{\partial}{\partial t}\left(\frac{1}{2}\rho u_i^2 + \rho e\right) + \frac{\partial}{\partial x_j}\left\{\left(\frac{1}{2}\rho u_i^2 + \rho e\right) u_j - \sigma_{ji} u_i + q_j\right\} - \rho F_i u_i = 0. \tag{2.3}$$

Equations (2.1), (2.2) and (2.3) hold under the assumption that the flow quantities are continuously differentiable, and express respectively conservation of mass, momentum and energy in the fluid. In (2.1) the variables involved are the fluid velocity $\mathbf{u}(\mathbf{x}, t) = (u_1, u_2, u_3)$ and the density $\rho(\mathbf{x}, t)$. Equation (2.2) involves additionally the stress tensor $\{\sigma_{ij}(\mathbf{x}, t)\}$ and $\mathbf{F}(\mathbf{x}, t)$, the total external body force per unit mass, which may incorporate gravity, Coriolis and other effects. Equation (2.3) involves still more quantities: the internal energy of the fluid per unit mass e, and the heat flux per unit surface area $\mathbf{q}(\mathbf{x}, t)$.

Equations (2.1), (2.2) and (2.3) do not form a complete system as there are more unknowns than equations. However, for most of this work, we will assume that the fluid is inviscid, so that the stress tensor involves only the pressure p through $\sigma_{ij} = -p\delta_{ij}$. We will also assume that the fluid is non-heat-conducting so that $\mathbf{q} = \mathbf{0}$, and that there is some functional relation between e, p, and ρ determined by experimental results and thermodynamics. With these three assumptions equations (2.1), (2.2) and (2.3) lead to the Euler equations, which *do* form a closed system.

To cast the Euler equations in the more usual non-conservation form, we first introduce the operator $\dfrac{D}{Dt} = \dfrac{\partial}{\partial t} + u_j \dfrac{\partial}{\partial x_j}$, the time derivative following an individual particle. This operator is usually called the total derivative. Therefore the mass conservation equation (2.1) becomes

$$\frac{D\rho}{Dt} + \rho \frac{\partial u_j}{\partial x_j} = 0 \Rightarrow \frac{D\rho}{Dt} + \rho \, \boldsymbol{\nabla} . \mathbf{u} = 0. \tag{2.4}$$

Then expanding out the partial derivatives in (2.2) and using (2.4) to eliminate the ρ derivatives, we obtain the Euler momentum conservation equation

$$\boldsymbol{\nabla} \, p + \rho \frac{D\mathbf{u}}{Dt} = \rho \mathbf{F}. \tag{2.5}$$

For the energy Euler equation, there are various forms one may adopt. Expanding out the derivatives in (2.3) and using (2.4) and (2.5) we can reduce it to

$$\rho \frac{De}{Dt} + p \, \boldsymbol{\nabla} . \mathbf{u} = 0. \tag{2.6}$$

Furthermore, eliminating the divergence of $\mathbf{u}$, using again (2.4), leads to

$$\frac{De}{Dt} - \frac{p}{\rho^2} \frac{D\rho}{Dt} = 0. \tag{2.7}$$

Moreover, we assume that the gas is ideal so that it obeys the equation of state

$$p = \mathcal{R} \rho T, \tag{2.8}$$

with $\mathcal{R}$ a characteristic constant of the particular gas under consideration. This is a good approximation under almost all normal conditions.

In ideal gases the internal energy is a function of temperature only, and we write $e = e(T)$. Furthermore, in many situations it is empirically found that the specific heats c_p and c_v are constants over large ranges of temperature; an ideal gas with constant specific heats is usually called *polytropic*. The specific heat at constant volume is $c_v = (de/dT)_v$ so if c_v is constant we have $e = c_v T$. Furthermore, the

specific heat at constant pressure is $c_p = (dh/dT)_p$, where $h = e + p/\rho$ is the enthalpy per unit mass, and if c_p is constant we have $h = c_p T$. Therefore for a polytropic gas e and h are both linear functions of temperature. From $p/\rho = h - e = (c_p - c_v)T$ and (2.8) we have $\mathcal{R} = (c_p - c_v)$, and it is also customary to define[1] $\gamma = c_p/c_v$ (see Whitham [126], p.153). Therefore (2.7) becomes

$$0 = \frac{De}{Dt} - \frac{p}{\rho^2}\frac{D\rho}{Dt} = \frac{c_v}{\mathcal{R}\rho}\frac{Dp}{Dt} - \left(\frac{c_v p}{\mathcal{R}\rho^2} + \frac{p}{\rho^2}\right)\frac{D\rho}{Dt}, \tag{2.9}$$

$$= \frac{c_v}{\mathcal{R}\rho}\left(\frac{Dp}{Dt} - \frac{\gamma p}{\rho}\frac{D\rho}{Dt}\right), \tag{2.10}$$

$$= c_v T \frac{D}{Dt}\left(\log\frac{p}{\rho^\gamma}\right). \tag{2.11}$$

Letting $S = c_v \log\dfrac{p}{\rho^\gamma} + S_0$, where S_0 is a constant, (2.11) takes the simple form

$$\frac{DS}{Dt} = 0, \tag{2.12}$$

where S is the entropy per unit mass, that arises in thermodynamics. Equation (2.12) states that S remains constant following a fluid particle. Flows that satisfy (2.12) are usually called *isentropic*. Furthermore, equation (2.12) can be recast in the simpler form

$$p\rho^{-\gamma} = \kappa = \text{constant, for a fluid particle.} \tag{2.13}$$

If additionally the entropy of every fluid particle is the same, $S = S_0$ thoughout the flow and the flow is called *homentropic*.

Finally, equation (2.10) shows that we can write (2.6) as

$$\frac{Dp}{Dt} = c^2\frac{D\rho}{Dt}, \tag{2.14}$$

where

$$c(p,\rho) = \sqrt{\frac{\gamma p}{\rho}} = \sqrt{\gamma\mathcal{R}T} \tag{2.15}$$

is the speed of sound with which sound waves propagate relative to the local fluid velocity $\mathbf{u}$ (see Whitham [126], pp. 161–163). In the rest of this thesis we will be using the latter form of the energy equation.

[1]For the air under everyday conditions γ is approximately equal to 1.4.

2.2 Rankine-Hugoniot conditions

In supersonic flows, discontinuities such as shocks or vortex sheets[2] arise and the Euler differential equations presented above do not hold on them. They need to be interpreted in the sense of distribution theory or replaced by an equivalent integral formulation which directly represents the physical laws. The integral formulation is derived by considering a fixed arbitrary volume occupied by the fluid, $\mathcal{V}$, with surface $\mathcal{S}$, and writing down the net balance for mass, momentum and energy for that region; a detailed derivation can be found in most gas dynamics books (see, for instance, Ockendon and Ockendon [82], Chapter 2) so we do not pursue it here. Even though the partial differential equations above are derived from an integral formulation we presented them as differential equations first, since in most of this work we will be using them rather than the integral formulation. For the Euler equations the integral formulation is

$$\frac{d}{dt}\int_{\mathcal{V}} \rho d\mathcal{V} + \int_{\mathcal{S}} \rho \mathbf{u}.d\mathbf{S} = 0, \tag{2.16}$$

$$\frac{d}{dt}\int_{\mathcal{V}} \rho \mathbf{u} d\mathcal{V} + \int_{\mathcal{S}} \rho \mathbf{u}(\mathbf{u}.d\mathbf{S}) + \int_{\mathcal{S}} p d\mathbf{S} = \int_{\mathcal{V}} \rho \mathbf{F} d\mathcal{V}, \tag{2.17}$$

$$\frac{d}{dt}\int_{\mathcal{V}} (\rho e + \frac{1}{2}\rho \mathbf{u}^2) d\mathcal{V} + \int_{\mathcal{S}} \left(\rho e + \frac{1}{2}\rho \mathbf{u}^2\right) \mathbf{u}.d\mathbf{S} + \int_{\mathcal{S}} p\mathbf{u}.\mathbf{n} d\mathbf{S} = \int_{\mathcal{V}} \rho \mathbf{u}.\mathbf{F} d\mathcal{V}. \tag{2.18}$$

From these integral equations we can deduce the correct relations for the jump of the flow quantities across a discontinuity. These relations are called the Rankine-Hugoniot (R-H) conditions; for the derivation see, for instance, Chapman [21], pp. 10–18. We consider a surface of discontinuity with velocity $\mathbf{V}$ and normal $\mathbf{n}$ where $\mathbf{V}$ is taken to be parallel to $\mathbf{n}$. The R-H conditions, corresponding respectively to (2.16), (2.17), and (2.18), are

$$[\rho(\mathbf{u} - \mathbf{V}).\mathbf{n}] = 0, \tag{2.19}$$

$$[\rho \mathbf{u}(\mathbf{u} - \mathbf{V}).\mathbf{n}] = -[p\mathbf{n}], \tag{2.20}$$

$$[\rho(e + \frac{1}{2}\mathbf{u}^2)(\mathbf{u} - \mathbf{V}).\mathbf{n}] = -[p\mathbf{u}.\mathbf{n}], \tag{2.21}$$

where [...] denotes a jump across the discontinuity. Note that $\mathbf{V}$ appears in (2.19)–(2.21) only through $\mathbf{V}.\mathbf{n}$, and from now on we let $\mathbf{V}.\mathbf{n} = V$. Also, note that the external force $\mathbf{F}$ does not appear in (2.19)–(2.21).

We first consider shock discontinuities. Shocks have non-zero mass flow across them and hence the relation $\rho(\mathbf{u}.\mathbf{n} - V) \neq 0$ holds. We can then subtract from (2.21)

[2] A vortex sheet can also be called a contact discontinuity.

the scalar product of $\mathbf{V}$ with equation (2.20), and use (2.19) to re-express the energy R-H condition (2.21) as

$$\left[e + \frac{p}{\rho} + \frac{(\mathbf{u} - \mathbf{V})^2}{2}\right] = 0. \tag{2.22}$$

We deduce from (2.22) that the total *head*

$$H = e + \frac{p}{\rho} + \frac{\mathbf{u}^2}{2} + \psi \tag{2.23}$$

is conserved across a stationary shock for which $\mathbf{V} = 0$. The symbol ψ is for the potential associated with an external conservative force $\mathbf{F} = -\boldsymbol{\nabla}\psi$ (note that $[\psi] = 0$). From (2.20) it follows that $\mathbf{u} \times \mathbf{n}$, the component of the fluid velocity tangential to the shock surface, is continuous across the shock (see, for instance, Chapman [21], pp. 85–87).

The R-H conditions do not determine the flow pattern uniquely. From the second law of thermodynamics the entropy can only increase when a particle crosses a shock; it is only by imposing this additional entropy condition that uniqueness can be ensured (see, for instance, Ockendon and Tayler [84], p. 84).

For vortex sheets, since there is no mass flow across, we have $\rho(\mathbf{u}.\mathbf{n} - V) = 0$. Therefore the normal component of the velocity $\mathbf{u}.\mathbf{n}$ is continuous, and the left-hand side of (2.20) is zero. Consequently the right-hand side gives that the pressure is continuous across the vortex sheet. Furthermore, equation (2.21) is automatically satisfied. The equations do not give any information about the jump in the tangential velocity $\mathbf{u} \times \mathbf{n}$ across the vortex sheet, so this jump is arbitrary. Also, for the same reason, no entropy condition is necessary and arbitrary values of the entropy may be taken at the two sides of the sheet.

2.3 Crocco's equation

Below, we derive Crocco's equation for a *smooth*, unsteady flow in an ideal gas

$$\boldsymbol{\nabla} H = -\frac{\partial \mathbf{u}}{\partial t} + \mathbf{u} \times \boldsymbol{\omega} + T\,\boldsymbol{\nabla} S, \tag{2.24}$$

which is needed in Section 2.4. From the momentum equation (2.5) and the vector identity

$$(\boldsymbol{\nabla} \times \mathbf{u}) \times \mathbf{u} = (\mathbf{u}.\boldsymbol{\nabla})\mathbf{u} - \boldsymbol{\nabla}\left(\frac{1}{2}\mathbf{u}^2\right), \tag{2.25}$$

we have

$$\frac{\partial \mathbf{u}}{\partial t} = -\boldsymbol{\omega} \times \mathbf{u} - \boldsymbol{\nabla}\left(\frac{1}{2}\mathbf{u}^2\right) - \frac{\boldsymbol{\nabla} p}{\rho} + \mathbf{F}. \tag{2.26}$$

Using the thermodynamic relation

$$TdS = de + pd(1/\rho) \Rightarrow TdS = dh - \frac{dp}{\rho}, \tag{2.27}$$

(see, for instance, Whitham [126]) we can eliminate $\boldsymbol{\nabla}\, p/\rho$ from (2.26) and deduce

$$\frac{\partial \mathbf{u}}{\partial t} = -\boldsymbol{\omega} \times \mathbf{u} + T\, \boldsymbol{\nabla}\, S - \boldsymbol{\nabla}\, h - \boldsymbol{\nabla} \left(\frac{1}{2} \mathbf{u}^2 \right) + \mathbf{F}. \tag{2.28}$$

Collecting the $\boldsymbol{\nabla}$ terms together on the left-hand side and using $\mathbf{F} = -\boldsymbol{\nabla}\, \psi$, we end up with equation (2.24) as required.

Note that taking the curl of (2.24) results in the vorticity equation

$$\frac{D\boldsymbol{\omega}}{Dt} = (\boldsymbol{\omega}.\, \boldsymbol{\nabla})\mathbf{u} - \boldsymbol{\omega}(\boldsymbol{\nabla}\, .\mathbf{u}) + \boldsymbol{\nabla}\, T \times \boldsymbol{\nabla}\, S. \tag{2.29}$$

2.4 Circulation theorem in a flow with shocks

In a flow with shocks it is important to determine how the amount of the vorticity produced downstream of a shock is related to the entropy jump at the shock. In the gas dynamics literature, this question is addressed using Crocco's equation. However, Crocco's equation relates $\boldsymbol{\omega} \times \mathbf{u}$, the component of vorticity perpendicular to $\mathbf{u}$, to the entropy gradients in the flow but does not say anything about $\boldsymbol{\omega}.\mathbf{u}$, the component of vorticity parallel to $\mathbf{u}$. The relation of both components of vorticity to the entropy change can be deduced from a Circulation Theorem, valid in the presence of shocks. To our knowledge, such a theorem does not exist in the literature so we prove it below (see also Allwright and Kaouri [8]).

We consider a closed curve $\mathcal{C}$ consisting of fluid particles moving with the flow. The circulation around this closed curve is $\Gamma = \int_{\mathcal{C}} \mathbf{u}.d\mathbf{x}$. We assume that there are shocks in the flow at which the R-H conditions hold and that m of them intersect $\mathcal{C}$ transversely, at the points $\mathbf{P}_i(t)$, $1 \leq i \leq m$ (for a schematic, where four shocks are shown, see Figure 2.1). The sense of integration in the integral defining Γ and the order in which we label the shock positions has to be taken the same. In general, there will be a discontinuity in the tangent to $\mathcal{C}$ at each shock position $\mathbf{P}_i(t)$.

We now write $\mathcal{C} = \sum_{i=1}^{n} \mathcal{C}_i$ where $\mathcal{C}_i$ is the part of $\mathcal{C}$ from $\mathbf{P_i}$ to $\mathbf{P_{i+1}}$, on which the flow is smooth. The circulation around $\mathcal{C}$ is then given by

$$\Gamma = \sum_{i=1}^{n} \int_{\mathcal{C}_i} \mathbf{u}.d\mathbf{x} = \sum_{i=1}^{n} \Gamma_i. \tag{2.30}$$

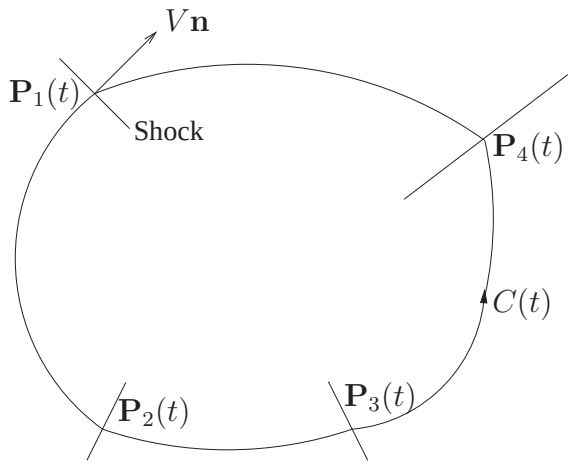

Figure 2.1: Closed material curve $C(t)$ cut by shocks at positions $\mathbf{P}_i(t)$. Here $1 \leq i \leq 4$.

To construct a circulation theorem we consider

$$\frac{d\Gamma}{dt} = \sum_{i=1}^{n} \frac{d}{dt}\left(\int_{\mathcal{C}_i} \mathbf{u}.d\mathbf{x}\right) = \sum_{i=1}^{n} \frac{d\Gamma_i}{dt}. \tag{2.31}$$

For each $\mathcal{C}_i$ we need to evaluate $\dfrac{d\Gamma_i}{dt} = \displaystyle\int_{\mathcal{C}_i} \mathbf{u}.d\mathbf{x}$. To do this we use the Transport Theorem for an open curve, proved in Appendix A; the general vector field $\mathbf{a}(\mathbf{x}, t)$ there is replaced by $\mathbf{u}(\mathbf{x}, t)$ here. This transport theorem is a slight modification of the standard transport theorem for an open material curve whose ends move with the fluid (see, Batchelor [14], p. 269). This gives

$$\frac{d}{dt}\int_{\mathcal{C}_i} \mathbf{u}.d\mathbf{x} = \mathbf{u}\left(\mathbf{P}_{i+1}^{-}\right).\dot{\mathbf{P}}_{i+1} - \mathbf{u}\left(\mathbf{P}_i^{+}\right).\dot{\mathbf{P}}_i + \int_{\mathbf{P}_i^{+}}^{\mathbf{P}_{i+1}^{-}} \left(\frac{\partial \mathbf{u}}{\partial t} + (\boldsymbol{\nabla} \times \mathbf{u}) \times \mathbf{u}\right).d\mathbf{x}. \tag{2.32}$$

From Crocco's equation (2.24), the integral term in the right-hand side of (2.32) becomes

$$\int_{\mathbf{P}_i^{+}}^{\mathbf{P}_{i+1}^{-}} \left(T\,\boldsymbol{\nabla} S - \boldsymbol{\nabla} H\right).d\mathbf{x} = \int_{\mathbf{P}_i^{+}}^{\mathbf{P}_{i+1}^{-}} T dS - H|_{\mathbf{P}_i^{+}}^{\mathbf{P}_{i+1}^{-}}. \tag{2.33}$$

Using (2.33) in (2.32), and summing up all the $\mathcal{C}_i$ contributions, we find

$$\frac{d\Gamma}{dt} = \sum_i \int_{\mathbf{P}_i^{+}}^{\mathbf{P}_{i+1}^{-}} T dS + \sum_i [H]_i + \sum_i \left(\mathbf{u}\left(\mathbf{P}_{i+1}^{-}\right).\dot{\mathbf{P}}_{i+1} - \mathbf{u}\left(\mathbf{P}_i^{+}\right).\dot{\mathbf{P}}_i\right). \tag{2.34}$$

The second term in the right-hand side of (2.34) is the sum of $[H]_i$, the jump in the total head H at the ith shock.

We will show now that the R-H conditions (2.19)–(2.21) lead to a simplified form of (2.34). Using the energy R-H condition (2.22) and defining $\mathbf{u}_i^{\pm} = \mathbf{u}(\mathbf{P}_i^{\pm})$, we find that

$$\sum_i [H]_i = \sum_i \mathbf{V}_i.(\mathbf{u}_i^+ - \mathbf{u}_i^-). \tag{2.35}$$

The terms involving the potentials ψ_i all add up to zero. Also, by regrouping the terms in pairs over the ith shock, the last term in the right-hand side of (2.34), can be expressed as

$$\sum_i \left(\mathbf{u}_{i+1}^-.\dot{\mathbf{P}}_{i+1} - \mathbf{u}_i^+.\dot{\mathbf{P}}_i \right) = -\sum_i \dot{\mathbf{P}}_i.(\mathbf{u}_i^+ - \mathbf{u}_i^-). \tag{2.36}$$

Adding (2.35) and (2.36) and dropping the subscripts we find that at each shock we have a term of the form $[\mathbf{u}.(\mathbf{V} - \dot{\mathbf{P}})]$. Using the vector identity

$$\mathbf{a}.\mathbf{b} = (\mathbf{a} \times \mathbf{c}).(\mathbf{b} \times \mathbf{c}) + (\mathbf{a}.\mathbf{c})(\mathbf{b}.\mathbf{c}), \tag{2.37}$$

(valid for any unit vector $\mathbf{c}$) we can write

$$\mathbf{u}^{\pm}.(\mathbf{V} - \dot{\mathbf{P}}) = (\mathbf{u}^{\pm} \times \mathbf{n}).((\mathbf{V} - \dot{\mathbf{P}}) \times \mathbf{n}) + (\mathbf{u}^{\pm}.\mathbf{n})((\mathbf{V} - \dot{\mathbf{P}}).\mathbf{n}), \tag{2.38}$$

where $\mathbf{n}$ is the normal to the shock at $\mathbf{P}$. In (2.38) the first term in the right-hand side is equal on both sides of the shock because the tangential velocity $\mathbf{u} \times \mathbf{n}$ is continuous across the shock. The second term is zero on both sides of the shock since $\dot{\mathbf{P}}.\mathbf{n} = \mathbf{V}.\mathbf{n} = V$ in order for $\mathbf{P}$ to stay on the shock. Therefore, equation (2.34) becomes

$$\frac{d\Gamma}{dt} = \sum_i \int_{\mathbf{P}_i^+}^{\mathbf{P}_{i+1}^-} T dS, \tag{2.39}$$

which can be written as

$$\frac{d\Gamma}{dt} = \int_{\mathcal{C}}{}' T dS. \tag{2.40}$$

The prime on the integral in the right-hand side of (2.40) signifies that it is only taken along the smooth parts of the flow; the entropy jumps *at* the shocks are *not* accounted for. To understand this lucidly, we consider a plane shock, with uniform incident flow. If the flow upstream of the shock has constant entropy S_0, then the circulation $\Gamma_0 = 0$; downstream of the shock, the entropy attains a higher but still contant value, S_0'. Since $dS_0 = dS_0' = 0$, from (2.40) we have $\dfrac{d\Gamma}{dt} = 0$, and therefore $\Gamma = \Gamma_0 = 0$. Therefore after a plane uniform shock there is no vorticity production (Stokes' theorem). However for a shock that is curved and/or with varying strength, from (2.40), there are entropy gradients downstream of the shock which result in a

non-zero value for the circulation, and generally lead to vorticity production. We remark that for simply connected regions, from Stokes' theorem, non-zero circulation leads to non-zero vorticity and vice versa. For multiply connected regions, e.g caused by an obstruction in the flow, we cannot apply Stokes' theorem to a curve encircling the obstruction. It is therefore possible to have non-zero circulation around a material curve that encircles the obstruction but zero vorticity in the fluid.

One very useful application of the circulation theorem proved above is for *weak* shocks, such as those involved in sonic booms. It is well-known that for weak shocks with strength of order ϵ, the entropy jump is of order ϵ^3. A general proof of this is found in Chapman [21], pp. 87–91 for normal shocks in an arbitrary gas[3]; the only necessary assumption is that the gas has a convex equation of state, that is $(\partial^2 p/\partial v^2)_S > 0$ where $v = 1/\rho$. Applying (2.40) to any closed material curve in the incident gas, we conclude that the vorticity in the flow behind a weak shock is also of order ϵ^3. This result is used in Chapter 4 to justify the use of potential flow downstream of a shock (up to secobd order in ϵ). Note that equation (2.40) can also be used as an additional check on the accuracy of numerical calculations for flows behind shocks of *any* strength.

The circulation theorem proved above is an extension of Kelvin's well-known Circulation theorem for barotropic flows and Bjerknes theorem [16]. Like those theorems, it is valid for any unsteady flow and can be applied in the presence of obstructions in the flow (e.g. an aerofoil).

We finally note that it is possible that at a certain instant $t = t^\star$, $\mathcal{C}(t)$ is tangential to a shock surface and the number of shocks crossing $\mathcal{C}$ in general changes. However for instantaneous tangencies the circulation Γ is continuous at $t^\star$. Therefore, if we allow $\dfrac{d\Gamma}{dt}|_{t^\star_-} \neq \dfrac{d\Gamma}{dt}|_{t^\star_+}$ equation (2.40) holds for $t < t^\star$ and $t > t^\star$. At vortex sheets, the problem is more fundamental and the theorem would need modification—see [8].

[3]In Liepmann and Roshko [70], p. 60 and Whitham [126], p. 176, the same result is proved, but for the special case of a polytropic gas.

Chapter 3

Linear acoustics and ray theory

In this chapter we first give a detailed account of the definitions used in the ray theory approach to sound propagation, especially as applied to sonic boom problems. We then solve a series of analytical examples of sound propagation in various model stratified atmospheres, which help us to clarify aspects of the long-range propagation of sound, and in particular of secondary boom. Special attention is drawn to the focusing of rays and boomrays. Where possible we compare our results with the numerical results for a typical atmopshere.

3.1 Linearised gas dynamics

We start from the Euler equations for unsteady compressible flow (2.4), (2.5) and (2.10). We shall linearise for small perturbations about an ambient state with pressure $p_0(\mathbf{x})$, density $\rho_0(\mathbf{x})$ and flow $\mathbf{u}_0(\mathbf{x})$. This ambient state must obey the equations

$$\boldsymbol{\nabla}.(\rho_0\mathbf{u}_0) = 0, \tag{3.1}$$

$$\boldsymbol{\nabla}\, p_0 + \rho_0\mathbf{g} = 0, \tag{3.2}$$

$$\mathbf{u}_0.(\boldsymbol{\nabla}\, p_0 - c^2\,\boldsymbol{\nabla}\,\rho_0) = 0. \tag{3.3}$$

We shall make the slightly more restrictive assumption that $\mathbf{u}_0.\,\boldsymbol{\nabla}\, p_0 = 0$, so also $\mathbf{u}_0.\,\boldsymbol{\nabla}\,\rho_0 = 0$ and $\boldsymbol{\nabla}.\mathbf{u}_0 = 0$. These assumptions hold, for instance, in a gravitationally stratified atmosphere with horizontal wind. Equation (3.2) expresses the fact that the ambient medium is in hydrostatic equilibrium. From this equation the atmospheric length-scale of variation $H = P_0/(D_0 g)$ can be identified, where P_0 and D_0 are respectively reference pressure and density values. The height H is usually called the scale height of the atmosphere.

In (2.4), (2.5) and (2.10) we set $p = p_0 + p'$, $\rho = \rho_0 + \rho'$ and $\mathbf{u} = \mathbf{u}_0 + \mathbf{u}'$, where p' and ρ' are small compared with the respective ambient values and $|\mathbf{u}'| \ll c$. Substituting into (2.4), (2.5) and (2.10) and linearising we obtain

$$\frac{\partial \rho'}{\partial t} + \boldsymbol{\nabla} .(\rho_0 \mathbf{u}' + \mathbf{u}_0 \rho') = 0, \tag{3.4}$$

$$\rho_0 \left(\frac{\partial \mathbf{u}'}{\partial t} + \mathbf{u}_0 . \boldsymbol{\nabla}\, \mathbf{u}' + \mathbf{u}' . \boldsymbol{\nabla}\, \mathbf{u}_0 \right) = - \boldsymbol{\nabla}\, p' - \rho' \mathbf{g}, \tag{3.5}$$

$$\frac{\partial p'}{\partial t} + \mathbf{u}_0 . \boldsymbol{\nabla}\, p' + \mathbf{u}' . \boldsymbol{\nabla}\, p_0 = c^2 \left(\frac{\partial \rho'}{\partial t} + \mathbf{u}_0 . \boldsymbol{\nabla}\, \rho' + \mathbf{u}' . \boldsymbol{\nabla}\, \rho_0 \right), \tag{3.6}$$

where $c = c(x, y, z)$ is the local speed of sound in an unperturbed atmosphere. To a good approximation the air can be considered to be a polytropic gas and therefore the speed of sound is $c = \sqrt{\gamma p_0 / \rho_0}$.

We shall see that the system (3.4)–(3.6) sustains acoustic waves, and these will be our main concern. However, it also sustains gravity waves; a detailed discussion of the combined theory of these two types of waves appears in Lighthill [72], Section 4.2. Acoustic waves involved in secondary sonic boom (SSB) propagation can be considered decoupled from internal gravity waves because the latter waves have a much larger period. The gravity term in the momentum equation (3.5) can therefore be neglected, even though the ambient pressure p_0 varies. (In Chapter 5, where we consider a moving thin aerofoil in a weakly stratified atmosphere with wind, we will retain the gravity term but we will show that its effects cancel out in the leading-order calculation of the wavefield.) Atmospheric gravity waves are however present in practice, due to normal atmospheric dynamics and these may affect SSB propagation, but we do not consider them here.[1]

In sonic boom research, linear acoustics play an important role since a moving thin aerofoil or a slender body causes only small perturbations to the ambient medium, and, in many cases, the squares of these perturbations can be assumed to be negligible, leading thus to a linear problem. The long-range propagation of secondary boom can be determined to a good approximation by linear theory, and this is what we are going to concentrate on in this chapter. However, in order to predict the amplitude of the boom correctly to first order nonlinear effects have to be retained; we shall discuss this in detail in Chapter 5.

The theory of linear acoustics in a stationary medium is sufficient for investigating the propagation of thermospheric SSBs and these will be our main concern in this

[1] Within the SOBER programme, observed atmospheric gravity wave structures were simulated [6] and it was found that these waves indeed alter appreciably some details of SSB propagation [7].

chapter. Stratospheric SSBs, occurring only in the presence of wind, will be briefly considered in Section 3.10, using linear acoustics in moving media.

To examine a stationary medium we now set $\mathbf{u}_0 = 0$. We also set $\mathbf{g} = \mathbf{0}$, as justified by our discussion above. Equations (3.4)–(3.6) can be reduced to a single equation for pressure. We first use (3.6) to eliminate $\dfrac{\partial \rho'}{\partial t}$ from (3.4) and then differentiate the resulting equation with respect to t to get

$$c^{-2} p'_{tt} + c^{-2} \frac{\partial \mathbf{u}'}{\partial t} . \boldsymbol{\nabla} p_0 + \rho_0 \boldsymbol{\nabla} . \frac{\partial \mathbf{u}'}{\partial t} = 0. \tag{3.7}$$

Combining (3.7) and $\dfrac{\partial \mathbf{u}'}{\partial t} = -\dfrac{1}{\rho_0} \boldsymbol{\nabla} p'$, obtained from (3.5), multiplying by $-c^2$, and dropping the dashes, we obtain the second-order wave equation

$$c^2 \boldsymbol{\nabla}^2 p - p_{tt} + \frac{1}{\rho_0} \boldsymbol{\nabla} p . (\boldsymbol{\nabla} p_0 - c^2 \boldsymbol{\nabla} \rho_0) = 0. \tag{3.8}$$

The wavelength of the perturbations is of the order of the body length L, which is around 10 m for a wing and around 100 m for the fuselage. Furthermore, for a typical atmosphere H is around 8 km. We can thus define a small parameter $\delta = L/H$ which is of order 10^{-3} for a wing, and of order 10^{-2} for the fuselage. We will non-dimensionalise equation (3.8) using $\mathbf{x} = L\hat{\mathbf{x}}$, $p = P_0 \hat{p}(\tilde{z})$, $\rho = D_0 \hat{\rho}(\tilde{z})$, $c = C_0 \hat{c}$, where $\tilde{z} = z/H = \delta \hat{z}$ and $C_0 = \sqrt{\gamma P_0 / D_0}$. We also take $t = \dfrac{L}{C_0} \hat{t}$. We obtain

$$\hat{c}^2 \hat{\boldsymbol{\nabla}}^2 \hat{p} - \hat{p}_{\hat{t}\hat{t}} + \frac{\delta}{\hat{\rho}_0} \hat{\boldsymbol{\nabla}} \hat{p} . (\frac{1}{\gamma} \tilde{\boldsymbol{\nabla}} \hat{p}_0 - \hat{c}^2 \tilde{\boldsymbol{\nabla}} \hat{\rho}_0) = 0, \tag{3.9}$$

where $\hat{\boldsymbol{\nabla}}$ denotes differentiation with respect to $\hat{\mathbf{x}}$, and $\tilde{\boldsymbol{\nabla}}$ denotes differentiation with respect to $\tilde{z}$. Since δ is small, at leading order in δ we drop the terms involving the gradients of p_0 and ρ_0, and we obtain the wave equation

$$c^2(\tilde{z}) \hat{\boldsymbol{\nabla}}^2 p - p_{\hat{t}\hat{t}} = 0. \tag{3.10}$$

In this form, we are looking for order 1 wavelengths in a slowly varying medium. Alternatively, we can divide (3.10) by δ^2, and let $\tilde{t} = \delta \hat{t}, \tilde{\mathbf{x}} = \delta \hat{\mathbf{x}}$, and then (dropping the tildes) we have

$$c^2(z) \boldsymbol{\nabla}^2 p - p_{tt} = 0, \tag{3.11}$$

where we would be looking for wavelengths of order δ (in a medium with order 1 variations), i.e. large wavenumber solutions.

We shall see in Chapter 4 that the wave equation geometry provides a good first approximation to the position of weak shocks, even though the shocks are an intrinsically nonlinear phenomenon. In Chapter 5, where we will address the introduction of nonlinear effects in a paradigm problem for the prediction of SSB amplitudes, we will also treat the stratification issue much more fully by retaining the terms of order δ.

The wave equation is ubiquitous; two fields in which it commonly arises are elasticity and electromagnetism. In electromagnetism, in free space, each component of the electric field vector $\mathbf{E}$ and the magnetic flux density vector $\mathbf{B}$ satisfy wave equations and the speed of light is given by $c = 1/\sqrt{\mu_0 \epsilon_0}$ where ϵ_0 is the electric permittivity and μ_0 the magnetic permeability. In isotropic linear elasticity, the displacement of a particle from an unstressed reference configuration $\mathbf{v}(\mathbf{x}, t)$, can be expressed as the sum of $\mathbf{v}_P = \boldsymbol{\nabla}\, \phi_P$ and $\mathbf{v}_S = \boldsymbol{\nabla} \times \mathbf{A}$ where ϕ_P and the components of $\mathbf{A}$ satisfy wave equations. (The subscript P stands for primary or pressure waves and the subscript S for secondary or shear waves.)

We proceed from now on with the paradigm problem of a point impulsive source at $(\mathbf{x}_0, t_0)$. We do not lose much generality by doing so, as the solution of the wave equation for an extended body can be expressed as a linear superposition of the solutions corresponding to such point sources.

A surface $\psi = 0$ is a characteristic surface of (3.11) if it obeys the *eikonal* equation (see Ockendon et al. [85])

$$c^2 |\, \boldsymbol{\nabla}\, \psi|^2 = \psi_t^2. \tag{3.12}$$

(Note that here and for some time we will consider $c = c(\mathbf{x})$ in order to give a more general exposition; we return to stratified media in Section 3.3.) We assume of course that $\psi = 0$ is a *non-singular* representation of the surface, so $\boldsymbol{\nabla}\, \psi$ and ψ_t do not vanish. When (3.12) is solved by Charpit's method [85], the trajectories passing through the source at $(\mathbf{x}_0, t_0)$, called *bicharacteristics*, are the curves on which information propagates [85, 21]. Bicharacteristics form a particular characteristic surface of (3.11), called the *ray conoid* through $(\mathbf{x}_0, t_0)$. The part of the ray conoid in $t > t_0$ is the *boundary* of the region of influence of $(\mathbf{x}_0, t_0)$, and the part in $t < t_0$ is the boundary of its dependence domain.

In order to solve equation (3.12), we recast it in the form

$$F = \frac{1}{2}\left(\psi_t - \frac{c^2}{\psi_t}(\psi_x^2 + \psi_y^2 + \psi_z^2)\right) = 0. \tag{3.13}$$

Letting $p = \psi_x, q = \psi_y, r = \psi_z, \lambda = \psi_t$, equation (3.13) becomes

$$F = \frac{1}{2}\left(\lambda - \frac{c^2}{\lambda}(p^2 + q^2 + r^2)\right) = 0. \tag{3.14}$$

(Note that p no longer represents the pressure.) Charpit's method reduces the non-linear partial differential equation (PDE) to a system of eight ordinary differential equations which yield the bicharacteristics. Bicharacteristics are also frequently called *rays* and from now on when we refer to rays it will be in this context. Also, frequently the ray conoid may be called *ray surface*. Charpit's equations for the coordinates $(\mathbf{x}, t) = (x, y, z, t)$ are

$$\frac{dx}{ds} = \frac{\partial F}{\partial p} = -c^2\frac{p}{\lambda}, \tag{3.15}$$

$$\frac{dy}{ds} = \frac{\partial F}{\partial q} = -c^2\frac{q}{\lambda}, \tag{3.16}$$

$$\frac{dz}{ds} = \frac{\partial F}{\partial r} = -c^2\frac{r}{\lambda}, \tag{3.17}$$

$$\frac{dt}{ds} = \frac{\partial F}{\partial \lambda} = \frac{1}{2} + \frac{c^2}{2\lambda^2}(p^2 + q^2 + r^2) = 1. \tag{3.18}$$

When $s = s_0$, $(\mathbf{x}, t)$ takes the initial value $(\mathbf{x}_0, t_0)$. Integrating equation (3.18) and taking $s_0 = t_0$ we deduce that $s = t$. Therefore the parameter *along* the rays is the time t, and this is why we use (3.13) instead of (3.12). The remaining four Charpit's equations for p, q, r and λ are

$$\frac{dp}{ds} = -\frac{\partial F}{\partial x} - p\frac{\partial F}{\partial \psi} = c_x\lambda/c, \tag{3.19}$$

$$\frac{dq}{ds} = -\frac{\partial F}{\partial y} - q\frac{\partial F}{\partial \psi} = c_y\lambda/c, \tag{3.20}$$

$$\frac{dr}{ds} = -\frac{\partial F}{\partial z} - q\frac{\partial F}{\partial \psi} = c_z\lambda/c, \tag{3.21}$$

$$\frac{d\lambda}{ds} = -\frac{\partial F}{\partial t} - r\frac{\partial F}{\partial \psi} = 0 \Rightarrow \lambda = \lambda_0. \tag{3.22}$$

In order to be able to solve the system the initial values $(p_0, q_0, r_0, \lambda_0)$ should also be provided, satisfying (3.14). Equation (3.22) gives that λ is conserved along the rays, and by rescaling (p, q, r) we can set $\lambda_0 = 1$. This homogeneity in time arises because the medium is time-independent and it is also expressed by the relation

$$\psi(\mathbf{x}, t) = t - \sigma(\mathbf{x}). \tag{3.23}$$

(The choice of $\lambda_0 > 0$ corresponds to the convention that $\psi > 0$ behind the surface and $\psi < 0$ ahead of it.) The family of surfaces $\sigma(\mathbf{x}) = t$ are the *wavefronts*. A

wavefront is a surface along which waveform features are received concurrently, and is a concept which is pivotal in the study of waves.

Since the outward unit local normal to the surface $\psi = 0$ is

$$\mathbf{n} = -\frac{\boldsymbol{\nabla}\,\psi}{|\,\boldsymbol{\nabla}\,\psi|} = -\frac{(p,q,r)}{\sqrt{p^2+q^2+r^2}} = -(p,q,r)c, \tag{3.24}$$

the set of scalar equations (3.15)–(3.18) can be abbreviated into the vector equation

$$\frac{d\mathbf{x}}{dt} = c\mathbf{n}, \tag{3.25}$$

which expresses the fact that along the rays the wavefront travels with speed c. Since from (3.23) we can write $\mathbf{n} = \boldsymbol{\nabla}\,\sigma/|\,\boldsymbol{\nabla}\,\sigma|$, relation (3.25) also expresses the fact that in a stationary medium the rays are orthogonal to the wavefronts. Furthermore, (3.19)–(3.22) can be abbreviated into

$$d(p,q,r)/dt = \boldsymbol{\nabla}\,c/c, \tag{3.26}$$

and therefore, differentiating (3.24) with respect to t and using (3.26) we find

$$\frac{d\mathbf{n}}{dt} = -\,\boldsymbol{\nabla}\,c + (\mathbf{n}.\,\boldsymbol{\nabla}\,c)\mathbf{n}. \tag{3.27}$$

Equation (3.27) dictates the evolution of $\mathbf{n}$ along rays and it thus expresses the refraction of acoustic rays by the sound speed gradient. In optics the same equation expresses the refraction of optical rays in a medium with a smoothly varying refractive index.

As a simple example, we determine the ray conoid for a point source at $(0,0,0)$ in a uniform medium. Charpit's equations (3.25) and (3.27) integrate to the ray parametric relations

$$x = -c_0^2 p_0 t, \quad y = -c_0^2 q_0 t, \quad z = -c_0^2 r_0 t, \tag{3.28}$$

and therefore the rays are straight. Eliminating t from (3.28) we obtain the ray cone

$$x^2 + y^2 + z^2 = c_0^2 t^2, \tag{3.29}$$

with vertex at $(0,0,0)$ and the axis of symmetry along the t-axis. The semivertical angle, β say, obeys $\tan\beta = c_0$. In Figure 3.1 we plot the ray cone, choosing $c_0 = 1$.

The constant t-sections of the ray cone give the familiar picture of concentric circular wavefronts generated by a stationary point source (see Figure 3.2).

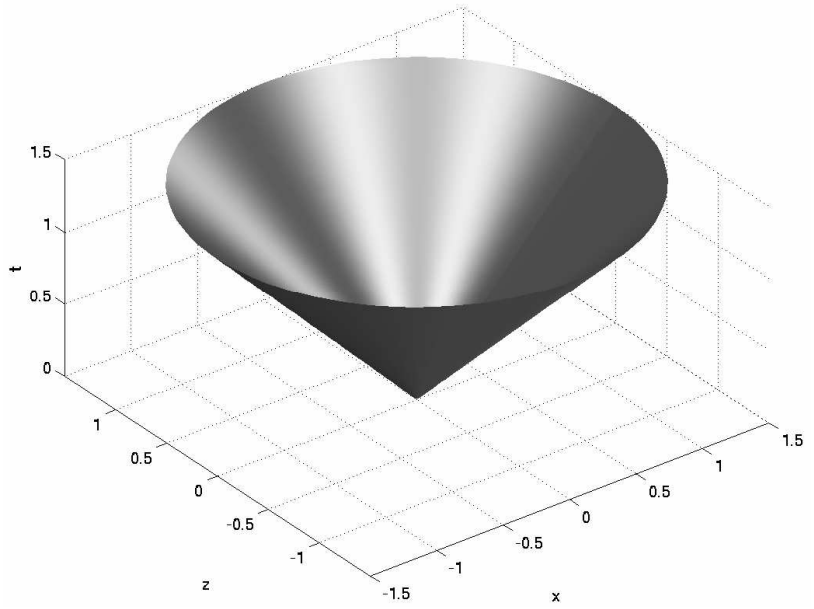

Figure 3.1: Ray cone for a uniform medium ($c_0 = 1$), in the (x, z, t) space.

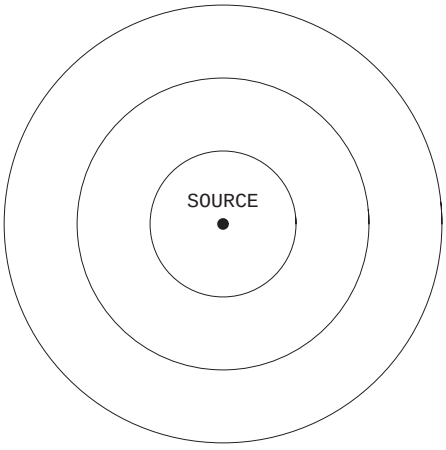

Figure 3.2: Wavefronts generated by a stationary point source in a uniform medium.

Note that the use of equations (3.25) and (3.27) for studying the propagation of sound in non-uniform media did not become established till the 20th century. They are very useful because, even though generally nonlinear, they are of first order and thus amenable to standard numerical techniques (see, for instance, the article by Moler and Solomon [80]). The procedure of determining the rays is frequently called *ray tracing*.

3.2 Geometrical Acoustics

The eikonal equation (3.12) also arises at the leading order of the high-frequency (WKB) approximation to the wave equation. The characteristics of this equation are also called rays. This is the framework of Geometrical Acoustics (GA). We can use a high-frequency approximation when the wavelength is much smaller than the characteristic propagation length in the problem. Also for light, where the wavelength is of order 10^{-7} m, the high-frequency approximation is often appropriate[2], and we refer to the framework of Geometrical Optics (GO). However, high-frequency approximations generally need more scrutiny in the case of sound or elastic waves, where the wavelength can be up to a few metres or kilometres.

Below we outline the GA ansatz, in a medium with an ambient state that is slowly varying in space. We first let the pressure $p = \Re(A\exp(ik\Theta))$, where $k = H/\lambda$ is large, with λ being a typical wavelength of the wave. The amplitude A and the wave phase Θ are both slowly varying in space and time, in the sense that they vary by order 1 when $\mathbf{x}$ varies by order 1. The terms of order k^2 in (3.11) give the eikonal equation[3]

$$\Theta_t^2 = c^2|\boldsymbol{\nabla}\,\Theta|^2, \tag{3.30}$$

which leads to the same bicharacteristics as those of the hyperbolic PDE framework presented above. Since the phase for a plane wave is $\Theta = \mathbf{k}.\mathbf{r} - \omega t$ we may define in general

$$\mathbf{k} = \boldsymbol{\nabla}\,\Theta, \quad \omega = -\frac{\partial\Theta}{\partial t}, \tag{3.31}$$

[2]except in optical fibres, photonic crystals, and so on

[3]Note that the term "eikonal" was introduced in optics by Bruns in 1895 but the concept was already known by Hamilton in 1832. The eikonal equation applicable to propagation of weak acoustic discontinuities was derived by Heller in 1953 [56] and by Keller in 1954 [65]. These derivations were for the more general case of acoustics in moving media.

so that $\mathbf{k}$ is the wavevector and ω the frequency. Therefore the eikonal equation (3.30) becomes

$$\omega^2 = c^2|\mathbf{k}|^2, \tag{3.32}$$

which is the dispersion relation for (3.11).

The word "ray" is somewhat ambiguous in sonic boom literature. We have seen above two uses of this word; in the hyperbolic PDE framework and in the GA framework. Furthermore, an acoustic ray may also stand for the stationary time path of sound just as an optical ray is the stationary path for light. According to this third definition, a ray obeys Fermat's principle.[4] The rays obtained by GA comply with Fermat's principle but the latter principle is more general than GA and can also cater for diffraction phenomena (see Pierce [94], p. 248). Finally, boomrays are also usually called rays in the sonic boom literature; these will be discussed in detail in Section 3.4.2.

3.3 Stratified media and Snell's law

To a first approximation we can assume that the atmosphere is stratified in the vertical direction, so that the local sound speed profile is a function only of the height z, that is $c(\mathbf{x}) = c(z)$. This is in fact an assumption made throughout this thesis, wherever we consider non-uniform media. Charpit's equations (3.15)–(3.22) simplify then to

$$\frac{dx}{dt} = -c^2(z)p_0, \ \frac{dy}{dt} = -c^2(z)q_0, \ \frac{dz}{dt} = -c^2(z)r, \tag{3.33}$$

$$p = p_0, \ q = q_0, \ \frac{dr}{dt} = \frac{c_z}{c}. \tag{3.34}$$

Equations (3.33)–(3.34) show that only r changes with height, and therefore any ray remains in the same vertical plane in which it starts. Since we can always find a coordinate system such that $q_0 = 0$, it is sufficient to pursue only a two-dimensional analysis, with x the horizontal coordinate and z the vertical coordinate. Let θ be the angle a ray makes with the positive x-axis. From (3.33) we have $\cos\theta = \dfrac{1}{c}\dfrac{dx}{dt} = -cp_0$, and since p_0 is constant, we obtain

$$\frac{c(z)}{\cos\theta} = \frac{c_0}{\cos\theta_0}. \tag{3.35}$$

[4]Fermat conjectured in 1657 that optical rays are *least-time* paths. It was Hamilton in 1833 who realised and postulated that they are in fact stationary-time paths with respect to the time of travel in adjacent ray paths. More than one century later (1972) Uginçius proved that the latter principle holds also for acoustic rays in moving media.

This is Snell's law, known to govern the propagation of optical rays in media where the refractive index may vary in the vertical direction. For propagation of sound in a stationary medium, Snell's law is equivalent to p and q being constant. In Section 3.10 we show that the latter is also true for stratified media with horizontal wind. Furthermore, from the first and third equations in (3.33), and using the eikonal equation $c^2(p_0^2 + r^2) = 1$ to express r in terms of p_0, we find

$$\frac{dz}{dx} = \pm\frac{r}{p_0} = \pm\frac{1}{p_0}\sqrt{\frac{1}{c^2} - p_0^2}. \tag{3.36}$$

Since $p_0 = -\cos\theta_0/c_0$, we find that a ray launched at (x_0, z_0) obeys the *ray integral*

$$x - x_0 = \pm\int_{z_0}^{z} \frac{c(z)\cos\theta_0/c_0}{\sqrt{1 - c^2(z)\cos^2\theta_0/c_0^2}}dz, \tag{3.37}$$

where the $\pm$ corresponds to upwards/downwards launching of the ray. The ray integral (3.37) provides an alternative way to calculate rays in stratified media; we can perform the single quadrature on the right-hand side rather than solve the system of Charpit's equations (3.33)–(3.34). However the denominator of (3.37) has a singularity at the turning points of the rays where $\cos\theta = c(z)\cos\theta_0/c_0 = 1$; it is thus preferable to deal directly with the ordinary differential equations if turning points are involved.

3.4 The Mach envelope

Let us now consider a *moving* point source, in a stationary, possibly non-uniform, medium. We denote the displacement of the source by $\mathbf{x}_0(t)$ and its velocity by $\mathbf{U}(t) = \dot{\mathbf{x}}_0(t)$. We also denote by $c_0(\mathbf{x}_0(t), t)$ the sound speed at the source position. We define the Mach number of the source as $M_0 = |\mathbf{U}|/c_0$. For a source moving supersonically we have $M_0 > 1$ and for a source moving subsonically we have $M_0 < 1$.

3.4.1 Mach envelope as envelope of ray conoids

A supersonic source moves faster than the waves it generates and the ray conoids form an envelope, called the Mach envelope.[5] If we represent the ray conoid emanating from $(\mathbf{x}_0(\tau), \tau)$ by $\psi(x, y, z, t; \tau) = 0$, so that τ is the conoid label, the envelope is determined as a function of x, y, z, and t by eliminating τ from the equations

$$\psi = 0 \quad \text{and} \quad \frac{\partial\psi}{\partial\tau} = 0. \tag{3.38}$$

[5]For motions that are supersonic for only part of the time, e.g. acceleration through the sound speed, an envelope is formed only by the supersonic part of the motion (see Chapter 6).

The Mach envelope is very important as it is (to a first approximation) the location of the intensification of the sound field that is called the sonic boom. The Mach envelope is also referred to as the Mach surface or Mach conoid. From now on we will denote it by $\Psi = 0$. We shall take the convention that $\Psi < 0$ ahead of the Mach surface (unshocked gas) and $\Psi > 0$ behind it (shocked gas).

We consider the simple example of a two-dimensional steady supersonic motion, in a uniform medium, and we derive the Mach envelope using condition (3.38) above. We choose the motion to be from right to left on the x-axis, and therefore $\mathbf{U} = (-U, 0)$ and $\mathbf{x}_0(t) = (-Ut, 0)$.

If $M_0 < 1$, at any fixed time t, all circular wavefronts are nested and no envelope is formed. In Figure 3.3 we plot three wavefronts. The disturbance due to the source

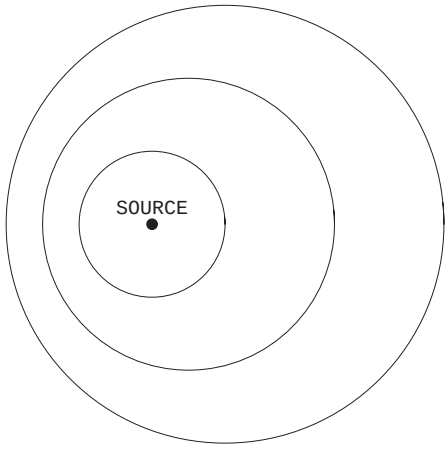

Figure 3.3: $M_0 < 1$: the wavefronts are nested, so no envelope is formed.

at time t, assuming that the motion started at $t = 0$, is confined inside the circle $|\mathbf{x}| \leq c_0 t$. For a source that travels for an infinitely long time the disturbance is felt throughout the whole fluid.

For $M_0 > 1$, at any fixed time $t > 0$, the source is outside the circular wavefront sent out from the source when it was located at $t = 0$. Therefore the source can only affect the flow behind it[6]; this is one of the key facts of supersonic flow. In Figure 3.4 we plot again three wavefronts; the difference from Figure 3.3 is obvious. The wavefronts are no longer nested and form the Mach envelope, which in this case is usually called the Mach wedge. All disturbances are confined inside this wedge.

[6]This is also true for an extended, sufficiently sharply-pointed source; for an extended blunt source a bow shock is formed in front of the source and the disturbed region of the flow is somewhat extended.

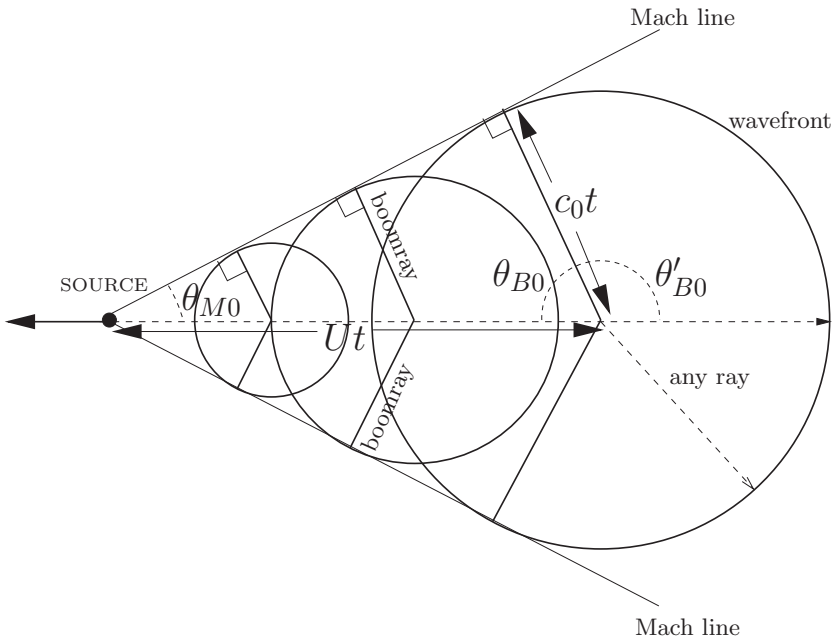

Figure 3.4: $M_0 > 1$: the wavefronts form an envelope. In two dimensions the envelope is a Mach wedge with opening semiangle the Mach angle $\theta_{M0} = \arcsin(1/M_0)$.

In Figure 3.5 the same supersonic motion is visualised in the (x, z, t)-space. The projection of the "tops" of these four cones on the (x, z)-plane is shown in Figure 3.6.

The ray conoid at $(\mathbf{x}_0(\tau), \tau)$ is

$$\psi_h(x, z, \tau; t) = (x + U\tau)^2 + z^2 - c_0^2(t - \tau)^2 = 0. \tag{3.39}$$

The Mach envelope is the locus of the points (x, z, t) satisfying conditions (3.38) which become here

$$\psi_h = 0, \quad \frac{\partial \psi_h}{\partial \tau} = 2U(x + U\tau) + 2c_0^2(t - \tau) = 0, \tag{3.40}$$

and lead to

$$x + U\tau = -\frac{c_0^2}{U}(t - \tau), \tag{3.41}$$

$$z = \pm\frac{c_0^2}{U}B_0(t - \tau), \tag{3.42}$$

where the Prandtl-Glauert parameter $B_0 = \sqrt{M_0^2 - 1}$ is real and positive only if $M_0 > 1$. The latter confirms that the Mach envelope exists only when the source moves supersonically. Eliminating τ from (3.41) and (3.42) we obtain the *Mach lines*

$$x + Ut = \pm B_0 z. \tag{3.43}$$

The condition $x + Ut \geq 0$ holds since from (3.41) $x + Ut = \frac{c_0^2}{U} B_0^2 (t - \tau) \geq 0$. The acute angle that the Mach wedge makes with the positive x-axis is the *Mach angle* $\theta_{M0} = \arcsin(1/M_0)$.

3.4.2 Boomrays

The Mach envelope can be alternatively, and more simply, determined as the locus of the tips of boomrays. Boomrays are the rays that, at launch, satisfy the condition

$$\mathbf{U}.\mathbf{n} = c_0 \Rightarrow \cos\theta_{B0} = \frac{1}{M_0}, \tag{3.44}$$

where θ_{B0} is the semivertical angle of the forward-facing conoid, ahead of the source, with its axis of symmetry along the direction of motion. This condition imposes that at launching, the component of the source velocity along the ray is *sonic*; then the signals emitted from the source when travelling along boomrays reinforce each other at the observer's position and are heard as a single "boom" (see Lighthill [72], pp. 196–197). From now on we will call (3.44) the "boomray condition".

It is a key result on sonic boom that out of all the rays launched, only boomrays have to be taken into account for determining the Mach conoid and the amplitude of sonic boom.[7] All rays except the boomrays carry sound that does not contribute to the sonic boom. We should stress that this property of boomrays holds for any supersonic motion in any medium, and hence it provides a straightforward method to construct the Mach envelope in any scenario. Lighthill has discussed boomrays for an isothermal medium where c is constant (see [72], p. 196) but the general result was proved in the SOBER report [5] in 2002.

We return to the simple two-dimensional example of steady supersonic motion in a uniform medium, to illustrate that this alternative approach is equivalent to that presented in the previous section. We parametrise the wavefronts with the angle θ measured from the positive x-axis so that

$$x + U\tau = c_0(t - \tau)\cos\theta, \tag{3.45}$$

$$z = c_0(t - \tau)\sin\theta. \tag{3.46}$$

From (3.45) and the envelope condition (3.41) we find that the angles $\pm\theta'_{B0}$ made with the positive x-axis obey the condition $\cos\theta'_{B0} = -1/M_0$. Therefore $\theta'_{B0} = \pm(\pi - \theta_{B0})$. The positive sign corresponds to the boomray launched upwards and the

[7] This is because boomrays always start and remain on the Mach envelope.

negative sign to the boomray launched downwards. Also, from (3.42) and (3.46) we obtain $\sin\theta'_{B0} = B_0/M_0$. Therefore in two dimensions there are two possible boomray directions. In Figure 3.5 we show on each of the ray cones the two boomrays (only the family launched downwards is clearly visible). The two families of boomrays are

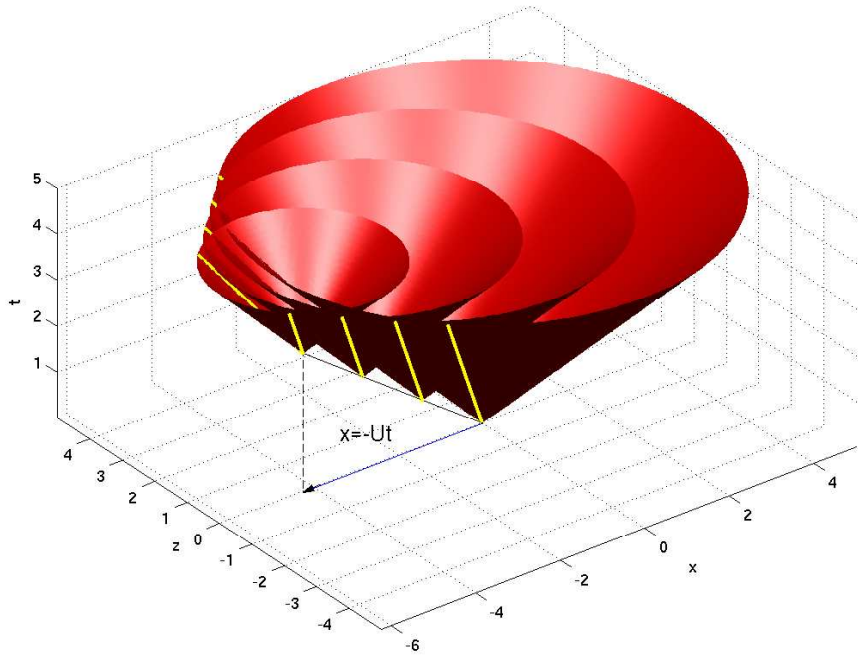

Figure 3.5: Visualisation of a two-dimensional supersonic motion in the (x, z, t)-space $(U = \sqrt{2}, c_0 = 1)$, for a point source moving in the negative x-direction. The source path $x = -Ut, z = 0$, is displayed by a solid straight line and its projection onto the (x, z)-plane by a solid arrow. The two boomrays, at angle $\theta_{B0} = \pm\pi/4$ to the direction of motion, are marked on each ray cone (only the family with $\theta_{B0} = -\pi/4$ is clearly visible here).

clearly visible in Figure 3.6.

In Chapter 6 we will show, for a uniform medium, that the boomrays are also those rays that carry sound to a given point in such a way that a ray emitted Δt later, arrives at the point with time difference of order Δt^n, where $n \geq 2$. For most points on the Mach envelope $n = 2$, but $n > 2$ can occur when the boomrays form a higher-order focusing object, such as a fold caustic ($n = 3$). Interestingly, we will also get the boomray equations when we look for the stationary phase points of the wavefield integral at a fixed observation point. This is shown in Appendix B.

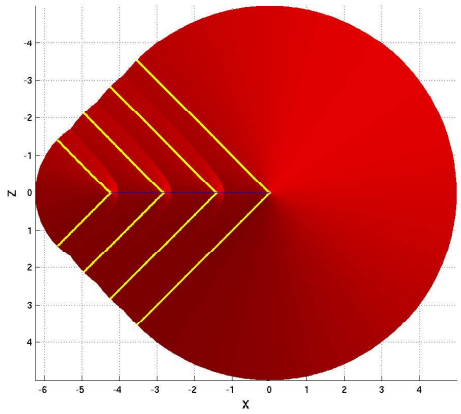

Figure 3.6: The view of Figure 3.5 in the (x, z)-space. Both families of boomrays are shown.

3.4.3 Mach envelope in the aerodynamic frame

A third, even simpler way to calculate the Mach envelope is available when the source is moving on a straight line with constant velocity. In this case it is natural to work in the aerodynamic frame moving with the source.

Assuming that the source is moving from right to left on the x-axis with speed U, we define the new travelling coordinate $X = x + Ut$. In this frame the source is fixed at $(0, 0, 0)$, there is an incident supersonic stream $\mathbf{U}' = (U, 0, 0)$ and the flow appears steady so that

$$p(x, y, z, t) = \Phi(x + Ut, y, z) = \Phi(X, y, z). \tag{3.47}$$

Then the partial derivatives are

$$\left(\frac{\partial}{\partial t}\right)_x = U\frac{\partial}{\partial X}, \qquad \left(\frac{\partial}{\partial x}\right)_t = \frac{\partial}{\partial X}, \tag{3.48}$$

and the wave equation (3.11) becomes

$$B^2\Phi_{XX} = \Phi_{yy} + \Phi_{zz}, \tag{3.49}$$

where $B = \sqrt{U^2/c^2 - 1}$ is the local Prandtl-Glauert parameter. The condition that there is no disturbance upstream becomes then $\Phi = 0, \Phi_x = 0$ on $X = 0$, so that if we think of X as time we are effectively looking for *causal* solutions to (3.49). The Mach surface in the original reference frame now becomes the ray cone through $(0, 0, 0)$ of (3.49), and if it is represented by $\Psi = 0$, then Ψ obeys the eikonal equation

$$B^2{\Psi_X}^2 = {\Psi_y}^2 + {\Psi_z}^2. \tag{3.50}$$

Returning again to our simple example of two-dimensional steady supersonic motion in a uniform medium, we indeed find that the (bi)characteristics of

$$B_0^2 \Phi_{XX} = \Phi_{zz}, \tag{3.51}$$

satisfying the condition $z = 0$ at $X = 0$ (with $X \geq 0$), are the Mach lines (3.43).

Returning to the general case, rearranging (3.50) and defining $P = \Psi_X, Q = \Psi_y$, $R = \Psi_z$ we obtain

$$F_1(P, Q, R) = B^2 P - \frac{Q^2 + R^2}{P} = 0. \tag{3.52}$$

This can be solved with Charpit's method, similarly to (3.12). However, applying the derivative transformations (3.48) directly to the eikonal (3.13), we have

$$F_2 = \frac{1}{2}\frac{c^2}{U}\left(B^2 P - \frac{Q^2 + R^2}{P}\right) = \frac{c^2}{2U} F_1(P, Q, R) = 0. \tag{3.53}$$

We can thus immediately deduce from Charpit's equations (3.25) and (3.27) that the analogous equations corresponding to F_2 are

$$\frac{d\mathbf{X}}{dt} = c\mathbf{N} + \mathbf{U}', \tag{3.54}$$

$$\frac{d\mathbf{N}}{dt} = -\boldsymbol{\nabla} c + (\mathbf{N}.\boldsymbol{\nabla} c)\mathbf{N}, \tag{3.55}$$

where

$$\mathbf{N} = -\boldsymbol{\nabla}\Psi/|\boldsymbol{\nabla}\Psi| = -\frac{1}{MP}(P, Q, R), \tag{3.56}$$

is the unit outward normal to the Mach surface at the position (X, y, z). The vector $\mathbf{N}$ coincides with $\mathbf{n}_B$, the unit vector in the direction of the boomray. Note that $\mathbf{n}_B$ (like the direction vector $\mathbf{n}$ for any ray) is independent of the velocity of the reference frame; this is why equation (3.55) is the same as equation (3.27).

The trajectories defined by (3.54) and (3.55), in the hyperbolic PDE framework, are the bicharacteristics of the Mach surface, and from now on we will refer to them as BICHs in order to provide a contrast with the bicharacteristics of the ray surface, which we are calling rays.

The unit vector in the direction of the BICHs is

$$\boldsymbol{\xi} = \frac{c\mathbf{N} + \mathbf{U}'}{|c\mathbf{N} + \mathbf{U}'|} = \frac{c}{M}\frac{1}{cB}\left(B^2, -\frac{Q}{P}, -\frac{R}{P}\right) = \left(\frac{B}{M}, -\frac{Q}{MBP}, -\frac{R}{MBP}\right). \tag{3.57}$$

Using (3.57) we deduce that $\cos\theta_{M0} = \boldsymbol{\xi}_0.\hat{\mathbf{e}}_\mathbf{x} = B_0/M_0$, where $\hat{\mathbf{e}}_\mathbf{x}$ is the unit vector in the x-direction. This shows that the initial acute angle of the BICHs (and the Mach

conoid) with the positive x-axis is the Mach angle $\theta_{M0} = \arcsin(1/M_0)$, as expected. More generally, at any height the BICH is at the local Mach angle to the x-axis, $\theta_M = \arcsin(1/M)$, since $\cos\theta_M = \boldsymbol{\xi}.\hat{\mathbf{e}}_\mathbf{x} = B/M$. Furthermore, the BICH passing through any position (X, y, z) is perpendicular to the boomray since the dot product of $\boldsymbol{\xi}$ with $\mathbf{N}$ is $\boldsymbol{\xi}.\mathbf{N} = \dfrac{c + \mathbf{U}'.\mathbf{N}}{|c\mathbf{N} + \mathbf{U}'|} = 0$.

In the aerodynamic frame, the causality of the PDE (3.49) dictates that any information introduced at a certain point will move along the BICHs. To see this physically take a point $\mathbf{X}$ on the Mach conoid. In stationary air, the portion of the shock front centered on $\mathbf{X} = (X, y, z)$, would advance a distance $c\mathbf{N}\delta t$ in time δt. However, in the aerodynamic frame, within the same time interval, the incident supersonic stream $\mathbf{U}' = (U, 0, 0)$ sweeps the shock front portion horizontally to the right by distance $U\delta t$. Therefore the new position of the shock front portion is $\mathbf{X} + \delta\mathbf{X} = \mathbf{X} + (c\mathbf{N} + (U, 0, 0))\delta t$ which leads to the equation (3.54), as required.

Equivalently, we can say that for a stationary observer the perceived direction of propagation is along the boomray, but for an observer moving with the source the perceived direction of propagation is along the BICH. Note that by construction the parameter along the BICHs is still the time t.

Up to now, we have presented three ways to derive the Mach envelope and illustrated each one with the two-dimensional example of a source with constant supersonic speed in a uniform atmosphere. For the latter example, extension into three dimensions is trivial: the wavefronts are spheres (t-sections of the ray cone (3.29)), the boomrays lie on the cone with semivertical angle θ_{B0}, ahead of the source position and the BICHS lie on the Mach cone

$$(x + Ut)^2 = B_0^2(y^2 + z^2), \tag{3.58}$$

which can also be found as the ray cone of $B_0^2\Phi_{XX} = \Phi_{yy} + \Phi_{zz}$, or as the body of revolution with the Mach lines (3.43) as its generators. However, for a general scenario of unsteady motion in an non-uniform medium the Mach envelope cannot, in most cases, be determined analytically. Below we pinpoint some examples where this is possible, with the aim of elucidating sonic boom propagation.

3.5 Stationary source in a model stratified atmosphere (two dimensions)

For a second analytical example, we consider a stratified medium with sound speed profile $c = \dfrac{1}{\sqrt{1-z}}$ in the region $z < 1$. Even though this profile has an unphysical

singularity at $z = 1$, where the speed of sound becomes infinite, we can take it as a representation of cases where $c(z)$ is increasing with height. Perhaps the simplest analytical example of a stratified medium that we could have taken is one with c varying linearly with z. The rays are then arcs of circles ([94], p. 385), and the dependence on the independent coordinates x, y, z, t appears through trigonometric functions. However, for the example here the Mach envelope will be determined as a polynomial in x, y, z, t, which makes the analysis easier. At the same time, this example gives rise to a quite complicated geometry with features that are relevant physically.

The analysis that we will present here for the stationary source will become directly relevant to the three-dimensional scenario with $B^2 = 1 - z$ with just a coordinate change.[8] Note that the scenario with $B^2 = 1 - z$ can be thought of as the canonical problem for the approximation of B near the reflection height in any atmosphere.

For a stationary source at $(0, 0, 0)$ we derive below the ray conoid. Since the propagation vector remains in the plane in which it originates, it is sufficient to remain in two spatial dimensions. Equation (3.11) becomes

$$(1 - z)p_{tt} = p_{xx} + p_{zz}. \tag{3.59}$$

Writing the eikonal equation (3.12) in the form

$$F_3 = (1 - z)\lambda^2 - (p^2 + r^2) = 0 \tag{3.60}$$

will enable us to determine the ray conoid analytically. Charpit's equations for (3.60) integrate to the following parametric relations for the rays,

$$x(\zeta) = -2p_0\zeta, \tag{3.61}$$

$$z(\zeta) = -\lambda_0^2\zeta^2 - 2r_0\zeta, \tag{3.62}$$

$$t(\zeta) = \frac{2}{3}\lambda_0^3\zeta^3 + 2\lambda_0 r_0\zeta^2 + 2\lambda_0\zeta, \tag{3.63}$$

$$p = p_0, \quad r(\zeta) = \lambda_0^2\zeta + r_0, \quad \lambda = \lambda_0. \tag{3.64}$$

(Equations (3.61)–(3.64) also appear in [86], p. 389.) Note that we do not take $\lambda_0 = 1$ because later on (Section 3.8) we will use equations (3.61)–(3.64), under the coordinate transformation $(x, z, t) \to (y, z, X)$, for directly determining the Mach surface in the three-dimensional scenario with $B^2 = 1 - z$. There λ_0 is associated with the X coordinate and cannot be taken equal to 1.

[8] Furthermore the analysis for $B^2 = 1 - z$ will pave the way for solving analytically the more complicated scenario $B^2 = 1 - |z|$, which provides a good insight into the geometry of the Mach envelope in a typical atmosphere, where calculations can only be done numerically—see Section 3.8.

The parameter along the rays is no longer the time t but we can readily see that $\dfrac{\partial t}{\partial \zeta} = 2\lambda_0(1-z) > 0$ (assuming $\lambda_0 > 0$). Therefore the time t increases monotonically with ζ and the qualitative behaviour of the ray will not be affected by using the parameter ζ instead of t.

To determine the ray conoid as an algebraic relation between x, z and t, we need to eliminate ζ, p_0, r and λ_0 from the equations (3.61)–(3.64). (We will study graphically the latter equations later.) From equation (3.61) we solve for $\zeta = -x/(2p_0)$ and substitute into (3.62) and (3.63). We obtain respectively

$$z = -\frac{1}{4}\left(\frac{\lambda_0}{p_0}\right)^2 x^2 + \left(\frac{r_0}{p_0}\right) x, \tag{3.65}$$

$$t = -\frac{1}{12}\left(\frac{\lambda_0}{p_0}\right)^3 x^3 + \frac{1}{2}\left(\frac{\lambda_0}{p_0}\right)\left(\frac{r_0}{p_0}\right) x^2 - \left(\frac{\lambda_0}{p_0}\right) x. \tag{3.66}$$

Because of the eikonal equation (3.60), the dimensionless ratios $\dfrac{\lambda_0}{p_0}$ and $\dfrac{r_0}{p_0}$ satisfy

$$\left(\frac{\lambda_0}{p_0}\right)^2 = 1 + \left(\frac{r_0}{p_0}\right)^2. \tag{3.67}$$

Letting $C = \dfrac{\lambda_0}{p_0}$ and $D = \dfrac{r_0}{p_0}$, we can write (3.65)–(3.67) as a system of three algebraic equations linked through the two parameters C and D:

$$C^2 = 1 + D^2, \tag{3.68}$$

$$z = -\frac{1}{4}(Cx)^2 + Dx, \tag{3.69}$$

$$t = -\frac{1}{12}(Cx)^3 + \frac{1}{2}CDx^2 - Cx. \tag{3.70}$$

From equation (3.69) we find $D(x, z, C)$, substitute in (3.68), rearrange and we get a quadratic in $(Cx)^2$,

$$(Cx)^4 + (Cx)^2(8z - 16) + 16(x^2 + z^2) = 0, \tag{3.71}$$

which gives the roots

$$\frac{1}{4}(Cx)^2 = (2 - z) \pm \sqrt{4(1-z) - x^2}. \tag{3.72}$$

For the two roots to be real, we need to impose the constraint $z \leq 1 - x^2/4$, which indicates a qualitative change in the behaviour of the wavefield, on the curve

$$z = 1 - \frac{x^2}{4}. \tag{3.73}$$

The two roots (3.72) are distinct and real *inside* the parabola (3.73), coalesce *on* it and become complex *outside*. This corresponds respectively to two distinct rays inside the parabola which coincide on it and vanish outside. Therefore the rays should be tangent to (3.72) and so this curve is a smooth envelope of rays—a *fold caustic* in the terminology of catastrophe theory [15]. In Section 3.5.3, for $c(z) = 1/\sqrt{1-z}$ we will solve the wave equation for a monochromatic stationary source, and observe that there is indeed a drastic change in the wavefield behaviour across this caustic.

We finally substitute $D(x, z, C)$ in the right-hand side of (3.70), square, and use (3.72) to eventually obtain the ray conoid

$$9t^2 = (2-z)(4-4z+4z^2+3x^2) \pm 8\left(1-z-\frac{x^2}{4}\right)^{3/2}. \tag{3.74}$$

The positive and negative signs in (3.74) correspond respectively to so-called "positive" and "negative" sheets of the ray conoid. These two sheets meet at the curve $z = 1 - \dfrac{x^2}{4}, t = \dfrac{2}{3}(2-z)^{3/2}$.

Note finally that the ray conoid for the more general case $c = c_0/\sqrt{1-\mu z}$ is obtained from (3.74) by taking $t \mapsto \mu c_0 t, x \mapsto \mu x$, $z \mapsto \mu z$:

$$9(\mu c_0 t)^2 = (2-\mu z)(4-4\mu z+4\mu^2 z^2+3\mu^2 x^2) \pm 8(1-\mu z-\mu^2 x^2/4)^{3/2}. \tag{3.75}$$

3.5.1 Wavefronts

Below we will examine the behaviour of the wavefronts as time t increases. For a wavefront (3.74) at $t = t_0 =$ constant, we will call the trace of the positive sheet on the plane $t = t_0$, the 'upper branch', and similarly the trace of the negative sheet will be called the 'lower branch'. These two branches meet at a 3/2-power cusp. This cusp is on the caustic $z = 1 - \dfrac{x^2}{4}$, which can therefore also be thought of as a locus of cusps (see Figure 3.7, where we plot some wavefronts for progressively larger times).

Firstly, for small times $t_0 \ll 1$ and $x \ll 1, z \ll 1$ we expand the negative branch expression in (3.74). We get

$$\begin{aligned} 9t_0^2 = (8-8z+8z^2+6x^2-4z+4z^2) - 8\left(1-\frac{3}{2}z-\frac{3}{8}x^2+\frac{3}{8}z^2+...\right) = 0 \\ \Rightarrow t_0^2 = x^2+z^2+... \end{aligned} \tag{3.76}$$

Therefore for small times t_0 the stratification is not felt and the wavefronts are circular to leading order. However, as t_0 increases, the stratification will be felt more strongly and the wavefronts are increasingly elongated in the vertical z direction, eventually

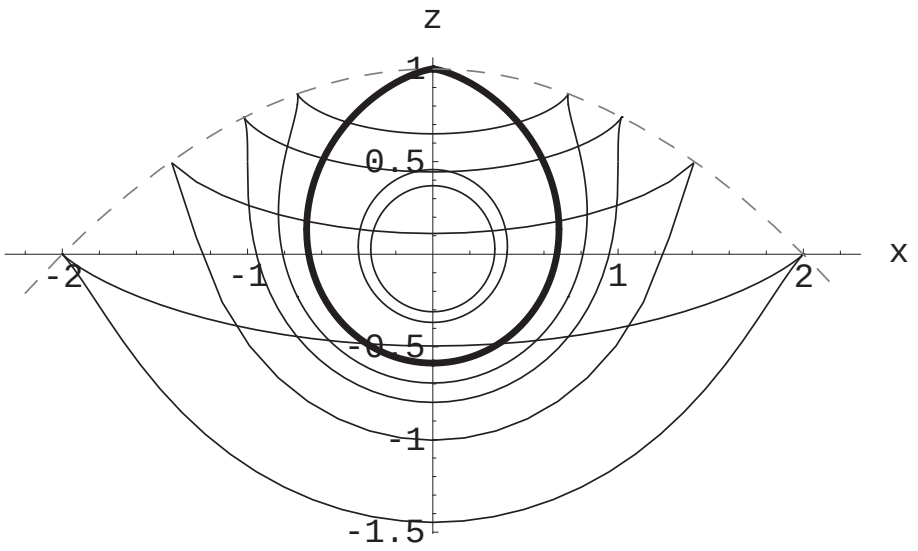

Figure 3.7: Selected wavefronts: for $t_0 < t_c = 2/3$ we show $t_0 = 1/3$, $t_0 = 1/2$. The marginal wavefront $t_c = 2/3$ is marked with a thicker line. The cusped wavefronts $t_0 = (1+\sqrt{2})/3$, $2\sqrt{2}/3$, $\sqrt{3/2}$ and $4\sqrt{2}/3$ are shown. As explained in the text, for $t_0 < t_c$ the wavefront has a vertical tangent only at one point, for $t_c < t_0 < 2\sqrt{2}/3$ at two points and nowhere for $t_0 > 2\sqrt{2}/3$. The caustic (locus of cusps) $z = 1 - x^2/4$ is plotted with a dashed line.

forming cusps. Below we investigate the onset of the cusps' appearance. At the critical time $t_c = \dfrac{2}{3}$, a discontinuity in the curvature appears in the wavefront. In order to investigate the behaviour of the wavefront near this curvature discontinuity, we set $\epsilon = t_0 - t_c$, for $t_0 > t_c$, and expand (3.74) using

$$x = 0 + \sqrt{\epsilon} x_1 + ..., \quad z = 1 - \epsilon^{2/3} z_1 + ... \tag{3.77}$$

Keeping terms up to order ϵ, we find that the wavefronts are approximated by

$$12 = 3x_1^2 \pm 8 z_1^{3/2} \Rightarrow 12\epsilon = 3x^2 \pm 8(1-z)^{3/2}, \tag{3.78}$$

where the positive sign is for the positive branch and the negative sign is for the negative branch. In Figure 3.8 we plot the approximate wavefront and the exact wavefronts for $\epsilon = 0$ (left plot) and $\epsilon = 0.01$ (right plot). The curvature discontinuity is clearly illustrated in the former case; in the right plot we can see that the curvature discontinuity has disappeared and two cusps have formed.

Now, the coordinates of the cusps, using (3.73) and (3.74) are found to be

$$x_{cu}(t_0) = \pm 2\sqrt{\left(\frac{9}{4}t_0^2\right)^{1/3} - 1}, \quad z_{\rm cu}(t)) = 2 - \left(\frac{3}{2}t_0\right)^{2/3}. \tag{3.79}$$

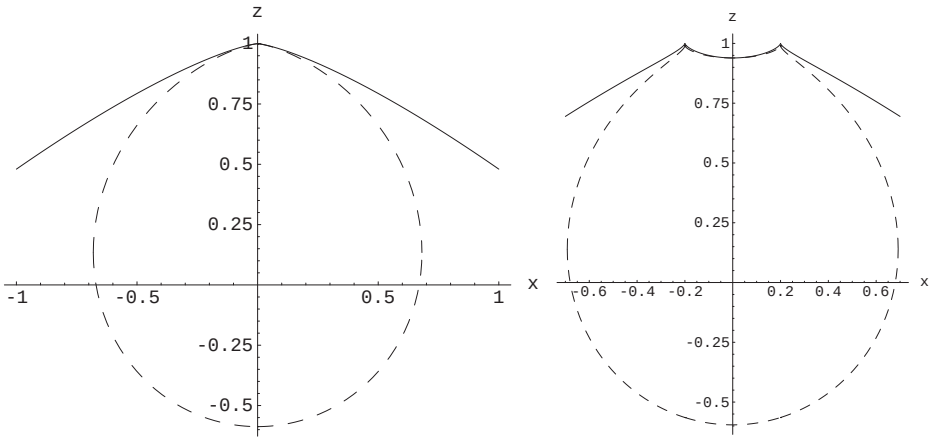

Figure 3.8: The local behaviour of the wavefronts for $\epsilon = 0$ (left) and $\epsilon = 0.01$ (right). When $\epsilon = 0$ there is a discontinuity in the curvature at $x = 0, z = 1, t_0 = 2/3$. The exact wavefronts are plotted with dashed lines.

Expressions (3.79) constitute a parametric representation of the cusps in terms of t_0. They give the constraint $t_0 \geq t_c$, which confirms that cusps exist only for $t_0 \geq t_c$. Since $x_{\rm cu}$ increases monotonically and $z_{\rm cu}$ decreases monotonically with t_0, the cusps move down and away from each other as t_0 increases. (Using $\epsilon = t_0 - 2/3$, from (3.79) we find, as expected, $x_{\rm cu} = \pm 2\epsilon^{1/2} + O(\epsilon^{3/2})$ and $z_{\rm cu} = 1 - O(\epsilon^{3/2})$.) Expressions (3.79) will be useful in Section (3.6).

To investigate the behaviour of the tangent to the wavefront, we differentiate (3.74) with respect to x to find that the slope of the tangent is given by

$$\frac{dz}{dx} = \frac{6x(z - 2 \pm S)}{(z-2)(4-8z) - R \pm 12S}, \tag{3.80}$$

where

$$R = 4 - 4z + 4z^2 + 3x^2 \text{ and } S = (1 - z - x^2/4)^{1/2}.$$

Setting $S = 0$ we deduce that the two branches of the wavefront have a common tangent at the cusp, that is the cusps are at zero angle. The wavefront tangent at the cusps is perpendicular to the caustic (3.73) because the rays are perpendicular to the wavefront at the cusp points.

It will be of use in Section 3.6 (where we construct the Mach envelope for a moving source in the same medium), to identify where the wavefronts have a vertical tangent: for this, we set the denominator of (3.80) equal to zero and use (3.74) to arrive at a cubic in z,

$$9t_0^2 = 4 + 12(1 - z) - 16(1 - z)^3. \tag{3.81}$$

Observing the roots of (3.81) we find that, as the time increases, for

- $0 < t_0 < 2/3$, the tangent is vertical for only one value of z.
- $2/3 < t_0 < 2\sqrt{2}/3$, cusps have formed and the tangent is now vertical at two values of z, one greater than $1/2$ and one less than $1/2$. Both these z values become $1/2$ at $t = 2\sqrt{2}/3$.
- $t_0 > 2\sqrt{2}/3$, the wavefront has nowhere a vertical tangent and it has a "cusped crescent"-like shape.

Figure 3.7 illustrates all the above cases.

3.5.2 Rays, formation of an envelope

We now return to the ray equations (3.61)–(3.63) to obtain an alternative but parallel viewpoint of the ray conoid/wavefronts behaviour.

Firstly, in Figure 3.9 we plot the rays in (x, z, t)-space for $t \leq 2/3$. Figure 3.10 is the projection of Figure 3.9 on the (x, z)-plane. In Figure 3.11 we plot the rays

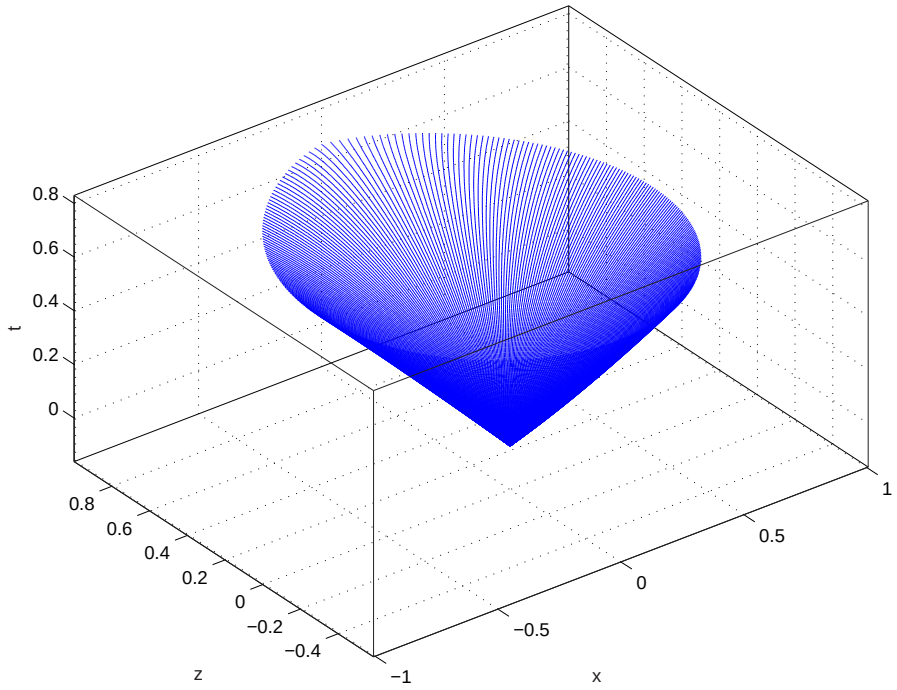

Figure 3.9: $t = 2/3$: ray conoid.

corresponding to the time $t_0 \leq 2\sqrt{2}/3$ in the (x, z, t)-space. We can see here that a

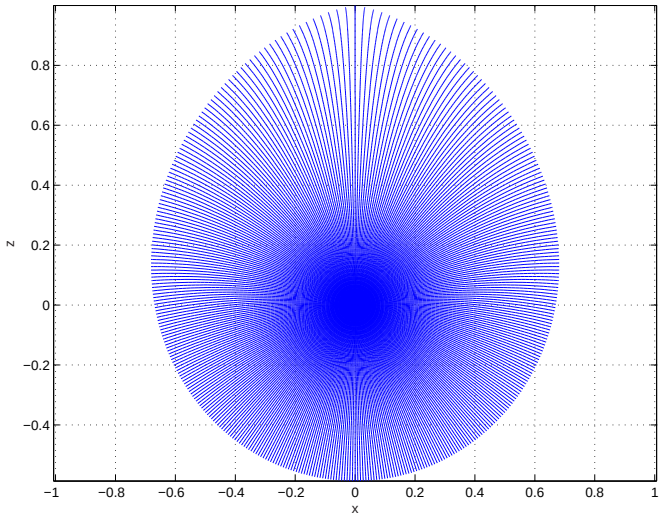

Figure 3.10: $t = 2/3$: rays.

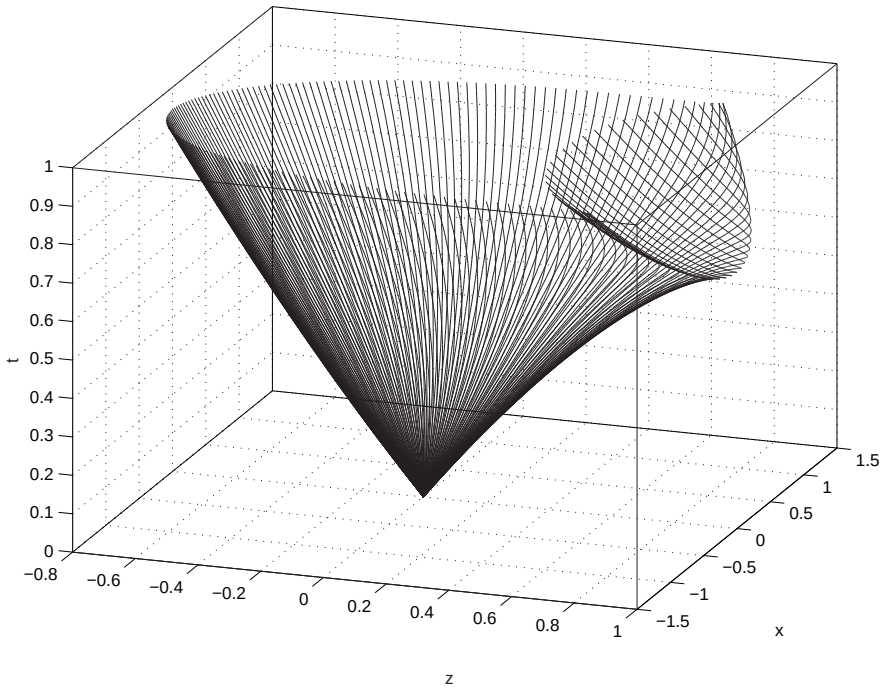

Figure 3.11: $t = \dfrac{2\sqrt{2}}{3}$: rays in the (x, z, t)-space.

fold has developed; the earliest point of the fold is at $x = 0$, $z = 1$, $t_c = 2/3$. The negative sheet of the ray conoid carries the rays that have not passed through the fold, and the positive sheet carries the rays that *have* passed through the fold.

In Figure 3.12 we plot the rays corresponding to the wavefront $t_0 = 2\sqrt{2}/3$ on the (x, z)-plane. (The latter figure could also have been obtained as an (x, z)-view of Figure 3.11.)

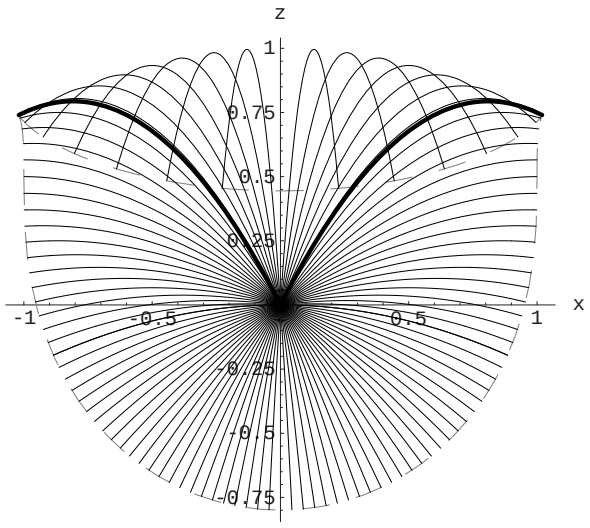

Figure 3.12: $t = \dfrac{2\sqrt{2}}{3}$: wavefront and rays. The cusp-rays (defined in the text), dividing the behaviour into upper and lower branch rays are plotted with a thicker line.

We concentrate attention on a particular wavefront with $t = t_0 > 2/3$, which has cusps. The ray pattern and the wavefront are symmetric with respect to the z-axis so we can work in $x \geq 0$. One ray goes through the cusp and it will be called the cusp-ray from now on. We recall that cusp-rays are tangent to the caustic. The cusp-ray divides the rays into two families: those that form the upper branch of the wavefront and those that form the lower branch. In Figure 3.12 the different behaviour for the rays of the lower and upper branch is clearly visible; the cusp-rays are plotted with a thicker line.

Note that it is also possible to express a cusp in terms of the angle $\theta = \theta_{\rm cu}$ the cusp-ray makes with the positive x-axis. Combining (3.65) and (3.73) we find $x = 2p_0/r_0$ and then from (3.73) we get $z = 1 - p_0^2/r_0^2$. Then from (3.79) we get $t_0 = -2/3r_0^3$ (note that $r_0 < 0$ for rays launched upwards). For the cusp-rays, $p_0 = \pm\cos\theta_{\rm cu}$, where the positive sign corresponds to the left cusp-ray and the negative sign to the

right cusp-ray, and $r_0 = -\sin\theta_{\rm cu}$. These lead to the following simple parametrisation for the cusps

$$x = 2\cot\theta_{\rm cu}, \tag{3.82}$$

$$z = 1 - \cot^2\theta_{\rm cu}, \tag{3.83}$$

$$t = \frac{2}{3\sin^3\theta_{\rm cu}}, \tag{3.84}$$

where $0 < \theta_{\rm cu} < \pi$.

Furthermore, a ray launched upwards spends equal times above the source height, before and after its maximum height, $z_{\max}$, determined from (3.62) by setting $dz/d\zeta = 0$. All rays launched downwards do not have any turning points since (3.62) gives $dz/d\zeta < 0$. Note that the above results on the behaviour of wavefronts and rays will be also relevant for Sections 3.4 and 3.8.

3.5.3 Amplitude due to a stationary monochromatic source

In this section, we calculate the amplitude of the wavefield due to a stationary, sinusoidal, point source situated at $(0, 0)$, in an non-uniform medium with the sound speed profile $c = 1/\sqrt{1-z}$. We will use linear wave theory, and we will show that there is a drastic qualitative change in the wavefield behaviour across the caustic $z = 1 - x^2/4$, as already indicated by studying the ray-pattern.

The wave equation (3.11) in this case can be written as

$$p_{tt} = c^2(p_{xx} + p_{zz}) + \delta(x)\delta(z)\Re(e^{i\omega t}). \tag{3.85}$$

We also need to impose two Sommerfield radiation conditions. Firstly, $p \to 0$ as $z \to \infty$. Secondly, for $z < 1$, and with the wavenumber being $k = \omega/c(z)$, we want $p_r + ikp = o(1/r)$ as $r \to \infty$, where $r = \sqrt{x^2 + z^2}$.

The solution for a more general time-varying source can be obtained by linear superposition. In the previous section we have plotted the ray-pattern and we found that no rays exist outside the fold caustic $z = 1 - x^2/4$. GA predicts an infinite value for the wavefield at the fold caustic (the wavefield intensity is inversely proportional to the ray tube area which becomes zero at the caustic [85]), and zero wavefield outside the caustic. The region outside the caustic is usually called a shadow zone. Here we will solve the full wave equation and find a *finite* wavefield on the caustic and a non-zero wavefield in the shadow zone.

There is no exact analytical solution for (3.85) for this choice of c. We can however make extended analytical progress. We give a summary of our procedure: for a

monochromatic disturbance equation (3.85) reduces to an inhomogeneous Helmholtz equation, on which we perform a Fourier transform in the x-direction. This leads to an inhomogeneous Airy equation (under a suitable transformation) which is then solved analytically with appropriate boundary conditions on the behaviour of solution at infinity and at the source height. The transform is then inverted numerically. This procedure is valid for all values of ω.

Starting, we substitute

$$p(x,z,t) = \Re(\exp(i\omega t)U(x,z)), \tag{3.86}$$

in (3.85) and we obtain the inhomogeneous Helmholtz equation

$$-\omega^2 U = c^2(U_{xx} + U_{zz}) + \delta(x)\delta(z). \tag{3.87}$$

We then take the Fourier Transform of (3.87) with respect to x, defining

$$\hat{U}(\alpha,z) = \int_{-\infty}^{\infty} U(x,z)\exp(i\alpha x)dx. \tag{3.88}$$

We thus obtain

$$\frac{d^2\hat{U}}{dz^2} + \left(\frac{\omega^2}{c^2} - \alpha^2\right)\hat{U} + \frac{\delta(z)}{c^2} = 0. \tag{3.89}$$

Note that equation (3.89) is valid for any choice of c; for the special case of $c^2 = 1/(1-z)$, and letting $\tilde{z} = \omega^{2/3}(z - 1 + \alpha^2/\omega^2)$ we obtain from it the inhomogeneous Airy equation

$$\frac{d^2\hat{U}}{d\tilde{z}^2} = \tilde{z}\hat{U} - \omega^{-2/3}\delta(\tilde{z} - \tilde{z}_s). \tag{3.90}$$

(We note that for a linear speed profile equation (3.89) reduces to a Bessel equation that admits solutions in terms of Bessel functions of imaginary arguments.) The general solution of (3.90) is given by

$$\hat{U}(\alpha,z) = \begin{cases} \hat{U}_1(\alpha,z) = A_1\mathrm{Ai}(\tilde{z}) + B_1\mathrm{Bi}(\tilde{z}), & \tilde{z} \geq \tilde{z}_s \\ \hat{U}_2(\alpha,z) = A_2\mathrm{Ai}(\tilde{z}) + B_2\mathrm{Bi}(\tilde{z}), & \tilde{z} \leq \tilde{z}_s \end{cases}$$

where $\mathrm{Ai}(x)$ is the Airy function of the first kind and $\mathrm{Bi}(x)$ is the Airy function of the second kind (see Figure 3.13) and $\tilde{z}_s$ is the value of $\tilde{z}$ at the source height $z = 0$. We have therefore four unknowns A_1, B_1, A_2, B_2 and to determine them, we need four conditions. The first condition to impose is that $\hat{U} \to 0$ as $\tilde{z} \to \infty$. Since $\mathrm{Bi}(\tilde{z}) \to \infty$ in this limit, we have to set $B_1 = 0$. The second condition is that $\hat{U}$ has to represent an outgoing wave as $\tilde{z} \to -\infty$. This leads to the relation $A_2 + iB_2 \to 0$ as $\tilde{z} \to -\infty$.

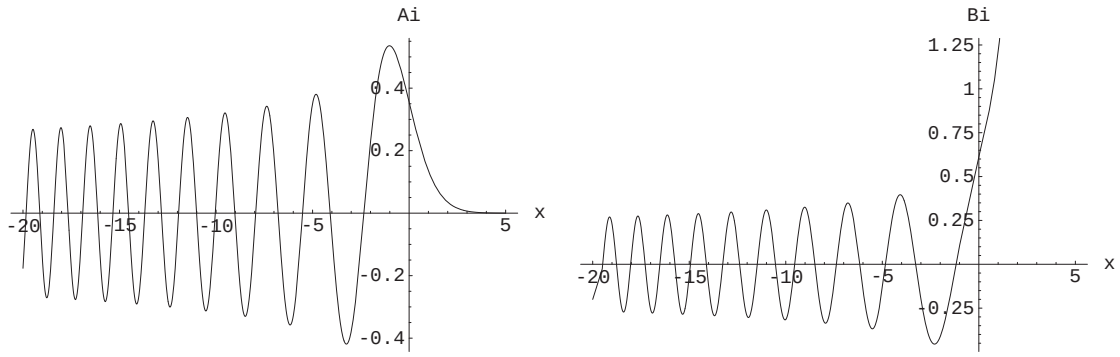

Figure 3.13: The Airy function of the first kind, Ai(x) and the Airy function of the second kind Bi(x) (left and right plot respectively).

The other two conditions are for matching $\hat{U}_1$ and $\hat{U}_2$ at $\tilde{z} = \tilde{z}_s$: we have to impose continuity in $\hat{U}$, that is

$$\hat{U}_1 = \hat{U}_2 \text{ at } \tilde{z} = \tilde{z}_s, \tag{3.91}$$

and also that the derivative in $\hat{U}$ has a jump. Integrating (3.90) with respect to $\tilde{z}$ from $\tilde{z} = \tilde{z}_s^-$ to $\tilde{z} = \tilde{z}_s^+$ we find that this jump is

$$\frac{d\hat{U}_1}{d\tilde{z}} - \frac{d\hat{U}_2}{d\tilde{z}} = -\omega^{-2/3} \text{at } \tilde{z} = \tilde{z}_s. \tag{3.92}$$

From now on, for convenience, $\hat{U}$ will stand for its scaled version $\omega^{2/3}\hat{U}$. Applying the four boundary conditions we obtain, after some algebra,

$$\hat{U}(\alpha, z) = \begin{cases} \hat{U}_1(\alpha, z) = \pi(i\text{Ai}(\tilde{z}_s) - \text{Bi}(\tilde{z}_s))\text{Ai}(\tilde{z}), & \tilde{z} \geq \tilde{z}_s \\ \hat{U}_2(\alpha, z) = \pi(i\text{Ai}(\tilde{z}) - \text{Bi}(\tilde{z}))\text{Ai}(\tilde{z}_s), & \tilde{z} \leq \tilde{z}_s. \end{cases} \tag{3.93}$$

Note that using the identity $\text{Ai}(\tilde{z}e^{-2i\pi/3}) = \frac{1}{2}e^{-i\pi/3}(\text{Ai}(\tilde{z}) + i\text{Bi}(\tilde{z}))$ (see [1], p. 446, expression (10.4.9)), we can conveniently write U in terms of Ai only:

$$\hat{U}(\alpha, z) = \begin{cases} \hat{U}_1(\alpha, z) = 2\pi i e^{i\pi/3}\text{Ai}(\tilde{z}_s e^{-2i\pi/3})\text{Ai}(\tilde{z}), & \tilde{z} \geq \tilde{z}_s \\ \hat{U}_2(\alpha, z) = 2\pi i e^{i\pi/3}\text{Ai}(\tilde{z}e^{-2i\pi/3})\text{Ai}(\tilde{z}_s), & \tilde{z} \leq \tilde{z}_s. \end{cases} \tag{3.94}$$

Inverting $\hat{U}(\alpha, z)$ we have

$$U(x, z) = \frac{1}{2\pi} \begin{cases} \int_{-\infty}^{\infty} \hat{U}_1(\alpha, z) \exp(-i\alpha x) d\alpha, & z \geq 0 \\ \int_{-\infty}^{\infty} \hat{U}_2(\alpha, z) \exp(-i\alpha x) d\alpha, & z \leq 0. \end{cases} \tag{3.95}$$

Moreover, because $\hat{U}_1$ and $\hat{U}_2$ are even functions of the Fourier variable α we can recast expression (3.95) as a cosine transform. (This reformulation will also make the

numerical integration that follows less time consuming.)

$$U(x,z;\omega) = \frac{1}{\pi}\begin{cases} \int_0^\infty \hat{U}_1(\tilde{z},\tilde{z}_s)\cos(\alpha x)d\alpha, & z \geq 0 \\ \int_0^\infty \hat{U}_2(\tilde{z},\tilde{z}_s)\cos(\alpha x)d\alpha, & z \leq 0. \end{cases} \tag{3.96}$$

There is no analytical evaluation of these one-dimensional integrals and so we will calculate them numerically. The interval of integration as seen in (3.96) is semiinfinite, and for our numerical method[9] we need to truncate at a suitably chosen cutoff value of α. For clarity we will integrate separately the real and imaginary part of the integrand in (3.96), and then we will evaluate $|U|$, the amplitude of the wavefield.

• **Cutoff value for α**

To determine an approximate cutoff value for α it is helpful to map out the behaviour of $\Re(\hat{U})$ and $\Im(\hat{U})$ in the (z,α) plane, where (apart from a constant factor)

$$\Re(\hat{U}) = \begin{cases} \mathrm{Bi}(\tilde{z}_s)\mathrm{Ai}(\tilde{z}), & \tilde{z} \geq \tilde{z}_s \\ \mathrm{Bi}(\tilde{z})\mathrm{Ai}(\tilde{z}_s), & \tilde{z} \leq \tilde{z}_s \end{cases} \tag{3.97}$$

and

$$\Im(\hat{U}) = \mathrm{Ai}(\tilde{z}_s)\mathrm{Ai}(\tilde{z}) \qquad \forall z. \tag{3.98}$$

We proceed with the help of the diagram in Figure 3.14. In this diagram we plot the curves $\tilde{z} = 0 \Leftrightarrow \tilde{\alpha} = \alpha/\omega = \sqrt{1-z}$ and $\tilde{z}_s = 0 \Leftrightarrow \tilde{\alpha} = 1$ (considering only positive α). There are four different regions: in Region I we have $\tilde{z}_s > 0, \tilde{z} > 0$, in Region II we have $\tilde{z}_s < 0, \tilde{z} > 0$, In Region III we have $\tilde{z}_s < 0, \tilde{z} < 0$, and in Region IV we have $\tilde{z}_s > 0, \tilde{z} < 0$. We first examine the behaviour of $\Im(\hat{U})$: In Region I both $\mathrm{Ai}(\tilde{z})$ and $\mathrm{Ai}(\tilde{z}_s)$ are decaying exponentially as $\alpha \to \infty$ (thinking of z as a fixed parameter). Since the asymptotic form for Ai as $\tilde{z} \to \infty$ is

$$\mathrm{Ai}(\tilde{z}) \sim \frac{1}{2\sqrt{\pi}}\tilde{z}^{-1/4}e^{-\frac{2}{3}\tilde{z}^{3/2}}, \tag{3.99}$$

and similarly for $\mathrm{Ai}(\tilde{z}_s)$, $\Im(\hat{U})$ decays exponentially in Region I. $\Im(\hat{U})$ decays also in regions II and IV because $\mathrm{Ai}(\tilde{z})$ and $\mathrm{Ai}(\tilde{z}_s)$ decay respectively, while the other juxtaposed Ai factor exhibits oscillatory behaviour. In Region III $\Im(\hat{U})$ is oscillatory and remains of order 1. Therefore we conclude that the order 1 part of $\Im(\hat{U})$ is always contained inside the parabola $\tilde{\alpha} = \sqrt{1-z}$ and $\Im(\hat{U})$ decays outside this parabola.

We then examine the behaviour of $\Re(\hat{U})$. In region III, also $\Re(\hat{U})$ is oscillatory and of order 1. In Region II and Region IV also $\Re(\hat{U})$ is decaying. However, for Region

[9] We will use the NAG integrator **d01akf** which is suitable for oscillating, non-singular integrands integrated over a finite interval.

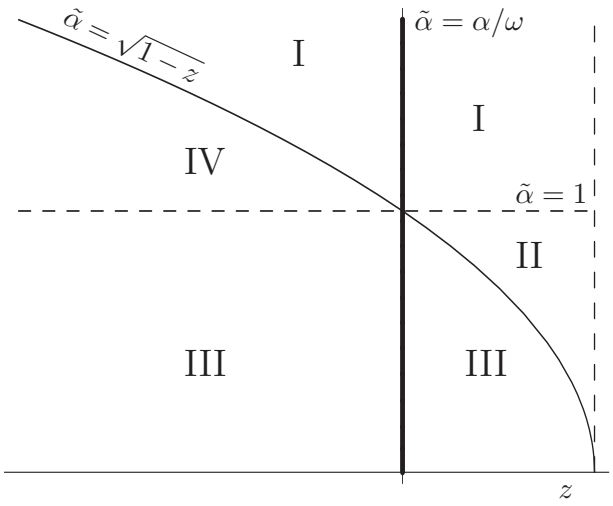

Figure 3.14: Diagram of $\tilde{\alpha} = \alpha/\omega$ versus z illustrating the four regions I, II, III and IV as discussed in the text.

I at first glance it is not obvious whether $\Re(\hat{U})$ is decaying or growing, because $\mathrm{Bi}(\tilde{z})$ is growing and $\mathrm{Ai}(\tilde{z})$ is decaying. We prove below that $\Re(\hat{U})$ in fact decays. In order to investigate simultaneously positive and negative values of z we write $\Re(\hat{U}) = \mathrm{Ai}(\tilde{z}_+)\mathrm{Bi}(\tilde{z}_-)$, where

$$\tilde{z}_+ = \max(\tilde{z}, \tilde{z}_s) = \omega^{2/3}(z_+ - 1) + \alpha^2\omega^{-4/3}, \tag{3.100}$$

$$\tilde{z}_- = \min(\tilde{z}, \tilde{z}_s) = \omega^{2/3}(z_- - 1) + \alpha^2\omega^{-4/3}, \tag{3.101}$$

with $z_+ = \max(z, 0)$ and $z_- = \min(z, 0)$. When $\alpha \to \infty$ we can use the asymptotic form for Ai and Bi. We therefore find that the exponential factor of the asymptotic form of $\Re(\hat{U})$ is

$$\exp\left(-\frac{2}{3}C^{3/2} + \frac{2}{3}D^{3/2}\right) \leq \exp(-(C-D)D^{1/2}), \tag{3.102}$$

where

$$C = (\omega^{2/3}(z_+ - 1) + \alpha^2\omega^{-4/3}), \quad D = (\omega^{2/3}(z_- - 1) + \alpha^2\omega^{-4/3}).$$

To derive the inequality (3.102) we used the fact that

$$\frac{f(C) - f(D)}{C - D} = f'(\xi), \text{ for some } D < \xi < C, \tag{3.103}$$

and that since we have $f(\xi) = \frac{2}{3}\xi^{3/2}$, $f'(\xi)$ is increasing and therefore satisfies $f'(\xi) > D^{1/2}$. The right-hand side of the inequality (3.102) is equal to

$$\exp(-\omega^{2/3}(z_+ - z_-)(\omega^{2/3}(z_- - 1) + \alpha^2\omega^{-4/3})^{1/2}), \tag{3.104}$$

and this tends to zero as $\alpha \to \infty$ when $z_+ > z_-$. Therefore we have proved that $\Re(\hat{U})$ decays in Region I, *except* when $z = 0$.

We therefore conclude that for a fixed $z = z_0 \neq 0$ and $\omega = \omega_0$ a reasonable cutoff value for α should be greater than $\omega_0\sqrt{1 - z_0}$. In the numerical integration below we will take the value of α appreciably larger than this estimated cutoff to ensure good accuracy in $|U|$.

• Plots of $\Re U$, $\Im U$ and $|U|$.

Below, we take the values $\omega = 10$ and $\omega = 30$ as representative cases of a moderate and a high frequency, and we show plots of $\Re(U)$, $\Im(U)$ and $|U|$.

$\diamond$ For $\omega = 10$, taking the cutoff value to be $\alpha = 25$, $\Re(U)$, $\Im(U)$ and $|U|$ are plotted in Figures 3.15–3.18.

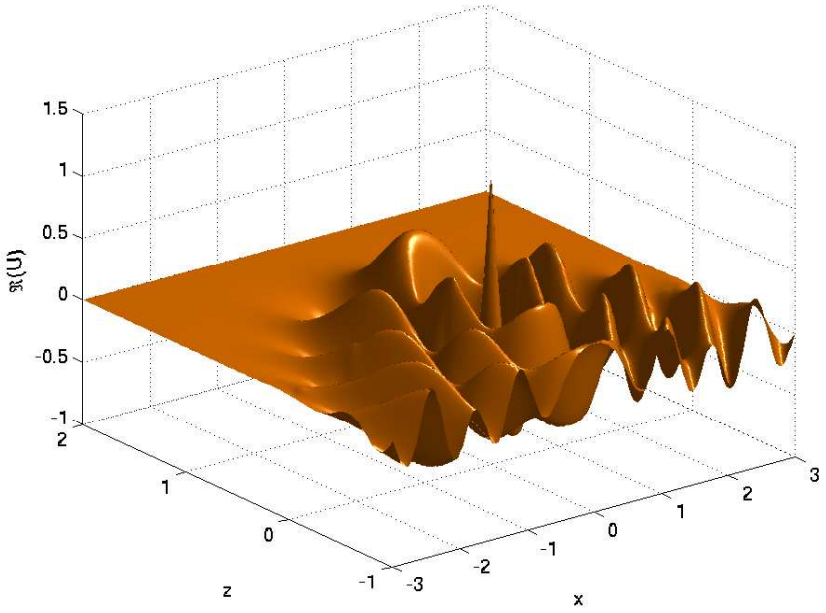

Figure 3.15: $\Re(U)$, $\omega = 10$.

$\diamond$ For $\omega = 30$, taking the cutoff value to be $\alpha = 50$, $\Re(U)$, $\Im(U)$ and $|U|$ are plotted in Figures 3.19–3.22.

In the plots of $\Re(\hat{U})$ and $\Im(\hat{U})$ we see the wavelike nature of the wavefield inside the caustic, and its decay in the shadow zone. In Figures 3.18 and 3.22 we see ridges, more closely spaced in the latter than the former, which we explain below. The behaviour of the wavefield for values of $z > 1$ is of interest, because $c(z)$ goes to infinity at $z = 1$ and therefore in Figures 3.18 and 3.22 we plot the wavefield up to

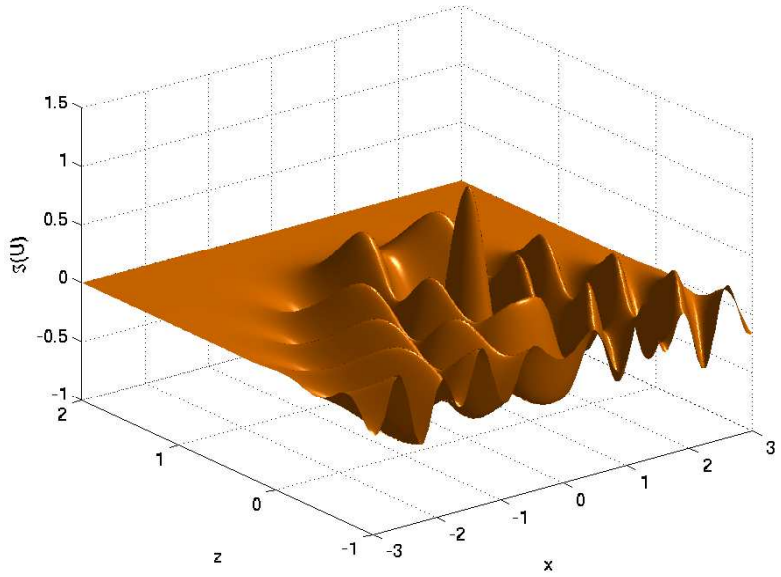

Figure 3.16: $\Im(U)$, $\omega = 10$.

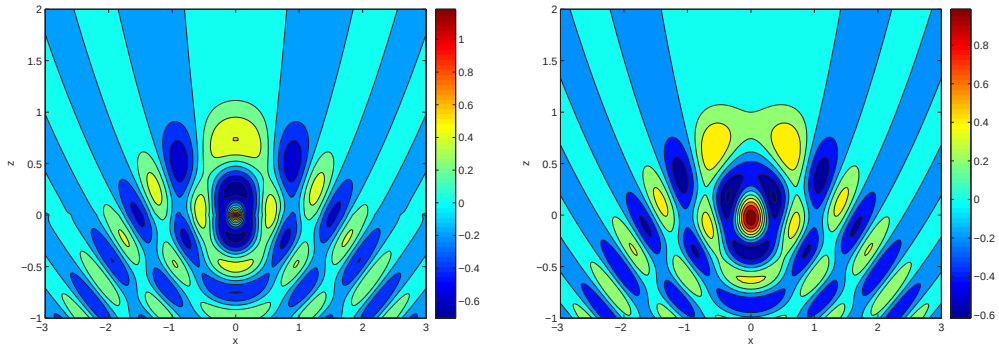

Figure 3.17: Contour plots for $\Re(U)$ and $\Im(U)$, $\omega = 10$.

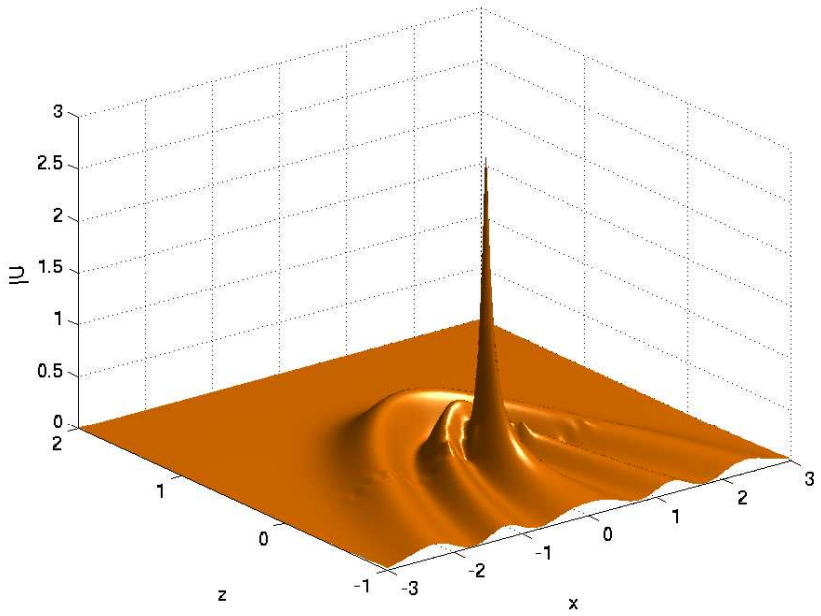

Figure 3.18: $|U|$, $\omega = 10$.

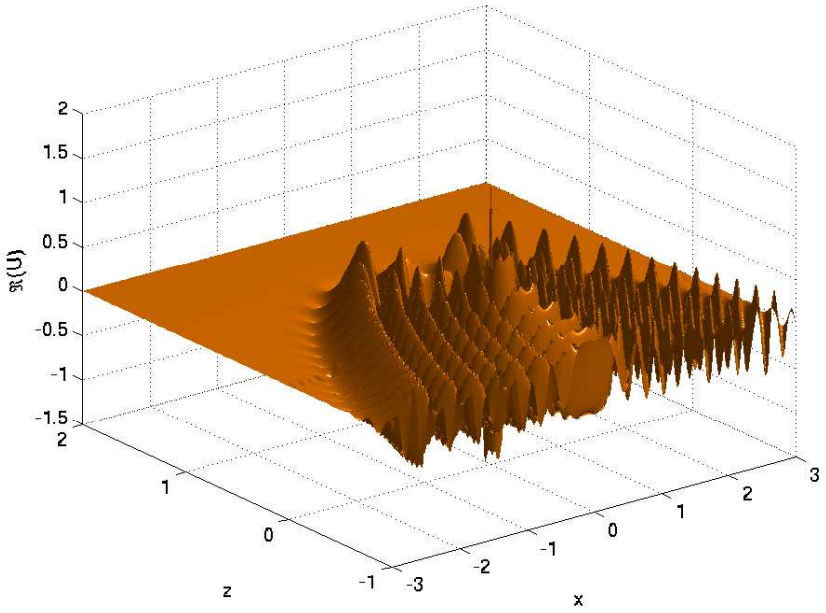

Figure 3.19: $\Re(U)$, $\omega = 30$.

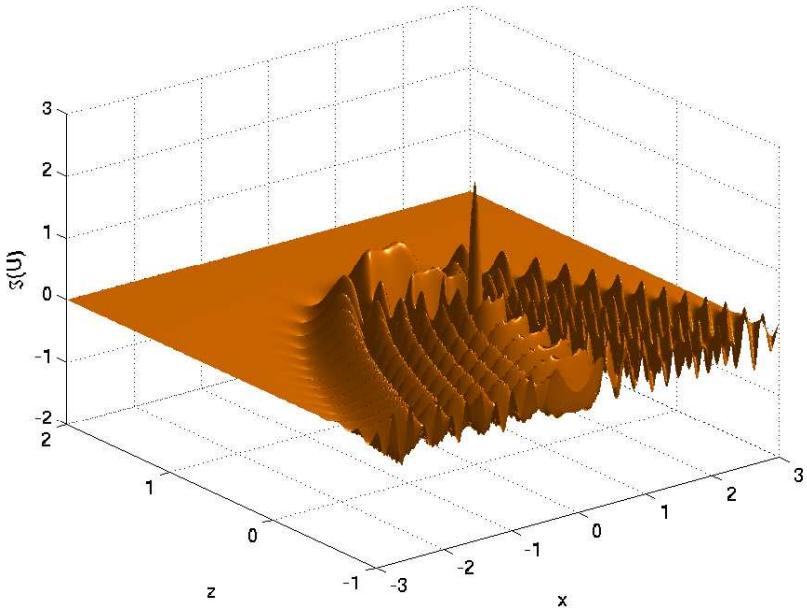

Figure 3.20: $\Im(U)$, $\omega = 30$.

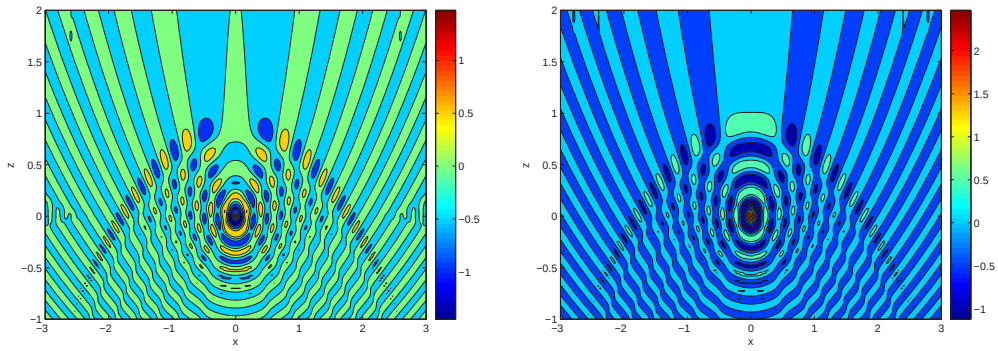

Figure 3.21: Contour plots for $\Re(U)$ and $\Im(U)$, $\omega = 30$.

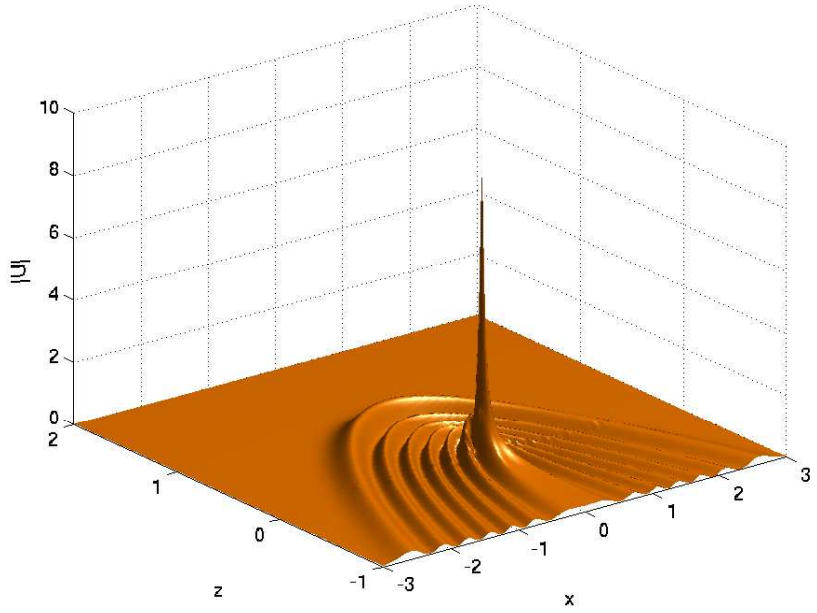

Figure 3.22: $|U|$, $\omega = 30$.

$z = 2$. We see that the wavefield decays for $z > 1$. We also note that Figures 3.18 and 3.22 exhibit some "rippling" along the line $z = 0$. This is a numerical artifact; when $z = 0$ and as $\alpha \to \infty$, the integral for $\Re(U)$ behaves like $\displaystyle\int^{\infty} \frac{\cos(\alpha x)}{\alpha} d\alpha$ and its convergence is delicate, so a very large cutoff value for α needs to be taken for an accurate result. This integral gives a logarithmic singularity at the source position, which manifests itself with large spikes in the Figures for $\Re(U)$ and $|U|$. (Whereas, as $\alpha \to \infty$ the integral for $\Im(U)$ behaves like $\displaystyle\int^{\infty} \frac{1}{\alpha} \exp\left(-\frac{4\alpha^3}{3\omega^2}\right) d\alpha$, which gives a finite value at the source.)

• Why the ridges appear

The ridges and valleys in Figures 3.18 and 3.22 correspond respectively to constructive and destructive interference of the waves, and we conclude this discussion by showing how the ridge positions can be calculated by the Geometrical Theory of Diffraction [19, 75]. As we have seen in the previous section at any one point (x, z) inside the caustic $z = 1 - x^2/4$, there are two rays passing through, taking respectively times t_1 and t_2 to carry the wave from the source to this point. The time t as a function of a point (x, z) is given by the ray conoid expression (3.74). If none of the rays passed through the caustic the constructive interference condition would be $t_2 - t_1 = nT$

where $T = 2\pi/\omega$ is the period of the waves, and n an integer. However, as we have established above, always exactly one of the two rays passes through the caustic. The phase of the wave is advanced by $\pi/2$ as the ray passes through the caustic (see for instance [94], p. 468), and therefore the constructive interference condition is modified to

$$t_2 - t_1 = \left(n + \frac{1}{4}\right) \frac{2\pi}{\omega}. \tag{3.105}$$

Using (3.74) we can plot the contour plots of $t_2 - t_1$ on the (x, z)-plane as n varies and for any fixed value of ω. To compare with Figures 3.18 and 3.22 we present contour plots for $\omega = 10$ (Figure 3.23(a)) and for $\omega = 30$ (Figure 3.23(b)). On these contour plots we superimpose also the caustic $z = 1 - x^2/4$ with a dashed line. We see that the locations of the maxima of the ridges agree very well with the contour locations. Note that this provides a nice verification of the accuracy of our numerical calculations.

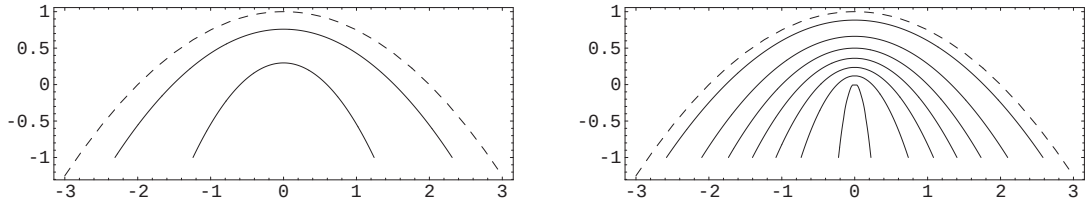

(a) $\omega = 10$ (b) $\omega = 30$

Figure 3.23: Contour plots of $t_2(x, z) - t_1(x, z)$ as n varies.

Inside the caustic two rays pass through each point (x, z), on the caustic the rays coincide (and are tangent to it), and outside of it there are no rays. This indicates that if we were to determine the stationary points of the integrals for $\Re(U)$ and $\Im(U)$ we would expect to find two real stationary phase points inside the caustic that coincide on the caustic, and become complex outside of it.

3.6 Steady supersonic motion in a model stratified atmosphere (two dimensions)

In this section we are going to determine analytically the Mach envelope for the steady source motion $(x_0(t) = -Ut, z_0(t) = 0)$ in the medium with $c(z) = 1/\sqrt{1-z}$. This

analysis is a paradigm problem for the behaviour of the Mach envelope in the vertical plane of motion in a medium where the sound speed is increasing with height. We will see that a fold caustic of boomrays is formed, corresponding to the appearance of a cusp on the Mach envelope.

In the aerodynamic frame, we can determine the Mach envelope as the characteristics of the equation

$$B^2\Phi_{XX} = \Phi_{zz}, \tag{3.106}$$

where $B^2 = B_0^2 - M_0^2 z$. Equation (3.106) is an equation of mixed type: it is elliptic for $B^2 < 0$, parabolic for $B = 0$ and hyperbolic for $B^2 > 0$. The parabolic line is determined by the condition $U = c(z)$, which is equivalent to $B(z) = 0$. This parabolic line will be called the sonic line and its height the sonic height from now on. Equation (3.106) can be recast into the canonical linear Tricomi equation $z\Phi_{XX} = \Phi_{zz}$, when we let $z \mapsto M_0^2(1-z)/B_0^2$, and $X \mapsto -B_0 X/M_0^2$.

The characteristics for equation (3.106) are

$$\textit{incident}\text{ characteristic: } X = -\frac{2}{3M_0^2}((B_0^2 - M_0^2 z)^{3/2} - B_0^3), \tag{3.107}$$

$$\textit{reflected}\text{ characteristic: } X = \frac{2}{3M_0^2}((B_0^2 - M_0^2 z)^{3/2} + B_0^3), \tag{3.108}$$

$$\text{downgoing characteristic: } X = \frac{2}{3M_0^2}((B_0^2 - M_0^2 z)^{3/2} - B_0^3), \tag{3.109}$$

and they are plotted in Figure 3.24. (Note that since we take $c_0 = 1$ we have $M_0 = U$ and $B_0 = \sqrt{U^2 - 1}$.) The most interesting feature of (3.107)–(3.109) is a 3/2-power cusp at $X = 2B_0^3/(3M_0^2)$, on the sonic line $z = B_0^2/M_0^2$. Such cusps are well-known features of the Tricomi equation, and from now on we will refer to them as Tricomi cusps. The terms "incident characteristic" and "reflected characteristic" are used because we can think of the perturbation from the source as moving along the incident characteristic, reflecting at the sonic line at the Tricomi cusp, and then moving along the reflected characteristic.

For any atmospheric sound speed profile near a sonic line we can expand $B^2(z) \approx B_0^2 + \nu z$, where ν is a constant, and end up with a scaled version of equation (3.106), which would give the local behaviour of the Mach surface in the vertical plane of flight. This observation gives our example general applicability. It is thus expected that on the Mach surface in a typical atmosphere we would observe such Tricomi cusps (as confirmed in Section 3.8, Figure 3.39).

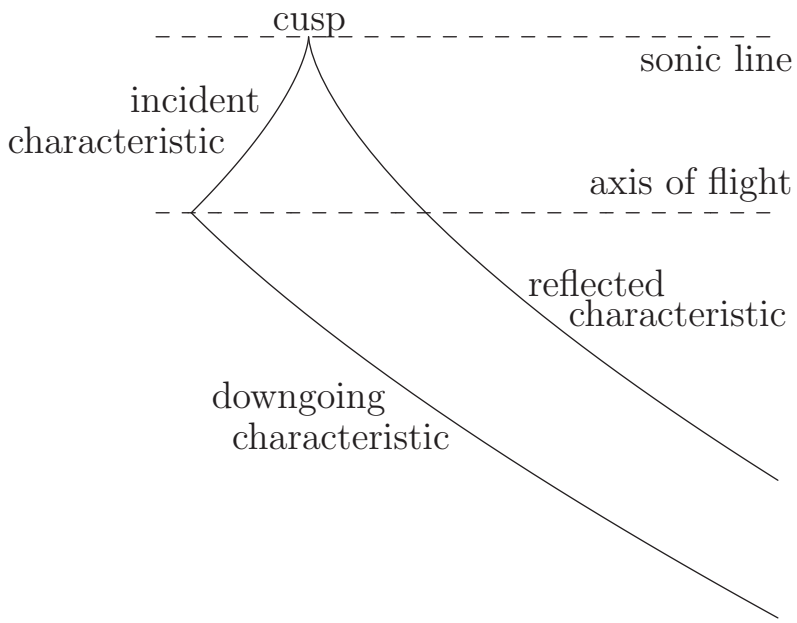

Figure 3.24: Characteristics of the Tricomi-type equation (3.106).

In Figure 3.25, for $U = \sqrt{2}$, we plot the wavefronts corresponding to $\tau = n\sqrt{2}/6, 0 \leq n \leq 7$ and time $t = 4\sqrt{2}/3$. We plot the Mach envelope with a thicker solid line. The wavefronts are denser near the Tricomi cusp of the Mach envelope, at the height $z = 1/2$ which also indicates focusing there. [10] The incident part of the envelope is outside the wavefronts but the reflected part of the envelope is inside the wavefronts. This becomes clearer with the schematic illustration in Figure 3.26. In Chapter 6, we shall see the same qualitative change in the Mach envelope of an accelerating motion in a uniform medium, and we will discuss it in more detail there.

We should stress that the stratification cusps of the individual wavefronts and the Tricomi cusps on the Mach envelope are unrelated, even if they are both 3/2-power cusps. The stratification cusps have nothing to do with the fact that the source is moving; they also exist in the wavefronts generated by a stationary source (see Figure 3.12) and are associated with the sound speed $c(z)$ becoming infinite at $z = 1$. For any U, the "distorted" cusp locus is easily determined by eliminating τ from the expressions (3.79), with $x_{\rm cu} = x + U\tau$, $t_0 = t - \tau$. We thus have

$$z = 1 - \frac{1}{4}(x + Ut)^2 - \frac{U^2}{9}(2 - z)^3 + \frac{U}{3}(x + Ut)(2 - z)^{3/2}, \tag{3.110}$$

[10] In the end of this section we will give more details on the way the wavefronts "conspire" to form the Mach envelope.

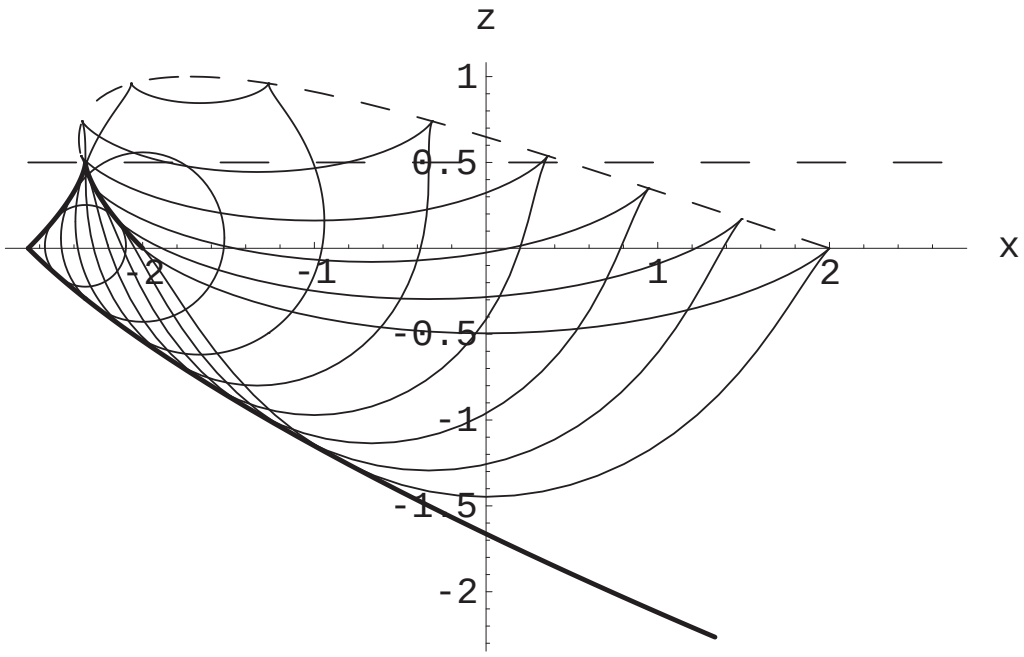

Figure 3.25: $U = \sqrt{2}$, $c_0 = 1$: Mach envelope as envelope of wavefronts in the medium $c = 1/\sqrt{1-z}$. The locus of cusps (as described in the text) is also shown (dashed curve). The sonic line is at $z = 1/2$, and also plotted with a dashed line.

Figure 3.26: Schematic diagrams for the formation of the incident and reflected parts of the Mach envelope (left and right respectively). In each case the thin curves are the wavefronts and the thick curve is their envelope.

which is also plotted in Figure 3.25 with a dashed line. Expression (3.110) reduces to $z = 1 - x^2/4$ when $U = 0$, as expected.

To derive the Mach envelope for any unsteady motion on a straight line in this medium as the envelope of wavefronts we write the family of wavefronts as

$$\psi(x, z, t, \tau) = 9(t-\tau)^2 - (2-z)(4 - 4z + 4z^2 + 3\tilde{x}^2) \pm 8\left(1 - z - \frac{\tilde{x}^2}{4}\right)^{3/2} = 0, \tag{3.111}$$

where $\tilde{x} = x - x_0(\tau)$; from the envelope condition (3.38) we get

$$\tilde{x}\frac{\partial \tilde{x}}{\partial \tau} = -\frac{3(t-\tau)}{(2-z) \pm 8\left(1 - z - \tilde{x}^2/4\right)^{1/2}}. \tag{3.112}$$

Eliminating τ from (3.111) and (3.112) would yield an expression for the Mach envelope in terms of x, z, and t.

However, it is far simpler to find the Mach envelope as the locus of the tips of boomrays, as discussed in Section 3.4.2. For any ray launched at the boomray angle $\theta'_{B0}(\tau)$ made with the positive x-direction we have

$$(p_0(\tau), r_0(\tau)) = -\left(\cos\theta'_{B0}(\tau), \pm\sin\theta'_{B0}(\tau)\right). \tag{3.113}$$

From (3.61)–(3.63), the boomray equations are

$$x(\zeta, \tau) = -\frac{2}{U(\tau)}\zeta + x_0(\tau), \tag{3.114}$$

$$z(\zeta, \tau) = -\zeta^2 \pm 2\frac{B_0(\tau)}{U(\tau)}\zeta, \tag{3.115}$$

$$t(\zeta, \tau) = \frac{2}{3}\zeta^3 \mp 2\frac{B_0(\tau)}{U(\tau)}\zeta^2 + 2\zeta + \tau. \tag{3.116}$$

The upper sign in the equations (3.113), (3.115), (3.116) correspond to upward launching and the lower sign corresponds to downward launching.[11] Considering the case of steady motion with some general speed U in the negative x-direction, since the medium is stratified in the z-direction, all boomrays have equal launching angles $\pm\theta'_{B0}$ that satisfy $\cos\theta'_{B0} = -1/M_0$, and $\sin(\pm\theta'_{B0}) = \pm B_0/M_0$. For steady motion, we first consider the boomrays launched upwards and using (3.115), we substitute z

[11] As a check, we use the boomray equations (3.114)–(3.116), in the condition (3.112) and this is then rewritten as a cubic in ζ,

$$2\zeta^3(1 - Up_0) + 6r_0\zeta^2(1 - Up_0) + 6\zeta(1 - Up_0) = 0, \tag{3.117}$$

which vanishes identically under the boomray condition $p_0 = 1/U$.

in the quantity $(B_0^2 - U^2 z)^{3/2}$. We find that this is equal to $(B_0 - U\zeta)^3$ if $\zeta < B_0/U$ but to $(U\zeta - B_0)^3$ if $\zeta > B_0/U$. The threshold value $\zeta = B_0/U$, corresponds to the maximum height of the boomrays which is the sonic height $z = B_0^2/U^2$. Now, using (3.114) and (3.116) we have

$$X = x + U\tau + U(t - \tau) = -\frac{2}{U}\zeta + 2\zeta U - 2B_0\zeta^2 + \frac{2U}{3}\zeta^3. \tag{3.118}$$

Therefore the Mach envelope in $z \geq 0$ is

$$-\frac{3U^2}{2}X = (B_0^2 - U^2 z)^{3/2} - B_0^3 = B^3 - B_0^3, \quad \text{for } \zeta < B_0/U, \tag{3.119}$$

$$\frac{3U^2}{2}X = (B_0^2 - U^2 z)^{3/2} + B_0^3 = B^3 + B_0^3, \quad \text{for } \zeta > B_0/U. \tag{3.120}$$

The Mach envelope parts (3.119) and (3.120) join at the Tricomi cusp. Now, for downward launching we similarly find that the boomrays form the part of the Mach envelope

$$\frac{3U^2}{2}X = (B_0^2 - U^2 z)^{3/2} - B_0^3 = B^3 - B_0^3. \tag{3.121}$$

Expressions (3.119)–(3.121) coincide, as expected, with expressions (3.107)–(3.109).

In Figure 3.27, and again for $U = \sqrt{2}$, we use the equations (3.114)–(3.116) to plot boomrays, emitted from equidistant source positions. The maximum height for a boomray is at the sonic line $z = 1/2$. We also use the expressions (3.119)–(3.121) to plot (with a dashed line) the Mach envelope. The *incident* envelope part (3.119) is the locus of the tips of boomrays that are launched upwards but have not yet reached their maximum height; the cusp corresponds exactly to a boomray with a turning point on the envelope; and the *reflected* envelope part (3.120) is the locus of the tips of boomrays that have already reached their maximum point and are descending. We see that a smooth envelope of boomrays (a fold caustic of boomrays), is formed at the sonic line $z = 1/2$. Summarising: *the incident envelope part is formed by boomrays that have* ***not*** *touched the caustic and the reflected envelope part is formed by boomrays that* ***have*** *touched the caustic.* In the aerodynamic frame the fold caustic "collapses" into a Tricomi cusp, which is stationary. We shall see later that in three dimensions this Tricomi cusp point generalises into a curve.

Finally, as promised, we give some more details on how wavefronts "conspire" to make up the Mach envelope. We imagine a boomray superimposed on the wavefronts of Figure 3.7. As time increases, a fixed ray, which for envelope purposes is the boomray, first forms a point on the lower branch of the wavefront $t = t_0$. At some

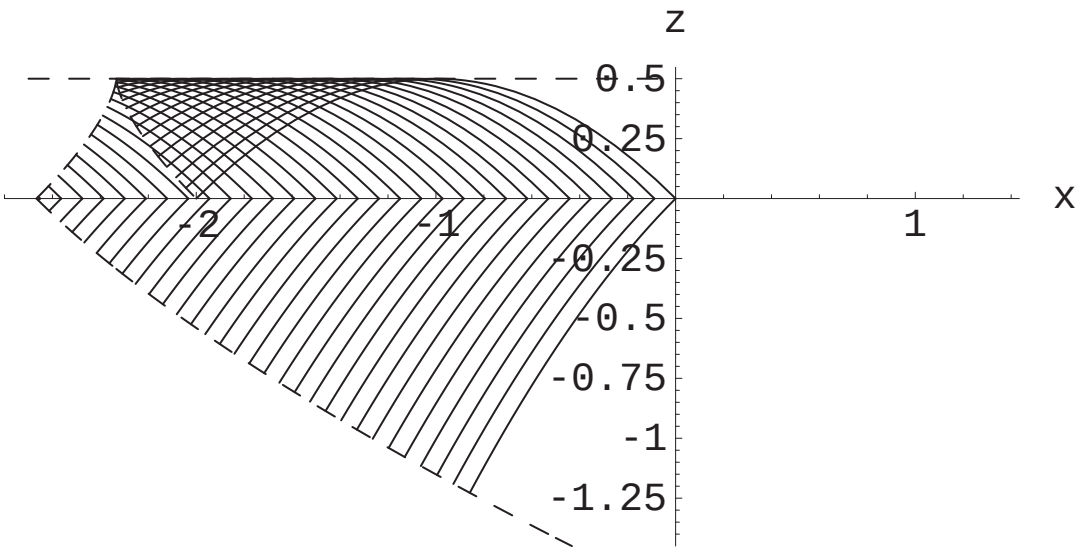

Figure 3.27: $U = \sqrt{2}$, $c_0 = 1$: Boomrays and the Mach envelope made up as the locus of their tips. The boomrays that form the reflected part of the envelope have touched a fold caustic. The Mach envelope and the sonic line are plotted with a dashed line.

switchover time $t = t_\star$ the ray forms a point on both branches, that is, it passes through one of the two wavefront cusps. For $t > t_\star$ the ray forms a point on the upper branch of the wavefront. Since the boomrays satisfy $\cos\theta'_{B0} = -1/M_0 = -1/U$, we have

$$t_\star = \frac{2U^3}{3(U^2-1)^{3/2}}. \tag{3.122}$$

Therefore for all wavefronts times $t < t_\star$ the cusp locus is on the left of the reflected Mach envelope, it crosses the Mach envelope at $t = t_\star$, and is on the right of it for $t > t_\star$. (At the sonic line, the wavefront contributing its cusps to the cusp locus there is $t = \frac{2}{3}(1 + 1/U^2)^{3/2}$.) For example, for $U = \sqrt{2}$ used in our examples above, this gives $t_\star = 4\sqrt{2}/3$) and therefore the intersection of the cusp locus (3.110) and the Mach envelope is on the source height $z = 0$, as it can be seen in Figure 3.25.

For any value of U we can show that, *below* the sonic line, the cusp locus and the reflected Mach envelope are very close to each other—in fact so near that when they are plotted on the computer (using Mathematica) they are virtually indistinguishable (we indeed see this in Figure 3.25).

The other general feature of the envelope formation we should make note of is that, for all U, at the Tricomi cusp the contributing wavefront has a vertical tangent, (and the boomray there has its turning point as we remarked above). This is a result

valid for the local behaviour near the sonic line in any steady motion in *any* stratified medium. From Section 3.5.1, for any U, the vertical-tangent wavefront is given by

$$t_{\rm vt}(U) = \frac{2\sqrt{U^2-1}(U^2+2)}{3U^3}, \tag{3.123}$$

and we can use the results in page 47 to determine, for any value of U, which vertical tangency is the one contributing to the Tricomi cusp.

3.7 Steady subsonic motion in a model stratified atmosphere (two dimensions)

It is also of interest to show the wavefront pattern in the medium $c = 1/\sqrt{1-z}$ when the source motion is subsonic. In this case no boomrays are emitted and hence no Mach envelope is formed. However we expect some interesting features to arise due to the medium stratification. In Figure 3.28 we plot 12 wavefronts for $M_0 = 1/2, t = 2$, and $\tau = n/6$, $n = 0, ..., 11$. The wavefronts that satisfy $t - \tau \leq 2/3$ are nested. Looking only at wavefronts of the latter type, Figure 3.28 is qualitatively similar to Figure 3.3 for steady subsonic motion. However the wavefronts with $t - \tau \geq 2/3$ are not nested due to the presence of the stratification cusps. A cusp locus forms as in Figure 3.7, given again by the analytical expression (3.110) and we plot it with a dashed line. Note that the sonic line is $z = 1 - 1/U^2 = -3$, and also shown with a dashed line. (The thicker line in Figure 3.28 represents the path of the source.)

3.8 Steady supersonic motion in two model stratified atmospheres (three dimensions)

3.8.1 Introduction and overview

For the stratified medium with sound speed profile $c = c_0/\sqrt{1-\mu z}$, we have analysed the geometry of the Mach envelope in two dimensions, and presented relevant plots for the case $c_0 = 1$, $\mu = 1$, at constant speed $U = \sqrt{2}$. We are now going to present analytical examples in three dimensions. We will assume a steady motion and work in the aerodynamic frame.

Of great practical interest is the intersection of the Mach surface with the ground, called the *carpet*. A *primary carpet* (PC) is formed by BICHs launched downwards and a *secondary carpet* (SC) is formed by BICHs launched upwards, which eventually

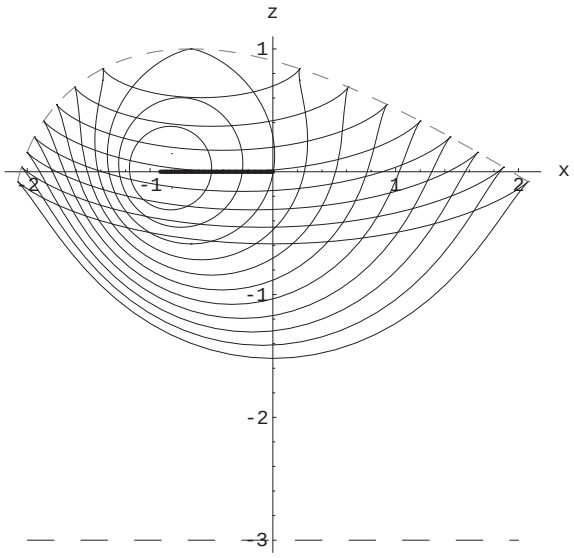

Figure 3.28: Subsonic motion with $U = 1/2$ in the stratified medium $c = 1/\sqrt{1-z}$. For $t = 2$, we show 12 wavefronts $\tau = n/6$, $n = 0, ..., 11$. The sonic line $z = -3$ and the locus of cusps (3.110) are also shown (with a dashed line).

reverse direction due to refraction and subsequently hit the ground. The Mach surface and the carpets are determined for two model atmospheres.

Firstly, we determine analytically the Mach surface and BICHs when the Prandtl-Glauert parameter is $B^2 = 1 - z$; through an appropriate coordinate change the analysis is closely related to the analysis for a stationary source in Section (3.5). In this scenario all the BICHs launched upwards are reflected back to the source height and eventually hit the ground. However in a real atmosphere, some of the BICHs are permanently trapped above the ground due to the stratospheric and thermospheric waveguide. Therefore we modify the model to $B^2 = 1 - |z|$, which gives rise to a waveguide behaviour. All calculations are again done analytically. The resulting geometry agrees qualitatively very well with the Mach surface and the BICHs under realistic atmospheric conditions, where they can only be determined numerically.

3.8.2 Bicharacteristics, Mach surface

For $c = c_0/\sqrt{1-\mu z}$, the ray (hyper)conoid in three dimensions is obtained by replacing x^2 with $x^2 + y^2$ in (3.75). We get

$$\begin{aligned}\psi(x,y,z) =&(2-\mu z)(4-4\mu z+4\mu^2 z^2+3\mu^2(x^2+y^2))\\ &\pm 8(1-\mu z-\mu^2(x^2+y^2)/4)^{3/2}-9(c_0\mu t)^2=0.\end{aligned} \tag{3.124}$$

One way to obtain the Mach surface for $B^2 = 1 - z$ would be to take the envelope of the ray conoids (3.124) with $c_0 = 1$, $\mu = 1/2$ and $U = \sqrt{2}$ (or fix $M_0 = U/c_0 = \sqrt{2}$ at the reference level $z_0 = 0$). However, this (lengthy) calculation can be circumvented since for steady flight we can work with BICHs. The BICHs simplify the calculations enormously as well as being the curves on which the boom propagates. Furthermore, we will show that a change of coordinates in the ray conoid expression (3.74) will give immediately the Mach surface here. When $B^2 = 1 - z$, the ordinary differential equations for the BICHs cannot be analytically integrated if they are in the form (3.54)–(3.55). We can resolve this if we work instead with the eikonal

$$F_1' = \frac{1}{2}F_1 = \frac{1}{2}\left(B^2 P - \frac{Q^2 + R^2}{P}\right) = 0, \tag{3.125}$$

which corresponds to the ordinary differential equations

$$\frac{d\mathbf{X}}{ds} = M\mathbf{N} + (M^2, 0, 0), \tag{3.126}$$

$$\frac{d\mathbf{N}}{ds} = M\left(-\frac{\boldsymbol{\nabla} c}{c} + (\mathbf{N}.\frac{\boldsymbol{\nabla} c}{c})\mathbf{N}\right), \tag{3.127}$$

obtained directly from (3.54)–(3.55) by setting $cdt = Mds$. Integrating them we obtain the BICHs equations

$$X(s; \mathbf{N}_0) = \frac{s^3}{12} + \frac{R_0}{P_0}\frac{s^2}{2} + (1 - z_0)s, \tag{3.128}$$

$$y(s; \mathbf{N}_0) = -\frac{Q_0}{P_0}s + y_0, \tag{3.129}$$

$$z(s; \mathbf{N}_0) = -\frac{s^2}{4} - \frac{R_0}{P_0}s + z_0, \tag{3.130}$$

$$P = P_0, \quad Q = Q_0, \quad r(s; \mathbf{N}_0) = \frac{P_0}{2}s + R_0, \tag{3.131}$$

where

$$\mathbf{N_0} = \left(-\frac{1}{M_0}, -\frac{Q_0}{M_0 P_0}, -\frac{R_0}{M_0 P_0}\right), \tag{3.132}$$

is the unit outward normal to the Mach surface (see (3.56)) at the source location.

It is convenient to employ a spherical polar parametrisation where the azimuthal angle φ is measured in the (y, z)-plane from the y-axis anticlockwise and θ is the angle made with the positive x-direction. We therefore let

$$P_0 = \cos\theta_0 = -\frac{1}{M_0} = \text{constant}, \tag{3.133}$$

and then

$$Q_0 = \sin\theta_0 \cos\varphi = \frac{B_0}{M_0}\cos\varphi, \text{ and } R_0 = \sin\theta_0 \sin\varphi = \frac{B_0}{M_0}\sin\varphi. \tag{3.134}$$

Substituting (3.133) and (3.134) into the BICH equations (3.128)–(3.131) we have

$$X(s;\varphi) = \frac{s^3}{12} - (B_0 \sin\varphi)\frac{s^2}{2} + (1 - z_0)s, \tag{3.135}$$

$$y(s;\varphi) = -(B_0 \cos\varphi)s + y_0, \tag{3.136}$$

$$z(s;\varphi) = -\frac{s^2}{4} + (B_0 \sin\varphi)s + z_0, \tag{3.137}$$

$$r(s;\varphi) = -\frac{s}{2M_0} + \frac{1}{M_0}(B_0 \sin\varphi), \tag{3.138}$$

where $B_0 = B(z_0) = \sqrt{1 - z_0}$. For BICHs launched upwards $0 \leq \varphi \leq \pi$ so $\sin\varphi > 0$, and for BICHs launched downwards $\pi \leq \varphi \leq 2\pi$ so $\sin\varphi < 0$.

To obtain the Mach surface we need to eliminate s and φ from (3.135)–(3.138). However, this is unnecessary if we apply the coordinate transformation

$$t \mapsto X, \quad x \mapsto y, \quad z \mapsto z \text{ (and } p \mapsto \Phi), \tag{3.139}$$

in equation (3.59), which then becomes equation (3.49). The ray conoid at $(0, 0, 0)$ of (3.59) is (3.74) and under the latter change of coordinates it leads immediately to the required Mach surface for $y_0 = z_0 = 0$

$$9X^2 = (2 - z)(4 - 4z + 4z^2 + 3y^2) \pm 8\left(1 - z - \frac{y^2}{4}\right)^{3/2}. \tag{3.140}$$

Note that this is the same change of coordinates with which the theory of unsteady cylindrical waves provides a shortcut in the analysis of the steady motion of an axisymmetric body—see, for instance, Whitham [126], Section 7.5, p. 224. (Should we wish to determine the Mach surface or any other expression for the more general case of $B^2 = a - bz$ we can use in (3.140) $(X, y, z) \mapsto (a^{3/2}X/b, ay/b, az/b)$.)

Obviously, the change of coordinates (3.139) makes the discussion of the features of the ray conoid (3.74) for the stationary source directly relevant to the analysis of the features of the Mach conoid (3.140) (and the discussion on the ray pattern there directly relevant to the BICHs here). Firstly, Figure 3.7 no longer represents wavefronts but instead (when we change the horizontal axis label to y) gives the constant X-sections of the Mach conoid as $X = X_0$ increases.

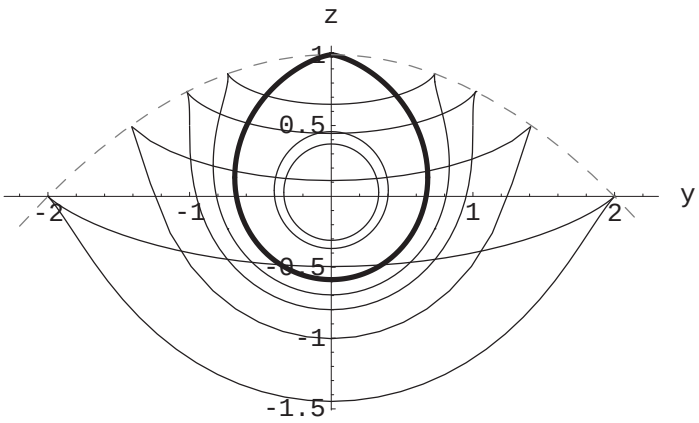

Figure 3.29: X-sections of the Mach conoid (3.140) for increasing X: for $X_0 < X_c = 2/3$ we show $X_0 = 1/3$ and $X_0 = 1/2$. The marginal section $X_0 = 2/3$ is marked with a thicker line. The cusped sections $X_0 = (1+\sqrt{2})/3$, $2\sqrt{2}/3$, $\sqrt{3/2}$ and $4\sqrt{2}/3$ are shown. Apart from the axes, this figure is exactly the same as Figure 3.7.

For $X_0 > X_c = 2/3$, each of these (y,z)-sections has cusps that are on the curve $z = 1 - y^2/4$. From the expressions (3.79) we have that the y and z coordinates of the two cusps visible on each (y,z)-section, are

$$y_{\rm cu} = \pm 2\sqrt{\left(\frac{9}{4}X_0^2\right)^{1/3} - 1}, \tag{3.141}$$

$$z_{\rm cu} = 2 - \left(\frac{3}{2}X_0\right)^{2/3}. \tag{3.142}$$

However there is a crucial difference; the curve

$$z = 1 - y^2/4, \quad X = (2/3)(2-z)^{3/2} \tag{3.143}$$

is now the "collapse" (into the aerodynamic frame) of the fold caustic surface of boomrays in the fixed reference frame, and from now on it will be called the *fold caustic curve*. Therefore its presence is much more significant as it indicates a region of boom focusing, rather than focusing of linear sound waves. Recall that in two dimensions there is only such focusing point, the Tricomi cusp (see Figures 3.27 and 3.25 and the related discussion in Section 3.6).

Furthermore, the discussion of Section 3.5.2 is also of relevance. Expressions (3.84), (3.82) and (3.83) give respectively the following parametrisation of the fold

caustic curve (3.143) in terms of the azimuthal angle φ_{fold}:

$$X_{\text{fold}} = \frac{2}{3}(1/\sin^3\varphi_{\text{fold}}), \tag{3.144}$$

$$y_{\text{fold}} = 2\cot\varphi_{\text{fold}}, \tag{3.145}$$

$$z_{\text{fold}} = 1 - \cot^2\varphi_{\text{fold}}. \tag{3.146}$$

Going back to a $X = X_0 =$ constant section ($X_0 > 2/3$) of the Mach surface:

- for $\varphi_{\text{fold}} \le \varphi \le \pi - \varphi_{\text{fold}}$ the BICHs have passed through the caustic and make up the positive sheet of the surface (3.140),
- for the remaining values of φ_{fold} the BICHs have not passed through the caustic and make up the negative sheet of the surface (3.140),

where $\varphi_{\text{fold}} = \arcsin(2/(3X_0))^{1/3}$ is determined from (3.144).

3.8.3 Primary and secondary carpets

We now consider a BICH launched upwards from height z_0, which is taken equal to zero. Its maximum height is reached at $z_{\max} = M_0^2 R_0^2 = B_0^2 \sin^2\varphi$ which is determined by setting in (3.130)

$$\frac{dz}{ds} = 0 \text{ which corresponds to } s_{\max} = 2M_0 R_0. \tag{3.147}$$

We are going to represent the ground with the plane $z = z_g =$ constant where $z_g < 0$. The BICHs hit z_g when s satisfies the quadratic $z_g = -s^2/4 + (B_0 \sin\varphi)s$. Choosing the positive root of the quadratic, we have

$$s_g(\varphi; z_g) = -2\frac{R_0}{P_0} + 2\sqrt{\left(\frac{R_0}{P_0}\right)^2 - z_g} = 2B_0 \sin\varphi + \sqrt{B_0^2 \sin^2\varphi - z_g} \tag{3.148}$$

The BICHs are plotted in Figure 3.30 and terminated when they hit $z_g = -1/2$. The location of the fold caustic curve can be identified. The $\varphi = \pi/2$ BICH attains its maximum on the caustic and has a cusp there, but all other BICHs are smooth and their maximum is not on the caustic curve. The $\varphi = \pi/2$ BICH is plotted with a thicker red line. A cusp is visible on this BICH; the cusp is the "tip" of the fold caustic at $X = 2/3, y = 0, z = 1$.

The $\varphi = \pi/2$ BICH can also be calculated by the method of Section 3.6, since the Mach envelope in two dimensions can be thought of as the projection of the Mach surface on the $y = 0$ plane. However in any other vertical plane, Π_1 say (defined

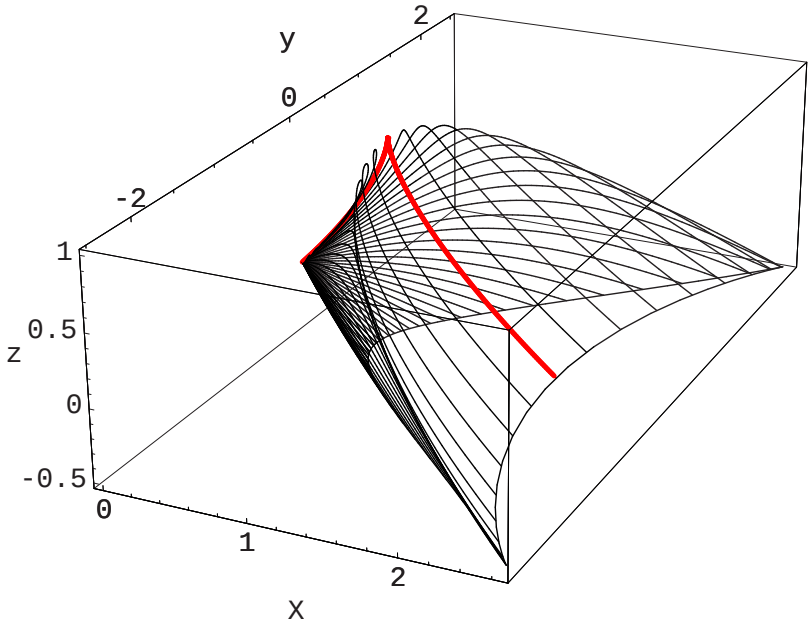

Figure 3.30: BICHs for the model atmosphere with local Prandtl-Glauert parameter $B^2 = 1 - z$. They are stopped at $z = z_g = -1/2$ and the corresponding carpet is plotted. The $\varphi = \pi/2$ BICH (plotted with a thicker red line) has its maximum at the sonic line $z = 1$. This maximum is a Tricomi cusp.

by the unit vector in the z direction, $\hat{\mathbf{e}}_\mathbf{z}$ and the BICH direction vector $\boldsymbol{\xi}$) the two-dimensional analysis does not carry through because the BICHs, unlike the boomrays, do not remain in the vertical plane they are launched in and do not satisfy Snell's law (3.35). (In fact, in a stratified atmosphere, the BICHs satisfy a generalised Snell's law (3.165), which is derived in Section 3.10.)

For any z_g the analytical expression for the carpet is found by substituting s_g from (3.148) into X and y in (3.135) and (3.136) respectively. Then

$$X_{\text{PC–SC}}(\varphi; z_g) = \frac{2}{3}\left(-\cos 2\varphi \sin\varphi - (2 - z_g + \cos 2\varphi)\sqrt{-z_g + \sin^2\varphi}\right), \qquad (3.149)$$

$$y_{\text{PC–SC}}(\varphi; z_g) = 2\cos\varphi\left(\sin\varphi + \sqrt{-z_g + \sin^2\varphi}\right). \qquad (3.150)$$

Expressions (3.149) and (3.150) give the primary carpet (PC) when $\pi \leq \varphi \leq 2\pi$, and the secondary carpet (SC) when $0 \leq \varphi \leq \pi$ (and hence the PC-SC subscript). The carpet, for $z_g = -1/2$, is plotted on Figure 3.30 and a separate picture of it is given in Figure 3.31, where the SC is the part of the curve with the thicker line. Even though this example is useful because it gives us a first taste of the SSB propagation in three dimensions, the PC and SC are joined because all BICHs eventually hit the

ground z_g. This is not the qualitatively correct behaviour for a real atmosphere and we will later consider the modified model atmosphere $B^2 = 1 - |z|$ which yields a more qualitatively correct carpet, whilst still being analytically tractable. We note

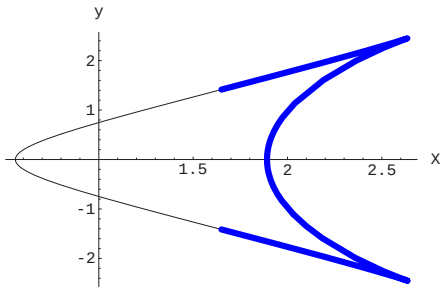

Figure 3.31: The carpet for $B^2 = 1 - z$ at $z = z_g = -1/2$. The primary and secondary carpets are joined because all BICHs launched upwards, eventually reach z_g.

that the carpet has two extreme points that are cusps. These cusps are the traces of the fold caustic curve (3.143) on the ground, and satisfy the relations (3.144)–(3.146). Therefore the width of the carpet, defined as the y-distance between these two cusps, is found simply to be $4\sqrt{1 - z_g}$, which increases with height.

Before moving on to a realistic atmosphere we would also like to analytically examine the phenomenon of the boom reflection at the ground. There are two points to comment on: the pressure recorded at the ground, and the continued propagation of the reflected boom. The former is of practical interest because for a receiver on the ground, the perceived boom is enhanced by reflection from the ground. The enhancement factor is generally a factor of 2 when assuming a perfectly reflecting ground (infinite acoustic impedance) but it may be smaller if the ground is soft, and larger if there are multiple reflectors of the boom (such as corners between the ground and walls).

For the same model profile $B^2 = 1 - z$ (and keeping $z_g = -1/2$), in Figure 3.32 we plot the BICHs reflecting from $z_g = -1/2$ once; we stop them when they hit z_g for a second time. We assume perfect reflection, so after a BICH hits z_g we just reverse the sign of $r(s_g(\varphi), \varphi)$, the z-component of the BICH direction vector, and calculate the subsequent trajectory using again equations (3.135)–(3.138). We see that two more caustic curves appear; one due to the reflected PC BICHs and one due to the reflected SC BICHs. We can also see that some of the reflected PC BICHs intersect with some of the SC BICHS. Such intersections, even though they are not caustics, are also places where the boom will be enhanced. Such intersections may occur under

realistic atmospheric conditions and it is desirable that they are not too near to the ground.

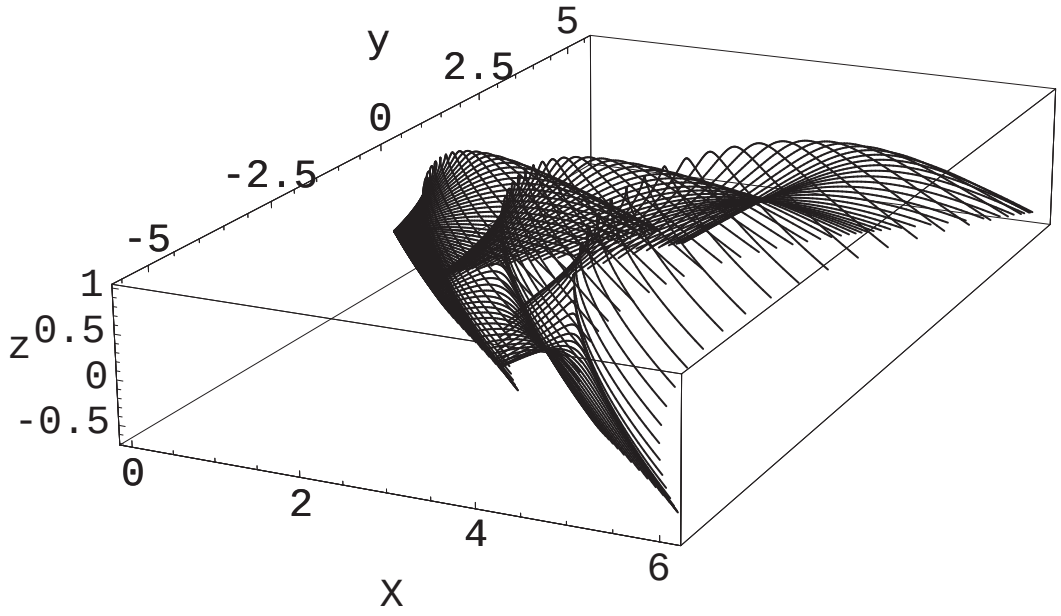

Figure 3.32: $B^2 = 1 - z$: BICHs reflecting off the z-level $z_g = -1/2$.

The corresponding carpet has been calculated again analytically as a function of φ—the lengthy formulae are not illuminating and hence not given here. Plotting the carpet expression in Mathematica, in Figure 3.33, we obtain two closed curves. The first closed curve starting from the left is the carpet that appeared already in Figure 3.31. The second closed curve is the carpet formed entirely by BICHs reflected off the ground. The part of the curve shown with a solid line is formed by reflected PC BICHs and the part of the curve shown with a dashed line corresponds to an indirect SC; it is formed by reflected SC BICHs. We again note that the carpets are closed curves because all BICHs eventually hit z_g.

Below we present the Mach surface and BICHs in a typical atmosphere, calculated numerically, and show the primary and secondary carpets. We then modify the model to $B^2 = 1 - |z|$, and determine the BICHs and carpets (still analytically). We will see that most of the qualitative features of the realistic carpet are captured by the latter model. Again we note that the "reflected" carpet is wider than the PC-SC carpet. The width increase with time is a general feature of SSB carpets, owing to the fact that the Mach conoid becomes larger with time.

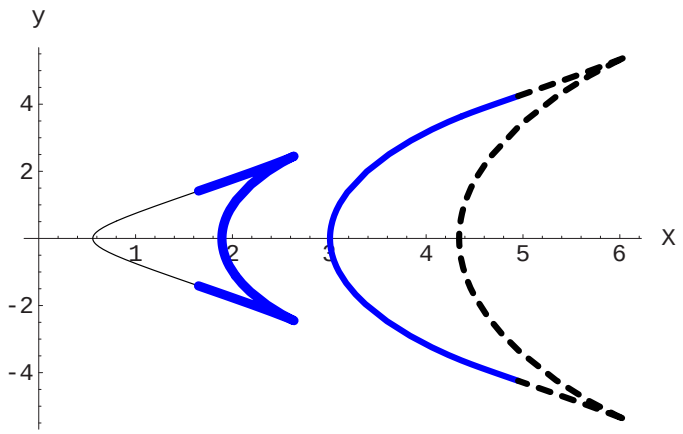

Figure 3.33: $B^2 = 1-z$: the carpet when we take into account reflection at $z_g = -1/2$. From left to right, the first closed curve is the carpet of Figure 3.31. The second closed curve is a "reflected" carpet; it consists of a part (solid line) formed by the reflected PC BICHs and a part (dashed line) that is formed by the reflected SC BICHs.

3.8.4 Numerical results for a real atmosphere; the analytical example $B^2 = 1 - |z|$

We consider a typical atmospheric sound speed profile c and the related plot of B^2 as in Figure 3.34. We integrate numerically the BICHs equations (3.54)–(3.55) (using

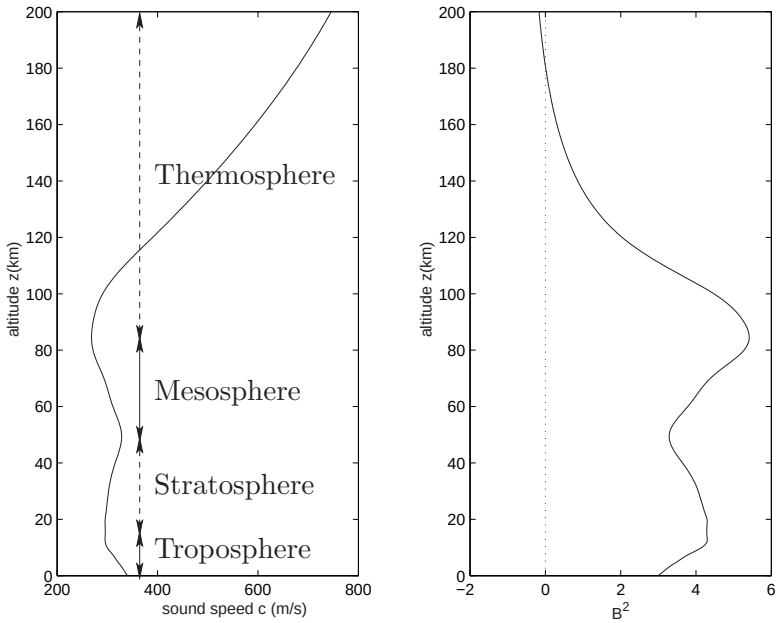

Figure 3.34: Typical sound speed profile for a real atmosphere (left) and the B^2 profile (right).

Matlab). We consider a supersonic aircraft (still modelled as a point source) flying at $z_0 = 18\,\text{km}$, and with $M_0 = \sqrt{2}$. The Mach surface is shown in Figure 3.8.4. Indeed we see that it looks like a deformed cone but we cannot draw more useful information from it. Therefore we will study its behaviour by looking at constant y and constant z sections. The traces of the BICHs on the ground are shown in Figure 3.36. We

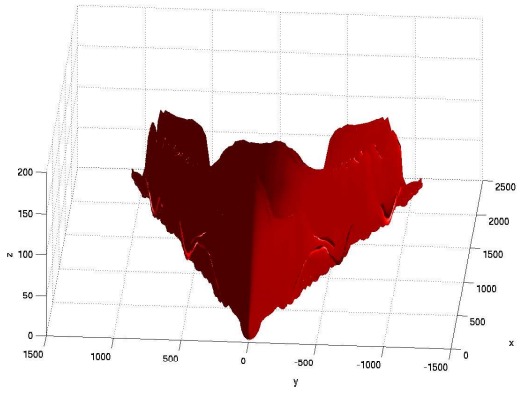

Figure 3.35: Mach surface for a typical stationary atmosphere, calculated numerically.

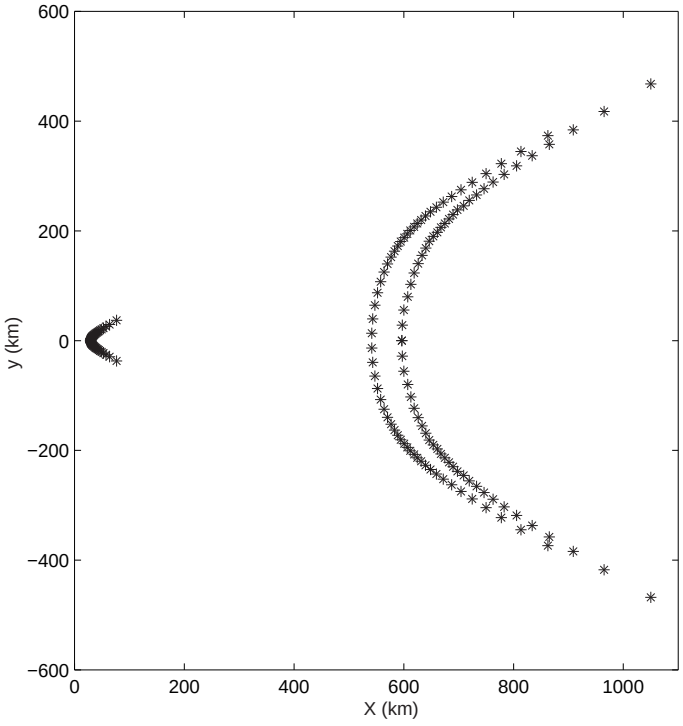

Figure 3.36: The carpet: PC, SC and indirect SC

observe that the PC (first curve from the left) and SC (the second and third curve

from the left) are disjoint and of finite extent (note that a curve here is taken to mean a collection of BICHs traces). Therefore we conclude that some of the BICHs do not reach the ground and we investigate this below.

For this it is easier to argue in terms of boomrays since they obey Snell's law $\cos\theta = c(z)\cos\theta_0/c_0$ (see Section 3.3). Applying it, we find that under almost all atmospheric conditions[12] a boomray that attains its maximum height in the stratosphere below 50 km can never reach the ground, because $c_g > c_{sp}$, where c_{sp} is the maximum value of the sound speed in the stratosphere. All such boomrays are therefore channelled or "trapped" in the stratosphere and we can refer to a *stratospheric waveguide*. Therefore in a windless atmosphere all boomrays that do reach the ground must attain their maximum height and "reflect" in the thermosphere around or above 110 km (according to Figure 3.34). Therefore, in a typical, stratified stationary atmosphere an SSB can only be thermospheric. Also in the thermosphere, if the "reflection" height is for a sound speed value that is less than c_g (heights between 50 km and 100 km) the boomrays are trapped between the thermosphere and some point in the troposphere above the ground, and we can refer to a *thermospheric waveguide*.

We can investigate the waveguide behaviour analytically, by considering $B^2 = 1 - |z|$ for which the sound speed profile has a minimum at $z = 0$. As in the previous analytical examples, we take $z_0 = 0$ and $z_g < 0$. (If we want to consider some other more general situation we can stretch and rescale accordingly.) This model can capture well the qualitative features of thermospheric SSBs. Since $B^2 = 1 - |z| = 1 + z$ for $z < 0$, all BICHs launched downwards attain a minimum at $z = -\sin^2\varphi$. Setting $z = z_g$ we find from the relevant BICH equations (we do not give them here as it is just a matter of algebra) that

$$s_g = \frac{2P_0}{R_0} \pm 2\sqrt{\left(\frac{P_0}{R_0}\right)^2 + z_g}, \tag{3.151}$$

and we need to pick the positive root. The square root in (3.151) gives that PC values of φ should satisfy

$$\sin^2\varphi \geq -z_g \tag{3.152}$$

and consequently since $\sin\varphi < 0$, we have $\pi + \arcsin(\sqrt{|z_g|}) \leq \varphi \leq 2\pi - \arcsin(\sqrt{|z_g|})$. The PC is then

$$X_{\mathrm{PC}} = -\frac{2}{3}(2 + \cos 2\varphi)\sin\varphi - \frac{2}{3}(2 + z_g + \cos 2\varphi)\sqrt{z_g + \sin^2\varphi}, \tag{3.153}$$

$$y_{\mathrm{PC}} = -2\cos\varphi(\sin\varphi + \sqrt{z_g + \sin^2\varphi}). \tag{3.154}$$

[12] except in arctic conditions where c_g may be very low

Above $z_0 = 0$, the BICHs are governed by $B^2 = 1 - z$. Therefore all of them return to $z_0 = 0$, pointing downwards. Their behaviour from then on will be governed by $B^2 = 1 + z$ so the considerations that led to the PC expressions again become valid. The SC expression is

$$X_{\rm SC} = \frac{1}{3}\left(-2\sqrt{z_g + \sin^2\varphi}(1 + z_g + 2\cos^2\varphi) + 10\sin\varphi + 2\sin 3\varphi + 2\cos 2\varphi \sin\varphi\right), \tag{3.155}$$

$$y_{\rm SC} = 2\cos\varphi(3\sin\varphi - \sqrt{z_g + \sin^2\varphi}). \tag{3.156}$$

The carpet condition (3.152) is still valid for the SC but since $\sin\varphi > 0$ we have $\arcsin(\sqrt{|z_g|}) \leq \varphi \leq \pi - \arcsin(\sqrt{|z_g|})$. BICHs not satisfying the carpet condition will never hit z_g, due to the symmetry of B^2 in the plane $z = 0$.

In Figure 3.37 we plot only BICHs that reach $z_g = -1/2$, and we also superimpose the PC and the SC. In Figure 3.38 we plot separately the carpet. Comparing Figures

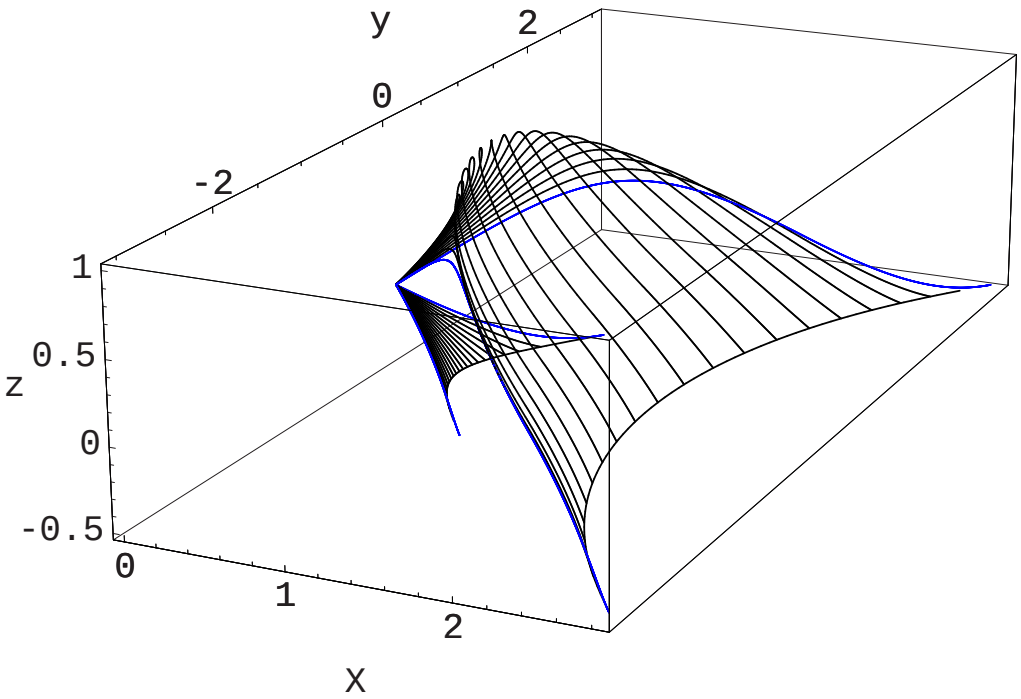

Figure 3.37: $B^2 = 1 - |z|$: BICHs that hit $z_g = -1/2$ are shown ($z_0 = 0$). Some BICHs never hit z_g. The limiting (grazing) BICHs are shown with a blue colour. The PC and SC are shown with solid curves, plotted using the analytical expressions (3.155) and (3.156).

3.36 and 3.38 we observe good qualitative agreement. In Figure 3.37, the PC is the

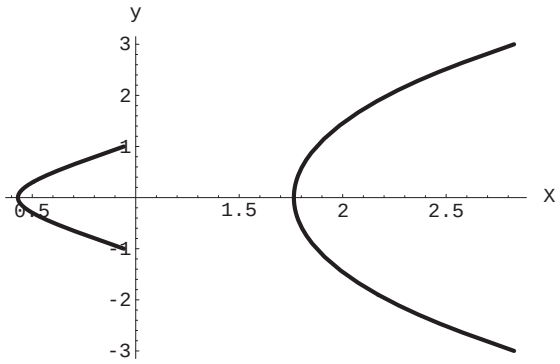

Figure 3.38: $B^2 = 1 - |z|$: the first open curve from the left is the PC at $z_g = -1/2$, and the second open curve is the SC.

first open curve from the left. The second open curve is the SC and it is formed by BICHs that were initially launched upwards, as we can see in Figure 3.37. Similarly in Figure 3.36 the first curve from the left is the PC and the second curve from the left is the SC formed by BICHs that returned from the thermosphere. The third curve from the left is an indirect SC formed by PC BICHs that reflected at the ground (assuming perfect reflection), went up and were returned to the ground again by the thermosphere. For the model atmosphere we did not consider any reflection at the ground, so we do not have an indirect SC.

The carpets of Figures 3.36 and 3.38 have finite extent due to the upward refraction of the BICHs. The SC is larger than the PC in both cases since the Mach conoid increases in lateral extent with the time of propagation of the boom. The width of the PC and SC increases with increasing height and Mach number.

Below we present in Figure 3.39 the cut of the Mach surface on the $y = 0$ plane containing the line of flight. The cusps we see are Tricomi cusps; they look very similar to the cusp we obtained for the analytical example in Section 3.6. This is to be expected since for any atmospheric condition near the sonic surface equation (3.49) becomes a Tricomi-type equation, as we already remarked in Section 3.6. In Figure 3.40 a cut of the Mach surface at height $z = 50\,\text{km}$ is taken. The solid curves correspond to BICHs that were launched upwards, i.e. their azimuthal angle satisfies $0 \leq \varphi \leq \pi$. The dashed curves are formed by BICHs that were launched downwards. In more detail, (and observing for clarity the horizontal line drawn at 50 km in Figure 3.39):

- The first (leftmost) solid curve is formed by upward BICHs before they reached the sonic line.

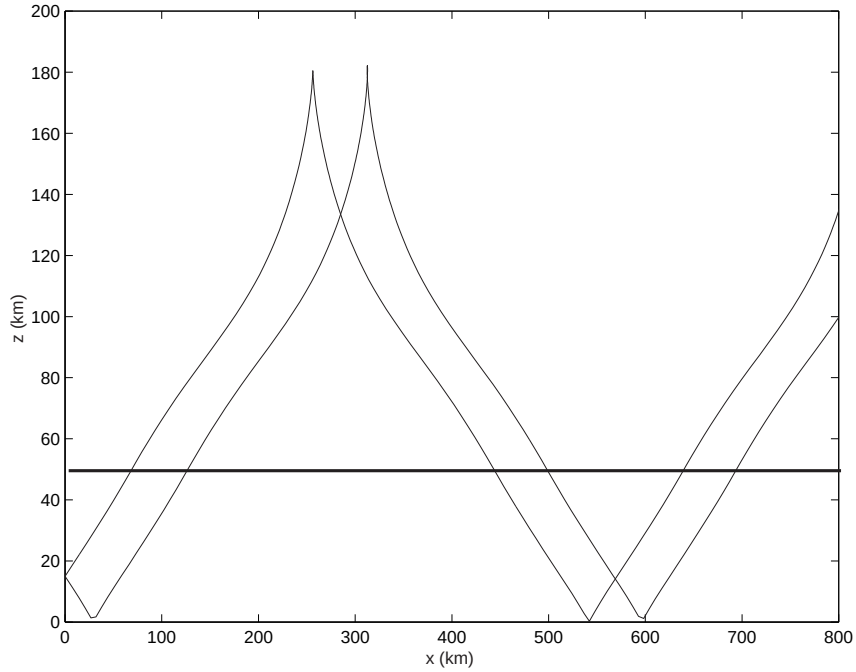

Figure 3.39: The $y = 0$ section of the Mach surface: Tricomi cusps are visible. The horizontal line at 50 km facilitates understanding of Figure 3.40 below.

- The second solid curve (which is joined to the first curve at cusp points) is formed by those BICHs that were reflected once from the sonic line.
- The third solid curve is formed by those BICHs that were also reflected off the ground once.
- The first (leftmost) dashed curve is by BICHs that were reflected off the ground once.
- The second dashed curve is formed by BICHs that were reflected at the ground, then from the sonic line.
- The third dashed curve is by BICHS that were reflected at the ground, then from the sonic line and at the ground for a second time.

The $y = 0$ line drawn coincides with the horizontal line drawn in Figure 3.39 and shows how the two figures are related geometrically.

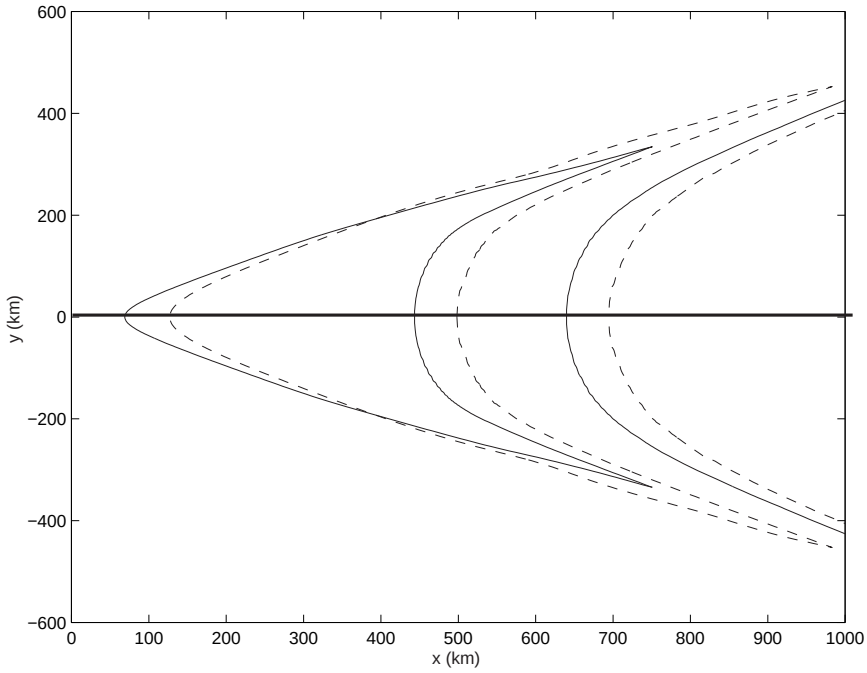

Figure 3.40: An (x, y)-cut of the Mach surface at $z = 50\,\text{km}$. The solid line curves track the behaviour of BICHs that were launched upwards ($0 \leq \varphi \leq \pi$) and the dashed line curves track the behaviour of BICHs that were launched downwards ($\pi \leq \varphi \leq 2\pi$).

3.9 Focusing

In this section we discuss focusing of sound waves and weak shock waves in general, consider some particular examples, and outline similarities and differences.

The word caustic[13] was adopted by Airy in 1838 to describe regions of light focusing [4]. An acoustical caustic is similarly a region of sound focusing. In the physical world the amplitude of light or sound at a caustic may be an order of magnitude larger than in any other region of the wavefield. Therefore caustics are desirable in applications where focusing of waves provides a benefit, e.g. in medical procedures such as ESWL (Extracorporeal Shock Wave Lithotripsy—the breaking of kidney stones by focusing shock waves [105]), but they are obviously an undesirable side effect in the sonic boom context.

An optical or acoustical caustic can be defined as an envelope of optical or acoustic rays (in the framework of GA or GO); there adjacent rays meet. At an envelope the ray tube area becomes zero [94] and the hence the amplitude predicted by GA is infinite. (It is a standard result of GA that the wavefield intensity is inversely proportional to the ray tube area.)

We consider a two-parameter family of rays labelled with parameters s_1, s_2 and t is the parameter along the rays. It can be shown formally that the ray tube area is proportional to the Jacobian of the transformation between the spatial coordinates and the ray parameters, given by

$$J(s_1, s_2, t) = \frac{\partial(x_1, x_2, x_3)}{\partial(s_1, s_2, t)}. \tag{3.157}$$

(See, for instance, [68].) Therefore when $J = 0$, the ray tube area is zero and a caustic can be alternatively defined as the locus of points for which $J = 0$. Caustics are therefore also the singularities of the map from the space coordinates to the ray parameters and hence sets of co-dimension 1; this means that in three dimensions they are surfaces and in two dimensions they are curves [68]. (This has been illustrated in all the examples we have seen previously.)

An infinite amplitude at the caustic obviously cannot agree with physical observations. This discrepancy of GA with the physical world indicates that the assumption on which GA is built, namely that the local gradients of the wavenumber are small (or equivalently that diffraction is negligible), breaks down.

However, even though GA fails to predict the correct amplitude at a caustic, it still accurately predicts the location and geometry of the caustics. This is true both

[13] the word comes from the greek word "kaiein" meaning "burning".

for focusing of linear waves and weak shock waves. For linear waves, this was nicely illustrated by our amplitude calculation in Section 3.5.3. We shall return to weak shock waves later in this section.

There are various types of foci: a fold caustic is a smooth envelope of rays and can also be called a *simple* focus. A cusp, also frequently called an arête, can also be called a *superfocus*, and it joins two fold caustics—the arête and the two fold caustics together are usually referred to as a cusp caustic. The fold caustic and the cusp caustic are in fact the two types of caustic most frequently encountered in practice. They are structurally stable in the sense that small perturbations in the conditions creating the caustic do not affect the caustic formation (see Nye [81]). The terms "fold caustic" and "cusp caustic" are transferred from "catastrophe theory" (see Berry [15]). A third type of focus is a perfect lens-like focus; this is structurally unstable [81].

Below, we discuss various examples in order to bring out the important points. A fold caustic of rays was illustrated in Figure 3.12 and a fold caustic of boomrays was illustrated in Figure 3.27. The behaviour of these two caustics is locally the same: at a point in the "illuminated" side of the caustic two rays pass through. These rays coincide when this point moves on the caustic; no rays exist in the shadow side of the caustic. In both cases the caustic is formed due to the stratification of the medium. We shall see in Chapter 6 that similar fold caustics of boomrays are formed due to acceleration and due to manoeuvres.

For an example of a cusp caustic formation in a stratified medium, we consider a point source at the origin in the medium with sound speed profile $c(z) = 2-\exp(-z^2)$. In Figures 3.41(a) and 3.41(b) we plot respectively the rays and wavefronts for $t_0 \leq 1$; no focusing has yet appeared.

In Figure 3.42 we plot the rays for $t \leq 4$. Cusp caustics are now observed. Comparing with examples mentioned above, the cusp is a new feature. In Figure 3.42 we also show a magnified view of the right caustic. For the rays near the x-axis, z is small so $c(z) \approx 1 + z^2$. A series of caustics forms at approximate distances

$$x_{Cn} = \pm n\pi(\sqrt{c/c''})|_{z=0} = \pm n\pi/\sqrt{2}, \quad n = 1, 2, 3, ... \tag{3.158}$$

along the x-axis. (For the general formula for the location of the cusps in any stratified medium see, for instance, Pierce [94] p. 392). In Figure 3.43 (and Figure 3.42), since $t \leq 4$, we see only the first caustics in the series at $x_{C1} = \pm\pi/\sqrt{2} = \pm 2.22$.

In Figure 3.43 we also plot the wavefronts. Inside the caustic the wavefronts are folded with cusps touching the caustic. In the same Figure, the right plot is a zoomed version of the wavefront pattern in the right caustic. These cusp caustics are very

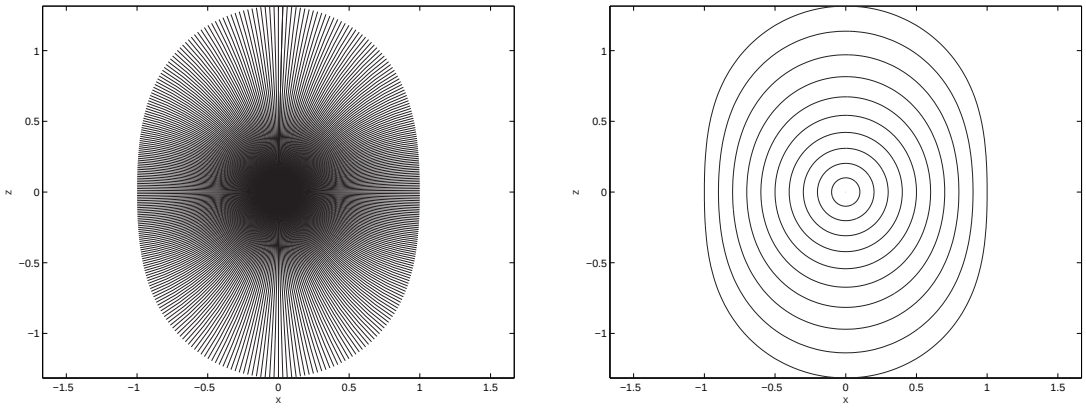

(a) Rays, $t \leq 1$.

(b) Wavefronts, $t \leq 1$.

Figure 3.41: Ray pattern and wavefronts for a stationary source in the stratified medium $c = 2 - \exp(-z^2)$, before focusing has begun.

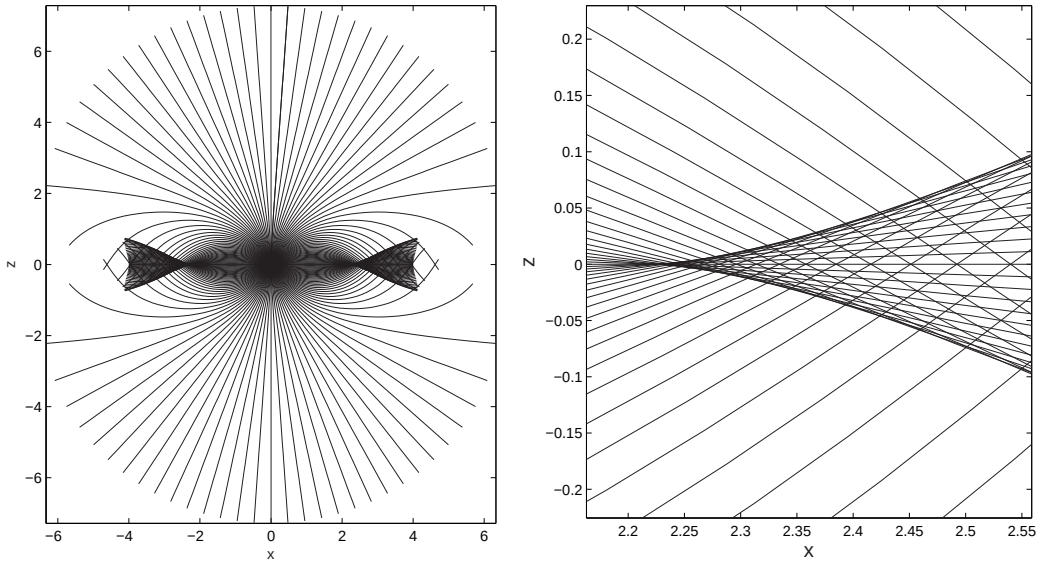

Figure 3.42: $c = 2 - \exp(-z^2)$, rays and their focusing leading to the formation of a caustic ($t = 4$).

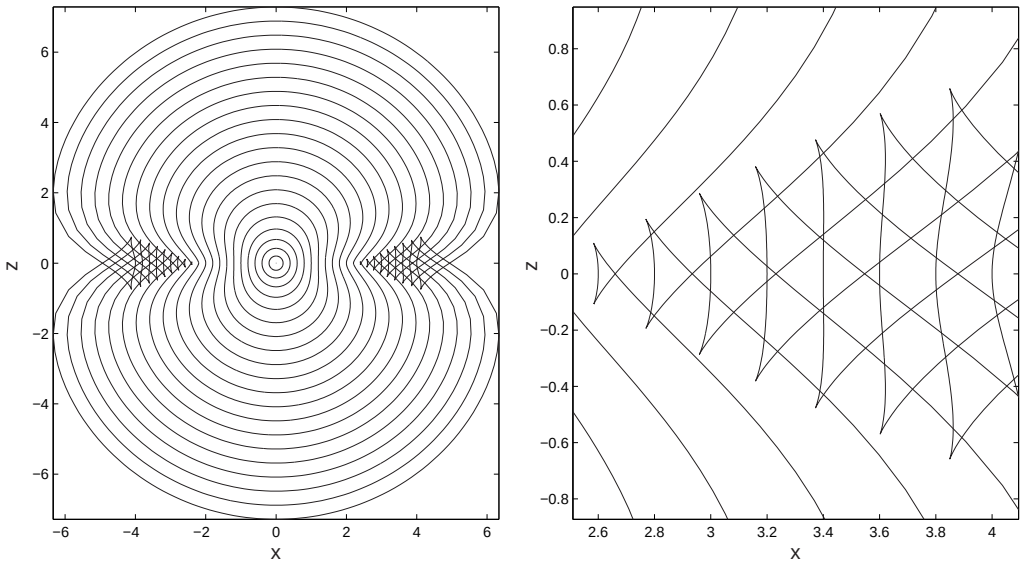

Figure 3.43: $c = 2 - \exp(-z^2)$, the folded wavefronts are shown ($t = 4$) taken at time intervals $\Delta t = 0.1$.

similar to the coffee-cup caustic, visible on the surface of coffee in a cup placed in the sun—see the photograph in Figure 3.44(a) from Nye [81].[14] The coffee-cup caustic consists of two fold caustics joined by a cusp.[15] The cusp is the brightest point of the caustic. In Figure 3.44(b) it is shown how the rays form the caustic by reflecting off the inside surface of the cup. At a point P in the illuminated side of the caustic four rays pass through. Three rays are reflected from the cup, at points A and B and C, and the fourth ray DP reaches P directly. When P moves to the right side of the caustic, the two reflected rays AP and BP coalesce but when P moves to the left side of the caustic, the two reflected rays CP and BP coalesce. When P is the cusp point all three rays AP, BP and CP coalesce. When P moves anywhere on the dark side of the caustic (shadow region) only two rays pass through (the two rays that have coalesced on the caustic do not exist in the shadow region).

Note that these geometrically similar cusp caustics come about from very different physical problems; in the stratified atmosphere example the caustic is formed because rays curve due to stratification, whereas in the case of the coffee-cup caustic the rays are straight and focusing occurs due to reflection at the cup. Examples of cusp caustics of boomrays are much more difficult to pinpoint[16] but we identified one such

[14]The list of optical caustics is very rich—see the same book for a wealth of optical caustics accompanied by real photographs.

[15]The first sketch of the coffee-cup caustic was by Leonardo da Vinci in 1508.

[16]A good part of the difficulty in creating a cusp caustic of boomrays arises from the fact that

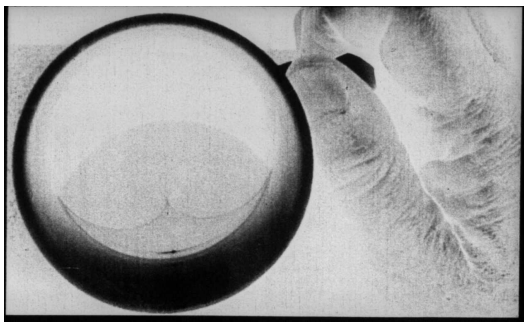

(a) Real photograph of a coffee-cup caustic (negative so that the caustic stands out.)

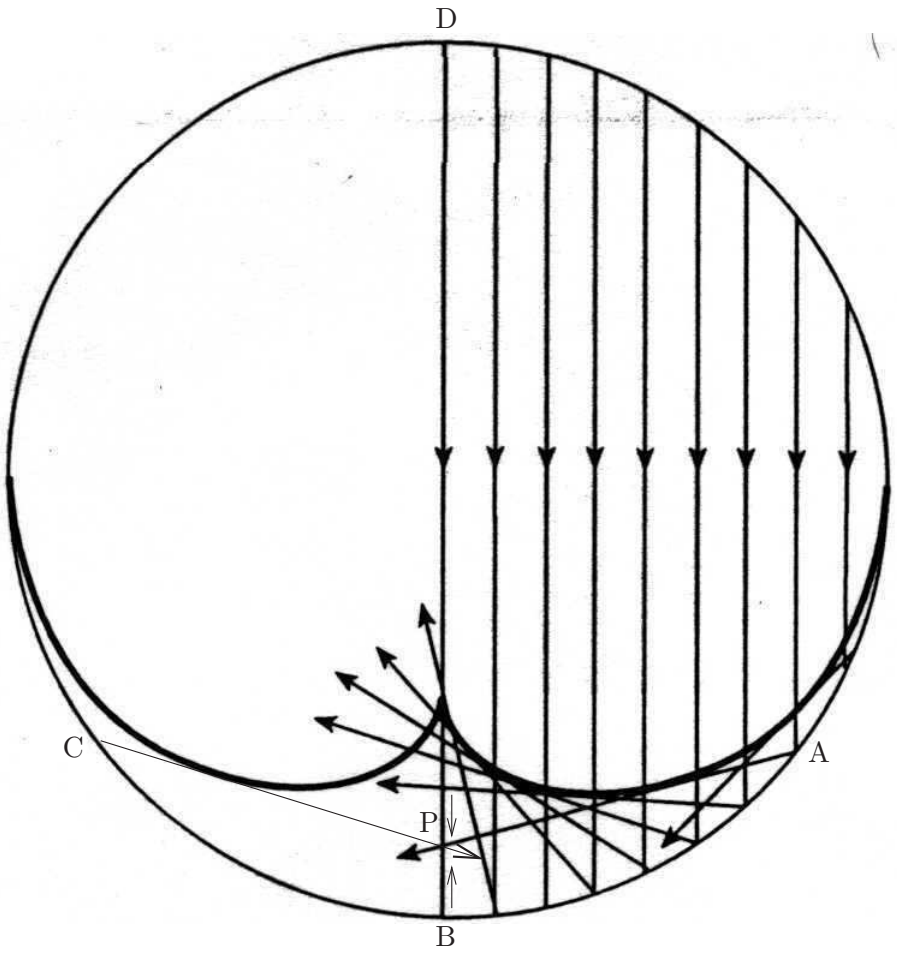

(b) The caustic shown as envelope of rays.

Figure 3.44: Photograph and sketch of rays for the coffee-cup caustic.

scenario, which can still be treated analytically. It will be discussed at the end of Chapter 6.

In all the examples of caustics mentioned above the *difference* in the number of rays across the caustic is exactly two. This is in fact a generic feature of all caustics (see Lighthill [72], Section 4.11, p. 385).

The remedy for the infinity of the wavefield predicted by GA at caustics has been the subject of intensive research, both for linear and nonlinear waves. The discrepancy between the physical world and GA predictions is due to diffraction, nonlinearity, dissipation and other effects that are not accounted for in the latter.

Assuming that diffraction effects are more important than the other neglected effects in the neighbourhood of the caustic, for linear monochromatic waves Buchal and Keller [19] and Ludwig [75] constructed the Geometrical Theory of Diffraction (GTD), which recovers diffraction effects to first order in an appropriately defined neighbourhood of the caustic, usually called the Diffraction Boundary Layer (DBL). It turns out that the consistent approximation of the Euler equations in the DBL is the linear Tricomi equation. The generic solution of the Tricomi equation for monochromatic waves is the Airy function. The solution in the DBL is then matched to the GA solution outside of the DBL.

Focusing may arise as an undesirable consequence of a supersonic flight. Focusing of the shock waves can have one or more of three causes:

1. Because the flight takes place in a non-uniform medium—a very likely scenario especially for SSBs and it is what we have concentrated on in this chapter.

2. Because the aircraft in every supersonic flight has to accelerate through the sound speed (but maybe also during other parts of the flight). This focusing is further discussed in Chapter 6; it will be shown that for constant acceleration in a uniform medium again a fold caustic of boomrays arises. We will also see there that a cusp caustic of boomrays arises when the same motion takes place in the stratified atmosphere $c = 1/\sqrt{1-z}$.

3. Because of other manoeuvres such as turns. Examples of various manoeuvres are also discussed in Chapter 6.

Flight tests [123, 47] suggest that the caustics that arise in sonic boom focusing are mainly fold caustics and much more rarely cusp caustics [76]. (Cusp caustics have only been documented in the flight tests by Wanner et al. in [123].) The primary

boomrays are always emitted at a fixed angle dictated by the boomray condition.

sonic boom enhancement factors observed are two to five times for a fold caustic and can be up to ten for a cusp caustic.

In sonic boom problems we are interested in the caustics of boomrays, rather than caustics of ordinary rays, but the local geometrical features of the former and the latter case are the same, as indicated by catastrophe theory [15] and as illustrated through the examples in this thesis. For weak shocks, experimental work by Sturtevant and Kulkarny [118] and by Marchiano et al. [77] supports the belief that deviation caused to the caustics' geometry by nonlinearity is negligible. Therefore geometrical results from linear waves are still accepted as relevant. It is believed, however, that in order to predict the correct amplitudes near caustics diffraction effects have to be complemented by nonlinear effects; we elaborate on this below.

When the wave incident on a fold caustic is a shock, the solution of the linear Tricomi equation is singular; an incoming double-shock N-wave is transformed into the so-called U-wave with two infinite peaks (this U-wave can be derived as the Hilbert transform of the N-wave —see article [109] by Rosales and Tabak). This is an unphysical result.

For a correct estimation of the associated wavefield at a fold caustic it seems that nonlinear effects need to be retained as a limiting mechanism. This assertion is supported again by the laboratory-scale experiments of Sturtevant and Kulkarny [118] and of Marchiano et al. [78]. When retaining both diffraction and nonlinear effects near fold caustics of weak shocks the nonlinear Tricomi equation $(z + \Phi_X)\Phi_{XX} = \Phi_{zz}$ arises as the consistent approximation of the Euler equations. The latter equation was first derived by Guiraud in 1965 [45], and again by Hayes in 1968 [53]. Pechuzal and Kevorkian [91] arrived at the same equation when they studied the focusing of shocks created by a supersonic source in a weakly stratified linear wind and in a two-dimensional uniform atmosphere. Similar equations were subsequently derived by Fung [41], Rosales and Tabak [109], and Auger [10]. Numerical solutions of the nonlinear Tricomi equation for a single shock were provided by the approximate method of the hodograph transform by Seebass [113], Gill and Seebass [43], and Fung [41]. By 2002, Cheng and Hafez [23] and many others had devised other numerical methods for solving the nonlinear Tricomi equation. A faster and more robust numerical method was introduced by Auger and Coulouvrat [11] in 2002. In 2003, Marchiano, Coulouvrat and Grenon in [77] applied this method to an incident N-wave for estimating the amplitudes created by acceleration through the sound speed at the ground track, using the Eurosup configuration derived from the European configuration for a future SST [37], in realistic atmospheric conditions.

On the other hand, for the wavefield at a cusp caustic, much less research has been done [29, 28, 25]. In the linear theory the generic function describing the solution at a cusp is the Pearcey function [90]. For an incoming shock wave the outgoing wave has again infinite singularities; the idea for remedial action is the same as for the fold caustic, that is by introducing nonlinearity as a limiting mechanism. The most recent work is by Coulouvrat [25]; he proposes that the KZ equation should be solved in the vicinity of the cusp and provides a description of how a numerical scheme could be developed to handle an incoming N-wave.

3.10 Sonic booms in an atmosphere with wind

Waves in fluids are generally affected by any underlying motion of the fluid, such as winds in the atmosphere or currents in the ocean. Below we will present briefly the theory of GA in a moving medium [17, 65, 87] in order to determine how atmospheric winds influence the SSB propagation. We consider a non-uniform background flow of the form $\mathbf{U}(\mathbf{x}) = (U_1(\mathbf{x}), U_2(\mathbf{x}), U_3(\mathbf{x}))$, taking place in a slowly varying atmosphere. We assume that the length-scale of variation of the ambient flow is much larger than the wavelength and therefore $\mathbf{U}(\mathbf{x})$ is slowly varying. This assumption is necessary if we are to retain the GA framework used for stationary media. Note that from now on we will refer to the ambient flow as "wind".

The ray equations valid in a moving medium are the ordinary differential equations

$$\dot{\mathbf{x}} = \frac{\partial \omega}{\partial \mathbf{k}}, \qquad \dot{\mathbf{k}} = -\frac{\partial \omega}{\partial \mathbf{x}}, \tag{3.159}$$

which are valid for any waves with the general dispersion relation $\omega = \omega(\mathbf{k}; \mathbf{x})$ (see Lighthill [72], equations (106)–(107) and the discussion on ray tracing in a wind, pp. 325–334). For sound waves in a stationary medium the local dispersion relation is $\omega_r = c(\mathbf{x})|\mathbf{k}|$, as we already noted in (3.32). The subscript r applied here stands for *rest* or *relative* because ω_r is the frequency of the waves relative to the ambient flow velocity. For sound waves in a moving medium the local dispersion relation is modified to

$$\omega(\mathbf{k}; \mathbf{x}) = \omega_r(\mathbf{k}) + \mathbf{U}(\mathbf{x}).\mathbf{k} = c(\mathbf{x})|\mathbf{k}| + \mathbf{U}(\mathbf{x}).\mathbf{k}, \tag{3.160}$$

and therefore equations (3.159) become

$$\frac{dx_i}{dt} = U_i + \frac{\partial \omega_r}{\partial k_i} = U_i + cn_i, \tag{3.161}$$

$$\frac{dk_i}{dt} = -k_j \frac{\partial U_j}{\partial x_i} - \frac{\partial \omega_r}{\partial x_i} = -k_j \frac{\partial U_j}{\partial x_i} - \frac{\partial c}{\partial x_i}|\mathbf{k}|. \tag{3.162}$$

Since $\mathbf{n} = \mathbf{k}/|\mathbf{k}|$ the system of equations (3.161)–(3.162) is closed. The right-hand side of (3.161) is the vector sum of the wind velocity and the direction vector of the ray when the fluid is at rest. The first term in the right-hand side of (3.162) represents refraction due to the gradients of the wind and the second term refraction due to gradients of the sound speed.

For typical atmospheric conditions the wind is in many cases approximately horizontal. We show below, generalising Lighthill's treatment in [72] for $\mathbf{U} = (U(z), 0, 0)$ to the case of $\mathbf{U} = (U(z), V(z), 0)$, whose magnitude *and* direction varies with height, and a stratified atmosphere we can derive a generalised Snell's law. Firstly, from the dispersion relation (3.160), and letting $\mathbf{k} = -(p, q, r) = (k, l, m)$, we have

$$\omega(\mathbf{k}; \mathbf{x}) = c|\mathbf{k}| + kU(z) + lV(z). \tag{3.163}$$

For a medium stratified in the z-direction equations (3.162) give that k and l are constant; since the changes are only in the z-direction only the component m changes. Furthermore ω is constant along a ray, since the derivative of ω along a ray is $\dfrac{d\omega}{dt} = \dfrac{\partial\omega}{\partial x_i}\dfrac{dx_i}{dt} + \dfrac{\partial\omega}{\partial k_i}\dfrac{dk_i}{dt} = 0$ (using equations (3.161) and (3.162)—see also [72], p. 319.) We then take

$$k = k_H \cos\psi, \qquad l = k_H \sin\psi, \qquad m = k_H \cot\vartheta, \tag{3.164}$$

where $k_H = \sqrt{k^2 + l^2}$, ψ is the *constant* azimuthal angle to the wind direction, and ϑ is the *variable* angle to the z-direction; we find that (3.163) then becomes the generalised Snell's law

$$\begin{aligned} &\frac{c(z)}{\sin\vartheta} + U(z)\cos\psi + V(z)\sin\psi = \frac{\omega}{k_H} = \text{constant} \\ &\Rightarrow \sin\vartheta = \frac{c(z)}{\omega k_H^{-1} - U(z)\cos\psi - V(z)\sin\psi}. \end{aligned} \tag{3.165}$$

When we take $U = V = 0$ and $\vartheta \mapsto \pi/2 - \theta$ we recover (3.35), the Snell's law in a stationary medium.

Relation (3.165) is very important because it can explain how a stratospheric SSB may arise. For a boomray to be reflected from a height $z = z_r$ in the stratosphere and then reach the ground, setting $V = 0$ in (3.165), we find that the condition

$$\cos\psi(U(z_r) - U_g) > c_g - c(z_r) \tag{3.166}$$

should be satisfied, where c_g is the ground sound speed and $c(z_r)$, the sound speed at the reflection height. This means that the difference in the wind speed between

the reflection height and the ground must be large enough in the direction of the boomray so that it compensates for the fact that c_g is greater than $c(z_r)$.

Note that from (3.163) we can write down

$$m(z) = \pm\sqrt{\left(\frac{\omega - kU(z)}{c(z)}\right)^2 - k^2 - l^2} \tag{3.167}$$

and equations (3.161) give

$$\frac{dy}{dz} = \frac{\partial\omega_r/\partial l}{\partial\omega_r/\partial m}, \quad \frac{dx}{dz} = \frac{U(z) + \partial\omega_r/\partial k}{\partial\omega_r/\partial m}, \tag{3.168}$$

where the right-hand sides are known functions of z and when integrated give the projections of the rays in the x and y plane respectively. This is not so useful for rays that go through a reflection point where m changes sign, and solving the ordinary differential equations directly is preferable.

For the most part in this chapter we have investigated the geometry of thermospheric SSBs and in this section we looked at stratospheric SSBs. It is also important to know what is the intensity associated with these two types of SSBs. This issue has been addressed within the SOBER programme, and it has been briefly discussed in the Introduction.

The link with the BICHs

There is still an interesting point to make here, as promised on page 73: If we take U to be a constant (and the medium stratified in the z-direction) equations (3.161)-(3.162) reduce to the equations for the BICH (3.54)–(3.55). Therefore the BICHs can be thought of as the rays in a medium with a "supersonic" stream $(U, 0, 0)$ and they satisfy the generalised Snell's law (3.165). (We no longer call $(U, 0, 0)$ the "wind" because wind is never supersonic.)

3.11 Other considerations

The well-defined impact areas shown in our simple models do not really materialise in real atmospheric conditions; variations in the atmospheric wind and temperature profiles may cause drastic changes to the character of the carpets.

Furthermore, in reality, the atmospheric parameters are given as data points sampled or predicted in certain intervals of time and at certain locations on the ground. Therefore the necessary interpolation needed to produce a smooth profile for the ambient properties of the atmosphere, such as temperature or pressure, inevitably introduces errors that may change the character of the computed carpet.

3.12 Summary and conclusions

In this chapter, we have first detailed the terms frequently used in sonic boom research. We presented a series of mainly analytical examples which showed how rays and boomrays arise as a means for studying long-range sound and sonic boom propagation in a non-uniform atmosphere. For the main part we looked at stationary media. In particular we illustrated a fold caustic of rays and a fold caustic of boomrays and in the latter case we have shown how this corresponds to a Tricomi cusp on the Mach envelope. The Mach envelope parts joining to each other through this Tricomi cusp were called "incident" and "reflected". We shall see in Chapter 6 that we can use the same labelling for the Mach envelope arising in acceleration through the sound speed.

For our three-dimensional examples we worked in the aerodynamic frame and traced the BICHs rather than the boomrays. This is an alternative, simpler, way to follow the boom in the case of steady level flight. In particular, the analytical example with $B^2 = 1 - |z|$ gave carpets qualitatively similar to those in a typical atmosphere.

Throughout the chapter we concentrated on the geometrical features of propagation, except in Section 3.5.3 where we have calculated the amplitude due to a stationary monochromatic source in the medium with sound speed profile $c = 1/\sqrt{1-z}$. In that example we have compared the full linear wave theory with the Geometrical Theory of Diffraction: we have shown that an order 1 wavefield exists inside the fold caustic $z = 1 - x^2/4$ where ray theory predicts two rays passing through each point, a larger amplitude exists near the caustic where the rays coalesce, and an exponentially decaying wavefield exists outside the caustic as also predicted by GTD. (Work on the amplitudes related to focusing will also be presented in Chapters 6 and 7.)

We have also discussed similarities and differences in the focusing of linear waves and weak shock waves, and related this discussion to our examples. Finally, we looked at ray tracing in a wind as a means for explaining stratospheric secondary booms.

Chapter 4

Steady supersonic flow in a uniform atmosphere

4.1 Introduction

In this chapter we are going to investigate the flow around aerofoils, moving at a constant supersonic speed $(-U, 0, 0)$ in a stationary uniform medium. The equations of motion are taken to be the Euler equations, as detailed in Chapter 2. This is a good approximation in most of the flow; we will neglect viscous and thermal effects which are confined to boundary layers around the body.

The chapter is structured as follows: firstly, the Euler equations are recast, under certain assumptions, into a scalar nonlinear equation for the velocity potential. Subsequently, the method of Matched Asymptotic Expansions (MAE) is used to derive consistent approximations of the potential equation near the aerofoil (near-field) and far from the aerofoil (far-field), in two and three dimensions. In the near-field a linear wave equation is derived at leading order. However, the linear approximation breaks down in the far-field due to small nonlinear effects that cumulatively become important there. In the far-field the consistent approximation of the potential equation at leading order is a so-called "Kinematic Wave Equation". Solving the latter equation determines the characteristics and shocks.

That the nonlinearities are important in the far-field is a well-known result in sonic boom research. In 1952 Whitham, in [124], used an ingenuous geometrical approach to include these nonlinearities. He created the so called "quasi-linear" theory based upon the hypothesis that the linear theory yields the correct values of perturbations along the characteristics as long as these characteristics are shifted appropriately in the far-field. These modified characteristics incorporate at leading order the effect of nonlinearity. Eventually the shifting of characteristics leads to their crossing, and

shocks have to be introduced to resolve the resulting multi-valued regions. On the other hand, Hayes in [51] derived the correct KWE at the far-field for planar bodies and bodies of revolution, but he did not employ formal asymptotic methods; he neglected terms in a somewhat ad hoc way based on physical intuition. However, the advantage of our asymptotic analysis here is that it is systematic and does not need to rely on such physical arguments. [1] Furthermore, it provides us with the means to calculate the higher orders, should we wish to do so.

4.2 Euler equations for steady flow

We define the Mach number of the aerofoil as $M_0 = U/c_0 > 1$ and the local Mach number of the flow as $M = |\mathbf{u}|/c_0$. For an aerofoil with $M_0 \ll 1$ (typically less than 0.3) the compressibility effects are usually negligible to first order and the flow is called *incompressible*. The flow is said to be *compressible* for larger values of M_0. It is called subsonic or supersonic if the flow velocity relative to the aerofoil is subsonic or supersonic everywhere; it is called transonic if there are both subsonic and supersonic regions: for typical aerofoils the subsonic regime is for M_0 from about 0.8 to 1.2. Note that for M_0 greater than about 5 the flow is called *hypersonic*. The exact cutoff values of M_0 are dependent on the particular configuration. In this thesis, the Mach number M_0 will always be large enough for compressibility effects to play an important role but we will not consider hypersonic flows.

It is convenient to work in the aerodynamic frame in which the aerofoil is stationary and there is an incident supersonic stream $(U, 0, 0)$. By defining the travelling coordinate $X = x + Ut$, the problem becomes time-independent, and the Euler equations (2.4), (2.5) and (2.12) simplify to

$$\boldsymbol{\nabla} . (\rho \mathbf{u}) = 0, \tag{4.1}$$

$$\boldsymbol{\nabla} p + \rho (\mathbf{u} \cdot \boldsymbol{\nabla}) \mathbf{u} = \mathbf{0}, \tag{4.2}$$

$$\mathbf{u}. \boldsymbol{\nabla} S = 0 \quad \text{or} \quad \mathbf{u}. \boldsymbol{\nabla} p = c^2 \mathbf{u}. \boldsymbol{\nabla} \rho, \tag{4.3}$$

for a smooth flow. Equation (4.3) gives that the entropy is constant along streamlines (fluid particle paths and streamlines coincide in steady flow). Furthermore, to a good approximation air is a polytropic gas (with $\gamma = 1.4$), so $c^2 = \gamma p/\rho$ and (4.3) becomes

$$\rho \, \mathbf{u}. \boldsymbol{\nabla} p = \gamma p \, \mathbf{u}. \boldsymbol{\nabla} \rho. \tag{4.4}$$

[1] Our MAE framework in two dimensions is very similar to that in Van Dyke [121] but MAE framework in three dimensions is more original.

We also need to impose appropriate boundary conditions. Firstly, at the surface of a stationary solid body, the direction of an inviscid flow must be tangential to the solid boundary[2]. Letting the surface of the aerofoil be described by the equation $G(x, y, z) = 0$, this boundary condition is expressed as

$$\mathbf{u} \cdot \boldsymbol{\nabla} G = 0. \tag{4.5}$$

Secondly, we need to specify a condition at infinity. A body in a supersonic stream does not influence the flow upstream, as we remarked in the previous chapter. This fact dictates that the disturbance to the flow by the aerofoil can only be outgoing.

Any body in a supersonic stream leads to shock formation in the flow. In the aerodynamic frame the supersonic streams are steady and the shocks are *stationary*. The flow upstream is steady and homentropic and Crocco's equation (2.24) reduces to

$$\boldsymbol{\nabla} H = \mathbf{u} \times \boldsymbol{\omega}. \tag{4.6}$$

Dotting (4.6) with $\mathbf{u}$ the right-hand side vanishes identically and we have

$$\mathbf{u}. \boldsymbol{\nabla} H = 0, \tag{4.7}$$

which says that the total head H is conserved along streamlines. Such a flow is usually called *isoenergetic*. If furthermore, $H = H_0 =$ constant for all streamlines at infinity, as is the case here, then H is a constant throughout the flow and the flow is usually called *homenergetic*. (The homenergetic condition $H = H_0$ is actually Bernoulli's law for steady compressible flow). Summarising, the flow upstream is steady, homentropic and homenergetic.

Across a shock the Rankine-Hugoniot conditions (2.19)–(2.21) hold. For stationary shocks, the energy Rankine-Hugoniot condition (2.22) gives that the total head H is conserved across the shock. The entropy jumps, however, to a higher value and the flow *after* the shock is in general not homentropic. Since the flow is steady, downstream of the shock, by (4.3), the entropy is constant, along streamlines and the flow, even though not homentropic, is isentropic. Summarising, the flow after a curved shock is still steady and homenergetic but isentropic.

A thin supersonic aerofoil with small thickness parameter ϵ produces weak shocks in the flow, with strength of order ϵ. As we discussed in Chapter 2, Section 2.4, for such weak shocks, the jump in entropy across the shock, is only of order ϵ^3 and,

[2]Recall that in a steady, inviscid flow streamlines can be replaced by stationary solid body surfaces or vice versa—see, for instance, Acheson [2].

by the Circulation equation (2.40), the vorticity is of order ϵ^3. Therefore the flow perturbation downstream of a weak shock is irrotational up to a relative error of order ϵ^2.

4.3 The velocity potential equation

For irrotational flows a velocity potential Φ can be defined and the system of Euler equations reduces to a single nonlinear scalar equation for Φ, which simplifies the analysis. Below, we derive a potential equation for steady flows, and then we seek an approximate solution using asymptotic methods in the case of an aerofoil in a supersonic stream, in two and three dimensions. The potential equation will be valid only up to order ϵ^2, due to the vorticity production.

Using in succession (4.1), (4.2) and (4.3), and setting $\mathbf{F} = 0$ since the ambient pressure $p_0 =$ is constant, we find that

$$c^2 \boldsymbol{\nabla} .\mathbf{u} = -c^2 \frac{\mathbf{u}. \boldsymbol{\nabla} \rho}{\rho} = -\frac{\mathbf{u}. \boldsymbol{\nabla} p}{\rho} = \mathbf{u}. (\mathbf{u}. \boldsymbol{\nabla} \mathbf{u}) . \tag{4.8}$$

Letting $\mathbf{u} = \boldsymbol{\nabla} \Phi$ where Φ is the velocity potential, (4.8) becomes

$$c^2 \boldsymbol{\nabla}^2 \Phi - \boldsymbol{\nabla} \Phi.(\boldsymbol{\nabla} \Phi. \boldsymbol{\nabla}(\boldsymbol{\nabla} \Phi)) = 0. \tag{4.9}$$

Note that in equation (4.9) we still have to express the local speed of sound c as a function of the velocity potential and this is possible through the homenergetic condition

$$H = H_0 \Rightarrow h + \frac{1}{2}|\mathbf{u}|^2 = h_0 + \frac{1}{2}U^2. \tag{4.10}$$

Equation (4.10) is valid upstream and downstream of the shocks, since H is conserved across stationary shocks.

For a polytropic gas $h = \dfrac{\gamma}{\gamma - 1}\dfrac{p}{\rho}$ and $c^2 = \gamma p/\rho$ and therefore equation (4.10) becomes

$$c^2 = c_0^2 + \frac{\gamma - 1}{2}(U^2 - |\boldsymbol{\nabla} \Phi|^2), \tag{4.11}$$

which relates the local speed of sound c and the ambient sound speed c_0. Combining (4.9) and (4.11) leads to the required potential equation

$$(c_0^2 + \frac{\gamma - 1}{2}(U^2 - |\boldsymbol{\nabla} \Phi|^2))\, \boldsymbol{\nabla}^2 \Phi - \boldsymbol{\nabla} \Phi.(\boldsymbol{\nabla} \Phi. \boldsymbol{\nabla}(\boldsymbol{\nabla} \Phi)) = 0. \tag{4.12}$$

Equation (4.12) is valid for any steady compressible flow since it was derived with no assumption on the size of the Mach number M_0.[3]

[3]For unsteady flows an analogous potential equation can be derived—see for instance Chapman [21] p. 62.

The body boundary condition (4.5) becomes

$$\boldsymbol{\nabla}\,\Phi.\boldsymbol{n}_G = \frac{\partial\,\Phi}{\partial n} = 0 \tag{4.13}$$

where $\boldsymbol{n}_G = \boldsymbol{\nabla}\,G$ is the normal to the aerofoil surface $G = 0$. The condition at infinity can be written as

$$\boldsymbol{\nabla}\,\Phi \to (U, 0, 0) \quad \text{as} \quad x \to -\infty. \tag{4.14}$$

Once Φ is determined, all flow quantities can be obtained. An expression for pressure in terms of Φ can be found by combining (4.11) and $c^2 = \gamma p/\rho$, where $\rho = (p/\kappa)^{1/\gamma}$ from the constant entropy condition (2.13) (valid here up to $O(\epsilon^2)$):

$$p = p_0 \left(1 + \frac{\gamma - 1}{2c_0^2}(U^2 - |\,\boldsymbol{\nabla}\,\Phi|^2)\right)^{\frac{\gamma}{\gamma-1}}. \tag{4.15}$$

Once we have obtained p we can go back to (2.13) to obtain ρ. We can obtain $T = p/\mathcal{R}\rho$, using the equation of state (2.8).

4.4 Two-dimensional supersonic flow

In this section we apply the steady supersonic flow theory presented above to the analysis of the flow around a two-dimensional thin aerofoil in a uniform supersonic stream. This analysis is applicable for

(a) flows in which conditions are identical in sections parallel to the (x, z)-plane, such as certain portions of wings (see Figure 4.1).

(b) flows around surfaces of any shape with their (x, z)-section varying only slowly with y. The flow is then *almost* identical in every (x, z)-plane. Case (a) is a special case of this.

We take an aerofoil symmetric with respect to the x-axis. We can then examine all the essential features of the flow by looking only in the half-plane $z > 0$. A symmetric geometry is non-lifting but the analysis that we will present can be easily extended to lifting aerofoils with asymmetric effects due to light camber and/or non zero, small, angle of attack (see, for instance, Chapman [21], pp. 145–151). Using cartesian coordinates x and z we consider an aerofoil profile $z = \pm G(x)$. The function $G(x)$ is usually called the *thickness function*. We take the chord length to be L, extending from $x = -L/2$ to $x = L/2$, and assume that $G_{\max} \ll L$ (see Figure 4.2). Both ends

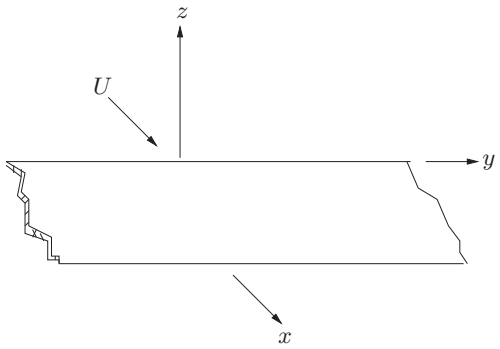

Figure 4.1: A body for which the induced supersonic flow can be analysed with two-dimensional theory.

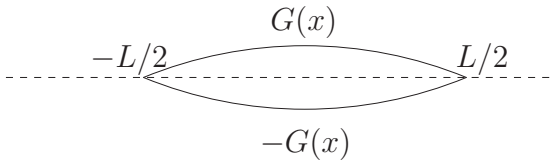

Figure 4.2: An aerofoil with thickness function $G(x)$ and chord L, symmetric with respect to the x-axis.

of the aerofoil are taken to be pointed. This will lead to the shocks being attached to the ends of the aerofoil. (If the aerofoil is blunt the shocks will be detached and stronger and the analysis becomes more complicated.) The thickness ratio of the aerofoil is defined by

$$\epsilon = \frac{G_{\max}}{L}, \tag{4.16}$$

and it is small, with a typical value of 0.1. We nondimensionalise both $\hat{x} = x/L$ and $\hat{z} = z/L$ and then $\hat{z}(\hat{x}) = \pm\epsilon\hat{G}(\hat{x})$ where $\hat{G}$ is a fixed $O(1)$ function and $-1/2 \leq \hat{x} \leq 1/2$. We will also nondimensionalise all velocities with U, the speed of the incident supersonic stream. The pressure p is nondimensionalised with its undisturbed value p_0 and ρ with its undisturbed value ρ_0. From now on, we will use nondimensional variables, but we will drop the hats for convenience.

4.4.1 Potential equation

In two dimensions, the potential equation (4.12) becomes

$$\Phi_{zz} - B_0^2\Phi_{xx} = M_0^2\{\frac{\gamma-1}{2}(\Phi_{xx}+\Phi_{zz})(\Phi_x^2+\Phi_z^2-1) + \Phi_{xx}(\Phi_x^2-1) + 2\Phi_x\Phi_z\Phi_{xz} + \Phi_z^2\Phi_{zz}\}, \tag{4.17}$$

where $B_0 = \sqrt{M_0^2 - 1}$ is the Prandtl-Glauert parameter, as already defined in the previous chapter. On the left-hand side of (4.19) we have the linear wave operator $\partial/\partial z^2 - B_0^2 \partial/\partial x^2$ and on the right-hand side all the nonlinear terms.

The aerofoil causes a weak disturbance of order ϵ to the uniform stream and therefore the velocity field is a superposition of the uniform incoming flow $\mathbf{U}_\infty = (1, 0, 0)$ and a perturbation velocity field $\epsilon \mathbf{u}'$, so that $\mathbf{u} = \mathbf{U}_\infty + \epsilon \mathbf{u}'$. Therefore the potential Φ is written as

$$\Phi = \Phi_\infty + \epsilon\phi = x + \epsilon\phi. \tag{4.18}$$

The first term on the right-hand side of (4.18) represents the potential for the uniform stream $\mathbf{U}_\infty$ and the perturbation potential ϕ is for $\mathbf{u}' = \boldsymbol{\nabla}\phi$. Inserting (4.18) into the equation (4.17) and dropping terms of order ϵ^3, we obtain an equation for the perturbation potential ϕ:

$$\begin{aligned}\phi_{zz} - B_0^2\phi_{xx} = {} & \epsilon M_0^2 \left\{(\gamma+1)\phi_x\phi_{xx} + (\gamma-1)\phi_x\phi_{zz} + 2\phi_z\phi_{xz}\right\} \\ & + \epsilon^2 M_0^2 \left\{ \frac{\gamma-1}{2}(\phi_{xx} + \phi_{zz})(\phi_x^2 + \phi_z^2) + \phi_z^2\phi_{zz} + \phi_x^2\phi_{xx} + 2\phi_x\phi_z\phi_{xz} \right\}. \end{aligned} \tag{4.19}$$

We also want to express the boundary conditions in terms of ϕ: since $u = \Phi_x = 1 + \epsilon\phi_x$, $v = \Phi_z = 0 + \epsilon\phi_z$ and the normal $\mathbf{n}_G$ is parallel to $(-\epsilon G'(x), 1)$, the boundary condition (4.13) becomes

$$\frac{\phi_z(x,z)}{1 + \epsilon\phi_x(x,z)} = G'(x) \quad \text{on} \quad z = \epsilon G(x). \tag{4.20}$$

The condition at infinity becomes

$$(\phi_x, \phi_z) \to (0, 0) \quad \text{as} \quad x \to -\infty. \tag{4.21}$$

4.4.2 Asymptotic analysis

Lowest-order perturbation potential

We tentatively assume the following asymptotic series for the perturbation potential ϕ, in integral powers of ϵ,

$$\phi(x, z, \epsilon) \sim \phi_1(x, z) + \epsilon\phi_2(x, z) + O(\epsilon^2). \tag{4.22}$$

Therefore we substitute (4.22) in (4.19) and we equate corresponding powers of ϵ in order to determine the equations satisfied by ϕ_1 and ϕ_2. At the lowest order we obtain

$$\phi_{1zz} - B_0^2\phi_{1xx} = 0. \tag{4.23}$$

Equation (4.23) is a homogeneous, second-order, wave equation with constant coefficients and has two families of characteristics $x \pm B_0 z = \text{constant}$. The general D'Alembert's solution in $z > 0$ is

$$\phi_1(x, z) = f(x - B_0 z) + g(x + B_0 z) = f(\xi) + g(\eta), \tag{4.24}$$

which is a superposition of waves propagating upwards and downwards. Setting $x = t$, $z = x$ and $B_0 = 1/c_0$ equation (4.24) becomes the familiar equation of one-dimensional propagation of sound waves, and we can consider linear acoustics and linear supersonic aerodynamics to be essentially the same subject.

Note that in $z < 0$ for a symmetric aerofoil the D'Alembert's solution can be obtained from (4.24) by taking $z \mapsto -z$ i.e. $\phi_1(x, z)|_{z<0} = f(\eta) + g(\xi)$, but for a general aerofoil a different set of f and g functions would be involved in the solution.

In order to equate corresponding powers of ϵ we should also transfer the body boundary condition (4.20) to the axis $z = 0$. Assuming that $\phi_k(x, z)$ are analytic at $z = 0$ we expand in Taylor series about $z = 0$

$$\phi_z(x, \epsilon G(x)) = \phi_z(x, 0+) + \epsilon G(x)\phi_{zz}(x, 0+) + O(\epsilon^2), \tag{4.25}$$

and similarly for $\phi_x(x, \epsilon G(x))$. Therefore to the lowest order, (4.20) becomes

$$\phi_{1z}(x, 0+) = G'(x). \tag{4.26}$$

For the lower part of the aerofoil $\phi_{1z}(x, 0-) = -G'(x)$ and therefore ϕ_{1z} has a jump of $2G'(x)$ for $-1/2 \leq x \leq 1/2$. There is no jump in ϕ_{1z} for $x > 1/2$ or $x < -1/2$. The upstream condition at this order is

$$(\phi_{1x}, \phi_{1z}) \to (0, 0) \qquad \text{as } x \to, -\infty. \tag{4.27}$$

where, from D' Alembert's solution (4.24)

$$\phi_{1x} = f'(\xi) + g'(\eta), \quad \phi_{1z} = -B_0 f'(\xi) + B_0 g'(\eta), \tag{4.28}$$

We consider a fixed $\eta = x + B_0 z$ characteristic. Letting $z \to \infty$, since η is fixed, we have $x \to -\infty$. Therefore from (4.27) and (4.28) we get

$$B_0\phi_{1x} + \phi_{1z} = 2B_0 g'(\eta) \to 0 \Rightarrow g \to g_0 \text{ as } x \to -\infty \text{ and } z \to \infty.$$

We set $g_0 = 0$, since only the gradient of ϕ is physically relevant. Therefore

$$\phi_1(x, z) = f(\xi). \tag{4.29}$$

A more physical way of arriving at relation (4.29) is to immediately discard the function g since, by the condition at infinity, only outgoing waves are possible.

Enforcing the boundary condition (4.26) we find $f = -G/B_0 + f_0$ where the constant f_0 is also set to zero. Therefore finally

$$\phi_1(x,z) = -\frac{G(\xi)}{B_0} = -\frac{G(x - B_0 z)}{B_0}, \tag{4.30}$$

i.e. at distance z from the aerofoil ϕ_1 is obtained by translating the function $-G(x)/B_0$ $B_0 z$ units to the right of the initial condition $\phi_1(x,0) = -G(x)/B_0$. The velocity field (u_1, v_1) is given as

$$u_1 = \phi_{1x} = -\frac{G'(\xi)}{B_0}, \quad v_1 = \phi_{1z} = G'(\xi) = -B_0 u_1. \tag{4.31}$$

Also in the (nondimensional) pressure relation (4.15), we put $\Phi = x + \epsilon\phi$ which gives

$$p = \left(1 + \frac{\gamma - 1}{2} M_0^2(-2\epsilon\phi_x - \epsilon^2(\phi_x^2 + \phi_z^2))\right)^{\gamma/(\gamma-1)}. \tag{4.32}$$

Expanding to bring down the exponent $\gamma/(\gamma - 1)$, we have

$$p = 1 - \frac{\gamma}{2} M_0^2(2\epsilon\phi_x + \epsilon^2(\phi_x^2 + \phi_z^2)) + \epsilon^2 \frac{\gamma M_0^4}{2} \phi_x^2 + O(\epsilon^3). \tag{4.33}$$

Assuming the asymptotic expansion $p \sim 1 + \epsilon p_1 + \epsilon^2 p_2 + O(\epsilon^3)$, from (4.22), the pressure at the lowest order is

$$p_1 = -\gamma M_0^2 \phi_{1x} = -\gamma M_0^2 u_1. \tag{4.34}$$

Now, the nondimensional homentropic flow condition is $p = \rho^\gamma$ and substituting in it the asymptotic expansion for p given above, and $\rho \sim 1 + \epsilon\rho_1 + \epsilon^2\rho_2 + O(\epsilon^3)$, we find at this order $p_1 = \gamma\rho_1$. Therefore from (4.34) we find

$$\rho_1 = -M_0^2 \phi_{1x} = -M_0^2 u_1. \tag{4.35}$$

We note that

$$(u_1, v_1, p_1, \rho_1) = u_1(1, -B_0, -\gamma M_0^2, -M_0^2), \tag{4.36}$$

i.e. the first-order flow variables can all be expressed as a function of u_1.

The above analysis is basically the linear Ackeret theory (see, for instance, [121]). The Ackeret theory is a sufficiently good approximation at and near the body (near-field). However, it represents disturbances which propagate with undiminished strength to infinity on the straight, *parallel* characteristics $x \pm B_0 z =$ constant and fails at

large distances from the aerofoil (far-field), where nonlinear effects accumulate becoming important. There the characteristics are no longer parallel, they cross, and shocks are formed. In Figure 4.3(a) we plot a schematic for the characteristics and the streamlines of the Ackeret theory, and in Figure 4.3(b) a schematic of characteristics in a modified nonlinear theory. In Figure 4.3(b) the solid-line curves entered by characteristics represent shocks and an expression for them will be derived later.

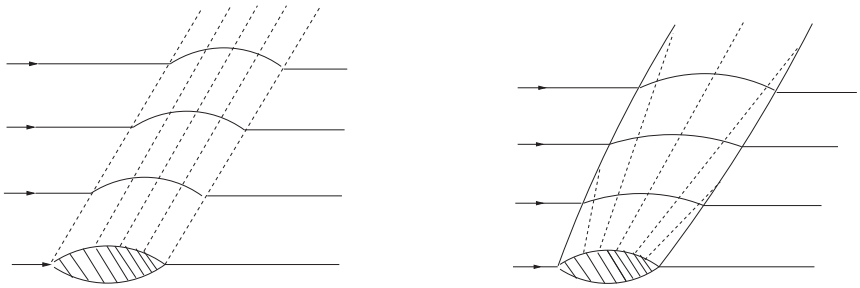

(a) Linear theory: the characteristics are straight and parallel. The arrowed curves are the streamlines.

(b) Nonlinear theory: the characteristics are no longer parallel and shocks appear.

Figure 4.3: Flow pattern above a supersonic thin aerofoil, showing the contrast between linear and nonlinear theory. Only the $z > 0$ plane is shown (assuming an aerofoil symmetric with respect to the x-axis).

Next order in the asymptotic expansion of the potential

In this section, we show the breakdown of the linear Ackeret theory by calculating the perturbation at the next order, ϕ_2, and showing that $\epsilon\phi_2$ becomes of order 1 when z is of order $1/\epsilon$. The equation that ϕ_2 obeys is

$$\phi_{2zz} - B_0^2\phi_{2xx} = M_0^2\{(\gamma+1)\phi_{1xx}\phi_{1x} + (\gamma-1)\phi_{1x}\phi_{1zz} + 2\phi_{1z}\phi_{1xz}\}. \tag{4.37}$$

From (4.30), ϕ_1 is a function of ξ only, and therefore $\phi_{1x} = \phi_{1\xi}$, $\phi_{1z} = -B_0\phi_{1\xi}$ which leads to a simpler form for (4.37), namely

$$\phi_{2zz} - B_0^2\phi_{2xx} = M_0^4(\gamma+1)\phi_{1\xi}\phi_{1\xi\xi}, \tag{4.38}$$

where we have used $1 + B_0^2 = M_0^2$. This is an inhomogeneous, second-order wave equation. As expected, the operator in the left-hand side is the same as that in the lowest order wave equation (4.23). We use (4.30), to express the right-hand side in (4.38) in terms of the thickness function G

$$\phi_{2zz} - B_0^2\phi_{2xx} = \frac{M_0^4}{B_0^2}(\gamma+1)G'(\xi)G''(\xi). \tag{4.39}$$

The boundary condition (4.20) at this order gives

$$\phi_{2z}(\xi = x, z = 0+) = \frac{1}{B_0}\{B_0^2 G(x)G''(x) - (G'(x))^2\} \text{ when } -1/2 \leq x \leq 1/2. \tag{4.40}$$

The upstream condition becomes $(\phi_{2x}, \phi_{2z}) \to (0, 0)$ as $x \to -\infty$.

Oblique coordinates; breakdown of the asymptotic expansion

We now change to the *oblique* coordinates (ξ, z), following Hayes [51] and Van Dyke [121], *p.*108. The equation (4.19) for the perturbation potential ϕ becomes

$$\phi_{zz} - 2B_0\phi_{z\xi} = \epsilon M_0^2\{(\gamma+1)M_0^2\phi_\xi\phi_{\xi\xi} + 2(\phi_z - \gamma B_0\phi_\xi)\phi_{\xi z} \tag{4.41}$$

$$+ (\gamma-1)\phi_\xi\phi_{zz} - 2B_0\phi_z\phi_{\xi\xi}\} + O(\epsilon^2). \tag{4.42}$$

We can determine the equation satisfied by $\phi_2(\xi, z)$, either by transforming (4.39) or by plugging in (4.41) the asymptotic expansion $\phi = \phi_1(\xi, z) + \epsilon\phi_2(\xi, z) + O(\epsilon^2)$ and taking the terms of order ϵ. We get

$$\phi_{2zz} - 2B_0\phi_{2z\xi} = \frac{M_0^4}{B_0^2}(\gamma+1)G'(\xi)G''(\xi), \tag{4.43}$$

and it is now clear why changing to oblique coordinates is useful: we can readily integrate (4.43) with respect to z and obtain the first-order (linear) hyperbolic partial differential equation

$$\phi_{2z} - 2B_0\phi_{2\xi} = \frac{M_0^4}{B_0^2}(\gamma+1)G'(\xi)G''(\xi)z + C(\xi), \tag{4.44}$$

where $C(\xi)$ is an arbitrary function of ξ. We can solve (4.44) with the method of characteristics.[4] The characteristics have constant slope $d\xi/dz = -2B_0$ and we recover the characteristic family

$$\xi + 2B_0 z = \eta = \eta_0 = \text{constant}. \tag{4.45}$$

The variation of ϕ_2 along these characteristics is given by the ordinary differential equation

$$\frac{d\phi_2}{dz} = \frac{M_0^4}{B_0^2}(\gamma+1)G'(\xi)G''(\xi)z + C(\xi). \tag{4.46}$$

From (4.45) we can express $\xi = \eta_0 - 2B_0 z$ in terms of z and the characteristic label η_0, and (4.46) becomes

$$\frac{d\phi_2}{dz} = \frac{M_0^4}{B_0^2}(\gamma+1)G'(\eta_0 - 2B_0 z)G''(\eta_0 - 2B_0 z)z + C(\eta_0 - 2B_0 z). \tag{4.47}$$

[4] Van Dyke [121] proceeds instead with an iteration method.

Integrating (4.47) with respect to z, we get

$$\phi_2(\xi,z)=\frac{M_0^4(\gamma+1)}{B_0^2}\int^z \tilde{z}G'(\eta_0-2B_0\tilde{z})G''(\eta_0-2B_0\tilde{z})d\tilde{z}+\int^z C(\eta_0-2B_0\tilde{z})d\tilde{z}, \quad (4.48)$$

and integrating by parts we get

$$\phi_2(\xi,z)=\frac{M_0^4(\gamma+1)}{B_0^2}\left(-\frac{z}{4B_0}(G'(\eta_0-2B_0z))^2+\frac{1}{4B_0}\int^z (G'(\eta_0-2B_0\tilde{z}))^2d\tilde{z}\right) -\frac{C_1(\xi)}{2B_0}+C_2(\eta_0). \quad (4.49)$$

We have two unknown functions: $C_1(\xi)$, which stands for the indefinite integral of C, and $C_2(\eta_0)$. Due to the condition at infinity, $C_2(\eta_0)$ must be set to 0 and C_1 is determined below from the body boundary condition

$$\phi_{2z}(\xi=x,0+)-B_0\phi_{2\xi}(\xi=x,0+)=\frac{1}{B_0}\{B_0^2G(x)G''(x)-(G'(x))^2\}. \quad (4.50)$$

From (4.49) we obtain the partial derivatives

$$\phi_{2z}=-\frac{M_0^4}{4B_0^3}(\gamma+1)(G'(\xi))^2, \quad (4.51)$$

$$\phi_{2\xi}=-\frac{M_0^4}{2B_0^3}(\gamma+1)G'(\xi)G''(\xi)z-\frac{M_0^4}{8B_0^4}(\gamma+1)(G'(\xi))^2-\frac{1}{2B_0}C(\xi), \quad (4.52)$$

and using them in (4.50), we obtain C in terms of G, G', G'' and M_0

$$C(x)=2B_0G(x)G''(x)-\frac{2}{B_0}(G'(x))^2+\frac{M_0^4}{4B_0^3}(\gamma+1)(G'(x))^2. \quad (4.53)$$

Inserting (4.53) into (4.52) and after some rearrangement, we get the horizontal component of the velocity at this order

$$u_2=\phi_{2\xi}=-\frac{M_0^4}{2B_0^3}(\gamma+1)G'(\xi)G''(\xi)z+\frac{G'(\xi)^2}{B_0^2}\left(1-\frac{M_0^4}{4B_0^2}(\gamma+1)\right)-G(\xi)G''(\xi), \quad (4.54)$$

where we assumed the asymptotic expansion $u=1+\epsilon u_1+\epsilon^2u_2+O(\epsilon^3)$. The result (4.54) is in agreement with Van Dyke, (see [121], p. 107, expression (6.24), where this result was found by iterating on the equation (4.19)), and *at* the surface, coincides also with the Busemann solution. From (4.54), the perturbation is

$$\epsilon\phi_2\sim(\epsilon z)(\gamma+1)\frac{M_0^4}{2B_0^3}(G')^2 \quad (4.55)$$

and therefore $\epsilon\phi_2$ is of order 1 when $(\epsilon z) \sim 1$. Therefore, when $z \sim 1/\epsilon$, the assumed asymptotic expansion (4.22) breaks down. Returning to dimensional variables, the breakdown occurs at a physical distance of order L/ϵ away from the aerofoil, roughly 10 aerofoil chord lengths away. The breakdown of the asymptotic expansion physically means that the nonlinear effects that we initially neglected in the near-field problem become *cumulatively* significant in the far-field and the nonlinear term $\phi_\xi\phi_{\xi\xi}$ in (4.41) can no longer be neglected. Hayes, in [51], included these nonlinear effects and derived the appropriate nonlinear equation using physical reasoning. In the next section we will follow a mathematically systematic approach, consistently modifying our asymptotic analysis in order to remedy the non-uniformity (4.55) of the asymptotic expansion (4.22) and derive the relevant equation valid in the far-field.

4.4.3 Far-field: Kinematic Wave Equation (KWE)

In order to determine the governing equation at the lowest order, in the far-field, we define the new coordinate

$$Z = \epsilon z. \tag{4.56}$$

Within the MAE framework, the region where z is of order 1 will be called the *inner region* and the region where Z is of order 1 the *outer region*. Using (4.56) in (4.41) we get

$$\epsilon^2\phi_{ZZ} - 2\epsilon B_0\phi_{Z\xi} = \epsilon M_0^4(\gamma+1)\phi_\xi\phi_{\xi\xi} + O(\epsilon^2), \tag{4.57}$$

where $\epsilon^2\phi_{ZZ}$ in the left-hand side is of order ϵ^2 and thus negligible within our order of accuracy but left in for clarity. The term $-2B_0\phi_{z\xi}$ in the left-hand side of (4.41) has become $-2\epsilon B_0\phi_{Z\xi}$ and hence balances the nonlinear term $\epsilon M_0^4(\gamma+1)\phi_\xi\phi_{\xi\xi}$. Assuming, for the outer region, the asymptotic expansion

$$\phi^{(o)}(\xi, Z) \sim \phi_1^{(o)}(\xi, Z) + O(\epsilon), \tag{4.58}$$

and substituting in (4.57) we obtain

$$\phi_{1\xi Z}^{(o)} + (\gamma+1)\frac{M_0^4}{2B_0}\phi_{1\xi}^{(o)}\phi_{1\xi\xi}^{(o)} = 0, \tag{4.59}$$

which is a second-order nonlinear hyperbolic equation for $\phi_1^{(o)}$. In the outer region, we have therefore derived consistenly the correct approximation to the potential equation (4.41). We deduce that $u_1^{(o)} = \phi_{1\xi}^{(o)}$, the lowest-order horizontal velocity in the outer region, satisfies the KWE

$$u_{1Z}^{(o)} + (\gamma+1)\frac{M_0^4}{2B_0}u_1^{(o)}u_{1\xi}^{(o)} = 0. \tag{4.60}$$

Since (4.60) is a first-order partial differential equation we need to impose one initial condition. This condition will be supplied by matching $u_1^{(o)}(\xi, Z)$ in the outer region with the expression $u_1(x,z) = u_1^{(i)}(x,z) = -G'(\xi)/B_0$ in the inner region (the superscript (i) has been employed for the inner region variables).

4.4.4 Solution of the Kinematic Wave Equation

We give below a solution of the KWE (4.60) for a general body shape $G(x)$, using the method of characteristics. Without loss of generality we will assume that the aerofoil extends over $-1/2 \leq x \leq 1/2$. We will let for convenience $D = (\gamma+1)M_0^4/2B_0$. We will not examine higher orders, so we will drop the subscript 1 from the flow variables at the first order.

Firstly, since $du^{(o)}/dZ = 0$ on the characteristic curves that have slope $d\xi/dZ = Du_1^{(o)}$, we conclude that $u^{(o)}$ is constant on the characteristic lines

$$\xi_0 = \xi - Du^{(o)}(\xi_0)Z. \tag{4.61}$$

The term $Du^{(o)}(\xi_0)Z$ in (4.61) is exactly the modification caused to the linear theory characteristics $\xi_0 = \xi$ by the nonlinear terms. The solution in the outer region, as long as it is single-valued, is

$$u^{(o)}(\xi, Z) = G_1(\xi_0). \tag{4.62}$$

The unknown function G_1 is to be determined by matching $u^{(o)}$ with $u^{(i)}$. We apply Van Dyke's matching principle

$$u^{\text{match}} = \lim_{Z\to 0}(u^{(o)}(\xi, Z)) = \lim_{z\to\infty}(u^{(i)}(\xi)) = u^{(i)}(\xi) \tag{4.63}$$

and using (4.31) and (4.62) we find $u^{\text{match}} = G_1(\xi) = -G'(\xi)/B_0$ which gives $G_1 = -G'/B_0$. Hence from (4.61) and (4.62)

$$u^{(o)}(\xi, Z) = -G'(\xi_0)/B_0, \tag{4.64}$$

on the characteristics

$$\xi_0 = \xi + D\frac{G'(\xi_0)}{B_0}Z. \tag{4.65}$$

A uniformly valid solution, as long as it is single-valued, is therefore

$$u(\xi, z) = u^{(o)}(\xi, z) + u^{(i)}(\xi, z) - u^{\text{match}} = -G'(\xi_0)/B_0, \tag{4.66}$$

on the characteristics

$$\xi_0 = x - B_0 z + \underbrace{D\frac{G'(\xi_0)}{B_0}\epsilon z}_{O(\epsilon) \text{ correction}} . \tag{4.67}$$

In the outer region, the $DG'(\xi_0)\epsilon z/B_0$ term in the characteristics (4.67) becomes of order 1, leading to the characteristics crossing and the continuous solution (4.66)–(4.67) becoming multi-valued. To obtain a unique solution, the shocks need to be inserted using the appropriate Rankine-Hugoniot and entropy conditions.

For an aerofoil with thickness function $G(x)$, with a maximum at a point $x_{\max}$ where $G'(x_{\max}) = 0$, G' has a positive and a negative part in relation to the undisturbed value $G' = 0$ and the same applies to $u = -G'/B_0$. In Figure 4.4 we plot a representative $G(x)$ and the corresponding $G'(x)$. A leading shock is formed with the

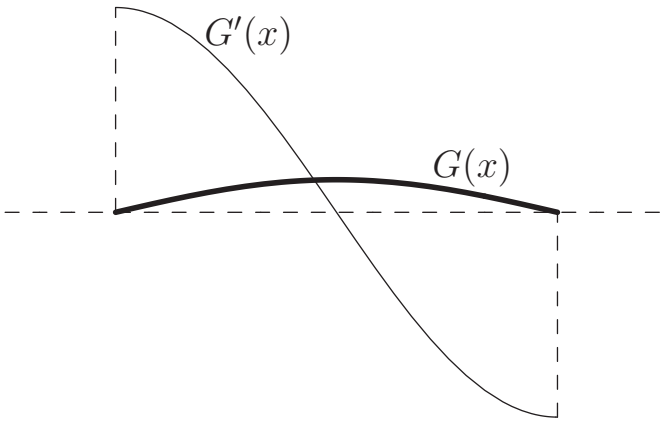

Figure 4.4: The upper part of an aerofoil with thickness function $G(x)$ (thicker line) and $G'(x)$ which has a positive and negative part in relation to the undisturbed value $G' = 0$ (since $G(-1/2) = G(1/2)$ the areas under the positive and negative part are equal).

parallel characteristics $\xi_0 = \xi$ entering it from the left, and the characteristics (4.67), where $G' > 0$ entering from the right. A trailing shock is formed with characteristics (4.67), for which $G' < 0$ entering from the left and the parallel characteristics $\xi_0 = \xi$ entering from the right. In the inner, linear theory, region, the two shocks are infinitely weak and coincide with the characteristics $\xi = \xi_0 = -1/2$, $\xi = \xi_0 = 1/2$ but in the outer region they deviate from the characteristics; we determine this deviation below.

We present below the simple analytical example of an aerofoil with a parabolic thickness function in a steady supersonic stream; we will calculate analytically the

characteristics, shock pattern and the wavefield. With this example we will be equipped to discuss further the case of a general G.

4.4.5 Analytical example: parabolic thickness function

We let

$$G(x) = -(x - 1/2)(x + 1/2) = 1/4 - x^2, \quad -1/2 \leq x \leq 1/2. \tag{4.68}$$

We write the KWE (4.60) in the conservation form

$$u_Z + \frac{D}{2}(u^2)_\xi = 0, \tag{4.69}$$

where we have dropped the superscript (o). This corresponds to the Rankine-Hugoniot relation

$$\text{shock 'slope'} = \frac{d\xi}{dZ} = \frac{D}{2}\frac{[u^2]}{[u]} = \frac{D}{2}(u_L^{\pm} + u_R^{\pm}), \tag{4.70}$$

where the superscript $\pm$ corresponds to the trailing/leading shock respectively. Subscripts L/R correspond to the solution to the left/right of either shock respectively.

The equation (4.69) is one of infinitely many conservation laws one can write for equation (4.60). It is however the only correct law (at this order) associated with the Euler equations. We can show this, if we write the compressible Euler equations in conservation form, change to oblique coordinates, substitute $Z = \epsilon z$, insert asymptotic expansions for u, v, p and ρ and equate the coefficients of the $O(\epsilon^2)$ terms.

For the leading shock, since the value of u on the left is $u_L^- = 0$ and on the right $u_R^-(\xi_0)$, the Rankine-Hugoniot condition (4.70) becomes

$$\frac{d\xi}{dZ} = \frac{D}{2}u_R^-(\xi_0) = -\frac{D}{2B_0}G'(\xi_0) = \frac{D}{B_0}\xi_0. \tag{4.71}$$

Equation (4.65) is, in general, transcendental in ξ_0 for an arbitrary G, but for the parabolic G (4.68) we find

$$\xi_0 = \frac{\xi}{1 + 2DZ/B_0}. \tag{4.72}$$

This step is in fact what makes our example analytically tractable. Combining (4.71) and (4.72),

$$\frac{d\xi}{dZ} = \frac{D}{B_0}\frac{\xi}{(1 + 2DZ/B_0)}, \tag{4.73}$$

which readily integrates to

$$1 + \hat{Z} = \lambda\xi^2, \tag{4.74}$$

where $\hat{Z} = 2DZ/B_0$. We find that $\lambda = 4$, by imposing $\xi \to \xi_0 = -1/2$ as $\hat{Z} \to 0$. The leading shock is the $2\xi^- = -\sqrt{1+\hat{Z}}$ portion of the parabola (4.74), with $\xi^- \leq -1/2$. The trailing shock is symmetric in the line $\xi = 0$ and therefore it is the $2\xi^+ = \sqrt{1+\hat{Z}}$ portion of the same parabola (4.74), with $\xi^+ \geq 1/2$. In Figure 4.5 we plot the shocks and some of the characteristics which they bisect. The distance between the two

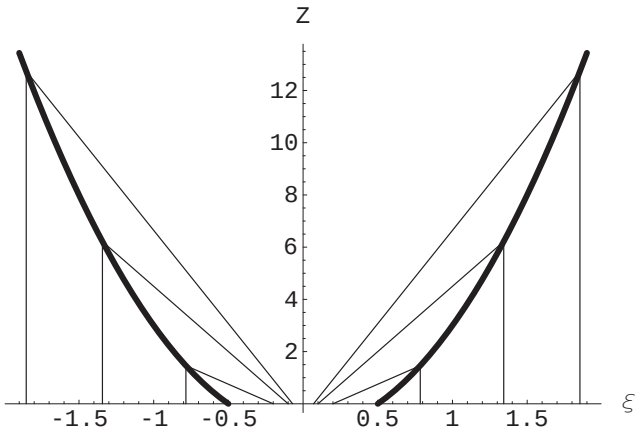

Figure 4.5: The characteristic diagram with the shock paths for the parabolic thickness function.

shocks at a fixed $\hat{Z} = \hat{Z}_0$, is given by $\xi^+ - \xi^- = \sqrt{1+\hat{Z}_0}$, which increases as the square root of Z, for large Z.

Having determined the geometry of the characteristic diagram, the method of characteristics gives immediately the wavefield. The jump of u at the leading shock is

$$[u^-] = u_R^- - u_L^- = u_R^- = -\frac{1}{B_0\sqrt{1+\hat{Z}_0}}. \tag{4.75}$$

At the trailing shock u has a positive jump u_L^+ which is of the same magnitude due to the symmetry. The smooth part of u between the shocks is $2\xi/(B_0(1+\hat{Z}_0))$ which varies linearly with ξ. We plot u in Figure 4.6 and mark the position of the leading and trailing shock, and the value of u at the corresponding jumps. As Z increases, the profile changes but the qualitative feature of a positive and negative part persists and furthermore the area under the positive/negative part of the profile remains the same (for the u-profile the area is $1/4B_0$). This area conservation property holds for any G and provides a geometrical way, alternative to the algebraic one employed here, to fit the shocks into the characteristic diagram. This method was devised by Whitham and it is usually called the *equal area rule* (for details see Whitham [126], pp. 42–46).

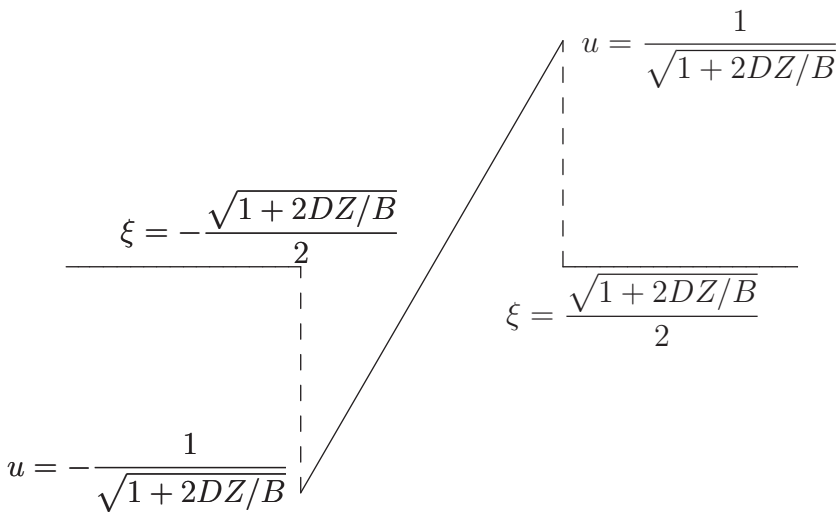

Figure 4.6: The profile of u.

The more physically relevant pressure signature may be obtained by taking $p = -\gamma M_0^2 u$; it resembles the letter N and it is usually called the N-wave. An N-wave is the typical pressure signature associated with a primary sonic boom and is discussed further below.

4.4.6 Asymptotic N-wave

In this section we return to the general G analysis. We restrict our attention to concave G. Then $G'' < 0$ and the characteristics emanating from the aerofoil do not cross for any $Z \geq 0$ (since $Z_{\text{cross}} = +(B_0/(DG''(\xi_0))$ is always negative); we thus only have a leading and a trailing shock as in the special parabolic thickness function above.

We take a point (ξ_s, Z_s) on the trailing shock. We parametrise the family of characteristics on the left with ξ_2 and the family of characteristics on the right with ξ_1. Therefore on the shock the expressions

$$\xi_s = \xi_1 + Du_R(\xi_1)Z_s, \tag{4.76}$$

$$\xi_s = \xi_2 + Du_L(\xi_2)Z_s \tag{4.77}$$

hold simultaneously. (We have dropped the superscript + from u_L and u_R.) The unknown quantities are ξ_s, ξ_1 and ξ_2 and the third relation required to close the system is furnished by the Rankine-Hugoniot relation (4.70). Since $u_R(\xi_1) = 0$ the three equations (4.76), (4.77) and (4.70) become respectively

$$\xi_s = \xi_1, \quad \xi_s = \xi_2 + Du_L(\xi_2)Z_s, \quad \frac{d\xi_s}{dZ_s} = \frac{D}{2}u_L(\xi_2). \tag{4.78}$$

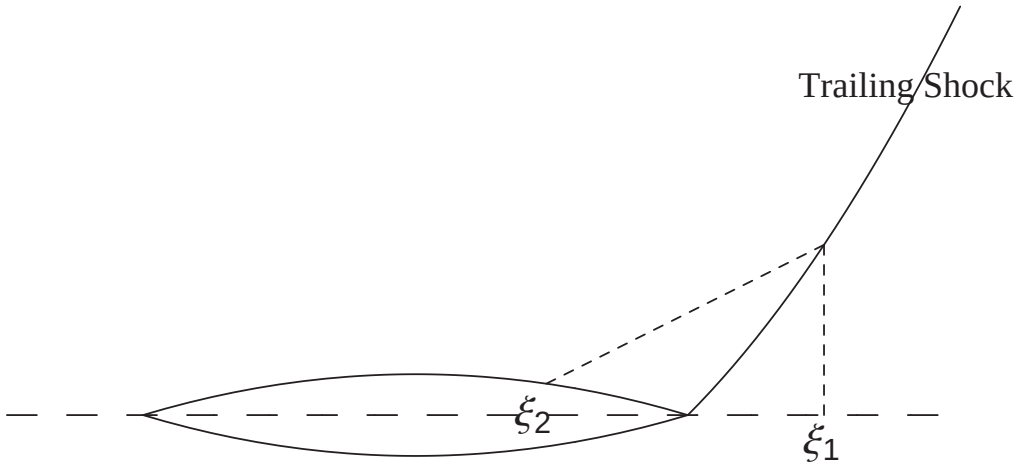

Figure 4.7: Schematic that shows the relation between the characteristic labels ξ_1 and ξ_2 mentioned in the text.

We can thus parametrise the shock with the characteristic label ξ_2. From the second relation in (4.78), and dropping the subscript from u_L, we have

$$\xi_s' = 1 + Du(\xi_2)Z_s' + Du'(\xi_2)Z_s, \tag{4.79}$$

where the prime denotes differentiation with respect to ξ_2. Similarly from the third (Rankine-Hugoniot) relation in (4.78), we have

$$\xi_s' = \frac{D}{2}u(\xi_2)Z_s'. \tag{4.80}$$

Combining (4.79) and (4.80) in order to eliminate ξ_s', we obtain the first-order ordinary differential equation

$$Z_s' + 2\frac{u'(\xi_2)}{u(\xi_2)}Z_s = -\frac{2}{Du(\xi_2)}. \tag{4.81}$$

Integrating this we obtain

$$\frac{1}{2}(Du(\xi_2))^2 Z_s = \int_{\xi_2}^{1/2} Du(\xi)d\xi \tag{4.82}$$

$$\Rightarrow Z_s(\xi_2) = \frac{2}{Du^2(\xi_2)}\int_{\xi_2}^{1/2} u(\xi)d\xi. \tag{4.83}$$

Therefore we have determined expressions for $\xi_s(\xi_2)$ and $Z_s(\xi_2)$ which can be used to plot the shock very easily for many profile choices.[5]

[5]The plotting will be exact in the cases that the integral $\int_{\xi_2}^{1/2} u(\xi)d\xi$ can be found exactly but even if this cannot be done it is very simple to calculate the one-dimensional quadrature numerically.

The parametric method applied above for fitting the shock is also going to be used (repeatedly) in Chapter 7. It can be applied to determine analytically any shock entered by characteristics with constant slope at either of its sides. The more general equal area rule could have been applied but this has not been necessary.

To determine the asymptotic behaviour of the solution of the KWE (4.60) we take the limit of (4.82) as $Z \to \infty$. Since ξ_2 decreases as Z_s increases we have that $\xi_2 \to \xi_m^+$, where $G'(\xi_m) = 0$. We thus find that asymptotically the shock strength is

$$u_s = u(\xi_2) \sim \sqrt{2A_1}\frac{1}{\sqrt{DZ_s}} \tag{4.84}$$

where A_1 = area in the positive part of $u = \int_{\xi_m}^{1/2} u(\xi)d\xi = \frac{G_{\max}}{B_0}$. Hence, from (4.77) and (4.84) the asymptotic shock position is

$$\xi_s \sim \sqrt{2A_1}\sqrt{DZ_s}. \tag{4.85}$$

Similarly for the leading shock, the asymptotic shock position and strength are given respectively by

$$\xi_s \sim -\sqrt{2A_2}\sqrt{DZ_s}, \quad u \sim -\sqrt{2A_2}\frac{1}{\sqrt{DZ_s}}, \tag{4.86}$$

where A_2 = area in the negative part of $u = \int_{-1/2}^{\xi_m} u(\xi)d\xi = A_1 = A$. Therefore the leading and trailing shocks are parabolae asymptotically. Lighthill had shown this in [71], in 1944, using a geometrical argument.

The solution *between* the two shocks is given asymptotically by the straight line segment

$$u \sim \xi/DZ, \qquad -\sqrt{2ADZ_{sF}} < \xi < \sqrt{2ADZ_{sT}}, \tag{4.87}$$

where the subscripts sF and sT signify the leading and trailing shock respectively. The expressions (4.85)–(4.87) can be used to determine the asymptotic N-wave profile for the pressure p. Since the shocks are parabolae asymptotically, the width of the N-wave increases with the square root of Z and the strength of the shocks decreases like $1/\sqrt{Z}$. This makes obvious how the linear theory disturbances, predicted to propagate undiminished to infinity on the straight parallel lines $\xi = \xi_0$, are weakened and "driven apart" by the nonlinear effects in the outer region. A schematic for the asymptotic N-wave appears in Figure 4.8.

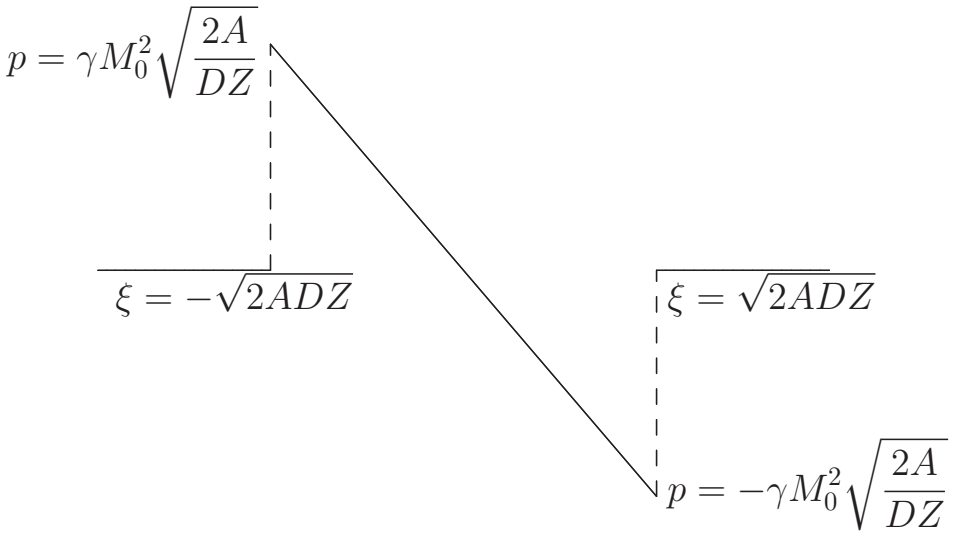

Figure 4.8: The asymptotic N-wave profile. A is the area under the positive/negative part and $D = \dfrac{(\gamma+1)M_0^4}{2B_0}$.

4.5 Axisymmetric supersonic flow

In this section we will look at the flow around three-dimensional bodies elongated in the x-direction. We will limit our attention to *bodies of revolution* which are *slender*.

For elongated bodies of revolution it is convenient to adopt cylindrical coordinates (x, r, θ) with the x-axis aligned with the body axis. The angle θ measures the inclination of the meridian (x, r)-plane from the (x, z)-plane (see Figure 4.9). The

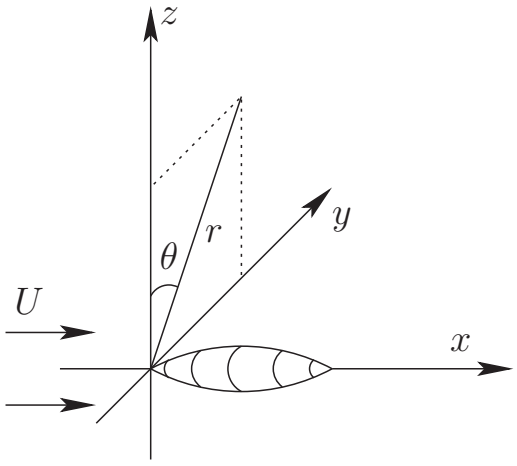

Figure 4.9: A (slender) axisymmetric body and the chosen system of cylindrical polar coordinates.

flow around a body of revolution $r = R(x), 0 \leq x \leq L$ is the *same* viewed from any

meridian plane, and does not depend on the angle θ (axisymmetric flow). We will assume an aerofoil with pointed ends. Nondimensionalising on the chord length, we have (in nondimensional variables) $r = \epsilon R(x)$ with the body axis occupying $0 \leq x \leq 1$ (see Figure 4.10). The parameter ϵ is small, typically 0.1 and it is usually called the slenderness ratio (the smaller ϵ is, the slenderer is the body). The presence of this small parameter will enable us to employ asymptotic methods to analyse the flow.

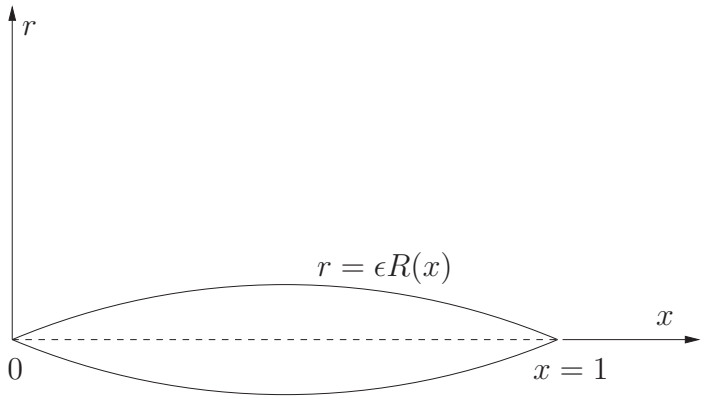

Figure 4.10: A meridional section of a slender body of revolution (which is nondimensionalised on the chord length).

We write the potential equation (4.12) in cylindrical polar coordinates, for axisymmetric flow (with no swirl)

$$\Phi_{xx} + \Phi_{rr} + \frac{\Phi_r}{r} = M_0^2 \{ \frac{\gamma - 1}{2} \left(\Phi_{xx} + \Phi_{rr} + \frac{\Phi_r}{r} \right) (\Phi_x^2 + \Phi_r^2 - 1) + \Phi_{xx}\Phi_x^2 + 2\Phi_x\Phi_r\Phi_{xr} + \Phi_r^2\Phi_{rr} \}. \tag{4.88}$$

Note that if we omit the Φ_r/r terms from (4.88) and exchange the coordinate r with the coordinate z we obtain the potential equation for planar flows. However it is precisely the presence of the $\dfrac{\Phi_r}{r}$ term that causes differences between the planar and axisymmetric flow, as will be shown below.

We set $\Phi = x + \epsilon^2\phi$ where ϕ is the perturbation potential and equation (4.88) then becomes

$$\phi_{rr} + \frac{\phi_r}{r} - B_0^2\phi_{xx} = \epsilon^2 M_0^2 \left\{ (\gamma + 1)\phi_x\phi_{xx} + (\gamma - 1)\phi_x \left(\phi_{rr} + \frac{\phi_r}{r} \right) + 2\phi_r\phi_{xr} \right\}$$
$$+ \epsilon^4 M_0^2 \left\{ \frac{\gamma - 1}{2} \left(\phi_{xx} + \phi_{rr} + \frac{\phi_r}{r} \right) (\phi_x^2 + \phi_r^2) + \phi_r^2\phi_{rr} + \phi_x^2\phi_{xx} + 2\phi_x\phi_r\phi_{xr} \right\}. \tag{4.89}$$

The body boundary condition (4.13) should be satisfied. In the current coordinate system it is expressed as

$$\frac{\Phi_r(x,\epsilon R(x))}{\Phi_x(x,\epsilon R(x))} = \frac{\epsilon^2\phi_r(x,\epsilon R(x))}{1+\epsilon^2\phi_x(x,\epsilon R(x))} = \epsilon R'(x). \tag{4.90}$$

The condition at infinity should be additionally satisfied and we will return to it later.

4.5.1 Asymptotic analysis

◇ Inner region (linear theory)

Linearised slender-body theory is well established and can be found in textbooks such as Whitham [126], Liepmann and Roshko [70] and Frankl and Karpovich [39]. The minor advantage of our exposition of this theory here is the explicit use of the small slenderness parameter ϵ.

Even though, as we have shown, for the two-dimensional problem the linear theory fails at large distances from the body it is still valuable because it gives the correct pressure forces acting on the body. Also from Whitham's point of view, as he explains in [124], the only failure of the linear theory at first order is that the characteristics it predicts are incorrect; otherwise the theory predicts correctly the values on the characteristics and hence the only modification needed to the linear theory is to shift appropriately the characteristics and introduce shocks in multi-valued regions.

We tentatively assume that the solution of (4.89) is represented by the asymptotic expansion

$$\phi \sim \phi_1 + \epsilon^\alpha\phi_2 + O(\delta(\epsilon)) \qquad \text{where } \alpha > 0 \text{ and } \delta(\epsilon) \ll \epsilon^\alpha; \tag{4.91}$$

α is later identified to be equal to 2. We will substitute the expansion (4.91) into the equation (4.89) and equate the coefficients of terms of same order in ϵ. (We emphasise however that the substitution in the boundary condition will be more subtle.) At leading order we obtain

$$\phi_{1rr} + \frac{1}{r}\phi_{1r} - B_0^2\phi_{1xx} = 0. \tag{4.92}$$

Under the change $x \to t$ and $1/B_0^2 \to c^2$ we obtain the well-known cylindrical waves equation

$$\phi_{1tt} - c^2(\phi_{1rr} + \frac{1}{r}\phi_{1r}) = 0,$$

which admits a solution (see Whitham [126], p. 220, expression (7.29))

$$\phi_1(r,t) = -\frac{1}{2\pi}\int_{-\infty}^{t-r/c} \frac{q(\zeta)}{\sqrt{(t-\zeta)^2 - r^2/c^2}}\,\mathrm{d}\zeta. \tag{4.93}$$

This solution represents only outgoing waves from a line source distribution with uniform strength $q(\zeta)$ per unit length. Therefore, we can transcribe (4.93) so that it gives the solution of (4.92) (see also [126] p. 224, expression (7.38))

$$\phi_1(x,r) = -\frac{1}{2\pi}\int_{0}^{x-B_0 r} \frac{m(\zeta)}{\sqrt{(x-\zeta)^2 - B_0^2 r^2}}\,\mathrm{d}\zeta, \tag{4.94}$$

where $m(\zeta)$ is to be determined by the body boundary condition. It is proved below that $m(x) = S'(x)$ where $S(x) = \pi R^2$, is the scaled cross-sectional area of the body at distance x from the nose. Therefore S' gives the rate at which the body pushes fluid out, and it can be interpreted as the strength of a "supersonic" monopole situated at x. The integral (4.94) can, thus, be interpreted as the field due to a distribution of "supersonic" monopoles along the axis, with density $S'(\zeta)$.

The upper limit in (4.94) is $\zeta = x - B_0 r$ due to the condition at infinity, which dictates that there is no downstream influence in a supersonic flow. Also, this implies that ϕ_1 is zero for $x < B_0 r$, upstream of the leading characteristic, and this sets the lower integration limit to zero.

The velocity perturbation field is given by $(u, v, 0)$=$(\phi_{1x}, \phi_{1r}, 0)$ with ϕ_1 given by (4.94). Since the denominator in the integrand of (4.94) vanishes at the upper limit $\zeta = x - B_0 r$, the differentation of ϕ_1 is subtle. Hadamard (see [46] and [112]) constructed rules to deal with this differentiation. Alternatively we can remove the singularity in (4.94), and hence differentiate straightforwardly, if we employ the transformation

$$x - \zeta = B_0 r \cosh\theta. \tag{4.95}$$

We obtain

$$\phi_1(x,r) = -\frac{1}{2\pi}\int_{0}^{\cosh^{-1}(x/B_0 r)} m(x - B_0 r\cosh\theta)\,\mathrm{d}\theta, \tag{4.96}$$

and differentiating we have

$$u_1 = \phi_{1x} = -\frac{1}{2\pi}\int_{0}^{\cosh^{-1}(\frac{x}{B_0 r})} m'(x - B_0 r\cosh\theta)\,\mathrm{d}\theta - m(0)\left(\frac{1}{\sqrt{x^2 - B_0^2 r^2}}\right), \tag{4.97}$$

$$v_1 = \phi_{1r} = -\frac{1}{2\pi}\int_{0}^{\cosh^{-1}(\frac{x}{B_0 r})} m'(x - B_0 r\cosh\theta)(-B_0\cosh\theta)\,\mathrm{d}\theta + m(0)\left(\frac{x}{r\sqrt{x^2 - B_0^2 r^2}}\right). \tag{4.98}$$

We will consider only bodies for which $m(0) = 0$ (and we will show later that this condition holds for a pointed aerofoil). Reverting to the original integration variable we have

$$u_1(x,r) = -\frac{1}{2\pi}\int_0^{x-B_0 r} \frac{m'(\zeta)}{\sqrt{(x-\zeta)^2 - B_0^2 r^2}}\,\mathrm{d}\zeta, \tag{4.99}$$

$$v_1(x,r) = \frac{1}{2\pi r}\int_0^{x-B_0 r} \frac{m'(\zeta)(x-\zeta)}{\sqrt{(x-\zeta)^2 - B_0^2 r^2}}\,\mathrm{d}\zeta. \tag{4.100}$$

◇ Applying the body boundary condition

The body boundary condition at leading order is written as

$$\epsilon\phi_{1r}(x, \epsilon R(x)) = R'(x). \tag{4.101}$$

In the earlier two-dimensional analysis we had transferred the body boundary condition to the axis $z = 0$. This was possible because ϕ_x and ϕ_z were analytic at $z = 0$. However for axisymmetric flows ϕ_r is not analytic at $r = 0$ so we cannot pursue the expansion of ϕ_{1r} about $r = 0$ in (4.101). To apply the body boundary condition we need to determine instead the asymptotic behaviour of $\phi_{1r}(x,r)$ as $r \to 0$. From (4.100) as $r \to 0$, it follows that[6]

$$2\pi r v_1(x,r) = \int_0^{x-B_0 r} \frac{m'(\zeta)(x-\zeta)}{\sqrt{(x-\zeta)^2 - B_0^2 r^2}}\,\mathrm{d}\zeta \to \int_0^x m'(\zeta)d\zeta = m(x). \tag{4.102}$$

Therefore

$$v_1(x,r) = \phi_{1r}(x,r) \sim \frac{m(x)}{2\pi r} \text{ as } r \to 0. \tag{4.103}$$

Using (4.103) in conjunction with (4.101), we find a relation between $m(x)$ and $R(x)$

$$\frac{m(x)}{2\pi R(x)} = R'(x) \Rightarrow m(x) = 2\pi R(x)R'(x) = S'(x). \tag{4.104}$$

(For an aerofoil with a pointed nose $R(0) = 0$ and relation (4.104) makes clear why we have set $m(0) = 0$ above.) Therefore from (4.94) we have

$$\phi_1(x,r) = -\frac{1}{2\pi}\int_0^{x-B_0 r} \frac{S'(\zeta)}{\sqrt{(x-\zeta)^2 - B_0^2 r^2}}\,\mathrm{d}\zeta. \tag{4.105}$$

[6]In (4.102), putting $s = \sqrt{(x-\zeta)^2 - B_0^2 r^2}$ leads to $-\int_0^{\sqrt{x^2 - B_0^2 r^2}} m'(x - \sqrt{s^2 + B_0^2 r^2})ds$. If we restrict attention to aerofoils for which m' is bounded and continuous then, as $r \to 0$, the latter integral tends to $-\int_0^x m'(x-s)ds = \int_0^x m'(\zeta)d\zeta$.

Also from (4.99) and (4.100) the perturbation velocities are

$$u_1(x,r) = -\frac{1}{2\pi}\int_0^{x-B_0 r} \frac{S''(\zeta)}{\sqrt{(x-\zeta)^2 - B_0^2 r^2}}\,\mathrm{d}\zeta, \tag{4.106}$$

$$v_1(x,r) = \frac{1}{2\pi r}\int_0^{x-B_0 r} \frac{S''(\zeta)(x-\zeta)}{\sqrt{(x-\zeta)^2 - B_0^2 r^2}}\,\mathrm{d}\zeta. \tag{4.107}$$

◇ Tail of the axisymmetric wave

For a finite planar aerofoil, with the thickness function $G(x)$ being zero except for the length interval $[0,1]$, the disturbance due to the aerofoil, in $z > 0$, is confined to $B_0 z < x < B_0 z + 1$ where $x = B_0 z$ is the characteristic emanating from the nose $(x = 0, z = 0)$ and $x = B_0 z + 1$ is the characteristic emanating from the trailing end $(x = 1, z = 0)$. Therefore for a fixed point downstream of $x = B_0 z + 1$, no disturbance is felt from the presence of the aerofoil.

However, for an axisymmetric body, of same (unit) length, a point (x, r) downstream of the characteristic cone at the trailing end, $x - B_0 r = 1$, *does* experience a disturbance, from all the upstream "supersonic" monopoles. For fixed $r = r_0$, $x > B_0 r_0 + 1$, we find that asymptotically as $x \to \infty$

$$\phi_1(x, r_0) \sim -\left\{\frac{1}{2\pi}\int_0^1 S'(\zeta)d\zeta\right\}\frac{1}{x} - \left\{\frac{1}{2\pi}\int_0^1 S(\zeta)d\zeta\right\}\frac{1}{x^2}. \tag{4.108}$$

For a body with a pointed nose and a pointing tail we have $S(0) = S(1)$ and therefore the coefficient in the leading term of the series (4.108) is zero. The coefficient of the second term is however always greater than zero and therefore ϕ_1 decays to zero with rate $O(1/x^2)$ as $x \to \infty$.

This so-called "tail" of the wave is a feature of waves in even dimensions. Here the dimension is defined as the integer n in the general wave equation

$$\phi_{tt} = c^2 \sum_{i=1}^{n} \phi_{x_i x_i}. \tag{4.109}$$

This is one of the important differences between waves in even and odd dimensions, first pointed out by Huygen. A schematic of the different behaviour is found in Figures 4.11(a) and 4.11(b).

◇ Pressure in the near-field

We want to calculate the leading-order pressure in the near field. We return to (4.15) and substitute $\Phi = x + \epsilon^2\phi$ which then becomes (in nondimensional form)

$$p = \left(1 - \frac{\gamma-1}{2}M_0^2\left(2\epsilon^2\phi_x + \epsilon^4\phi_x^2 + \epsilon^4\phi_r^2\right)\right)^{\gamma/(\gamma-1)} \tag{4.110}$$

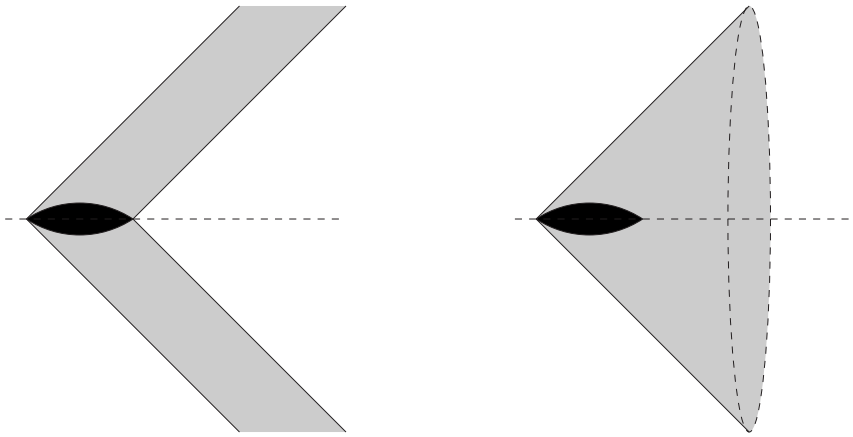

(a) Planar problem (uniform medium).

(b) Axisymmetric problem (uniform medium).

Figure 4.11: The difference between planar and axisymmetric problems is sketched. In axisymmetric flow the wave has a "tail" as explained in the text.

For a consistent approximation of (4.110) near the body, we have to identify the lowest-order terms. Firstly, we have shown already that $v_1 = \phi_{1r} \sim m(x)/(2\pi r)$ near the body. Also, from the irrotationality relation $u_{1r} = v_{1x}$ we obtain $\phi_{1x} \sim \dfrac{m'(x)}{2\pi} \ln r$. Then

- $\epsilon^2 \phi_{1x} \sim \epsilon^2(\ln \epsilon + \ln R)$
- $\epsilon^4 \phi_{1r}^2 \sim \dfrac{\epsilon^2}{R^2}$
- $\epsilon^4 \phi_{1x}^2 \sim \epsilon^4(\ln \epsilon + \ln R)^2 \ll \epsilon^4 \phi_{1r}^2$ for small ϵ.

Therefore, near the body and for small ϵ, the nonlinear term $\epsilon^4 \phi_{1r}^2$ contains the same power of ϵ as $\epsilon^2 \phi_{1x}$ (if we except the $\ln \epsilon$ factor) and the consistent approximation for the near-field pressure at leading order is

$$p = 1 - \epsilon^2 \frac{\gamma M_0^2}{2} \left(2\phi_{1x} + \epsilon^2 \phi_{1r}^2\right). \tag{4.111}$$

4.5.2 Near Mach cone, and far-field approximations

Now, we are going to investigate the region near the leading Mach characteristic, $\xi = x - B_0 r = 0$, and at large distances from the aerofoil. Mathematically we

consider the (Whitham) region (see [126], p. 227)

$$\frac{\xi}{r} \ll 1. \tag{4.112}$$

In this region the nonlinear effects are of order 1 and shocks are formed. The strength of the disturbance is greater in this region so we capture sufficiently accurately the qualitative behaviour of the far-field solution by limiting our attention there while we can benefit from being able to treat it analytically.

To proceed, we factor the denominator of the integrand in (4.105) as follows:

$$\phi_1(x,\xi) = -\frac{1}{2\pi}\int_0^\xi \frac{S'(\zeta)}{\sqrt{(\xi-\zeta)(\xi-\zeta+2B_0r)}}\,\mathrm{d}\zeta, \tag{4.113}$$

$$= -\frac{1}{2\pi}\frac{1}{\sqrt{2B_0r}}\int_0^\xi \frac{S'(\zeta)}{\sqrt{\xi-\zeta}}\left(1+\frac{\xi-\zeta}{2B_0r}\right)^{-1/2}\mathrm{d}\zeta, \tag{4.114}$$

$$= -\frac{1}{2\pi}\frac{1}{\sqrt{2B_0r}}\int_0^\xi \frac{S'(\zeta)}{\sqrt{\xi-\zeta}}\,\mathrm{d}\zeta + O\left(\frac{1}{r^{3/2}}\int_0^\xi S'(\zeta)\sqrt{\xi-\zeta}\,\mathrm{d}\zeta\right). \tag{4.115}$$

◇ The Whitham function

As $\dfrac{\xi}{r} \to 0$, (4.115) reduces to the asymptotic result

$$\phi_1 \sim \frac{1}{2\pi\sqrt{2B_0r}}\int_0^\xi \frac{S'(\zeta)}{\sqrt{\xi-\zeta}}\,\mathrm{d}\zeta. \tag{4.116}$$

To obtain analogous asymptotic expressions for ϕ_{1x} and ϕ_{1r} in the Whitham region we return to (4.106) and (4.107) and follow the same method of expansion seen in (4.113)–(4.115). We then have

$$\phi_{1x} \sim -\frac{1}{\sqrt{2B_0r}}F(\xi), \tag{4.117}$$

$$\phi_{1r} \sim \frac{B_0}{\sqrt{2B_0r}}F(\xi), \tag{4.118}$$

where

$$F(\xi) = \frac{1}{2\pi}\int_0^\xi \frac{S''(\zeta)}{\sqrt{\xi-\zeta}}\,\mathrm{d}\zeta$$

is called the Whitham Function.

However, we expect that cumulatively the nonlinear effects become important and shocks will form in the far-field in a similar way to that encountered in the planar analysis. We can pinpoint quantitatively when the linear theory breaks down by determining when the asymptotic expansion (4.91) becomes non-uniform. We do this below.

4.5.3 Breakdown of the asymptotic expansion

The next order of the asymptotic analysis in the inner region (upon setting $\alpha = 2$ in (4.91)) gives the inhomogeneous wave equation

$$\phi_{2rr} + \frac{\phi_{2r}}{r} - B_0^2\phi_{2xx} = M_0^2\left\{(\gamma+1)\phi_{1x}\phi_{1xx} + (\gamma-1)\phi_{1x}\left(\phi_{1rr} + \frac{\phi_{1r}}{r}\right) + 2\phi_{1r}\phi_{1xr}\right\}. \tag{4.119}$$

Restricting attention to the Whitham region, we can use expressions (4.117) and (4.118) to determine the second-order derivatives

$$\phi_{1xx} \sim -\frac{F'(\xi)}{\sqrt{2B_0 r}}, \quad \phi_{1rx} \sim \frac{B_0}{\sqrt{2B_0 r}}F'(\xi), \quad \phi_{1rr} \sim -\frac{B_0^2}{\sqrt{2B_0 r}}F'(\xi), \tag{4.120}$$

as $r \to \infty$, where $F'(\xi) = \dfrac{1}{2\pi}\left(\displaystyle\int_0^\xi \frac{S'''(\zeta)}{\sqrt{\xi-\zeta}}\,\mathrm{d}\zeta + \frac{S''(0)}{\sqrt{\xi}}\right)$. Substituting the expressions (4.120) in the right-hand side of (4.119) we get, as $r \to \infty$,

$$\phi_{2rr} + \frac{\phi_{2r}}{r} - B_0^2\phi_{2xx} \sim \frac{M_0^4}{2B_0}(\gamma+1)\frac{F(\xi)F'(\xi)}{r}. \tag{4.121}$$

The right-hand side of equation (4.121) contains the non-uniform term $M_0^4(\gamma+1)F(\xi)F'(\xi)/(2B_0 r)$ which is inversely proportional to r. When nonlinearity becomes important this term will balance the (curvature) term ϕ_{2r}/r in the left-hand side so that $\phi_{2r}/r \sim 1/r$; then ϕ_{2r} will be an order 1 quantity. We conclude that, since $\phi_{1r} \sim 1/\sqrt{r}$, the asymptotic expansion $\phi_{1r} + \epsilon^2\phi_{2r}$ breaks down when

$$\frac{1}{\sqrt{r}} \sim \epsilon^2 \Rightarrow r \sim \frac{1}{\epsilon^4}. \tag{4.122}$$

4.5.4 Derivation of a Kinematic Wave Equation

To derive an appropriate nonlinear equation governing the disturbance in the Whitham region we rewrite the potential equation (4.89) in oblique coordinates:

$$\begin{aligned}\phi_{rr} - 2B_0\phi_{r\xi} + \frac{1}{r}(\phi_r - B_0\phi_\xi) = \epsilon^2 M_0^2\{&(\gamma+1)M_0^2\phi_\xi\phi_{\xi\xi} - 2\gamma B_0\phi_\xi\phi_{\xi r} + \\ &(\gamma-1)\phi_\xi(\phi_{rr} + \frac{1}{r}(\phi_r - B_0\phi_\xi)) + 2\phi_r\phi_{r\xi} - 2B_0\phi_r\phi_{\xi\xi}\} + O(\epsilon^4).\end{aligned} \tag{4.123}$$

To remove the secularity we define a new rescaled variable

$$Y = \epsilon^4 r, \tag{4.124}$$

motivated by (4.122). We also need to scale the perturbation potential in order to be able to match consistently with the near field. We set:

$$\phi = \epsilon^2 \tilde{\phi} \tag{4.125}$$

We can obtain the scalings for r and ϕ by substituting $Y = \epsilon^{\mu} r$, $\phi = \epsilon^{\nu}\tilde{\phi}$ in equation (4.123) and balance terms out so that the governing equation at leading order involves the nonlinear term $\phi_{\xi}\phi_{\xi\xi}$.

Using the scalings (4.124) and (4.125) in (4.123)and setting $\tilde{\phi} = \tilde{\phi}_1 + O(\epsilon)$ we find

$$\tilde{\phi}_{1\xi Y} + \frac{(\gamma+1)M_0^4}{2B_0}\tilde{\phi}_{1\xi}\tilde{\phi}_{1\xi\xi} = -\frac{\tilde{\phi}_{1\xi}}{2Y}. \tag{4.126}$$

We let $\tilde{u}_1 = \tilde{\phi}_{1\xi}$, the horizontal perturbation velocity in the far-field, and we obtain the inhomogeneous KWE

$$\tilde{u}_{1Y} + \frac{(\gamma+1)M_0^4}{2B_0}\tilde{u}_1\tilde{u}_{1\xi} = -\frac{\tilde{u}_1}{2Y}. \tag{4.127}$$

4.5.5 Solution of the Kinematic Wave Equation

In order to render the KWE (4.127) homogeneous, we perform the transformation

$$\tilde{u}_1 = Y^{-1/2}C(\xi, Y).$$

We thus obtain

$$C_Y + DY^{-1/2}CC_{\xi} = 0, \tag{4.128}$$

where again $D = M_0^4(\gamma+1)/2B_0$. By the method of characteristics $C = C(\xi_0) =$ constant on the characteristics with slope $d\xi/dY = DCY^{-1/2}$. Therefore the solution to (4.127) is given by

$$\tilde{u}_1 = Y^{-1/2}C(\xi_0), \tag{4.129}$$

on the characteristics

$$\xi_0 = \xi - 2DC(\xi_0)Y^{1/2}. \tag{4.130}$$

We note that these characteristics are *parabolae*—in contrast with the straight lines found in the planar case.

The far-field solution (4.129)–(4.130) should be matched to the solution in the inner region in order to determine the unknown function C. In the Whitham region $\xi/r \ll 1$, we apply the Van Dyke's matching principle

$$\lim_{Y\to 0}(\sqrt{Y}\tilde{u}_1(\xi, Y)) = \lim_{r\to\infty}(\sqrt{r}u_1(\xi, r)). \tag{4.131}$$

The left-hand side in (4.131), in terms of the inner region variables ξ, r and u_1, is $C(\xi)$, and the right-hand side is given by $-F(\xi)/\sqrt{2B_0}$. Therefore we conclude that $C(\xi) = -F(\xi)/\sqrt{2B_0}$. Consequently, a uniformly valid solution, as long as it is single-valued, is

$$u = -\frac{F(\xi_0)}{\sqrt{2B_0 r}}, \tag{4.132}$$

on the characteristics

$$\xi_0 = \xi + \kappa\epsilon^2 F(\xi_0) r^{1/2}. \tag{4.133}$$

where

$$\kappa = \frac{(\gamma+1)M_0^4}{2^{1/2}{B_0}^{3/2}} = D\sqrt{\frac{2}{B}}. \tag{4.134}$$

The solution to the axisymmetric KWE presented here agrees exactly with the solution Whitham provided through his nonlinearisation technique—see [126] p. 332, expression (9.67) and p. 333, expressions (9.70), (9.71). We have thus provided a systematic derivation of this well-known Whitham result. The only difference in our solution is the appearance of the ϵ^2 factor in the correction to the linear theory characteristics. This is of course implied in the Whitham expressions since his F function is ϵ^2 times our function F here.

We know that the solution becomes multi-valued when characteristics cross at $r \sim 1/\epsilon^4$ and shocks form at the physical distance L/ϵ^4. If we take $\epsilon = 0.1$ this gives that the shocks form at distance $\sim O(10^3$ km). The shocks need to be determined through the appropriate Rankine-Hugoniot and entropy conditions. Two shocks will be formed, a leading and a trailing one.

The asymptotic behaviour of the leading shock can be determined in a straightforward manner either by applying an appropriate area conservation rule or using a parametric method similar to that we used to determine the planar flow shocks. In the planar flow the shocks were asymptotically parabolae (as $z \to \infty$, but in axisymmetric flow, as $r \to \infty$, we will show that the leading shock is asymptotic to a surface whose meridian surface is a quartic (it is of the form $\xi = -b_1 r^{1/4}$).

We first consider a point (ξ_s, Y_s) on the leading shock. We parametrise the family of characteristics on the left of the shock with ξ_1 and the family of characteristics on the right with ξ_2 in a similar way to that in the planar flow analysis for the trailing shock. Therefore on the shock the expressions

$$\xi_s = \xi_1 + 2DC(\xi_1)Y_s^{1/2}, \tag{4.135}$$

$$\xi_s = \xi_2 + 2DC(\xi_2)Y_s^{1/2} \tag{4.136}$$

hold simultaneously. The unknown quantities are ξ_s, ξ_1 and ξ_2 and the third relation required to close the system is furnished by the Rankine-Hugoniot relation

$$\frac{d\xi_s}{dY_s} = \frac{D}{2}(C(\xi_1) + C(\xi_2))Y_s^{-1/2}. \tag{4.137}$$

Ahead of the leading shock the disturbance is zero and therefore $C(\xi_1) = 0$. Hence the three equations (4.135), (4.136) and (4.137) become respectively

$$\xi_s = \xi_1, \quad \xi_s = \xi_2 + 2DC(\xi_2)Y_s^{1/2}, \quad \frac{d\xi_s}{dY_s} = \frac{D}{2}C(\xi_2)Y_s^{-1/2}. \tag{4.138}$$

We will parametrise the shock with the characteristic label ξ_2. From the second relation in (4.138) we have

$$\xi_s' = 1 + DC(\xi_2)Y_s^{-1/2}Y_s' + 2DC'(\xi_2)Y_s^{1/2}, \tag{4.139}$$

where the prime denotes differentiation with respect to ξ_2. Similarly from the third (Rankine-Hugoniot) relation in (4.138), we have

$$\xi_s' = \frac{D}{2}C(\xi_2)Y_s^{-1/2}Y_s'. \tag{4.140}$$

Combining (4.139) and (4.140) in order to eliminate ξ_s', we obtain the first-order nonlinear ordinary differential equation

$$Y_s' + 4\frac{C'(\xi_2)}{C(\xi_2)}Y_s = -\frac{2Y_s^{1/2}}{DC(\xi_2)}. \tag{4.141}$$

We now use the transformation $w = Y_s^{1/2}$ in (4.141) and obtain

$$w' + 2\frac{C'(\xi_2)}{C(\xi_2)}w = -\frac{1}{DC(\xi_2)}. \tag{4.142}$$

This is precisely the same equation as (4.81) which we had integrated and obtained (4.82). Therefore we have

$$C(\xi_2)^2 Y_s^{1/2} = -\frac{1}{D}\int_0^{\xi_2} C(\xi')d\xi', \tag{4.143}$$

Therefore, since $C = -F/\sqrt{2B_0}$ we get

$$F(\xi_2) \sim \left(\frac{2}{\kappa}\int_0^{\xi_2} F(\xi')d\xi'\right)^{1/2} Y_s^{-1/4} \tag{4.144}$$

where κ is defined in (4.134). Hence, asymptotically the shock position is given by

$$\xi_s \sim \xi_2 - \left(2\kappa\int_0^{\xi_2} F(\xi')d\xi'\right)^{1/2} Y_s^{1/4}, \tag{4.145}$$

$$= \xi_2 - \left(2\kappa\int_0^{\xi_2} F(\xi')d\xi'\right)^{1/2} \epsilon r_s^{1/4}, \tag{4.146}$$

which agrees with the Whitham expression in [126], p. 335, expression (9.77), apart from the ϵ factor, bearing in mind that Whitham's F is ϵ^2 ours. Consequently, using (4.129) and (4.144), we find that the jump of u on the shock is given by

$$[\tilde{u}_s] \sim -\frac{1}{\sqrt{2B_0}}\left(\frac{2}{\kappa}\int_0^{\xi_2} F(\xi')d\xi'\right)^{1/2} Y_s^{-3/4}. \tag{4.147}$$

The fact that for flow around bodies of revolution the width of the N-wave varies as $r^{1/4}$ and the shock strength as $r^{-3/4}$ was first noted by DuMond et al. in [35]. Using the relation $\tilde{p} = -\gamma M_0^2 \tilde{u}$ we can express (4.147) in terms of the pressure jump across the shock, $[p_s]$. We find

$$[\tilde{p}_s] \sim \frac{\gamma M_0^2}{\sqrt{2B_0}}\left(\frac{2}{\kappa}\int_0^{\xi_2} F(\xi')d\xi'\right)^{1/2} Y_s^{-3/4}. \tag{4.148}$$

Using (4.134) in (4.148) along with $Y_s = \epsilon^4 r$ and $[\tilde{p}_s] = \epsilon^{-2}[p_s]$ (so that we write the expression in terms of original variables—see (4.125)) we find

$$[p_s] \sim \frac{2^{1/4}\gamma}{(\gamma+1)^{1/2}}(M_0^2-1)^{1/8}\left(\int_0^{\xi_2} F(\xi')d\xi'\right)^{1/2} \epsilon^{-1} r^{-3/4}. \tag{4.149}$$

In the physical variables the pressure is $p = p_0(1+\epsilon^2 p_s)$ and therefore its jump is

$$\left[\frac{p}{p_0}\right] = \epsilon^2[p_s] \sim \frac{2^{1/4}\gamma}{(\gamma+1)^{1/2}}(M_0^2-1)^{1/8}\left(\int_0^{\xi_2} F(\xi')d\xi'\right)^{1/2} \epsilon r^{-3/4}, \tag{4.150}$$

which agrees with Whitham [126], p. 336, expression (9.78). The latter formula shows that the strength of a primary boom has a very weak dependence on the Mach number M_0 and decreases with distance like $r^{-3/4}$. Information about the geometry of the aerofoil is encompassed in the term $\left(\int_0^{\xi_2} F(\xi')d\xi'\right)^{1/2}$.

We have thus derived asymptotic expressions for the leading shock position and strength. Determining the trailing shock surface is more complicated due to the tail of the wave. This is also of the form $\xi = b_2 r^{1/4}$ and details are found in Whitham's paper [124]. The asymptotic form of the wave is an N-wave as in the planar analysis except that here the disturbance downstream of the trailing shock is non-zero, due to the presence of the tail.

Chapter 5

Two-dimensional steady supersonic motion in a stratified medium with wind

This chapter extends the work of Chapter 4 to show how small nonlinear and stratification effects become cumulatively important in the far-field for the scenario of a steadily moving supersonic aerofoil in a weakly stratified atmosphere and with a weakly stratified wind. This scenario constitutes a paradigm problem for secondary sonic boom.

5.1 Introduction

In this chapter we investigate two-dimensional flow around a *thin* supersonic aerofoil of chord length L, moving at constant speed U, along the x-axis, from right to left, in a medium weakly stratified in the z-direction, with a horizontal weakly stratified wind. As in the previous chapter the aerofoil velocity is $(-U, 0)$ but now the ambient pressure $p_0(z)$, density $\rho_0(z)$ and temperature $T_0(z)$ are all varying. The altitude of flight, $z = 0$, will be taken to be the reference level, and the pressure and density values there are denoted by P_0 and D_0 respectively. We will represent the wind with $\mathbf{w}_0(z) = (w_0(z), 0)$, and therefore the air-speed of the aerofoil is $U_0 = U + w_0(0)$. The Mach number of the aerofoil is then $M_0 = U_0/c_0 = U_0\sqrt{D_0/(\gamma P_0)}$, and we assume that $M_0 > 1$.

As in the previous chapter, we take the aerofoil to be symmetric with respect to its axis of motion, and with a thickness function G, and we denote by ϵ again the thickness ratio $G_{\max}/L$; this is typically of order 10^{-1}. A thin aerofoil induces weak perturbations to the ambient medium and all shocks are weak. We have shown that

for a uniform medium the strength of the shocks is of order ϵ. In a stratified medium the order of the perturbations may change but it will still involve a positive power of ϵ. The ambient properties vary on the scale height of the atmosphere $H = P_0/(D_0 g)$, already introduced in Chapter 3; for a typical atmosphere H is around 8 km. Therefore we can identify a second small parameter $\delta = L/H$ which is of order 10^{-3}, as we did in Chapter 3; however here we will address the stratification effects more fully.

The presence of the small parameters ϵ and δ points to the use of asymptotic methods. Abandoning the assumption of potential flow we will seek consistent approximations to the Euler equations, in various regions of interest. For typical atmospheric conditions it is reasonable to proceed with the assumption $\delta \ll \epsilon^2$. We will employ the method of Matched Asymptotic Expansions to show that

- Near the aerofoil nonlinear and stratification effects are negligible to leading order and the Euler equations are approximated by a linear wave equation with constant coefficients as that of the previous chapter. This region will be the inner region (or near-field).
- At distance $\dfrac{L}{\epsilon}$ from the aerofoil (about 10 aerofoil lengths away), nonlinear effects become of order 1 but stratification effects are still negligible. We will call this the middle region (or mid-field). The Euler equations will be approximated by a KWE which is the same as the KWE in the far-field in the previous chapter.
- Further out stratification effects also become of order 1, at distance $\dfrac{L}{\delta} \gg \dfrac{L}{\epsilon^2} \gg \dfrac{L}{\epsilon}$ (about 1000 aerofoil lengths away). We will call this region the outer region (or far-field). A more complicated KWE then arises.

Our work is related to work by Helfand [55] and Pechuzal and Kevorkian [91]. Helfand studied the simpler scenario of a thin aerofoil in a stationary atmosphere with a weakly stratified temperature profile and Pechuzal and Kevorkian studied the scenario of a thin aerofoil in a uniform atmosphere with a weakly *linearly* stratified wind. Both these studies employed the method of Multiple Scales and the stratification parameter δ was assumed to be of order ϵ.

5.2 The Euler equations and nondimensionalisation

Since the motion is steady we again adopt the aerodynamic frame of reference, in which the aerofoil is stationary and with the stream $(U + w_0(z), 0)$ incident on it.

Therefore the Euler equations (2.4), (2.4), (2.14), upon switching to the travelling coordinate $X = x + Ut$ become

$$(\rho u)_X + (\rho v)_z = 0, \tag{5.1}$$

$$p_X + \rho u u_X + \rho v u_z = 0, \tag{5.2}$$

$$p_z + \rho u v_X + \rho v v_z = -\rho g, \tag{5.3}$$

$$\rho(u p_X + v p_z) = \gamma p(u \rho_X + v \rho_z). \tag{5.4}$$

We note that in contrast with Chapter 3, we will retain the term $-\rho g$ in the momentum equation and will show consistently that internal gravity waves are not excited at the order we will be working to. (In Chapter 3, we had neglected this term because for secondary sonic boom propagation acoustic waves are decoupled from the gravity waves.) We further note that the naming of the dependent variables is somewhat unconventional in that we take v to be the velocity in the z-direction, and w_0 to be the wind in the x-direction. Also, from now on, for notational convenience, we will denote X by x.

We nondimensionalise the system (5.1)–(5.4) using $\hat{x} = x/L$, $\hat{z} = z/L$ and

$$u = U_0(\hat{u}_0(\delta\hat{z}) + \epsilon\bar{u}),\ v = \epsilon U_0 \bar{v},\ p = P_0(\hat{p}_0(\delta\hat{z}) + \epsilon\bar{p}),\ \rho = D_0(\hat{\rho}_0(\delta\hat{z}) + \epsilon\bar{\rho}). \tag{5.5}$$

In expression (5.5) we have defined

$$\hat{u}_0(\delta\hat{z}) = \frac{U + w_0(z)}{U_0}, \tag{5.6}$$

so that $\hat{u}_0(0) = 1$, and similarly $\hat{p}_0(0) = 1$ and $\hat{\rho}_0(0) = 1$. Dropping the hats and defining, for convenience, a new variable $\tilde{z} = \delta z$, we find the nondimensional equations

$$\epsilon(u_0\bar{\rho}_x + \rho_0\bar{u}_x + \rho_0\bar{v}_z) + \epsilon^2((\bar{\rho}\bar{u})_x + (\bar{\rho}\bar{v})_z) + \epsilon\delta\rho_{0\tilde{z}}\bar{v} = 0, \tag{5.7}$$

$$\epsilon(\bar{p}_x + \gamma M_0^2\rho_0 u_0\bar{u}_x) + \gamma M_0^2\epsilon^2(\rho_0\bar{u}\bar{u}_x + u_0\bar{\rho}\bar{u}_x + \rho_0\bar{v}\bar{u}_z) + \gamma M_0^2\epsilon^3(\bar{\rho}\bar{u}\bar{u}_x + \bar{\rho}\bar{v}\bar{u}_z) + \gamma M_0^2\epsilon\delta\rho_0 u_{0\tilde{z}}\bar{v} + \gamma M_0^2\epsilon^2\delta u_{0\tilde{z}}\bar{\rho}\bar{v} = 0, \tag{5.8}$$

$$\epsilon(\bar{p}_z + \gamma M_0^2\rho_0 u_0\bar{v}_x) + \gamma M_0^2\epsilon^2(\rho_0\bar{u}\bar{v}_x + u_0\bar{\rho}\bar{v}_x + \rho_0\bar{v}\bar{v}_z) + \gamma M_0^2\epsilon^3(\bar{\rho}\bar{u}\bar{v}_x + \bar{\rho}\bar{v}\bar{v}_z) = -\delta(p_{0\tilde{z}} + \rho_0) - \epsilon\delta\bar{\rho}, \tag{5.9}$$

$$\epsilon(\rho_0 u_0\bar{p}_x) + \epsilon^2(\rho_0\bar{u}\bar{p}_x + \rho_0\bar{v}\bar{p}_z + u_0\bar{\rho}\bar{p}_x) + \epsilon^3(\bar{\rho}\bar{u}\bar{p}_x + \bar{\rho}\bar{v}\bar{p}_z) + \epsilon\delta\rho_0 p_{0\tilde{z}}\bar{v} + \epsilon^2\delta p_{0\tilde{z}}\bar{\rho}\bar{v} = \gamma\epsilon(p_0 u_0\bar{\rho}_x) + \gamma\epsilon^2(p_0\bar{u}\bar{\rho}_x + p_0\bar{v}\bar{\rho}_z + u_0\bar{p}\bar{\rho}_x) + \gamma\epsilon^3(\bar{p}\bar{u}\bar{\rho}_x + \bar{p}\bar{v}\bar{\rho}_z) + \gamma\epsilon\delta p_0\rho_{0\tilde{z}}\bar{v} + \gamma\epsilon^2\delta\rho_{0\tilde{z}}\bar{p}\bar{v}. \tag{5.10}$$

In equation (5.9) the first term on the right-hand side, $-\delta(p_{0\tilde{z}} + \rho_0)$, is zero because of the hydrostatic balance relation $p_{0\tilde{z}} = -\rho_0$. Note that in the nondimensionalised system above we have presented the terms in ascending order in the powers of ϵ.

5.2.1 Inner region (near-field)

When we substitute the Taylor series

$$\rho_0(\delta z) = \rho_0(0) + \delta z \rho_{0\tilde{z}}(0) + O(\delta^2), \tag{5.11}$$

$$p_0(\delta z) = p_0(0) + \delta z p_{0\tilde{z}}(0) + O(\delta^2), \tag{5.12}$$

$$u_0(\delta z) = u_0(0) + \delta z u_{0\tilde{z}}(0) + O(\delta^2), \tag{5.13}$$

into (5.7)–(5.10), we find that the lowest-order stratification terms involve $\epsilon\delta z$. Since we are going to deal with terms only of order ϵ and order ϵ^2 these stratification terms are negligible.

Next, we assume that the perturbations can be represented by the asymptotic series

$$\bar{\rho}(x,z) \sim \rho_1 + \epsilon\rho_2 + O(\epsilon^2), \tag{5.14}$$

$$\bar{p}(x,z) \sim p_1 + \epsilon p_2 + O(\epsilon^2), \tag{5.15}$$

$$\bar{u}(x,z) \sim u_1 + \epsilon u_2 + O(\epsilon^2), \tag{5.16}$$

$$\bar{v}(x,z) \sim v_1 + \epsilon v_2 + O(\epsilon^2). \tag{5.17}$$

We substitute (5.14)–(5.17) into (5.7)–(5.10) and we obtain at order ϵ the linear system

$$\rho_{1x} + u_{1x} + v_{1z} = 0, \tag{5.18}$$

$$p_{1x} + \gamma M_0^2 u_{1x} = 0, \tag{5.19}$$

$$p_{1z} + \gamma M_0^2 v_{1x} = 0, \tag{5.20}$$

$$p_{1x} - \gamma\rho_{1x} = 0. \tag{5.21}$$

Eliminating p_1 and ρ_1 from (5.18)–(5.21) we obtain the following linear wave equation for u_1:

$$u_{1zz} - B_0^2 u_{1xx} = 0. \tag{5.22}$$

Equation (5.22) is the consistent leading-order approximation of the Euler equations in the near-field. Note that

$$v_{1x} - u_{1z} = 0 \tag{5.23}$$

holds, and therefore the *vorticity* at this order is zero. (This is obtained by integrating (5.19) with respect to x, differentating with respect to z, and using the resulting

relation in (5.20) to eliminate p_{1z}. All integration constants are set to zero due to the upstream conditions.) The characteristics of equation (5.22) are the straight lines $\xi = x - B_0 z$, $\eta = x + B_0 z$ and the D'Alembert solution is $\phi_1(\xi, \eta) = f(\xi) + g(\eta)$. Concentrating on the half-plane $z > 0$ the flow quantities at order ϵ are

$$u_1 = -\frac{G'(\xi)}{B_0}, \quad v_1 = -B_0 u_1(\xi), \quad p_1 = -\gamma M_0^2 u_1(\xi), \quad \rho_1 = -M_0^2 u_1(\xi), \tag{5.24}$$

just as in (4.31), (4.34) and (4.35) from Chapter 4. Then, proceeding to order ϵ^2 we find:

$$\rho_{2x} + u_{2x} + v_{2z} = -\rho_1(u_{1x} + v_{1z}) - (u_1\rho_{1x} + v_1\rho_{1z}), \tag{5.25}$$

$$p_{2x} + \gamma M_0^2 u_{2x} = -\gamma M_0^2(u_1 u_{1x} + v_1 u_{1z} + \rho_1 u_{1x}), \tag{5.26}$$

$$p_{2z} + \gamma M_0^2 v_{2x} = -\gamma M_0^2(u_1 v_{1x} + v_1 v_{1z} + \rho_1 v_{1x}), \tag{5.27}$$

$$p_{2x} - \gamma\rho_{2x} = -\rho_1 p_{1x} + \gamma p_1\rho_{1x} + (\gamma u_1\rho_{1x} - u_1 p_{1x}) + (\gamma v_1\rho_{1z} - v_1 p_{1z}). \tag{5.28}$$

The left-hand side at order ϵ^2 is the same as that of the order ϵ system, upon changing the subscript $''1''$ to $''2''$ (as expected). We use the order ϵ solution (5.24) to evaluate the right-hand sides of the system (5.25)–(5.28) in terms of u_1 and subsequently use $u_1 = -\dfrac{G'(\xi)}{B_0}$. We obtain

$$\rho_{2x} + u_{2x} + v_{2z} = 2M_0^4 u_1 u_{1\xi} = 2\frac{M_0^4}{B_0^2} G'G'', \tag{5.29}$$

$$p_{2x} + \gamma M_0^2 u_{2x} = 0, \tag{5.30}$$

$$p_{2z} + \gamma M_0^2 v_{2x} = 0, \tag{5.31}$$

$$p_{2x} - \gamma\rho_{2x} = \gamma(\gamma - 1) M_0^4 u_1 u_{1\xi} = \gamma(\gamma - 1)\frac{M_0^4}{B_0^2} G'G'', \tag{5.32}$$

where the dash signifies differentation with respect to ξ. Integrating (5.30) with respect to x we obtain $p_2 = -\gamma M_0^2 u_2(x, z) + f(z)$. The undetermined function $f(z)$ will be set to zero because there is no disturbance upstream. Differentating with respect to z and combining with (5.31) we obtain

$$v_{2x} - u_{2z} = 0,$$

from which we deduce that the flow is still irrotational at this order. Also the linear combination $\gamma(5.29) + (5.32) - (5.30)$ gives

$$v_{2z} - B_0^2 u_{2x} = (\gamma + 1)\frac{M_0^4}{B_0^2} G'G''. \tag{5.33}$$

We set $u_2 = \phi_{2x}$, $v_2 = \phi_{2z}$ and (5.33) gives

$$\phi_{2zz} - B_0^2 \phi_{2xx} = (\gamma+1) M_0^4 u_1 u_{1\xi} = (\gamma+1) \frac{M_0^4}{2B_0} (G'G''), \tag{5.34}$$

which is, as expected, equation (4.38) of Chapter 4. We have already solved (4.38) by reverting to the oblique coordinates $\xi = x - B_0 z, z$ and have found that at distances $z \sim 1/\epsilon$ we have $\epsilon\phi_2 \sim \phi_1$, which causes the asymptotic expansion for ϕ to become nonuniform. This nonuniformity arises because nonlinear effects accumulate to an order 1 effect at physical distances $z \sim L/\epsilon$ from the aerofoil. We had thus defined there a second region where this nonuniformity was removed by incorporating nonlinear terms at the leading order which balanced the secular term $(\gamma+1)M_0^4 u_1 u_{1\xi}$. This led to the KWE (4.60). Here however, beyond this second region there is a third region (at distance $z \sim \dfrac{L}{\delta}$), where stratification will become equally important to nonlinearity; we will call the second region "middle region" and the third region "outer region".

5.2.2 Middle region (mid-field)

In order to investigate the "middle region" where nonlinearity is an order 1 effect we are going to switch to the coordinates $Z = \epsilon z$ and $\xi = x - B_0 z$. In the "middle region" Z and ξ are order 1. This region is at physical distances of order L/ϵ from the aerofoil. We will pursue the derivation of the KWE (4.60) in terms of all 4 flow quantities u, v, p and ρ. It is helpful to recall that the partial derivatives in terms of the new variables are $\dfrac{\partial}{\partial x} = \dfrac{\partial}{\partial \xi}$ and $\dfrac{\partial}{\partial z} = \epsilon \dfrac{\partial}{\partial Z} - B_0 \dfrac{\partial}{\partial \xi}$.

Writing then the system (5.7)–(5.10) in terms of Z and ξ, and collecting terms of the same order together, we have

$$\epsilon(u_0 \bar{\rho}_\xi + \rho_0(\bar{u}_\xi - B_0 \bar{v}_\xi)) + \epsilon^2((\rho_0 \bar{v})_Z + (\bar{\rho}\bar{u})_\xi - B_0(\bar{\rho}\bar{v})_\xi) + O(\epsilon^3) = 0, \tag{5.35}$$

$$\epsilon(\bar{p}_\xi + \gamma M_0^2 \rho_0 u_0 \bar{u}_\xi) + \gamma M_0^2 \epsilon^2(\rho_0 u_{0Z} \bar{v} + \rho_0 \bar{u}\bar{u}_\xi - \rho_0 B_0 \bar{v}\bar{u}_\xi + u_0 \bar{\rho}\bar{u}_\xi) + O(\epsilon^3) = 0, \tag{5.36}$$

$$\epsilon(-B_0 \bar{p}_\xi + \gamma M_0^2 \rho_0 u_0 \bar{v}_\xi) + \epsilon^2 \bar{p}_Z + \gamma M_0^2 \epsilon^2(\rho_0 \bar{u}\bar{v}_\xi - \rho_0 B_0 \bar{v}\bar{v}_\xi + u_0 \bar{\rho}\bar{v}_\xi) + O(\epsilon^3, \epsilon\delta) = 0, \tag{5.37}$$

$$\epsilon \rho_0 u_0 \bar{p}_\xi + \epsilon^2(\rho_0(\bar{u} - B_0\bar{v})\bar{p}_\xi + u_0 \bar{\rho}\bar{p}_\xi) =$$
$$\gamma \epsilon p_0 u_0 \bar{\rho}_\xi + \gamma \epsilon^2(p_0(\bar{u} - B_0\bar{v})\bar{\rho}_\xi + u_0 \bar{p}\bar{\rho}_\xi) + O(\epsilon^3, \epsilon\delta). \tag{5.38}$$

Substituting in (5.35)–(5.38) the Taylor series

$$\rho_0\left(\frac{\delta}{\epsilon} Z\right) = 1 + \frac{\delta}{\epsilon} Z \rho_{0\tilde{z}}(0) + O\left(\left(\frac{\delta}{\epsilon}\right)^2\right), \tag{5.39}$$

and similarly for $p_0\left(\frac{\delta}{\epsilon}Z\right)$, and $u_0\left(\frac{\delta}{\epsilon}Z\right)$ we find that the lowest-order stratification terms are of order δ (they arise from $\epsilon \times \frac{\delta}{\epsilon}Z$). Since $\delta \ll \epsilon^2$ these terms are still not involved in the order ϵ and ϵ^2 we are retaining below. Furthermore, the gravity term on the right-hand side of equation (5.37) is equal to $-\epsilon\delta\bar{\rho}$ is and hence also negligible.

We assume that in this region perturbations are represented by the asymptotic expansions

$$\bar{\rho}(\xi, Z) \sim \rho_1 + \epsilon\rho_2 + O(\epsilon^2), \tag{5.40}$$

$$\bar{p}(\xi, Z) \sim p_1 + \epsilon p_2 + O(\epsilon^2), \tag{5.41}$$

$$\bar{u}(\xi, Z) \sim u_1 + \epsilon u_2 + O(\epsilon^2), \tag{5.42}$$

$$\bar{v}(\xi, Z) \sim v_1 + \epsilon v_2 + O(\epsilon^2). \tag{5.43}$$

We insert the asymptotic expansions (5.40)–(5.43) in equations (5.35)–(5.38) and we obtain at order ϵ

$$\rho_{1\xi} + u_{1\xi} - B_0 v_{1\xi} = 0, \tag{5.44}$$

$$p_{1\xi} + \gamma M_0^2 u_{1\xi} = 0, \tag{5.45}$$

$$-B_0 p_{1\xi} + \gamma M_0^2 v_{1\xi} = 0, \tag{5.46}$$

$$p_{1\xi} - \gamma\rho_{1\xi} = 0. \tag{5.47}$$

At order ϵ^2 we obtain

$$\rho_{2\xi} + u_{2\xi} - B_0 v_{2\xi} = -\{\rho_1(u_1 - B_0 v_1)\}_\xi - v_{1Z}, \tag{5.48}$$

$$p_{2\xi} + \gamma M_0^2 u_{2\xi} = -\gamma M_0^2\left((u_1 - B_0 v_1)u_{1\xi} + \rho_1 u_{1\xi}\right), \tag{5.49}$$

$$-B_0 p_{2\xi} + \gamma M_0^2 v_{2\xi} = -\gamma M_0^2\left((u_1 - B_0 v_1)v_{1\xi} + \rho_1 v_{1\xi}\right) - p_{1Z}, \tag{5.50}$$

$$p_{2\xi} - \gamma\rho_{2\xi} = -\rho_1 p_{1\xi} + \gamma p_1\rho_{1\xi} - (u_1 - B_0 v_1)p_{1\xi} + \gamma(u_1 - B_0 v_1)\rho_{1\xi}. \tag{5.51}$$

The order ϵ equations (5.44)–(5.47) constitute a linear system of three equations in four unknowns. Therefore we can express v_1, p_1 and ρ_1 as functions of the undetermined function $u_1(\xi, Z)$ as follows

$$v_1 = -B_0 u_1, \quad p_1 = -\gamma M_0^2 u_1, \quad \rho_1 = -M_0^2 u_1. \tag{5.52}$$

We note that expressions (5.52) are identical to (5.24).

In order to determine u_1 we need to go to order ϵ^2. We use (5.52) in the right-hand side of equations (5.48)–(5.51) to express all terms as a function of this undetermined

solution $u_1(\xi, Z)$. We obtain

$$\rho_{2\xi} + u_{2\xi} - B_0 v_{2\xi} = B_0 u_{1Z} + 2M_0^4 u_1 u_{1\xi}, \tag{5.53}$$

$$p_{2\xi} + \gamma M_0^2 u_{2\xi} = 0, \tag{5.54}$$

$$-B_0 p_{2\xi} + \gamma M_0^2 v_{2\xi} = \gamma M_0^2 u_{1Z}, \tag{5.55}$$

$$p_{2\xi} - \gamma \rho_{2\xi} = \gamma(\gamma - 1) M_0^4 u_1 u_{1\xi}. \tag{5.56}$$

Comparing the order ϵ^2 system in the middle region (5.53)–(5.56) with the order ϵ^2 system in the inner region (5.29)–(5.32) we find that the rescaling of z has led to the appearance of two more terms in the right-hand side of the former; $B_0 u_{1Z}$ in the continuity equation (5.53) and $-p_{1Z} = \gamma M_0^2 u_{1Z}$ in the Z-momentum equation (5.55). These terms are precisely the ones that will balance the nonuniform terms of the form $u_1 u_{1\xi}$. Also it is this aforementioned ascent of terms from order ϵ to order ϵ^2 that renders the system at order ϵ indeterminate in the middle region.

For the order ϵ^2 system (5.53)–(5.56) to have a solution a consistency condition needs to be satisfied, given by the linear combination of equations (5.53)–(5.56)

$$\gamma M_0^2 (5.53) - (5.54) + B_0 (5.55) + M_0^2 (5.56). \tag{5.57}$$

This (upon division by the factor $2\gamma M_0^2 B_0$) leads to the KWE

$$u_{1Z} + \frac{\gamma + 1}{2B_0} M_0^4 u_1 u_{1\xi} = 0, \tag{5.58}$$

which is equation (4.60) of the previous chapter (upon dropping the superscript from u_1^o).

In the previous chapter we showed that for a general (concave) thickness function $G(x)$ (see Figure 4.4), the solution of (5.58) is an N-wave asymptotically (see Figure 4.8). However we note that for the current scenario stratification effects come in at distances L/δ and the signature may not have attained its asymptotic form by then. In the next section we will derive a KWE with nonconstant coefficients and a non-zero right-hand side that governs the wavefield behaviour in the outer region, to leading order.

5.2.3 Outer region (far-field)

We now investigate the outer region where nonlinearity and stratification effects are both of order 1: since z will be of order $1/\delta$ the appropriately rescaled vertical variable is $\tilde{z} = \delta z$. In the horizontal direction, the deviation of (x, z) from the linear acoustic

characteristic through $(0,0)$ is $\xi = x - \int_0^z B(s)ds$ where B is the Prandtl-Glauert parameter in the outer region

$$B(\tilde{z}) = \sqrt{M_0^2 u_0^2(\tilde{z}) \frac{\rho_0(\tilde{z})}{p_0(\tilde{z})} - 1}, \tag{5.59}$$

We have seen that in the middle region the deviation of the nonlinear characteristics from the linear is of order ϵ when the vertical coordinate is of order 1. Therefore in the outer region we expect ξ to be of order ϵ/δ. So we choose our scaled horizontal variable to be $\zeta = \delta\xi/\epsilon$. Note that B is now a function of $\tilde{z}$ and we shall restrict attention to the hyperbolic region where B is real. In this outer region the gradients of the ambient quantities are of order 1. With these scalings we are still near the leading shock and far from the aerofoil since $\xi/z = \epsilon\zeta/\tilde{z} \ll 1$. It is helpful to note that the partial derivatives in terms of the new variables are $\dfrac{\partial}{\partial x} = \dfrac{\delta}{\epsilon}\dfrac{\partial}{\partial \zeta}$ and $\dfrac{\partial}{\partial z} = \delta\dfrac{\partial}{\partial \tilde{z}} - \dfrac{\delta}{\epsilon}B\dfrac{\partial}{\partial \zeta}$.

We first rescale equations (5.7)–(5.10) to obtain their new form in terms of ζ and $\tilde{z}$. It is not worthwhile to present all the resulting cumbersome equations. We will present only the rescaled form of equation (5.9) in order to discuss the gravity terms:

$$\delta(-B\bar{p}_\zeta + \gamma M_0^2 \rho_0 u_0 \bar{v}_\zeta) + \epsilon\delta(\bar{p}_{\tilde{z}} + \gamma M_0^2(\rho_0(\bar{u} - B\bar{v})\bar{v}_\zeta + u_0\bar{\rho}\bar{v}_\zeta)) + O(\epsilon^2\delta) = -\epsilon\delta\bar{\rho} \tag{5.60}$$

We assume, as usual, that the perturbations in the outer region are represented by the following asymptotic expansions

$$\bar{\rho}(\zeta,\tilde{z}) \sim \rho_1 + \epsilon\rho_2 + O(\epsilon^2)), \tag{5.61}$$

$$\bar{p}(\zeta,\tilde{z}) \sim p_1 + \epsilon p_2 + O(\epsilon^2)), \tag{5.62}$$

$$\bar{u}(\zeta,\tilde{z}) \sim u_1 + \epsilon u_2 + O(\epsilon^2)), \tag{5.63}$$

$$\bar{v}(\zeta,\tilde{z}) \sim v_1 + \epsilon v_2 + O(\epsilon^2)). \tag{5.64}$$

From (5.60) and (5.61) we conclude that the gravity term $\epsilon\delta\rho_1$ will appear in the order $\epsilon\delta$ order of the analysis.

We obtain at order δ the system

$$u_0\rho_{1\zeta} + \rho_0 u_{1\zeta} - B\rho_0 v_{1\zeta} = 0, \tag{5.65}$$

$$p_{1\zeta} + \gamma M_0^2 u_0 \rho_0 u_{1\zeta} = 0, \tag{5.66}$$

$$-Bp_{1\zeta} + \gamma M_0^2 u_0 \rho_0 v_{1\zeta} = 0, \tag{5.67}$$

$$p_{1\zeta} - \gamma\frac{p_0}{\rho_0}\rho_{1\zeta} = 0. \tag{5.68}$$

Equations (5.65)–(5.68) can be solved in terms of u_1 as

$$v_{1\zeta} = -Bu_{1\zeta}, \tag{5.69}$$

$$p_{1\zeta} = -\gamma M_0^2 \rho_0 u_0 u_{1\zeta}, \tag{5.70}$$

$$\rho_{1\zeta} = -M_0^2 \rho_0^2 \frac{u_0}{p_0} u_{1\zeta}. \tag{5.71}$$

Integrating (5.69)–(5.71) with respect to ζ we obtain the relations

$$v_1 = -Bu_1(\zeta, \tilde{z}), \quad p_1 = -\gamma M_0^2 \rho_0 u_0 u_1(\zeta, \tilde{z}), \quad \rho_1 = -M_0^2 \rho_0^2 \frac{u_0}{p_0} u_1(\zeta, \tilde{z}), \tag{5.72}$$

where u_1 is an undetermined function that will be determined at order $\epsilon\delta$. At order $\epsilon\delta$ we obtain the system

$$u_0\rho_{2\zeta} + \rho_0(u_{2\zeta} - Bv_{2\zeta}) = -\{\rho_1(u_1 - Bv_1)\}_\zeta - (\rho_0 v_1)_{\tilde{z}}, \tag{5.73}$$

$$p_{2\zeta} + \gamma M_0^2 \rho_0 u_0 u_{2\zeta} = -\gamma M_0^2 \left(v_1 \rho_0 u_{0\tilde{z}} + \rho_0(u_1 - Bv_1)u_{1\zeta} + u_0\rho_1 u_{1\zeta}\right), \tag{5.74}$$

$$-Bp_{2\zeta} + \gamma M_0^2 \rho_0 u_0 v_{2\zeta} = -p_{1\tilde{z}} - \gamma M_0^2 \left(\rho_0(u_1 - Bv_1)v_{1\zeta} + u_0\rho_1 v_{1\zeta}\right) - \rho_1, \tag{5.75}$$

$$u_0\rho_0 \left(p_{2\zeta} - \gamma \frac{p_0}{\rho_0}\rho_{2\zeta}\right) = (\gamma p_0 \rho_{0\tilde{z}} - \rho_0 p_{0\tilde{z}})v_1 - p_{1\zeta}(\rho_0(u_1 - Bv_1) + u_0\rho_1) + \gamma\rho_{1\zeta}(p_0(u_1 - Bv_1) + u_0 p_1). \tag{5.76}$$

We use relations (5.72) to express the right-hand side of the equations (5.73)–(5.76) in terms of u_1 and we obtain

$$u_0\rho_{2\zeta} + \rho_0(u_{2\zeta} - Bv_{2\zeta}) = 2M_0^4 \frac{\rho_0^3 u_0^3}{p_0^2} u_1 u_{1\zeta} + (\rho_0 B u_1)_{\tilde{z}}, \tag{5.77}$$

$$p_{2\zeta} + \gamma M_0^2 \rho_0 u_0 u_{2\zeta} = \gamma M_0^2 \rho_0 u_{0\tilde{z}} B u_1, \tag{5.78}$$

$$-Bp_{2\zeta} + \gamma M_0^2 \rho_0 u_0 v_{2\zeta} = \gamma M_0^2 (\rho_0 u_0 u_1)_{\tilde{z}} + M_0^2 \rho_0^2 \frac{u_0}{p_0} u_1, \tag{5.79}$$

$$p_{2\zeta} - \gamma \frac{p_0}{\rho_0}\rho_{2\zeta} = \gamma(\gamma - 1) M_0^4 \frac{\rho_0^2 u_0^2}{p_0} u_1 u_{1\zeta} + \frac{B}{u_0}\left(p_{0z} - \gamma \frac{p_0}{\rho_0}\rho_{0\tilde{z}}\right) u_1. \tag{5.80}$$

For the order $\epsilon\delta$ system (5.77)–(5.80) to have a solution, a consistency condition needs to be satisfied. This is given by the linear combination

$$\gamma M_0^2 u_0 (5.77) - (5.78) + B(5.79) + M_0^2 u_0^2 \frac{\rho_0}{p_0} (5.80), \tag{5.81}$$

which leads to the following KWE for u_1 (upon division by the factor $2\gamma M_0^2 u_0 \rho_0 B$ and using $p_{0\tilde{z}} = -\rho_0$):

$$u_{1\tilde{z}} + \frac{\gamma + 1}{2B} M_0^4 u_0^3 \frac{\rho_0^2}{p_0^2} u_1 u_{1\zeta} = -\frac{1}{2}\frac{(\rho_0 B)_{\tilde{z}}}{\rho_0 B} u_1. \tag{5.82}$$

Generally we need to solve the KWE numerically; either through the method of characteristics or through a numerical scheme applied directly to the equation.

Applying the method of characteristics to equation (5.82) we have that u_1 obeys the ODE

$$\frac{du_1}{d\tilde{z}} = -\frac{1}{2}\frac{(\rho_0 B)_{\tilde{z}}}{\rho_0 B}u_1 \tag{5.83}$$

on the characteristics defined by the slope

$$\frac{d\zeta}{d\tilde{z}} = \frac{\gamma+1}{2B}M_0^4 u_0^3 \frac{\rho_0^2}{p_0^2}u_1. \tag{5.84}$$

Solving (5.83) we can deduce that along the characteristics u_1 varies according to simple relation

$$u_1 = A_1(\rho_0 B)^{-1/2}, \tag{5.85}$$

along each characteristic

$$\zeta - \frac{\gamma+1}{2}M_0^4 \int_0^{\tilde{z}} \frac{u_0^3(s)\rho_0^2(s)}{B(s)p_0^2(s)}u_1 ds = \zeta_0. \tag{5.86}$$

Substituting u_1 from (5.85) in (5.86) we obtain

$$\zeta - \frac{\gamma+1}{2}M_0^4 A_1(\zeta_0)\int_0^{\tilde{z}} \frac{u_0^3\rho_0^2}{B(s)p_0^2}(\rho_0 B)^{-1/2}ds = \zeta_0. \tag{5.87}$$

Note that the amplitude expression (5.85) becomes infinite when $B = 0$, at the sonic *height*, where the source speed relative to the wind is equal to the sound speed. This indicates that the asymptotic procedure breaks down there. A fourth region needs to be introduced with B taken as a third small parameter. Pechuzal and Kevorkian [91] have undertaken this for the simpler case of a uniform medium that has a horizontal linearly stratified wind. They deduced that the consistent approximation of the Euler equations in this sonic region is a nonlinear Tricomi equation. It remains an open question what is the analogous equation in our scenario.

Matching

The middle-region solution, in the region between the shocks, is given by

$$u^{(m)} = -\frac{G'(\xi_0)}{B_0} \text{ where } \xi_0 = \xi - Du^{(m)}Z, \quad D = \frac{(\gamma+1)M_0^4}{2B_0}. \tag{5.88}$$

To match the outer region solution with the middle region we multiply the outer region expression (5.87) by ϵ/δ and also write $\tilde{z} = \frac{\delta}{\epsilon}Z$: we have

$$\tilde{\xi} - \frac{\epsilon}{\delta}A_1 D \int_0^{\frac{\delta}{\epsilon}Z} F(s)ds = \xi_0 \tag{5.89}$$

where $F(s) = \frac{B_0 u_0^3 \rho_0^2}{B p_0^2}(\rho_0 B)^{-1/2}$. In (5.89), since the upper limit $\frac{\delta}{\epsilon}Z$ is small, we can expand the integrand $F(s)$ in a Taylor series. From this Taylor series we then retain the leading term $F(0) = 1/\sqrt{B_0}$. As we tend to the middle region, since $\tilde{\xi} \to \xi$, (5.89) becomes

$$\xi - \frac{A_1}{\sqrt{B_0}}DZ = \xi_0. \tag{5.90}$$

Comparing (5.90) and (5.88) we conclude that $A_1 = -G'/\sqrt{B_0}$.

The characteristic expression (5.86) incorporates both stratification and nonlinear effects. Therefore it would provide a way to quantify the error in the linear theory which was employed in Chapter 3 to calculate the path of secondary sonic boom propagation.

Summarising our results: in the near-field and the mid-field, to leading order, the analysis turned out to be equivalent to that of Chapter 4, but in the far-field an inhomogeneous KWE arose that accounted also for order 1 stratification effects. Therefore we can say that, at leading order, shocks are formed as in a uniform medium and then get affected by stratification. This might have not been the case if we had looked at a different balance of δ and ϵ.

Finally we note that in the approximations of the Euler equations presented above there is no direct excitation of gravity waves, even though the motion takes place in a gravitationally stratified atmosphere. This is so because, at the order we are working to, the sound waves are decoupled from gravity waves as the wavenumber $1/L$ is large compared with $1/H$. This condition for decoupling is given by Lighthill—see [72], Section 4.2, expression (29), p. 291.

Chapter 6

Acceleration and deceleration through the sound speed, manoeuvres

6.1 Introduction

In this chapter we return to the framework of linear acoustics introduced in Chapter 3. We will determine the wavefront pattern, Mach envelope, and the pressure field due to a point source moving in a stationary uniform medium. Our analysis will be based on the linearised gas dynamics equations, reduced to a single equation for pressure. We are going to deal with the following types of motion that are of interest in sonic boom research: steady motion, motions with acceleration and deceleration through the sound speed, and manoeuvres.

The chapter is divided into two parts: two-dimensional problems and three-dimensional problems. For the purposes of determining the geometry this distinction in the dimension is not important if the source moves in a straight line, since the three-dimensional geometrical pattern is obtained simply by revolution of the two-dimensional geometrical pattern about the axis of the source motion. However, as we will see there are fundamental differences in the corresponding wavefield, due to the differences in the Riemann function.

In two dimensions we will solve the steady motion problem (Section 6.2.2), the constant acceleration problem (Section 6.2.3) and the constant deceleration problem (Section 6.2.4). Even though for the steady motion problem closed-form solutions can be found almost trivially, such solutions cannot be found for accelerating and decelerating motions in general. In the case of constant acceleration and constant deceleration motions closed-form solutions can be found in terms of standard elliptic

integrals but we will not do this here; we will present instead a simple method of approximation for obtaining a closed-form expression for the wavefield near the Mach envelope, in the *time domain*.

In three dimensions, we will also solve the steady motion problem exactly, and then modify the method of approximation developed for two dimensions to calculate the wavefield near the Mach envelope.

The linearised gas dynamics equations, presented in Chapter 3, for a stationary, uniform ambient medium with sources reduce to a scalar equation for pressure

$$\boldsymbol{\nabla}^2 p - \frac{1}{c_0^2}\frac{\partial^2 p}{\partial t^2} = -\rho_0 \frac{\partial q}{\partial t} = -\gamma(\mathbf{x}, t), \tag{6.1}$$

where q is the time rate of change of the volume excluded from the fluid by the source per unit volume. In order to obtain the source term in the right-hand side of equation (6.1) we have replaced the zero in the right-hand side of the linearised mass conservation equation by $\rho_0 q$. The initial conditions to be imposed are

$$p = 0, \quad \frac{\partial p}{\partial t} = 0 \text{ at } t = 0. \tag{6.2}$$

The Riemann function $G(\mathbf{x}, t; \mathbf{x}_0, \tau)$ corresponding to a unit point impulsive source satisfies

$$\boldsymbol{\nabla}^2 G - \frac{1}{c_0^2}\frac{\partial^2 G}{\partial t^2} = -\delta(t-\tau)\delta(\mathbf{x}-\mathbf{x}_0), \tag{6.3}$$

where $\mathbf{x}_0 = (x_0, y_0, z_0)$. From causality considerations G and $\dfrac{\partial G}{\partial t}$ are zero for $t < \tau$. Therefore in free space, in three dimensions the Riemann function is

$$G_3(\mathbf{x}, t; \mathbf{x}_0, \tau) = \frac{\delta(t - \tau - R/c_0)}{4\pi R}, \tag{6.4}$$

where $R = |\mathbf{x} - \mathbf{x}_0|$ (see [85]). The disturbance due to the source propagates with speed c_0 on the wavefronts

$$Q_3 = c_0^2(t-\tau)^2 - R^2 = 0, \tag{6.5}$$

in the region $t > \tau$. Therefore the disturbance arrives at an observation point distance R away from the source at time R/c_0 after it was emitted; it then ceases instantaneously. By the superposition principle, the solution to (6.1) is given by

$$p = \iiiint G_3(\mathbf{x}, t; \mathbf{x}_0, \tau)\gamma(\mathbf{x}_0, \tau) dx_0 dy_0 dz_0 d\tau. \tag{6.6}$$

This integral extends over all $\mathbf{x}_0$ and τ but of course the integrand is zero when $t < \tau$ (since $G_3 = 0$ then) and when $\mathbf{x}_0$ lies outside the source region $S(\tau)$ at time τ (since there $\gamma = 0$). So the integral could alternatively be written as restricted to $\tau < t$ and $\mathbf{x}_0$ in $S(\tau)$.

From (6.4) and evaluating the τ-integral in (6.6) we find that a solution of (6.1) is

$$p = \iiint \frac{\gamma(\mathbf{x}_0, t - R/c_0)}{4\pi R} dx_0 dy_0 dz_0, \tag{6.7}$$

the well-known "retarded potential" solution [85].

Note that we can also introduce a velocity potential ϕ through the relation $p = -\rho_0 \dfrac{\partial \phi}{\partial t}$. We then obtain, from (6.1), the inhomogeneous potential equation

$$\boldsymbol{\nabla}^2 \phi - \frac{1}{c_0^2} \frac{\partial^2 \phi}{\partial t^2} = q(\mathbf{x}, t), \tag{6.8}$$

with initial conditions

$$\phi = 0, \quad \frac{\partial \phi}{\partial t} = 0 \text{ at } t = 0. \tag{6.9}$$

The solution is then (using (6.7)) given by

$$\phi = -\iiint \frac{q(\mathbf{x}_0, t - R/c_0)}{4\pi R} dx_0 dy_0 dz_0. \tag{6.10}$$

In two dimensions (x and y), the Riemann function is

$$G_2(x, y, t; x_0, y_0, \tau) = \frac{c_0}{2\pi} \frac{H(Q_2) H(t - \tau)}{\sqrt{Q_2(x, y, t; x_0, y_0, \tau)}}, \tag{6.11}$$

where

$$Q_2 = c_0^2 (t - \tau)^2 - (x - x_0)^2 - (y - y_0)^2, \tag{6.12}$$

and H stands for the Heaviside function.[1] The presence of the Heaviside function ensures that G_2 takes only real values. The wavefronts are the circles $Q_2 = 0$ and the

[1] We can determine G_2 either by solving equation (6.3) directly or by evaluating

$$G_2(x, y) = \int_{-\infty}^{\infty} G_3(x, y, z) dz = \int_{-\infty}^{\infty} \frac{\delta(g(z))}{4\pi R} dz,$$

where $g(z) = t - \tau - R(z)/c_0$. Therefore $G_2 = 0$ when $Q_2 < 0$, and when $Q_2 > 0$, using the integration property of the δ function,

$$G_2 = \sum \frac{1}{4\pi R(z) |g'(z_R)|}, \tag{6.13}$$

disturbance does not cease instantaneously after it arrives at an observation point; since $G_2 \sim \dfrac{1}{2\pi t}$ as $t \to \infty$ the disturbance decays to zero only as $t \to \infty$ (this is the so-called tail of the cylindrical waves). Due to its tail G_2 is very different from G_3. A nice discussion of dimensionality and the wave equation appears in Ockendon et al. [82], Section 4.6.8.

The general solution for the two-dimensional problem is therefore (by superposition of terms of the form (6.11))

$$p(x, y, t) = \iiint G_2(x, y, t; x_0, y_0, \tau)\gamma(x_0, y_0, \tau)dx_0 dy_0 d\tau, \tag{6.15}$$

where again the integrand is zero when $t < \tau$ (since $G_2 = 0$ then) and when $\mathbf{x}_0$ lies outside the source region at time τ (since there $\gamma = 0$).

6.2 Two-dimensional problems

We will first consider two-dimensional problems (and we take the independent variables to be x and z). For a point source of unit strength moving on the path $(x_0(t), z_0(t))$, from (6.15), the pressure field $p(x, z, t)$ is

$$p(x, z, t) = \frac{c_0}{2\pi} \int_{-\infty}^{t} \frac{H(Q(\tau))d\tau}{\sqrt{Q(\tau)}}, \tag{6.16}$$

where Q is given by (6.12) (dropping the subscript).

6.2.1 Mach envelope equations for any unsteady motion

Below we derive the parametric equations for the Mach envelope for any unsteady motion in a uniform medium, by seeking the envelope of the wavefronts $Q(\tau) = 0$. We thus set $\dfrac{\partial Q}{\partial \tau} = 0$ in (6.12) and this leads to the relation

$$x_0'(x - x_0(\tau)) + z_0'(z - z_0(\tau)) - c_0^2(t - \tau) = 0, \tag{6.17}$$

where the dash denotes differentation with respect to τ. Solving (6.17) for $(x - x_0)$ we have

$$x_0'(x - x_0) = c_0^2(t - \tau) - z_0'(z - z_0), \tag{6.18}$$

summed over $z_R = \pm\sqrt{Q_2}$ for which $g(z_R) = 0$. This leads to

$$G_2 = \sum_{z_R = \pm\sqrt{Q_2}} \frac{c_0}{4\pi|z_R|} = \frac{c_0}{2\pi\sqrt{Q_2}}. \tag{6.14}$$

For a more geometrical derivation see also Whitham [126] pp. 234–235.

and substituting into $Q = 0$ we obtain the quadratic in $(z - z_0)$

$$(z - z_0)^2({x_0'}^2 + {z_0'}^2) - 2z_0' c_0^2 (t - \tau)(z - z_0) + c_0^2 (t - \tau)^2 (c_0^2 - {x_0'}^2) = 0. \tag{6.19}$$

This gives

$$z - z_0 = \frac{c_0(t - \tau)}{{x_0'}^2 + {z_0'}^2} \left(c_0 z_0' \pm x_0' \sqrt{{x_0'}^2 + {z_0'}^2 - c_0^2} \right), \tag{6.20}$$

which is real only if ${x_0'}^2 + {z_0'}^2 > c_0^2$, that is for supersonic parts of the motion. Equation (6.20) gives an expression for z in terms of the parameter τ. The analogous parametric expression for x in terms of the parameter τ is

$$x - x_0 = \frac{c_0(t - \tau)}{{x_0'}^2 + {z_0'}^2} \left(c_0 x_0' \mp z_0' \sqrt{{x_0'}^2 + {z_0'}^2 - c_0^2} \right). \tag{6.21}$$

When the motion is on a straight line with $z_0 = 0$ the parametric expressions (6.20) and (6.21) simplify to

$$x - x_0(\tau) = \frac{c_0^2 (t - \tau)}{x_0'}, \tag{6.22}$$

$$z = \pm \frac{c_0(t - \tau)}{x_0'} \sqrt{{x_0'}^2(\tau) - c_0^2}. \tag{6.23}$$

6.2.2 Steady motion

6.2.2.1 Supersonic motion

Starting from the simplest example, we are going to determine the wavefield for steady motion in a straight line. To make the problem more realistic, we consider a finite-start problem in which there is no source before $t = 0$, and $x_0(t) = -Ut$ for $t \geq 0$, with $U > c_0$. The wavefronts emitted for $t \geq 0$ form an envelope which is the truncated Mach wedge

$$X^2 = B_0^2 z^2, \quad 0 \leq X \leq \frac{c_0^2 B_0^2 t}{U},$$

where $X = x + Ut$ is the travelling coordinate. Note that for a source moving for an *infinite* time with constant speed the Mach wedge extends to infinity ($X \geq 0$), as we have seen in Chapter 3. Since all the sound from the source is located inside the region defined by the initial wavefront and the Mach envelope, as plotted in Figure 6.1, the pressure p is zero outside this region.

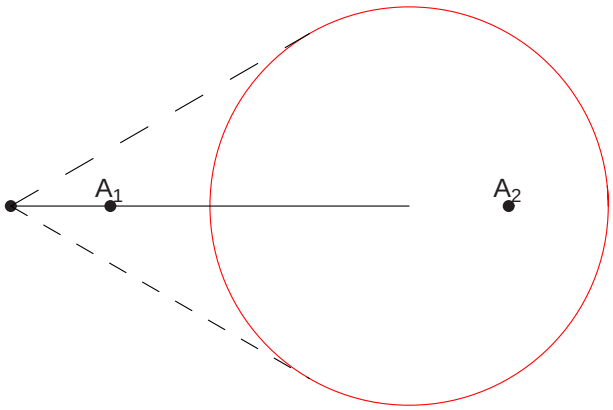

Figure 6.1: Schematic of the Mach wedge and the initial wavefront (IW). The point A_1 is outside the IW and A_2 is inside the IW. (The horizontal line represents the path of the source.)

Below we determine the wavefield inside the region. Setting $x_0(\tau) = -U\tau$ and $z_0 = 0$ in (6.12) we have

$$Q = -(U^2 - c_0^2)\tau^2 - 2\tau(xU + c_0^2 t) - (x^2 + z^2 - c_0^2 t^2). \tag{6.24}$$

Therefore Q is a quadratic in τ with roots τ_1 and τ_2 given by

$$c_0^2 B_0^2 \tau_{1,2} = -(xU + c_0^2 t) \pm c_0 \sqrt{(x + Ut)^2 - B_0^2 z^2}. \tag{6.25}$$

where τ_1 corresponds to the negative sign in front of the square root and τ_2 to the positive sign. We now consider a control point $A = (x, z)$. Since A is inside the Mach wedge both τ_1 and τ_2 are real and distinct. (When A is *on* the Mach wedge, τ_1 and τ_2 coincide.)

When A is outside the initial wavefront (IW) we have $0 < \tau_1 < \tau_2$, but when A is inside the IW, τ_1 becomes negative. Below we plot Q at two points (inside the Mach wedge) in order to exhibit the transition in the sign of the roots: the left picture shows Q for the point $A_1 = (-(U + c_0)t/2, 0)$ outside the IW, and the right picture shows Q for the point $A_2 = (-(c_0 - U)t/2, 0)$ inside the IW.
The pressure field $p(x, z, t)$ outside the IW is given by

$$\frac{2\pi}{c_0} p(x, z, t) = \int_{\tau_1}^{\tau_2} \frac{d\tau}{\sqrt{Q(\tau)}}, \tag{6.26}$$

and from (6.24) we have

$$2\pi B_0 p(x, z, t) = \int_{\tau_1}^{\tau_2} \frac{d\tau}{\sqrt{(\tau_2 - \tau)(\tau - \tau_1)}}, \tag{6.27}$$

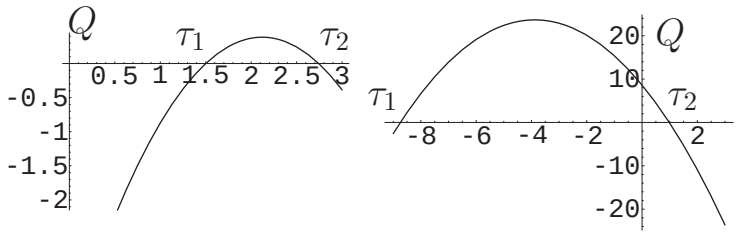

Figure 6.2: The quadratic Q at two points inside the Mach wedge, A_1 outside the IW (left plot) and $A = A_2$ (right plot). The points A_1 and A_2 are shown in Figure 6.1. On the left plot both roots of Q are positive but on the right plot τ_1 has become negative. (We have chosen $c_0 = 1$, $U = \sqrt{2}$, $t = 3$.)

where τ_1 and τ_2 are given by (6.25). Performing the transformation

$$\tau = \tau_1 \cos^2\theta + \tau_2 \sin^2\theta, \tag{6.28}$$

we have $\tau = \tau_1 \Rightarrow \theta_1 = 0$, and $\tau = \tau_2 \Rightarrow \theta_2 = \pi/2$. Therefore the integral (6.27) gives the simple expression

$$p = \frac{1}{2B_0}. \tag{6.29}$$

We conclude that the wavefield is *constant* for all points inside the Mach wedge and outside the IW. The pressure field p_{0s} inside the IW is given by

$$2\pi B_0 p_{0s}(x,z,t) = \int_0^{\tau_2} \frac{d\tau}{\sqrt{(\tau_2-\tau)(\tau-\tau_1)}}, \tag{6.30}$$

and is not constant as shown below. Performing again the transformation (6.28) we find $\theta_2 = \pi/2$ but $\theta_1 = \frac{1}{2}\arccos\left(\frac{\tau_2+\tau_1}{\tau_2-\tau_1}\right)$. Therefore (6.30) becomes

$$2\pi B_0 p_{0s}(x,z,t) = 2(\theta_2 - \theta_1) = \pi - \arccos\left(\frac{\tau_2+\tau_1}{\tau_2-\tau_1}\right), \tag{6.31}$$

where

$$\frac{\tau_2+\tau_1}{\tau_2-\tau_1} = -\frac{xU + c_0^2 t}{c_0\sqrt{(x+Ut)^2 - B_0^2 z^2}}. \tag{6.32}$$

Therefore

$$p_{0s}(x,z,t) = \frac{1}{2B_0} - \frac{1}{2\pi B_0}\arccos\left(-\frac{xU + c_0^2 t}{c_0\sqrt{(x+Ut)^2 - B_0^2 z^2}}\right), \tag{6.33}$$

$$= \frac{1}{2\pi B_0}\arccos\left(\frac{xU + c_0^2 t}{c_0\sqrt{(x+Ut)^2 - B_0^2 z^2}}\right). \tag{6.34}$$

Note that p_{0s} joins continuously to p since $p_{0s} = p$ implies $\tau_1 = 0$ which is the value of τ for points on the IW. At the points $(x = -c_0^2 t/U, z = \pm t/M_0)$, where the IW meets the Mach wedge both the numerator and denominator in the right-hand side of (6.32) are zero and there is a discontinuity. Figure 6.3 superimposes $2\pi p$ and $2\pi p_{0s}$ $(U = \sqrt{2}, c_0 = 1, t = 3)$.

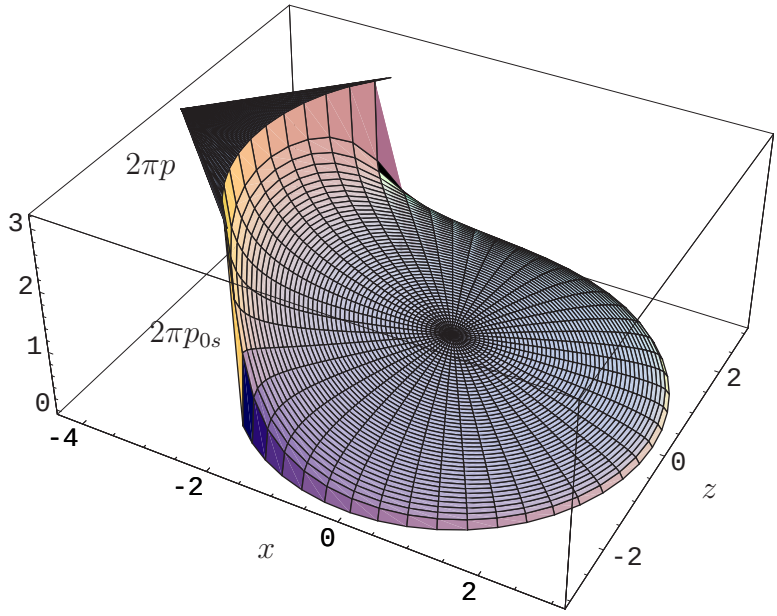

Figure 6.3: Plot of $2\pi p_{0s}$ where p_{0s} is the wavefield inside the IW when the point source travels with constant speed from right to left, $U = \sqrt{2}$,$c_0 = 1$,$t = 3$.

6.2.2.2 Subsonic motion

Since we are going to examine subsequently acceleration and deceleration through the sound speed it is also useful to determine the geometry and the wavefield for a subsonic steady motion.

We assume again a finite start with the source "switched on" at $t = 0$. Since in subsonic motion all wavefronts are nested, at any time instant $t_0 > 0$ all the disturbance is found inside the IW $x^2 + z^2 = c_0^2 t_0^2$. The expression for the quadratic Q is again (6.24) but now, since $c_0 > U$, Q has a minimum and not a maximum. We define $\beta_0^2 = 1 - U^2/c_0^2$ and then the two roots of Q are given by

$$c_0^2 \beta_0^2 \tau_{1,2} = (xU + c_0^2 t) \pm c_0 \sqrt{(x + Ut)^2 + \beta_0^2 z^2}, \tag{6.35}$$

where τ_1 is the root corresponding to the negative sign and τ_2 the root corresponding to the positive sign.

Since $(x+Ut)^2+\beta_0^2 z^2 > 0$ for any point (x,z), the roots are always real and distinct. This is equivalent to $\dfrac{\partial Q}{\partial \tau}$ not becoming zero (and consistent with the fact that in subsonic motions no envelope of the wavefronts can be formed). The only exception to this is the source position $x=-Ut, z=0$ where $\dfrac{\partial Q}{\partial \tau}$ and the roots coalesce. Furthermore, when the point (x,z) is inside the IW the product and sum of the roots are both positive so the roots are both positive.

Moreover, since the wavefronts are nested there is a unique τ_1, satisfying $0<\tau_1<t$, at which $Q=0$. Using this geometrical information the wavefield integral (6.7) becomes

$$p_{\text{sub}}(x,z,t)=\frac{c_0}{2\pi}\int_0^{\tau_1}\frac{d\tau}{\sqrt{Q}}=\frac{1}{2\pi\beta_0}\int_0^{\tau_1}\frac{d\tau}{\sqrt{(\tau_1-\tau)(\tau_2-\tau)}}. \tag{6.36}$$

This can be calculated exactly if we let $\tau=\tau_1\cosh^2 u-\tau_2\sinh^2 u$; we get

$$p_{\text{sub}}(x,z,t)=\frac{1}{\pi\beta_0}\int_{-u_L}^{0}du=\frac{1}{\pi\beta_0}u_L, \tag{6.37}$$

$$\text{where } u_L=\frac{1}{2}\cosh^{-1}\left(\frac{\tau_1+\tau_2}{\tau_2-\tau_1}\right) \text{ and } \frac{\tau_1+\tau_2}{\tau_2-\tau_1}=\frac{xU+c_0^2 t}{c_0\sqrt{(x+Ut)^2+\beta_0^2 z^2}}. \tag{6.38}$$

From the last expression we find, as expected, that the wavefield is infinite at the source.

In order to see the precise nature of the singularity, we consider points near the source, with $x=-Ut+r\cos\phi$, $z=r\sin\phi$ where r is small. From (6.35) we have

$$c_0^2\beta_0^2\tau_{1,2}=c_0^2\beta_0^2 t+rU\cos\phi\pm rc_0\sqrt{\cos^2\phi+\beta_0^2\sin^2\phi}. \tag{6.39}$$

Using (6.39) in (6.37)–(6.38) we obtain

$$p_{\text{source}}=\frac{1}{2\pi\beta_0}\cosh^{-1}\left(\frac{c_0^2\beta_0^2 t+rU\cos\phi}{c_0 r\sqrt{\cos^2\phi+\beta_0^2\sin^2\phi}}\right). \tag{6.40}$$

Therefore as $r\to 0$ we have

$$p_{\text{source}}\sim\frac{1}{2\pi\beta_0}\ln\left(\frac{2tc_0\beta_0^2}{r\sqrt{\cos^2\phi+\beta_0^2\sin^2\phi}}\right), \tag{6.41}$$

which gives a logarithmic singularity as $r\to 0$. The analogous three-dimensional calculation can be found in Goldstein [44] pp. 45–50.

6.2.3 Acceleration through the sound speed

We now consider a point source accelerating through the sound speed—a problem of great interest in sonic boom research since any supersonic vehicle must do this. Flight tests, recorded in [123], indicate that acceleration through the sound speed leads to the formation of a focused boom with amplitudes 2 to 5 times that of a primary boom. It is a well-known fact in the early sonic boom literature that an envelope of boomrays is formed during such a motion. In agreement with the more recent sonic boom literature and the earlier parts of this thesis we will be calling this envelope of boomrays a fold caustic. This fold caustic corresponds to the formation of a cusp on the Mach envelope. These cusps had been reported as novel features in the 1953 paper by Lilley et al. [73] and their position had been determined there.[2] We feel that, up to now, the connection of these cusps to the fold caustic has not been illustrated clearly nor explained adequately and we will strive to achieve both these tasks below.

Furthermore, in Rosales and Tabak [109] when caustics of linear waves are reviewed it is shown that a Hilbert transform relates the waves before focusing to those after focusing. The waves before focusing are called "incident" and the waves after focusing are called "reflected".[3] There it is emphasised that a simple discontinuity "converts" through the Hilbert transform to a logarithmic singularity. The latter work employed *high-frequency* approximations.

However, as far as we know, no global approximation of the amplitude was made in the literature. Below we also pursue this task, using the full linear wave theory and working in the *time domain*.[4] We find that significant progress can be made analytically: using our detailed exposition of the underlying geometry we locate and identify the singularities of the linear solution. This breakdown of the linear theory indicates that the underlying small-amplitude approximation is no longer valid and indicates that nonlinear effects should be introduced. However, the introduction of nonlinearities in this problem is not an easy task. For a discussion of the introduction of nonlinear effects when modelling the focusing of weak shock waves we refer the reader to Section 3.9; we recall from there that the current consensus in the literature is that a nonlinear Tricomi equation should be solved to get the correct

[2] Also, the wavefront patterns were confirmed with experiments in a shallow water tank, making use of the 'hydraulic' analogy.

[3] We have already used these terms in Chapter 3 and we will also be using them here.

[4] We found after this work was completed that the method we use has close connections with the time-domain method of Friedlander, in [40], pp. 67–70. Also, it would be interesting to explore the connection of our work to the time-domain method used by Chapman in [22].

amplitudes near a fold caustic. This equation has been recently solved numerically by Coulouvrat et al. for the scenario of constant-acceleration of a supersonic aircraft [27]. However, in the next chapter, we will take a different approach and we will investigate *mainly analytically* the re-introduction of nonlinear terms for a simpler one-dimensional problem but one which is already quite complicated in its own right.

If the acceleration is a constant α and we scale time with c_0/α and space with c_0^2/α then we get a dimensionless problem in which the sound speed and acceleration are both equal to 1. So $x_0(t) = -t^2/2$, and we assume $z_0 = 0$. We define $U(t) = x_0'(t)$ to be the velocity, $M_0(t) = |U(t)|$ the Mach number, and $B_0(t) = \sqrt{M_0^2 - 1}$ the Prandtl-Glauert parameter. For the motion under consideration $U(t) = t$, $M_0(t) = t$ and $B_0(t) = \sqrt{t^2 - 1}$; the motion becomes supersonic at $t = 1$.

• Geometry

Below we discuss algebraically and geometrically the structure of the Mach envelope. A discussion of the geometrical features can be found in [73, 102] and the Appendix of [91], but we believe that the exposition here brings a better understanding as it clarifies how this geometrical structure is related to the appearance of certain logarithmic singularities in the wavefield and the associated breakdown of the linear theory.

Now, from (6.12) the wavefronts are given by

$$Q(x, z; t, \tau) = (t - \tau)^2 - \left(x + \frac{1}{2}\tau^2\right)^2 - z^2 = 0, \tag{6.42}$$

so Q is quartic in τ, and quadratic in x, z and t. From (6.22) and (6.23) the parametric equations describing the Mach envelope are

$$x_E(\tau, t) = -\frac{1}{2}\tau^2 - \left(\frac{t - \tau}{\tau}\right), \tag{6.43}$$

$$z_E(\tau, t) = \pm(t - \tau)\left(1 - \frac{1}{\tau^2}\right)^{1/2}, \tag{6.44}$$

in the range $1 \leq \tau \leq t$. It is possible to eliminate τ from (6.43) and (6.44) and the resulting equation for the envelope is cubic in t^2 and z^2 and quartic in x, but we shall find the parametric form more convenient.

In Figure 6.4 we plot the Mach envelope for $t = 1.2, 1.5, 2, 3$. When $t_\star = 2$ the source catches up with the disturbance it sent out at $\tau = 0$ so we also plot the wavefront $x^2 + z^2 = t_\star^2$. In Figure 6.4 we can see that the Mach envelope has two cusps which join a wedge-like part of the envelope with an arc-like part. These two

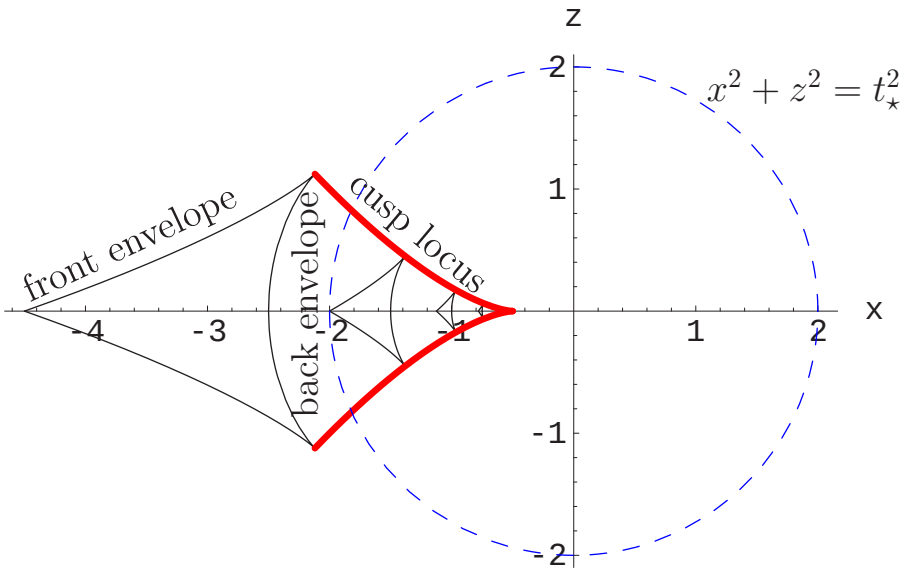

Figure 6.4: The Mach envelope for the times $t = 1.2, 1.5, 2, 3$, generated by a point source moving with constant acceleration from right to left. The cusp locus (thicker, red line) is plotted along with the wavefront $x^2 + z^2 = t_\star^2$ (dotted blue line), where $t_\star = 2$ is the time at which the source catches up with its initial disturbance.

parts will be called respectively the *front envelope* and *back envelope*. The cusps are singular points of the envelope and can be readily determined analytically by setting $\dfrac{\partial^2 Q}{\partial \tau^2} = 0$ or $\dfrac{\partial x_E}{\partial \tau} = \dfrac{\partial z_E}{\partial \tau} = 0$. From (6.43) and (6.44) the latter condition leads to

$$\tau_c = t^{1/3}. \tag{6.45}$$

The wavefront with $\tau = \tau_c$ contributes to the envelope its two cusp points, and it has centre $(x_0(\tau_c) = -t^{2/3}/2, 0)$ and radius $r_c = t - t^{1/3}$. Therefore the front envelope is given by equations (6.43)–(6.44) over the τ-range $t^{1/3} \le \tau \le t$, and the back envelope by the same equations but over the τ-range $1 \le \tau \le t^{1/3}$. Substituting $\tau_c = t^{1/3}$ in (6.43) and (6.44), we find that the coordinates of the cusps, for any $t \ge 1$, are

$$x_c = x_E(\tau_c) = 1 - \frac{3}{2}t^{2/3}, \quad z_c = z_E(\tau_c) = \pm(t^{2/3} - 1)^{3/2}. \tag{6.46}$$

Eliminating t from (6.46) we find that the cusp locus is

$$z_c^2 = \left(-\frac{2}{3}x_c - \frac{1}{3}\right)^3, \tag{6.47}$$

which is a semicubical parabola starting at the sonic point $(-1/2, 0)$ where the source speed is equal to the sound speed. The cusp locus (6.47) is plotted with a thicker line in Figure 6.4.

In Figure 6.5 we plot the boomrays, the special rays launched at the sonic angle $\theta_b = \arccos(1/M_0)$ to the direction of motion. Note that the Mach envelope could have also been obtained as the locus of the tips of the boomrays, as discussed in Chapter 3, Section 3.4.2. Here, boomrays are straight lines emitted for each τ in $1 \leq \tau \leq t$. At the sonic time $\tau = 1$, θ_b is zero and the boomrays are coincident. The angle θ_b steadily increases with τ. We also plot the Mach envelope with a dashed

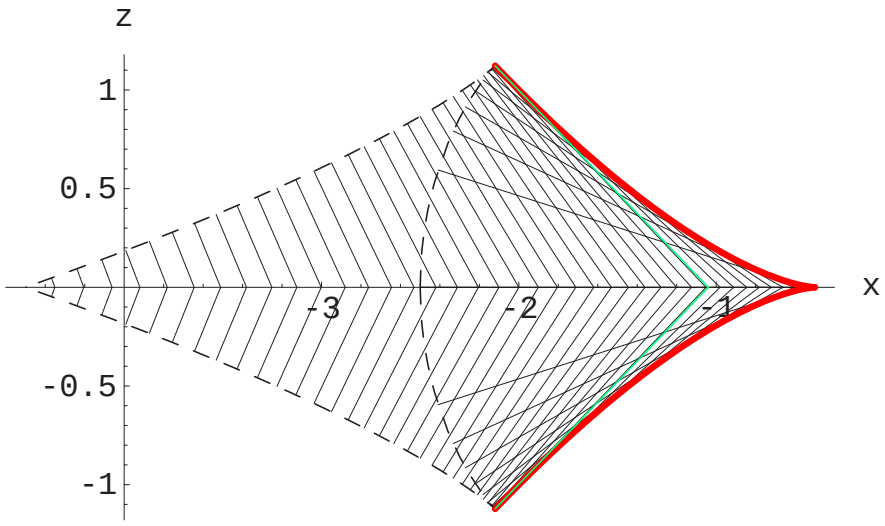

Figure 6.5: The boomrays form a fold caustic ($t = 3$), shown with a thicker red line. The boomrays passing through the cusps ($\tau_E = t^{1/3}$) are plotted with green. The Mach envelope is plotted with a dashed line.

line, the cusp locus (6.47) with a thicker red line, and the boomrays passing through the cusps with green. Figure 6.5 illustrates the fact that the cusp locus (6.47) is also a fold caustic of boomrays. We shall show this below.

Before doing so we stop to observe that the fold caustic in Figure 6.5 is qualitatively similar to the fold caustic of boomrays that arises in steady motion in a stratified medium in Chapter 3, Figure 3.27: in both cases for a fixed time t the boomrays that contribute to the front envelope have *not* passed through the fold caustic, but the boomrays that contribute to the back envelope *have* touched the caustic. In Chapter 3, the front envelope is the so-called "incident characteristic" and the back envelope is the so-called "reflected characteristic". There we used the terms "incident" and "reflected" because we thought of the perturbation as propagating on the incident characteristic, reflecting from the sonic line *at* the Tricomi cusp, and subsequently travelling on the reflected characteristic. Even though here the motion is unsteady and we cannot switch to the aerodynamic frame, for any fixed time t the cusps on the

envelope can still be thought of as Tricomi cusps in the same way, and we shall indeed use this term often from now on. We also saw in Chapter 3 that in the fixed frame the Tricomi cusp moves at the local sound speed; similarly in the current scenario the Tricomi cusp is also moving with the speed of sound. We shall see more scenarios where fold caustics occur at the end of this chapter; they will all have qualitatively the same behaviour. This qualitative similarity unifies this thesis and makes the work in this chapter relevant to all scenarios where a fold caustic arises. This is of course compatible with catastrophe theory which considers all fold caustics to be essentially the same, locally [15].

We shall now show that the cusp locus is a fold caustic (smooth envelope) of boomrays. The cusp locus (6.47) agrees with the expression by Dempsey in [32], but there it was obtained in a different way, by using two focusing conditions as he calls them. For the case of rectilinear acceleration, he derived these focusing conditions as a limiting case of the focusing conditions for motion in a circle. Below we will derive these conditions directly.

We will consider any two rays emitted at small distance ϵ apart as shown in Figure 6.6. The ray from A is emitted at time τ and the ray from B is emitted time $\Delta\tau$

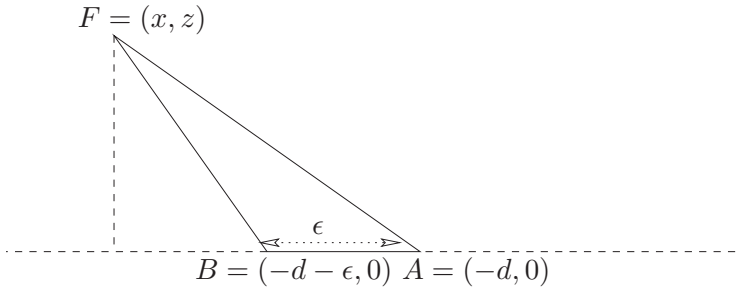

Figure 6.6: Two boomrays at distance ϵ apart, emitted from points A and B at time difference $\Delta\tau$, meeting at a point F.

later. Hence

$$x_A = -\frac{\tau^2}{2}, \quad U_A = U = -\tau \tag{6.48}$$

$$x_B = -\frac{(\tau + \Delta\tau)^2}{2}, \quad U_B = -(\tau + \Delta\tau). \tag{6.49}$$

Since $x_B = -d - \epsilon$, $(\tau + \Delta\tau)^2 = 2(d + \epsilon)$, and therefore $\Delta\tau(\epsilon) = -\tau + \sqrt{2(d + \epsilon)}$ (discarding the negative root). Expanding the time difference between the arrivals at

F, $t_{BF} + \Delta\tau(\epsilon) - t_{AF}$ as a series in powers of ϵ we find

$$\begin{aligned} t_{BF} + \Delta\tau(\epsilon) - t_{AF} =& \epsilon \left(\frac{1}{\tau} + \frac{x+d}{\sqrt{(x+d)^2 + z^2}} \right) + \\ & \frac{\epsilon^2}{2} \left(-\frac{1}{\tau^3} - \frac{(x+d)^2}{((x+d)^2 + z^2)^{3/2}} + \frac{1}{\sqrt{(x+d)^2 + z^2}} \right) + \\ & \frac{\epsilon^3}{2} \left(\frac{1}{\tau^5} + \frac{(x+d)^3}{((x+d)^2 + z^2)^{5/2}} - \frac{x+d}{((x+d)^2 + z^2)^{3/2}} \right) + O(\epsilon^4). \end{aligned} \tag{6.50}$$

Setting the coefficient of the order ϵ term to zero we recover the boomray condition $\cos\theta_b = \dfrac{1}{|U|}$ (discussed in Chapter 3) where θ_b is the acute angle between AF and AB. The boomray condition can be thought of as a "first-order focusing condition" for the rays. Now, we look for an envelope of boomrays by setting the coefficient of the order ϵ^2 term to zero. From the resulting relation and the boomray condition, we obtain the "second-order focusing condition"

$$x + d = -U^2 \sin^2\theta_b. \tag{6.51}$$

For the points such that the boomray condition and condition (6.51) are satisfied, the boomray signals arrive with a time difference of order ϵ^3. Eliminating τ from these two conditions we obtain again the cusp locus expression (6.47). So we have proved that the cusp locus is a curve of second-order focusing. Furthermore, the coefficient of ϵ^3 is always positive so in a constant acceleration motion we cannot have any focus of order higher than second.

Wavefront pattern

In this section we will discusss the wavefront pattern further, and explain how a wavefront emitted at time $t = \tau \geq 1$ contributes to the Mach envelope. In Figure 6.7 we plot the wavefronts for various values of τ in the interval $0 \leq \tau \leq t$ when $t = 3$; we also plot the cusp locus with a thicker, red line. We observe a distinct geometrical difference between the front and the back envelope; the $t^{1/3} \leq \tau \leq t$ wavefronts envelope the front envelope from the *inside*, that is the front envelope is formed in a similar way to the Mach wedge, but the $1 \leq \tau \leq t^{1/3}$ wavefronts envelope the back envelope from the *outside*. This difference is shown more clearly in the schematic diagrams of Figure 6.8. An algebraic criterion for distinguishing the two types of envelope formation appears also below. In Chapter 3, the same qualitative change took place in the wavefront pattern associated with a fold caustic of boomrays:

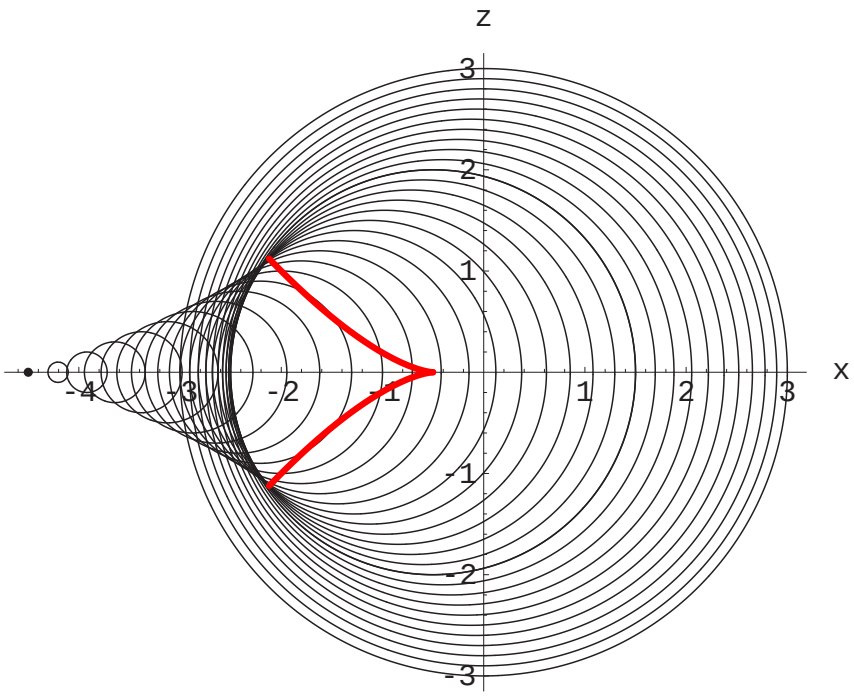

Figure 6.7: The wavefront pattern generated by an accelerating source from right to left ($t = 3$).

this was, for example the case in Figure 3.25: the incident characteristic was on the outside of the wavefronts and the reflected characteristic was inside the wavefronts.

Figure 6.8: Schematic diagrams for the formation of the front and back parts of the Mach envelope (left and right respectively). In each case the thin curves are the wavefronts and the thick curve is their envelope.

Although at first glance it might look a complicated task, we can describe easily the formation of the back envelope with the help of Figure 6.9. The key is to plot the $\tau = 1$ and $\tau = t^{1/3}$ wavefronts. The $\tau = 1$ wavefront is tangent to the back envelope at the point D and the two boomrays are horizontal and coincident. This wavefront intersects the front envelope on the left of the cusp points C_1 and C_2. As τ increases

the boomrays diverge from each other more and more, till they reach C_1 and C_2 (when $\tau = t^{1/3}$). While the boomrays are diverging from each other the intersection points of the corresponding wavefront move closer to the cusps (we could say that the wavefront"rolls backwards" towards the cusp).

The back envelope is a new feature, produced by the acceleration of the source and from now on it will be called the *acceleration caustic*. The noun "caustic" in the new name for the back envelope will be justified when we calculate the associated amplitude; we will find that the amplitude is finite on the front envelope but becomes infinite on the acceleration caustic.

We can also express the difference between the front and back envelope in an algebraic way. Firstly, both on the front and back envelope $Q = 0$ and $\dfrac{\partial Q}{\partial \tau} = 0$ at $\tau = \tau_E$. This dictates that $\tau = \tau_E$ is at least a *double* root of the quartic Q. Calculating

$$\left(\frac{\partial^2 Q}{\partial \tau^2}\right)_{\tau_E} = 2 - 2x_E - 3{\tau_E}^2, \tag{6.52}$$

and using (6.43) in (6.52) to express x_E in terms of τ_E we obtain

$$\left(\frac{\partial^2 Q}{\partial \tau^2}\right)_{\tau_E} = 2\frac{t - {\tau_E}^3}{\tau_E}. \tag{6.53}$$

Therefore at the cusp $\dfrac{\partial^2 Q}{\partial \tau^2} = 0$ and $\tau = \tau_c$ is a triple root of Q. At any envelope point Q has either a local maximum or a local minimum. We thus deduce the following algebraic criterion for distinguishing the front from the back envelope:

- on the front envelope $\dfrac{\partial^2 Q}{\partial \tau^2} < 0 \Rightarrow Q$ has a local maximum.[5].
- at the cusp $\dfrac{\partial^2 Q}{\partial \tau^2} = 0 \Rightarrow Q$ has a point of inflexion.
- on the back envelope $\dfrac{\partial^2 Q}{\partial \tau^2} > 0 \Rightarrow Q$ has a local minimum.

In Appendix A the above algebraic criterion formulated in the time domain will be reinterpreted in the frequency domain in terms of the eigenvalues of appropriately defined matrices.

[5]That the front envelope is qualitatively similar to the Mach wedge is also confirmed by finding that for steady motion $Q_{\tau\tau} = -2(U^2 - 1)$ which is also negative.

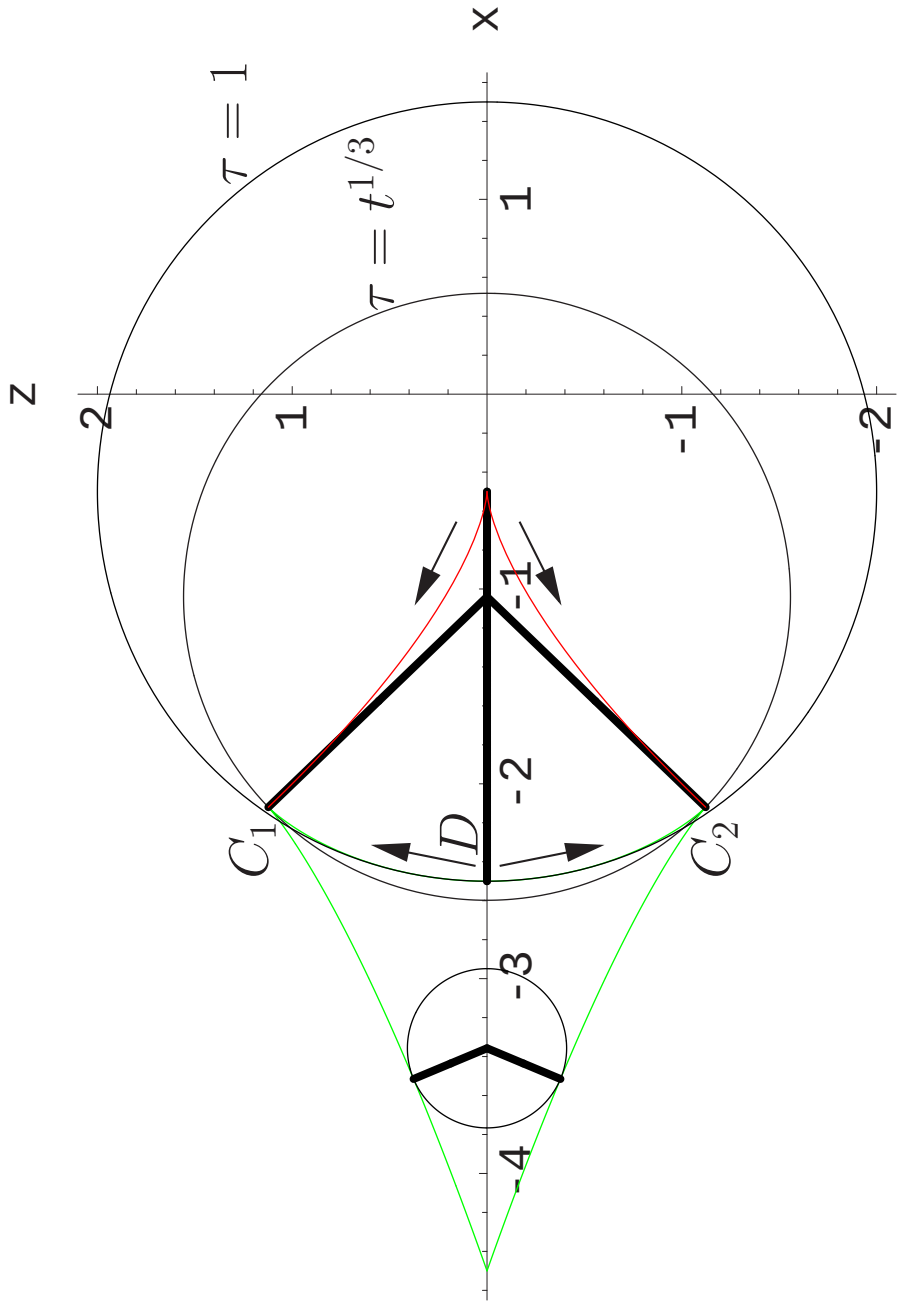

Figure 6.9: The formation of the back envelope ($t = 3$): The Mach envelope and the fold caustics are plotted with green and red respectively. We plot the wavefront $\tau = t^{1/3}$ passing through the cusps C_1 and C_2 and the associated boomrays; we also plot the wavefront $\tau = 1$ touching the back envelope at the point D where the boomrays coalesce. The wavefronts for the values of τ between 1 and $t^{1/3}$ always cross the front envelope and therefore have two distinct contact points that touch the back envelope from outside.

Since the amplitude is proportional to $\int_0^t \frac{H(Q(\tau))d\tau}{\sqrt{Q(\tau)}}$, the aforementioned difference in the behaviour of Q directly relates to corresponding differences in the amplitudes at the front envelope, the back envelope, and the cusp. We will investigate this in detail in the next section.

•Wavefield

We have plotted above the wavefront pattern and Mach envelope associated with constant acceleration through the sound speed and we have discussed their features. Using that information, we are now going to approximate appropriately the wavefield integral (6.16) near the front envelope, near the acceleration caustic and near the cusp. (In Section 6.2.4 we will extend the same method to calculate approximate amplitudes near the Mach envelope for a motion with constant deceleration through the sound speed.)

The wavefield at a certain point (x, z) is determined by the integral (6.16). For a moving point source of unit strength that starts moving at time $\tau = 0$, no contribution comes from values of t that are less than zero. Also when (x, z) is outside the Mach envelope and outside the IW, as explained above, $Q < 0$ and $p = 0$. Therefore, to summarise, the integral (6.16) is defined only over the first quadrant of the Q-τ plane.

Since Q is a quartic the limits of integration are more difficult to determine algebraically than those of the steady motion. It would be possible to obtain an expression for p everywhere in the region of influence, in terms of standard elliptic integrals, but we will not do this here as it is unnecessarily complicated. To determine only the singular part of the wavefield near the Mach envelope that is associated with the sonic boom it is enough to perform a simple approximation on the integral. *On* the envelope Q has either a double or triple root so we can determine all four of its roots analytically. Expanding Q from (6.42) as a polynomial in τ we obtain

$$-4Q(\tau, x, z, t) = \tau^4 - 4(1 - x)\tau^2 + 8t\tau - 4(t^2 - x^2 - z^2). \tag{6.54}$$

For any envelope point, since $\tau = \tau_E$ is a double root, Q satisfies the relation

$$-4Q = (\tau - \tau_E)^2 g(\tau) \text{ where } g(\tau) = (\tau - \tau_3)(\tau - \tau_4). \tag{6.55}$$

Therefore

$$\text{Sum of roots} = S_Q = 2\tau_E + \tau_3 x + \tau_4 = 0, \tag{6.56}$$

$$\text{Product of roots} = P_Q = \tau_E^2 \tau_1 \tau_4 = 4(x_E^2 + z_E^2 - t^2). \tag{6.57}$$

From (6.56) and (6.57) we can write down the sum S_{34} and product P_{34} of the two unknown roots τ_3 and τ_4,

$$S_{34} = \tau_3 + \tau_4 = -2\tau_E, \quad P_{34} = \tau_3\tau_4 = 4\frac{(x_E^2 + z_E^2 - t^2)}{\tau_E^2}. \tag{6.58}$$

Note that $g(\tau) = \tau^2 - S_{34}\tau + P_{34}$. Hence

$$\tau_3 = -\tau_E - 2\sqrt{\frac{t}{\tau_E}}, \quad \tau_4 = -\tau_E + 2\sqrt{\frac{t}{\tau_E}}. \tag{6.59}$$

The relation (6.59) gives further information on the behaviour of Q at the Mach envelope:

- For the acceleration caustic: since $1 < \tau_E < t^{1/3}$ from (6.59) we have $\tau_4 > \tau_E$; however τ_3 is always negative and hence less than τ_E.

- For the front envelope: from $t^{1/3} < \tau_E < t$ and (6.59) we have $\tau_4 < \tau_E$. Since $\tau_3 < \tau_4$ now both roots τ_3 and τ_4 are less than the double root τ_E. By (6.59) τ_3 is always negative, but τ_4 becomes positive if $\tau > \tau_E^\star$. Setting $\tau_4 = 0$ in (6.59) we obtain $\tau_E^\star = 4^{1/3}t^{1/3}$, and also from (6.58) $x_E^2 + z_E^2 = t^2$ holds. From these two relations we conclude that the IW $x^2 + z^2 = t^2$ crosses the envelope at the points contributed by the boomrays emitted at $\tau_E^\star$. Imposing $\tau_E^\star < t$ we find as expected that we need $t > 2$ for such an intersection to be possible. Note also that for all t we have $\tau_E^\star = 4^{1/3}t^{1/3} > \tau_c = t^{1/3}$, and so the IW never crosses the acceleration caustic.

- At the cusp: $\tau = t^{1/3} \Rightarrow \tau_4 = \tau_E$. Therefore there is a triple root at the cusp, as we already remarked. Summarising, we can say that when approaching the cusp from the front envelope τ_4 approaches τ_E from the left, and when approaching from the back envelope τ_4 approaches τ_E from the right.

In Figure 6.11 we plot Q as a function of τ at seven points representative of the various regions of interest shown in Figure 6.10: A is a point outside the front envelope (and outside the IW), B is on the front envelope (and outside the IW), C is inside the envelope (and outside the IW), D is the cusp, E is *on* the left of the acceleration caustic and inside the IW, F is *on* the acceleration caustic and G is on the right of the acceleration caustic and inside the IW. Below, we will use these results to find consistent approximations to Q and hence to the wavefield integral (6.16). From the transition ABC and EFG in Figures 6.10–6.11, the algebraic criterion in p. 156, and the geometrical differences between the front envelope and the back envelope it

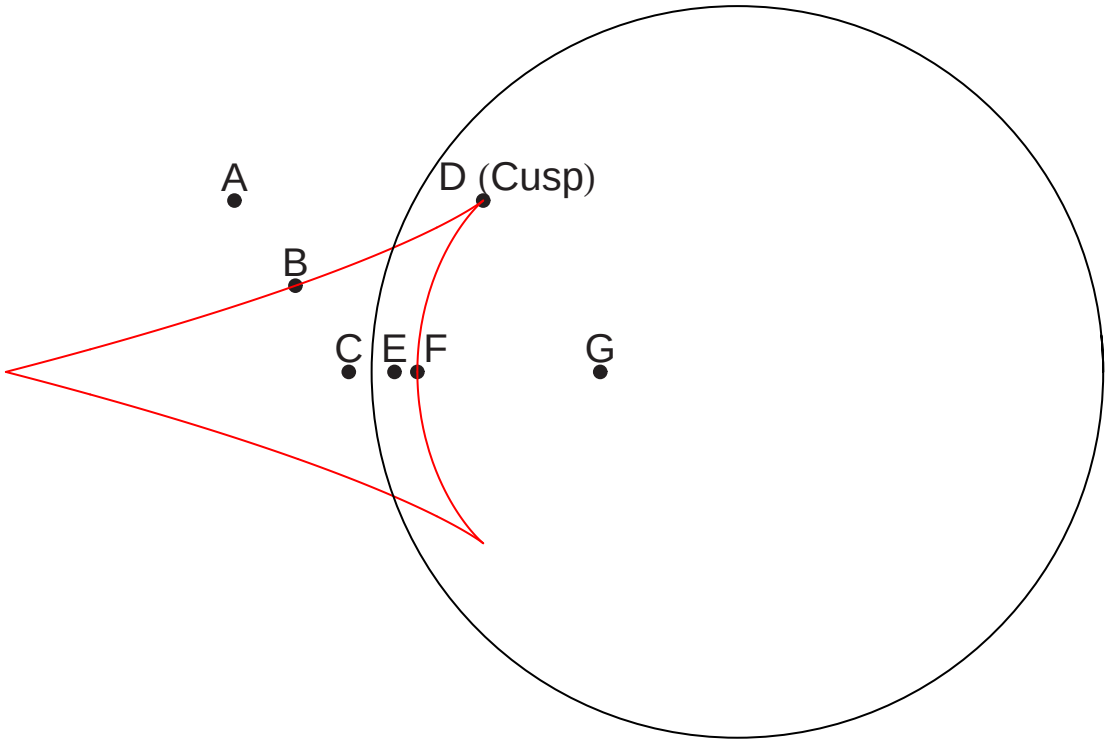

Figure 6.10: Plot of the Mach envelope, the initial wavefront and indication of the typical points A, B, C, D, E, F and G.

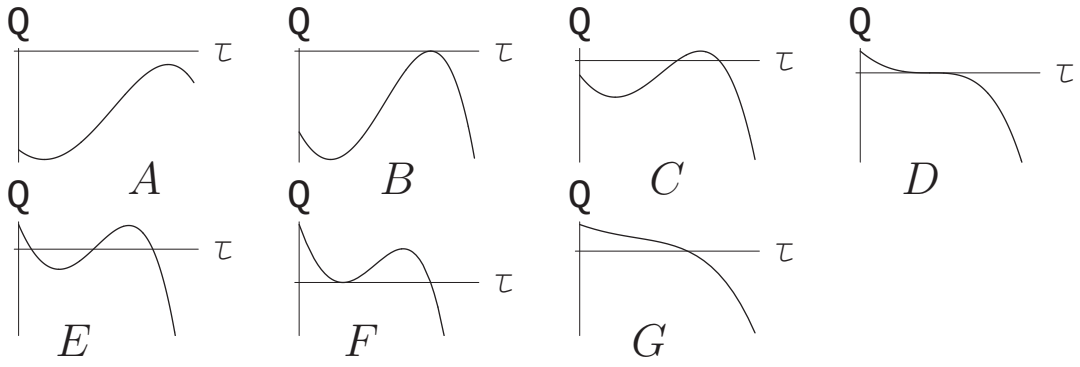

Figure 6.11: Plot of Q at points A, B, C, D, E, F and G in Figure 6.10.

is obvious that the wavefield on the back envelope is of a different nature from the wavefield on the front envelope.

Let us take a general point (x_E, z_E) anywhere on the envelope (with t considered a fixed parameter). Since the acceleration caustic is never parallel to the x-axis we will keep z_E fixed and we will obtain the approximation to the wavefield integral as a function of x where $|x - x_E|$ is small. The small parameter of the asymptotic procedure will be taken to be proportional to $|x - x_E|^\alpha$ where α is greater than zero and to be determined.

Under the assumption of $|x - x_E|$ being small, the quartic Q will be approximated with lower-order polynomials, while retaining in each region its most important features. Roughly the idea of the approximation method we will use is the following: since Q has a local maximum/minimum at any front/back envelope point, two roots of Q are enough to reconstruct the local behaviour and Q will be approximated with a quadratic there; Q will be approximated with a cubic near the cusp since it has a point of inflexion there and three roots are in play. These approximations for Q will enable us to find approximations to the amplitude analytically.

We consider any point near the envelope and expand $Q(\tau, x; z_E, t)$ in a Taylor series about the envelope point $(\tau_E, x_E; z_E, t)$, using $Q = \dfrac{\partial Q}{\partial \tau} = 0$ on the envelope. We obtain

$$Q(\tau, x; z_E, t) = \left(\frac{\partial Q}{\partial x}\right)_E (x - x_E) + \frac{1}{2}\left(\frac{\partial^2 Q}{\partial \tau^2}\right)_E (\tau - \tau_E)^2 + h.o.t \tag{6.60}$$

We let

$$C_1 = \left(\frac{\partial Q}{\partial x}\right)_E = -2x_E - \tau_E^2 = 2\frac{t - \tau_E}{\tau_E} > 0 \quad \text{for } 1 \le \tau \le t, \tag{6.61}$$

$$\text{and } C_2 = \frac{1}{2}\left(\frac{\partial^2 Q}{\partial \tau^2}\right)_E = \frac{t - \tau_E^3}{\tau_E} \quad \begin{cases} < 0 \text{ for } t^{1/3} \le \tau_E \le t \\ > 0 \text{ for } t \le \tau_E \le 1. \end{cases} \tag{6.62}$$

So, from (6.60) we conclude that for any point (x, z) near the envelope with $\epsilon^2 \sim |x - x_E|$ the τ-roots of Q are perturbed by $O(\epsilon)$. We will denote the perturbed roots by τ_1', τ_2', τ_3' and τ_4'.

◇ Wavefield near the front envelope

We pick the point (x_E, z_E) on the front envelope. We will consider points at small distance $|x - x_E|$ from this point. Without loss of generality, we can take (x_E, z_E) so that $\tau_E \ge 4^{1/3} t^{1/3}$ so that the wavefield outside the envelope is zero.[6]

[6] At a point on the front envelope but inside the IW, there is an extra contribution to the

From the general expression (6.16) and using (6.60), (6.61) and (6.62), we obtain for $x > x_E$ (see plot C in Figure 6.11)

$$2\pi p(x; z_E, t) \sim \frac{1}{\sqrt{|C_2|}} \int_{\tau_1'}^{\tau_2'} \frac{d\tau}{\sqrt{(\tau_2' - \tau)(\tau - \tau_1')}}, \tag{6.63}$$

where

$$\tau_1' = \tau_E - \sqrt{\frac{C_1}{C_2}(x_E - x)},$$
$$\tau_2' = \tau_E + \sqrt{\frac{C_1}{C_2}(x_E - x)}.$$

The roots τ_3' and τ_4' are both negative.

From the calculations for steady motion (6.27)–(6.29) the integral (6.63) immediately evaluates to

$$p(x, z_E, t) \sim \frac{1}{2\sqrt{|C_2|}}. \tag{6.64}$$

Hence, as $x \to x_E$ the pressure jump across the front envelope is given by

$$p(x_E^+, z_E, t) - 0 = \frac{1}{2\sqrt{|C_2|}} = \frac{1}{2}\left(\frac{\tau_E}{\tau_E^3 - t}\right)^{1/2}. \tag{6.65}$$

We plot the jump (6.65) in Figure 6.12 for $t^{1/3} \le \tau_E \le t - 0.001$. The jump near the source, as $\tau_E \to t$, is

$$p(t, t) = \frac{1}{2}\frac{1}{\sqrt{t^2 - 1}}. \tag{6.66}$$

Since the local Prandtl-Glauert parameter $B_0 = \sqrt{\tau^2 - 1}$ takes the value $\sqrt{t^2 - 1}$ in the limit $\tau_E \to t$, (6.66) agrees with the steady motion result (6.29) and provides another verification of the similarity between the Mach wedge and the front envelope.

However as $\tau_E \to t^{1/3}$ the jump tends to infinity. This indicates that the quadratic approximation for Q is insufficient at the cusp and more terms would need to be retained in the Taylor series (6.60) for Q. We leave the analysis of the wavefield near the cusp for later.

---

wavefield, given by $\int_0^{\tau_4'} \frac{d\tau}{\sqrt{Q}}$ (see plot E in Figure 6.11). However, this contribution is continuous across the envelope and since we are interested in the abrupt jump in the wavefield due to the singular contribution $\int_{\tau_1'}^{\tau_2'} \frac{d\tau}{\sqrt{Q}}$ we do not lose any generality by considering points outside the IW.

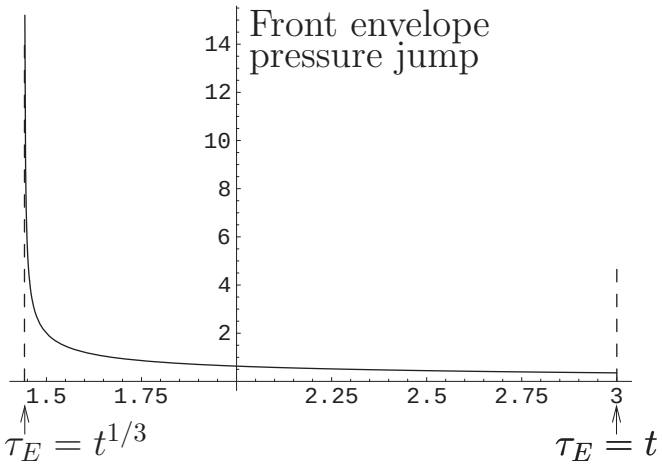

Figure 6.12: Pressure jump on the front envelope.

◇ **Wavefield near the acceleration caustic**

We now consider a point (x_E, z_E) on the acceleration caustic and we again wish to find the wavefield at small distance $|x - x_E|$ from this point (where $z = z_E$ is taken to be fixed as before).

To calculate the singular behaviour of the wavefield at points near this acceleration caustic again we again note that only two of the four roots of Q are in play. We consider first the wavefield on the left of the acceleration caustic. We are going to denote the four perturbed roots by $\tau_{3L}, \tau_E - \epsilon, \tau_E + \epsilon, \tau_{4L}$, where $\epsilon = \sqrt{\dfrac{C_1}{C_2}(x_E - x)}$ is taken the same as in the front envelope calculations. We note that this is already an approximate representation of the roots; in fact the two roots near τ_E are $\tau_E \pm \epsilon + O(\epsilon^2)$ and $\tau_{3L} = \tau_3 + O(\epsilon^2)$, $\tau_{4L} = \tau_4 + O(\epsilon^2)$. As $\epsilon \to 0$ these roots tend respectively to $(\tau_3, \tau_E, \tau_E, \tau_4)$. The pressure field p_L on the *left* of the acceleration caustic is given by

$$2\pi p_L = \underbrace{\int_0^{\tau_E - \epsilon} \frac{d\tau}{\sqrt{Q}}}_{J_{1A}} + \underbrace{\int_{\tau_E + \epsilon}^{\tau_{4L}} \frac{d\tau}{\sqrt{Q}}}_{J_{1B}}, \tag{6.67}$$

where

$$-4Q = ((\tau - \tau_E)^2 - \epsilon^2) g_L(\tau) \text{ and } g_L(\tau) = (\tau - \tau_{4L})(\tau - \tau_{3L}). \tag{6.68}$$

The wavefield on the right of the acceleration caustic is given by

$$2\pi p_R = \underbrace{\int_0^{\tau_E} \frac{d\tau}{\sqrt{Q}}}_{J_{2A}} + \underbrace{\int_{\tau_E}^{\tau_{4R}} \frac{d\tau}{\sqrt{Q}}}_{J_{2B}}, \tag{6.69}$$

where

$$-4Q = ((\tau - \tau_E)^2 + \epsilon^2) g_R(\tau) \text{ and } g_R(\tau) = (\tau - \tau_{3R})(\tau - \tau_{4R}). \tag{6.70}$$

As $\epsilon \to 0$, both $g_L(\tau)$ and $g_R(\tau)$ tend to $g(\tau)$.

We will first evaluate J_{1A} and J_{2A} and compare them as they both deal with the range of integration $0 \leq \tau \leq \tau_E$ (see Figure 6.18, plot E). Firstly for

$$J_{1A} = \int_0^{\tau_E - \epsilon} \frac{f_L(\tau) d\tau}{\sqrt{(\tau - \tau_E)^2 - \epsilon^2}}, \tag{6.71}$$

where $f_L(\tau) = \sqrt{\dfrac{-4}{g_L(\tau)}}$, to extract the singular behaviour, we split the numerator as $f_L(\tau) = f_L(\tau_E) + (f_L(\tau) - f_L(\tau_E))$: therefore

$$J_{1A} = \underbrace{\int_0^{\tau_E - \epsilon} \frac{f_L(\tau_E) d\tau}{\sqrt{(\tau - \tau_E)^2 - \epsilon^2}}}_{J_{1A(i)}} + \underbrace{\int_0^{\tau_E - \epsilon} \frac{(f_L(\tau) - f_L(\tau_E)) d\tau}{\sqrt{(\tau - \tau_E)^2 - \epsilon^2}}}_{J_{1A(ii)}}. \tag{6.72}$$

The first integral $J_{1A(i)}$ contains the singular behaviour of J_{1A} and $J_{1A(ii)}$ tends to a finite limit as $\epsilon \to 0$ which is negligible in comparison with the singular part. Therefore we have

$$J_{1A(i)} = f_L(\tau_E) \cosh^{-1}\left(\frac{\tau_E}{\epsilon}\right) \tag{6.73}$$

$$= f_L(\tau_E) \ln\left(\frac{\tau_E}{\epsilon} + \sqrt{\left(\frac{\tau_E}{\epsilon}\right)^2 - 1}\right), \tag{6.74}$$

and as $\epsilon \to 0$ we have

$$J_{1A(i)} = f(\tau_E)\left(-\ln \epsilon + \ln(2\tau_E)\right) + o(1). \tag{6.75}$$

Therefore $J_{1A(i)}$ gives rise to a logarithmic singularity of strength $f(\tau_E)$. Now, for

$$J_{1A(ii)} = \int_0^{\tau_E - \epsilon} \frac{(f_L(\tau) - f_L(\tau_E)) d\tau}{\sqrt{(\tau - \tau_E)^2 - \epsilon^2}}, \tag{6.76}$$

letting $\epsilon \to 0$ we obtain

$$J_{1A(ii)} \to \int_0^{\tau_E} \frac{(f(\tau) - f(\tau_E)) d\tau}{(\tau_E - \tau)}, \tag{6.77}$$

which is finite. Now, in the same fashion we have adopted for (6.72), we write

$$J_{2A} = \underbrace{\int_0^{\tau_E} \frac{f_R(\tau_E)d\tau}{\sqrt{(\tau-\tau_E)^2+\epsilon^2}}}_{J_{2A(i)}} + \underbrace{\int_0^{\tau_E} \frac{(f_R(\tau)-f_R(\tau_E))d\tau}{\sqrt{(\tau-\tau_E)^2+\epsilon^2}}}_{J_{2A(ii)}}. \tag{6.78}$$

Again, the first integral $J_{2A(i)}$ contains the singular behaviour of J_{2A} and $J_{2A(ii)}$ tends to a finite limit as $\epsilon \to 0$. Now

$$J_{2A(i)} = f_R(\tau_E)\sinh^{-1}\left(\frac{\tau_E}{\epsilon}\right) \tag{6.79}$$

$$= f_R(\tau_E)\ln\left(\frac{\tau_E}{\epsilon} + \sqrt{\left(\frac{\tau_E}{\epsilon}\right)^2+1}\right), \tag{6.80}$$

and as $\epsilon \to 0$ we have

$$J_{2A(i)} = f(\tau_E)\left(-\ln\epsilon + \ln(2\tau_E)\right) + o(1). \tag{6.81}$$

Therefore $J_{2A(i)}$ also gives rise to a logarithmic singularity of strength $f(\tau_E)$. We thus conclude that the logarithmic singularities from $J_{1A(i)}$ and $J_{2A(i)}$, respectively on the left and on the right of the acceleration caustic, are of equal strength. Lastly, letting $\epsilon \to 0$ in the finite part of J_{2A},

$$J_{2A(ii)} = \int_0^{\tau_E} \frac{(f_R(\tau)-f_R(\tau_E))d\tau}{\sqrt{(\tau-\tau_E)^2+\epsilon^2}}, \tag{6.82}$$

we have that

$$J_{2A(ii)} \to \int_0^{\tau_E} \frac{(f(\tau)-f(\tau_E))d\tau}{(\tau_E-\tau)}. \tag{6.83}$$

Therefore we also conclude that as $\epsilon \to 0$ the integrals $J_{1A(ii)}$ and $J_{2A(ii)}$ tend to the same *finite* limit. This finite integral is negligible in comparison with the singular part and we are not going to calculate it precisely.

The range of integration $\tau_E + \epsilon \leq \tau \leq \tau_4$ is dealt with similarly. We find

$$J_{1B(i)} = f_L(\tau_E)\cosh^{-1}\left(\frac{\tau_4-\tau_E}{\epsilon}\right) \tag{6.84}$$

$$= f_L(\tau_E)\ln\left(\frac{\tau_4-\tau_E}{\epsilon} + \sqrt{\left(\frac{\tau_4-\tau_E}{\epsilon}\right)^2-1}\right), \tag{6.85}$$

and as $\epsilon \to 0$

$$J_{1B(i)} = f(\tau_E)\left(-\ln\epsilon + \ln(2(\tau_4-\tau_E))\right) + o(1). \tag{6.86}$$

Also on the right of the acceleration caustic

$$J_{2B(i)} = f_R(\tau_E)\sinh^{-1}\left(\frac{\tau_4-\tau_E}{\epsilon}\right) \tag{6.87}$$

$$= f_R(\tau_E)\ln\left(\frac{\tau_4-\tau_E}{\epsilon}+\sqrt{\left(\frac{\tau_4-\tau_E}{\epsilon}\right)^2+1}\right), \tag{6.88}$$

and as $\epsilon \to 0$

$$J_{2B(i)} = f(\tau_E)\left(-\ln\epsilon + \ln(2(\tau_4-\tau_E))\right) + o(1). \tag{6.89}$$

We also find that as $\epsilon \to 0$, $J_{1B(ii)}$ and $J_{2B(ii)}$ tend to the same finite limit $\int_{\tau_E}^{\tau_4} \frac{(f(\tau)-f(\tau_E))d\tau}{(\tau-\tau_E)}$. Since

$$J_1 = J_{1A(i)} + J_{1B(i)} + J_{1A(ii)} + J_{1B(ii)}, \tag{6.90}$$

as $\epsilon \to 0$, putting together all the results from above, we have

$$J_1 = -2f(\tau_E)\ln(\epsilon) + O(1), \tag{6.91}$$

and similarly

$$J_2 = J_{2A(i)} + J_{2B(i)} + J_{2A(ii)} + J_{2B(ii)}. \tag{6.92}$$

It remains to find $f(\tau_E)$ so that we can determine the strength of the logarithmic singularities. Since

$$f(\tau_E) = \sqrt{\frac{-4}{g(\tau_E)}}, \tag{6.93}$$

using (6.58) we obtain

$$f(\tau_E;t) = \sqrt{\frac{\tau_E}{t-\tau_E^3}}. \tag{6.94}$$

Therefore $f(\tau_E)$ blows up as $\tau_E \to t^{1/3}$. We plot $f(\tau_E)$ in Figure 6.13 for $1 \le \tau_E \le t^{1/3} - 0.001$. Note that at the point where boomrays coalesce, we have $f(1;t) = \sqrt{\frac{1}{t-1}}$ which is finite for any $t > 1$; this point has no other significance beyond this fact. Comparing the jump on the front envelope and the strength of the logarithmic singularity $f(\tau_E, t)$ we see that both involve the function $\sqrt{\frac{\tau_E}{|t-\tau_E^3|}}$.

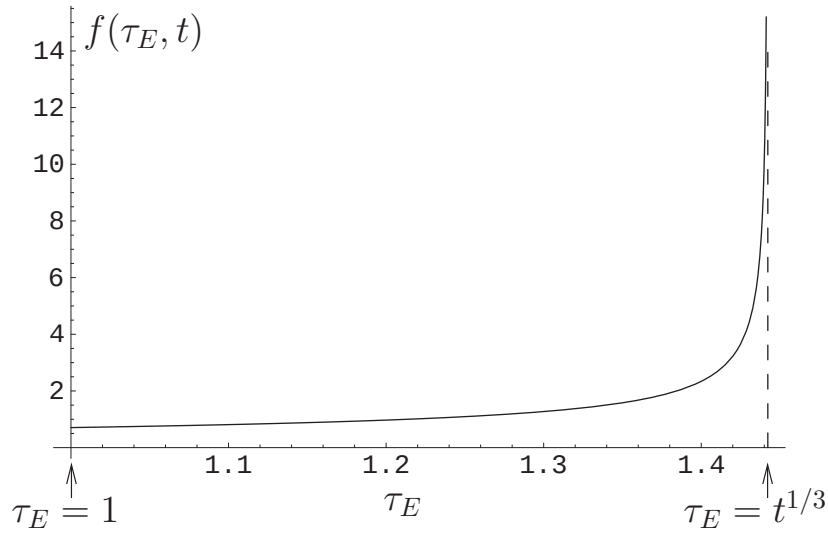

Figure 6.13: Plot of $f(\tau_E, t)$ as a function of τ_E, where $-2f(\tau_E, t)$ is the strength of the logarithmic singularity.

It is also of interest to determine how $f(\tau_E)$ is related to $|z - z_c|$ where z_c is the z-coordinate at the cusp and $|z - z_c|$ small. We find

$$f(\tau_E) \sim \frac{1}{6^{1/4}} \frac{(\tau_c^2 - 1)^{-1/8}}{\tau_c} (z_E - z_c)^{-1/4},$$

and using $\tau_c = t^{1/3}$ we have

$$f(\tau_E) \sim \frac{1}{6^{1/4}} t^{-1/6} (t^{2/3} - 1)^{-1/8} (z_E - z_c)^{-1/4}. \tag{6.95}$$

◇ Wavefield near the cusp

At the cusp the truncated Taylor series (6.60) is not a sufficient approximation since $\dfrac{\partial^2 Q}{\partial \tau^2} = 0$. Still fixing our attention on points on a horizontal line $z = z_c$, we retain the next term up in the series in τ which is the term with $\dfrac{\partial^3 Q}{\partial \tau^3} = 0$: we have

$$Q(\tau, x; z_c, t) = \left(\frac{\partial Q}{\partial x}\right)_c (x - x_c) + \frac{1}{6} \left(\frac{\partial^3 Q}{\partial \tau^3}\right)_c (\tau - \tau_c)^3 + h.o.t, \tag{6.96}$$

where $\left(\dfrac{\partial Q}{\partial x}\right)_c$ is given as a function of τ and t in (6.61) and $\left(\dfrac{\partial^2 Q}{\partial \tau^2}\right)_c = -6\tau$. Therefore we rewrite (6.96) as

$$\begin{aligned} Q(\tau, x; z_c, t) =& 2\frac{t - \tau_E}{\tau_E}(x - x_c) - \tau_c(\tau - \tau_c)^3 + h.o.t. && (6.97) \\ =& C_1(x - x_c) - C_3(\tau - \tau_c)^3 + h.o.t. && (6.98) \end{aligned}$$

where $C_1 = 2\dfrac{t-\tau_E}{\tau_E}$ (as before) and $C_3 = \tau$.

We first consider $x > x_c$ and we let

$$\epsilon^3 = \frac{C_1}{C_3}(x - x_c) > 0. \tag{6.99}$$

Then from the integral (6.16) we have

$$2\pi p_{CR}(x; z_c, t) \sim \frac{1}{\sqrt{C_3}} \int_0^{\tau_c+\epsilon} \frac{d\tau}{\sqrt{\epsilon^3 - (\tau - \tau_c)^3}}. \tag{6.100}$$

Making the change of variables $\dfrac{\tau - \tau_c}{\epsilon} = v$ (where $v < 1$) in (6.100) we obtain

$$2\pi p_{CR}(x; z_c, t) = \frac{\epsilon^{-1/2}}{\sqrt{C_3}} \int_{-\tau_c/\epsilon}^{1} \frac{dv}{\sqrt{1 - v^3}}. \tag{6.101}$$

As $\epsilon \to 0$ we have

$$2\pi p_{CR} \sim \frac{\epsilon^{-1/2}}{\sqrt{C_3}} \int_{-\infty}^{1} \frac{dv}{\sqrt{1 - v^3}}, \tag{6.102}$$

where $\displaystyle\int_{-\infty}^{1} \frac{dv}{\sqrt{1 - v^3}} = 4.20655$ is found numerically.

We now take $x < x_c$ so that we have a point on the left of the cusp. We keep the (6.99) definition of ϵ so that $\epsilon < 0$. Then

$$2\pi p_{CL}(x; z_c, t) = \frac{1}{\sqrt{C_3}} \int_0^{\tau_c-|\epsilon|} \frac{d\tau}{\sqrt{-|\epsilon|^3 - (\tau - \tau_c)^3}}. \tag{6.103}$$

Letting $\dfrac{\tau - \tau_c}{|\epsilon|} = v$ (where $v < -1$) in (6.103) we obtain

$$2\pi p_{CL} = \frac{|\epsilon|^{-1/2}}{\sqrt{C_3}} \int_{-\tau_c/|\epsilon|}^{-1} \frac{dv}{\sqrt{-1 - v^3}}. \tag{6.104}$$

As $|\epsilon| \to 0$ we have

$$2\pi p_{CL} \sim \frac{|\epsilon|^{-1/2}}{\sqrt{C_3}} \int_{-\infty}^{-1} \frac{dv}{\sqrt{-1 - v^3}}, \tag{6.105}$$

where $\displaystyle\int_{-\infty}^{-1} \frac{d\tau}{\sqrt{-1 - v^3}} = 2.42865$.

Therefore on the horizontal line $z = z_c$ we can determine the behaviour of the wavefield as a function of x, where x is at small distance to the left or to the right of x_c. It is also of interest to determine the wavefield near the cusp when approaching (x_c, z_c) from directions other than the horizontal, but we do not pursue this here. We emphasise that the singularities we identified are not transient, they propagate with the speed of sound for all times t.

6.2.4 Deceleration through the sound speed

We now consider another motion of great practical relevance. We consider a point source moving along the x-direction, from left to right in steady supersonic motion, with $M_0 > 1$ and which starts decelerating uniformly at $\tau = 0$. We thus have that

$$x_0(t) = M_0 t \quad t \leq 0, \tag{6.106}$$

$$x_0(t) = M_0 t - t^2/2 \quad 0 \leq t \leq M_0. \tag{6.107}$$

The motion is supersonic for $t < M_0 - 1$. At $t = M_0 - 1$ the source speed equals the sound speed and for $M_0 - 1 < t < M_0$ the motion is subsonic. The source stops at $t = M_0$. Below we will calculate the geometry and the associated wavefield. Pictures of the geometry are found in [73]. Virtually no discussion of the amplitudes was located in the literature.

• **Geometry**

For times $t < M_0 - 1$ the wavefront pattern and Mach envelope are qualitatively the same as that of steady supersonic motion but new features appear when $t \geq M_0 - 1$. In Figure 6.14(a) we plot the wavefront pattern for $t = M_0$. We see that for $M_0 - 1 \leq \tau \leq M_0$ the wavefronts are nested and do not contribute to the envelope. In Figure 6.14(b) we present the same plot but also superimpose the boomrays. The boomrays are emitted at angle $\pm\theta_b$ to the direction of motion, where $\cos\theta_b = \dfrac{1}{|x_0'|} = \dfrac{1}{M_0 - \tau}$. Therefore the angle θ_b decreases as τ increases, and this corresponds to a defocusing effect. The two boomrays emitted at the sonic time $\tau = M_0 - 1$ *coincide* with θ_b being zero, and the slope discontinuity in the envelope on the x-axis, that is present in supersonic motion, vanishes. The latter envelope point is called from now on the sonic point of the envelope. Note that no boomrays are emitted for $\tau > M_0 - 1$. The sonic wavefront emitted at time $\tau = M_0 - 1$ is tangent to the envelope at the sonic point for all times $t \geq M_0 - 1$. Figure 6.14 reveals the features of the Mach envelope. For the steady supersonic part of the motion the Mach envelope is the usual Mach wedge truncated at the point contributed by the boomrays that are emitted at $\tau = 0$. For the supersonic deceleration part of the motion, when $0 \leq \tau < M_0 - 1$, the envelope equations (6.22) and (6.23) become

$$x_E = M_0\tau - \frac{\tau^2}{2} + \frac{t - \tau}{M_0 - \tau}, \tag{6.108}$$

$$z_E = \pm(t - \tau)\sqrt{1 - \frac{1}{(M_0 - \tau)^2}}. \tag{6.109}$$

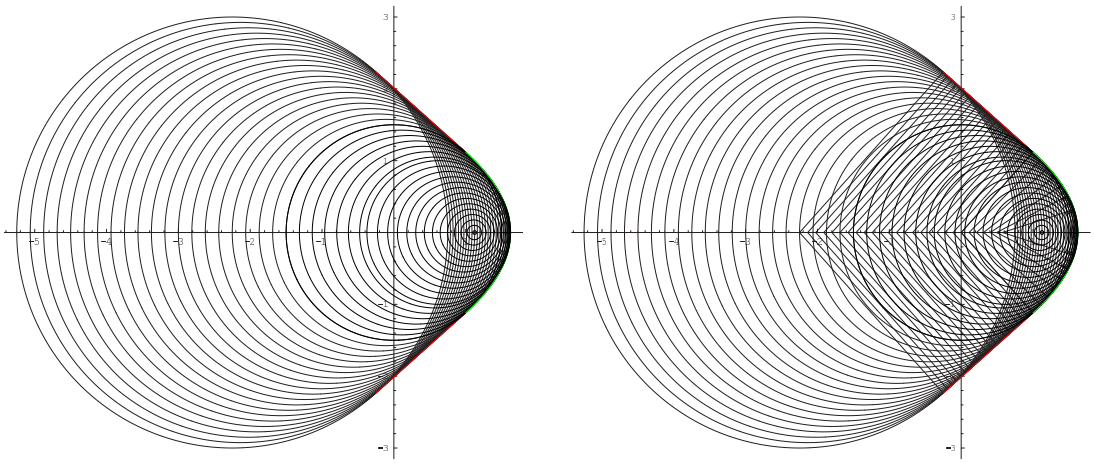

(a) The wavefronts for $t = M_0$; they form the Mach envelope for $\tau \leq M_0 - 1$) but they are nested for $M_0 - 1 \leq \tau \leq M_0$.

(b) Same as Figure 6.14(a) but also the boomrays are superimposed.

Figure 6.14: $t = M_0$: wavefront pattern and boomrays.

In Figure 6.15 we plot the envelope at the four times $t = M_0 - 1.25, M_0 - 1, M_0, M_0 + 1$. As we expect, on the x-axis for $t = M_0 - 1.25$ the envelope has a slope discontinuity but for the other three snapshots it is rounded.

There are thus important differences in the geometry of the acceleration and the deceleration scenarios. The boomrays of the acceleration scenario focus and form a fold caustic, which corresponds to the appearance of a Tricomi cusp on the Mach envelope. However the boomrays of deceleration do not focus, no caustic is formed and no cusp appears on the envelope; the only focusing point is the sonic point and we will return to this later. Therefore acceleration and deceleration through the sound speed are quite different geometrically. These geometrical differences lead to considerable differences in the associated wavefield.

• **Wavefield**

The pressure field for a decelerating point source with $x_0(t)$ as in (6.106)–(6.107) is given by the integral

$$p(x, z, t) = \frac{1}{2\pi} \int_{-\infty}^{t} \frac{H(Q(\tau))d\tau}{\sqrt{Q(\tau; x, z, t)}}, \tag{6.110}$$

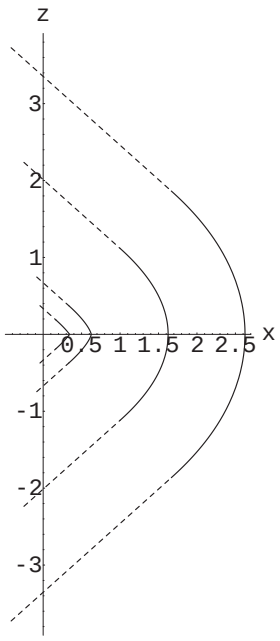

Figure 6.15: The Mach envelope for $t = M_0 - 1.25, M_0 - 1, M_0, M_0 + 1$ ($M_0 = 1.5$). The dotted part is the steady supersonic motion envelope and the solid line part is the deceleration envelope.

where

$$Q = H(-\tau)Q_s + H(\tau(M_0 - \tau))Q_d,$$

$$\text{with } Q_s = (t-\tau)^2 - (x - M_0\tau)^2 - z^2, \tag{6.111}$$

$$\text{and } Q_d = (t-\tau)^2 - (x - M_0\tau + \frac{\tau^2}{2})^2 - z^2 \tag{6.112}$$

$$= -\frac{\tau^4}{4} + M_0\tau^3 + (1 - x - M_0)\tau^2 + 2(M_0 x - t)\tau + (t^2 - x^2 - z^2). \tag{6.113}$$

The polynomial Q_d is of fourth-order in τ and therefore (6.110) is generally an elliptic integral again. As in Section 6.2.3 we will approximate this integral near the Mach envelope with a simpler expression by approximating Q_d with lower-order polynomials.

First, we prove that in a general decelerating motion in a straight line it is impossible for more than two wavefronts to pass through the same point and therefore only two roots of Q are relevant in switching on and off the $H(Q(\tau))$ factor in (6.110). To prove this we suppose that the source passes through the distinct points $x_1 < x_2 < x_3$ at $\tau_1 < \tau_2 < \tau_3$ and that the three wavefronts emitted at these times *do* go through (x, z) at $t > \tau_3$. Therefore $\sqrt{z^2 + (x - x_i)^2} = t - \tau_i$ holds for $i = 1, 2, 3$. We let now

$X_i = x - x_i$ and therefore $X_1 > X_2 > X_3$. The mean source speed over $[\tau_1, \tau_2]$ is

$$\bar{u}_{12} = \frac{x_2 - x_1}{\tau_2 - \tau_1} = \frac{X_1 - X_2}{\sqrt{z^2 + X_1^2} - \sqrt{z^2 + X_2^2}}, \tag{6.114}$$

and similarly over $[\tau_2, \tau_3]$ the mean speed is $\bar{u}_{23}$. If the motion is decelerating then $\bar{u}_{23} < \bar{u}_{12}$ which can also be written as $1/\bar{u}_{12} < 1/\bar{u}_{23}$, i.e.

$$\frac{\sqrt{z^2 + X_1^2} - \sqrt{z^2 + X_2^2}}{X_1 - X_2} < \frac{\sqrt{z^2 + X_2^2} - \sqrt{z^2 + X_3^2}}{X_2 - X_3}. \tag{6.115}$$

However inequality (6.115) is impossible because $\sqrt{z^2 + X^2}$ is a convex function; the left-hand side of (6.115) is the slope of the chord BC (see Figure 6.16) and the right-hand side is the slope of the chord AB and for a convex function the former slope is greater than the latter slope. Therefore not more than two wavefronts can pass

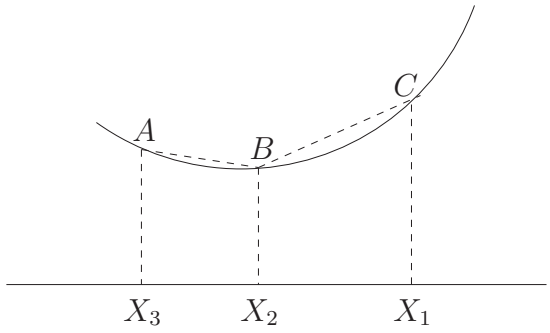

Figure 6.16: For a convex function the slope of the chord AB is less than the slope of the chord BC.

through a point in the region of influence.[7] In this case the wavefronts are exactly two. This is because $Q < 0$ as $\tau \to -\infty$ and at $\tau = t$ but for some τ we have $Q > 0$ because (x, z) is inside the region of influence; this means that Q becomes zero at exactly two values of τ. We denote these roots by τ_1 and τ_2. The maximum value of Q is attained for a τ_m such that $\tau_1 < \tau_m < \tau_2$. If (x, z) is outside the region of influence we have $Q < 0$, and the integral (6.110) is zero.

We can think of the region of influence as composed of three regions, according to whether the two wavefronts are both from Q_s, both from Q_d or one from each. We will discuss these regions with the help of Figure 6.18, where we plot Q for the five points A, B, O, C, D shown in Figure 6.17. The first region is on the left of the IW

[7]For a general accelerating motion the inequality (6.115) is reversed and therefore there could be points in the region of influence where three wavefronts may go through. For the constant acceleration case, considered earlier, such points have indeed been identified; they were the cusps.

and A is a typical point in this region. The wavefield at any point in this region is entirely determined by Q_s and $\tau_{1S} < \tau_{2S} < 0$, where τ_{1S} and τ_{2S} are the two roots of Q_s as calculated in Section 6.2.2.1). We will call this a Type I region. We can say that the presence of the decelerating part of the motion is not "felt" in this region. The wavefield integral (6.110) reduces then to

$$p = \frac{1}{2\pi} \int_{\tau_{1S}}^{\tau_{2S}} \frac{d\tau}{\sqrt{Q_s}} = \frac{1}{2B_0}. \tag{6.116}$$

Similarly the region on the right of the IW is entirely determined by Q_d and $0 < \tau_{1D} < \tau_{2D}$, where τ_{1D} and τ_{2D} are those two roots of Q_d that coalesce when D moves *on* the envelope. We will call this a Type II region. The point D is a typical point in this region. Points in the Type II region do not "feel" the presence of the steady supersonic motion. The wavefield integral (6.110) is then

$$p = \frac{1}{2\pi} \int_{\tau_{1D}}^{\tau_{2D}} \frac{d\tau}{\sqrt{Q_d}}, \tag{6.117}$$

and will be evaluated later, near the envelope.

The third region is inside the IW itself. This is a "hybrid" region where we have to use both Q_s and Q_d to determine the wavefield. Then $\tau_{1S} < 0 < \tau_{2D}$ and we will call this region a Type I-II region; the point O (the origin) is a typical point in this region. The wavefield integral (6.110) is then

$$p = \frac{1}{2\pi} \int_{\tau_{1S}}^{0} \frac{d\tau}{\sqrt{Q_s}} + \frac{1}{2\pi} \int_{0}^{\tau_{2D}} \frac{d\tau}{\sqrt{Q_d}}. \tag{6.118}$$

The points B and C on the IW have been chosen to show the threshold behaviour: B is on the IW part that separates the Type I region from the Type I-II region and therefore $\tau_{2S} = \tau_{2D} = 0$ there. The point C is on the IW that separates the Type II region from the Type I-II region and therefore $\tau_{1S} = \tau_{1D} = 0$ there. We are only interested in the behaviour of the wavefield near the envelope where the sonic boom is located. For points near the Mach envelope and in the Type I region the pressure is given by $1/(2B_0)$. For points near the envelope and in the Type II region the analysis is entirely similar to that in the accelerating case:

$$Q_d \approx -|C_1|(x - x_E) - |C_2|(\tau - \tau_E)^2, \tag{6.119}$$

$$\text{where } C_1 = \left(\frac{\partial Q_d}{\partial x}\right)_E = 2(M_0\tau_E - \frac{\tau_E^2}{2} - x_E) = -2\frac{t - \tau_E}{M_0 - \tau_E} < 0 \text{ for all } 0 < \tau_E < M_0 - 1, \tag{6.120}$$

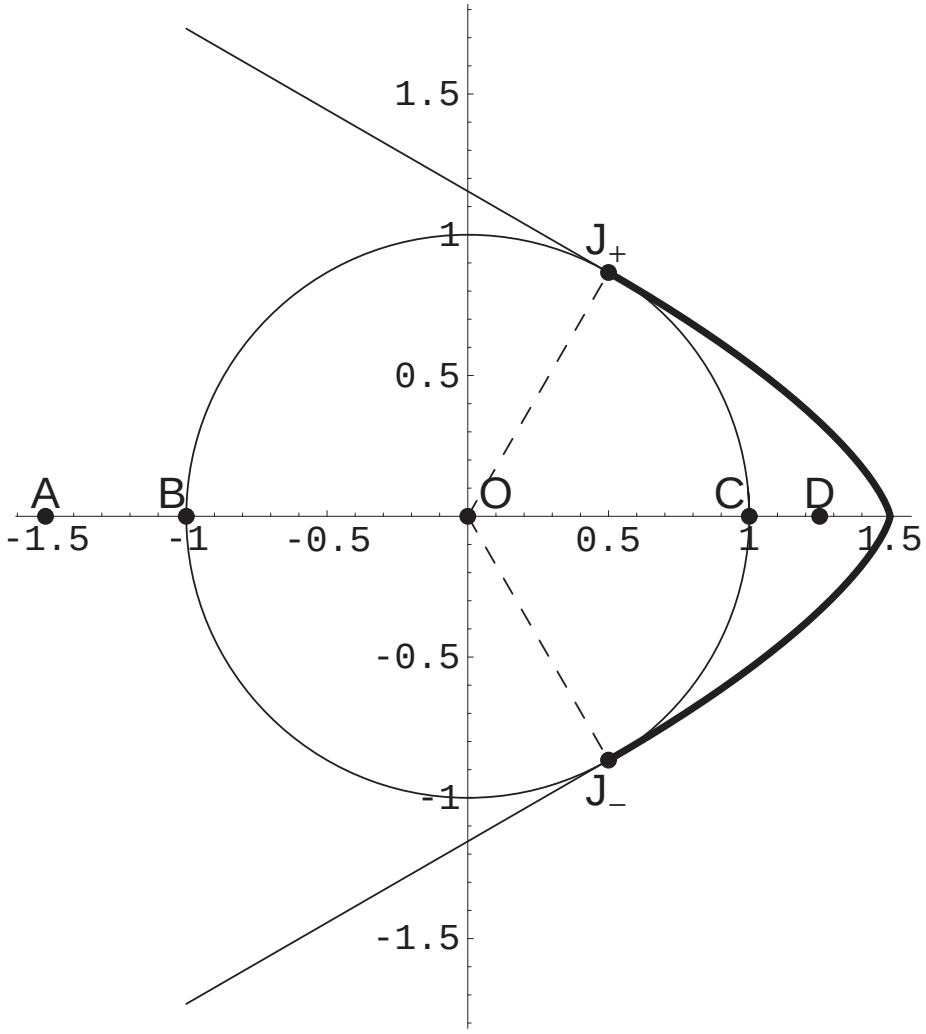

Figure 6.17: The envelope and the initial wavefront for $t = M_0 - 1$. In Figure 6.18 we plot the behaviour of Q at the points A, B, O, C and D.

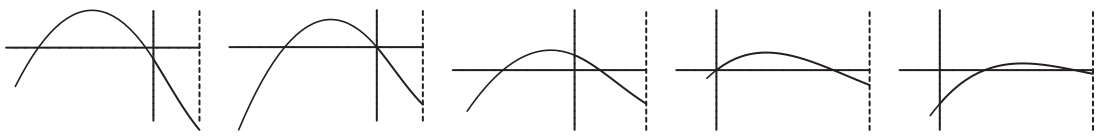

Figure 6.18: Plot of Q at points A, B, O, C and D as shown in Figure 6.17.

and

$$C_2 = \left(\frac{1}{2}\frac{\partial^2 Q_d}{\partial \tau^2}\right)_E = (1-(M_0-\tau_E)^2) - \frac{t-\tau_E}{M_0-\tau_E}, \text{ for all } 0<\tau_E<M_0-1. \tag{6.121}$$

At any envelope point $\dfrac{\partial^2 Q_d}{\partial \tau^2}$ is negative and Q_d has a local maximum. We recall that $\dfrac{\partial^2 Q_d}{\partial \tau^2}$ was also negative in steady supersonic motion (see Section 6.2.2.1), which of course confirms again the qualitative similarity between these two scenarios.

We substitute (6.119) in the integral (6.117). For $x = x_E$ the quadratic expression (6.119) has a double root at $\tau = \tau_E$; for $x < x_E$ (6.119) has two real roots

$$\tau'_{1D,2D} = \tau_E \pm \sqrt{|C_1|/|C_2|}\sqrt{x-x_E}, \tag{6.122}$$

which approximate the exact roots τ_{1D} and τ_{2D}. Therefore the integral (6.117) yields

$$p \sim \frac{1}{2\sqrt{|C_2|}}. \tag{6.123}$$

As $\tau_E \to 0$ we find $p \to \dfrac{1}{2\sqrt{B_0^2 + t/M_0}}$ and hence there is a jump discontinuity in the wavefield along the $\tau_E = 0$ boomray passing through the points where the Mach envelope of the steady part meets the Mach envelope of the deceleration part (labelled as $J_\pm$ in Figure 6.17). This discontinuity is 0 only when $t = 0$. In Figure 6.19 we plot the pressure jump across the envelope, for $-(M_0-1) \le \tau_E \le M_0 - 1$ and $t = M_0$ ($M_0 = 1.5$). We see the discontinuity at $\tau_E = 0$ and also that the pressure jump is increasing with τ_E.

Similarly, in the Type I-II region, near the points $J_\pm$, and for all times t, we use (6.119) in (6.118) and obtain

$$p = \frac{1}{2\pi B_0}\left(-\pi + \arccos\left(\frac{\tau_{1S}+\tau_{2S}}{\tau_{1S}-\tau_{2S}}\right)\right) + \frac{1}{2\pi\sqrt{|C_2|}}\left(\pi - \arccos\left(\frac{\tau'_{1D}+\tau'_{2D}}{\tau'_{1D}-\tau'_{2D}}\right)\right). \tag{6.124}$$

As expected, the expression (6.124) reduces to the Type I result $p = 1/(2B_0)$ when $\tau_{2S} = \tau_{2D} = 0$ and it reduces to the Type II result $p = 1/(2\sqrt{|C_2|})$ when we set $\tau_{1S} = \tau_{1D} = 0$. The roots $\tau'_{1D} < 0 < \tau'_{2D}$ are the expressions (6.122) and $\tau_{1S} < 0 < \tau_{2S}$ are the roots of Q_s.

Note that, at the leading envelope point for $t < M_0 - 1$ we have $\dfrac{\partial^2 Q_d}{\partial \tau^2} = 2(1-(M_0-\tau)^2) < 0$ and for $t > M_0 - 1$ we have $\dfrac{\partial^2 Q_d}{\partial \tau^2} = -2(t - M_0 + 1) < 0$.

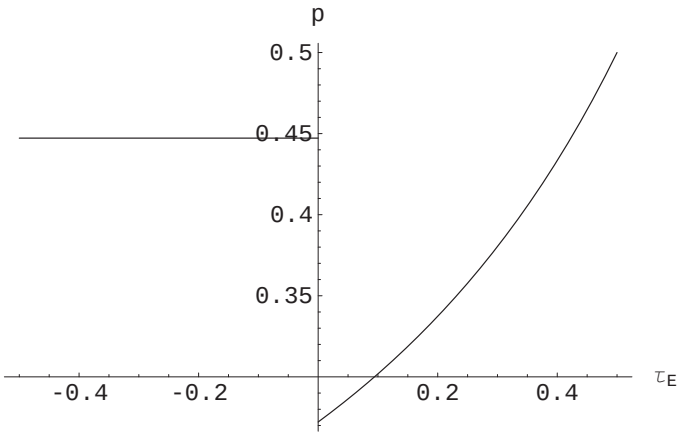

Figure 6.19: The pressure jump on the deceleration envelope, for $-(M_0-1) \le \tau_E \le M_0 - 1$, $t = M_0$ ($M_0 = 1.5$).

So at $t = M_0 - 1$ we have $\dfrac{\partial^2 Q_d}{\partial \tau^2} = -2(t - M_0 + 1) = 0$ and the pressure is singular at the sonic point, as deduced from (6.123)). Now, three roots of Q_d coalesce and therefore a cubic approximation for Q_d should be taken. A more detailed study of the singularity will not be undertaken here.

The other issue worth noting is that for $t > M_0 - 1$, $\dfrac{\partial^2 Q_d}{\partial \tau^2}$ is negative at all envelope points but *positive* at the source position. Therefore the wavefield is singular at the source. In order to investigate the singularity at the source, it is again sufficient to approximate the quartic Q_d near the source by a quadratic; we have

$$Q_d \approx (1 - (M_0 - t)^2)(\tau - t)^2 - (x - x_0(t))^2, \tag{6.125}$$

where $x_0(t) = M_0 t - t^2/2$. Hence in

$$p = \frac{1}{2\pi} \int_{M_0 - 1}^{t-\delta} \frac{d\tau}{\sqrt{Q_d}}, \tag{6.126}$$

$$\tag{6.127}$$

where $\delta = (x - x_0)/\sqrt{(1 - (M_0 - t)^2)}$, we let $t - \tau = \delta \cosh u$ and we obtain

$$p = \frac{1}{2\pi} \frac{1}{\sqrt{(1 - (M_0 - t)^2)}} \cosh^{-1}\left(\frac{t - (M_0 - 1)}{\delta}\right) \quad \text{for } M_0 - 1 < t < M_0. \tag{6.128}$$

We have thus derived a logarithmic singularity, as expected by the calculation for the steady subsonic motion. Note that for $t > M_0$ the source is switched off so the source singularity vanishes.

Note on the exact roots of the quartic Q_d

On the envelope the four roots of Q_d are τ_E, τ_E, τ_3, τ_4 where

$$\tau_{3,4} = 2M_0 - \tau_E \pm 2\frac{\sqrt{M_0 - t}}{\sqrt{M_0 - \tau_E}}. \tag{6.129}$$

We will take τ_3 to be the root with the negative sign in (6.129), and τ_4 the root with the positive sign in (6.129), so that $\tau_4 > \tau_3$. The roots τ_3 and τ_4 are real when the two conditions $t \leq M_0$ and $\tau_E \leq M_0$ hold. There is no physical reason to comply with the first condition; we can choose to consider any time t. However the second condition has to be satisfied for all t since it ensures that the source has speed greater than zero. For $t < M_0 - 1$

$$\tau_3 - \tau_E = 2\frac{(M_0 - \tau_E)^{3/2} - (M_0 - t)^{1/2}}{(M_0 - \tau_E)^{1/2}} > 0 \tag{6.130}$$

when $\tau_E < M_0 - (M_0 - t)^{1/3}$ so both τ_3 and τ_4 are greater than τ_E. Since only two out of the four roots are ever coincident we know that $\dfrac{\partial^2 Q_d}{\partial \tau^2} \neq 0$. When $t = M_0 - 1$, the root τ_3 coalesces with the double root τ_E at the sonic point and $\dfrac{\partial^2 Q_d}{\partial \tau^2} = 0$, as already remarked.

6.2.5 Manoeuvres

We now consider the wavefronts, boomrays and the Mach envelope for a motion on a curved path in a uniform medium, so that we can discern some of the features of sonic booms due to manoeuvres of a supersonic aircraft. Flight tests with manoeuvring are documented in the articles [123, 97, 34]. We will see that the type of focusing in most of the motions examined below is restricted to the formation of a fold caustic, like those formed in the other two scenarios we studied: acceleration through the sound speed and steady motion in the stratified medium $c = 1/\sqrt{1 - z}$. When the geometry is qualitatively similar, the mathematical analysis of the wavefield can be deduced from that for the acceleration scenario, seen earlier, and we hence we will not bother with amplitude questions here.

For a general trajectory $(x_0(t), z_0(t))$, the Mach number at any point is equal to $M_0 = \sqrt{{x_0'}^2 + {z_0'}^2}$ and the direction of the motion is given by z_0'/x_0'. When $M_0 < 1$ the motion is subsonic and no boomrays are emitted. When $M_0 \geq 1$, two boomrays are emitted, respectively at angle $\pm\theta_b$ to the direction of motion, where $\theta_b = \cos^{-1}(1/M_0)$.

We will call the boomrays corresponding to $-\theta_b$ right-pointing boomrays and the boomrays corresponding to $+\theta_b$ left-pointing boomrays. The corresponding equations

are for the

$$\text{left-pointing boomrays: } x - x_0 = \cos(\theta + \theta_b)s, \quad z - z_0 = \sin(\theta + \theta_b)s \tag{6.131}$$

$$\text{right-pointing boomrays: } x - x_0 = \cos(\theta - \theta_b)s, \quad z - z_0 = \sin(\theta - \theta_b)s, \tag{6.132}$$

where $\sin\theta = \dfrac{z_0'}{M_0}$, $\quad \cos\theta = \dfrac{x_0'}{M_0}$ and $0 \le s \le t-\tau$. (When $M_0 = 1$, the two boomrays are coincident with the direction of motion.)

Let us represent a point in the source trajectory by the plane polar coordinates (r, θ), as most of the motions considered below can be conveniently treated in this coordinate system. Denoting by $\hat{\mathbf{e}}_r$ and $\hat{\mathbf{e}}_\theta$ the unit vectors in the radial and transverse directions, we have that the velocity and acceleration of the source are given by

$$\dot{\mathbf{r}} = \dot{r}\hat{\mathbf{e}}_r + r\dot{\theta}\hat{\mathbf{e}}_\theta, \quad \ddot{\mathbf{r}} = (\ddot{r} - r\dot{\theta}^2)\hat{\mathbf{e}}_r + (r\ddot{\theta} + 2\dot{r}\dot{\theta})\hat{\mathbf{e}}_\theta. \tag{6.133}$$

For a circular trajectory with radius $r = R_0$ the direction of motion is tangential to the trajectory and $M_0 = R_0\dot{\theta}$. The source is taken to move anticlockwise. When $M_0 < 1$ is constant (we take $R_0 < 1, \dot{\theta} = 1$) the motion is entirely subsonic, no boomrays are emitted, and no Mach envelope is formed. In Figure 6.20 we plot the wavefront pattern arising from motion in a circle of radius $R_0 = 0.75$ (with change in direction of angle π). (Note that in all plots below the source trajectory is plotted with a red thicker line.) We can observe in Figure 6.20 a congestion of wavefronts at a certain region. This indicates intensification of the amplitude there and it can be thought of as the "precursor" of the Mach envelope that will be formed when $M_0 > 1$ (see Figure 6.21(a) below).

When $M_0 > 1$ (we now take $R_0 = 2$ but still $\dot{\theta} = 1$), in Figure 6.21(a) we plot the wavefronts and the Mach envelope. Note that the Mach envelope curves in this section are drawn using the parametric equations (6.20) and (6.21), with a blue thicker line (unless indicated otherwise). In Figure 6.21(b) we plot the boomrays and the Mach envelope. Since M_0 is constant, the boomrays are always emitted at constant angles $\pm\theta_b$, but the change in the direction of motion causes the left-pointing boomrays to focus, forming a fold caustic. This caustic is qualitatively the same as the fold caustic due to acceleration in a straight line and steady motion in a stratified atmosphere. The same picture with 6.21(a) appears in [73] and many subsequent articles.[8]

Secondly, we consider motion in a circle but with increasing angular velocity, say $\dot{\theta} = \tau$ (the source is again moving anticlockwise). In Figure 6.22(a) we plot the wavefront pattern and the Mach envelope, and in Figure 6.22(b) we plot the boomrays

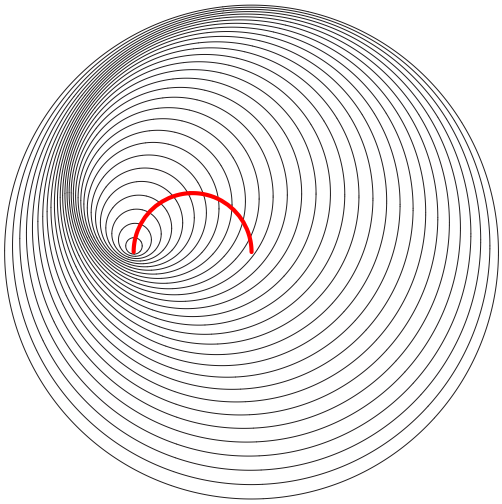

Figure 6.20: The wavefront pattern for a circular motion with radius $R_0 = 0.75 < 1$ and angular velocity $\dot{\theta} = 1$.

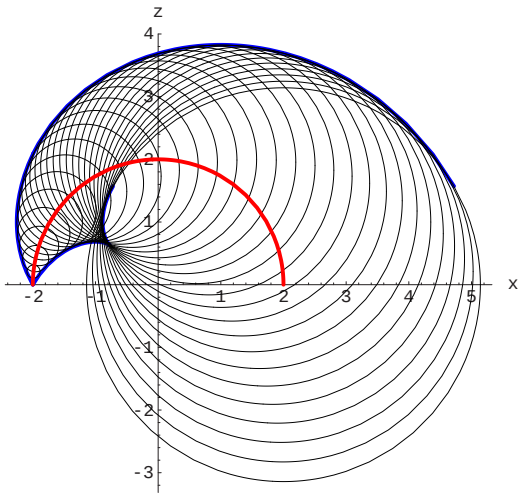

(a) The wavefront pattern and the Mach envelope.

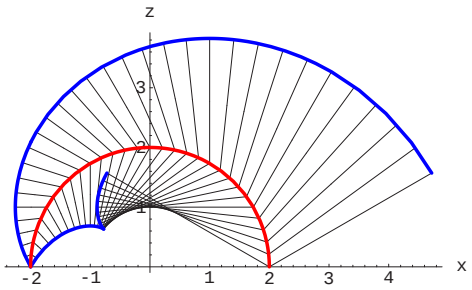

(b) The boomrays and the Mach envelope.

Figure 6.21: Circular motion with constant angular velocity ($M_0 = 2$ with $R_0 = 2$ and $\dot{\theta} = 1$).

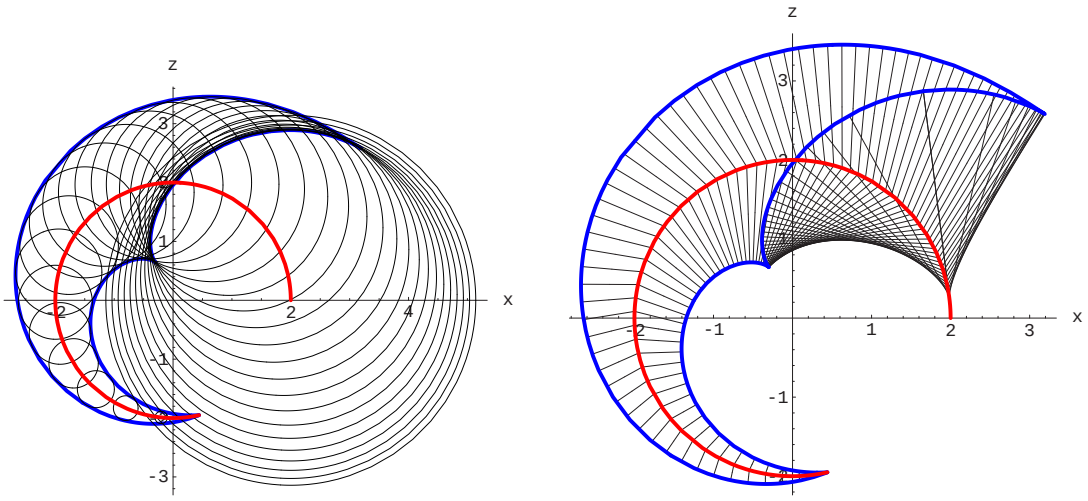

(a) The wavefront pattern and the Mach envelope.

(b) The boomrays and the Mach envelope.

Figure 6.22: Motion in a circle with non-constant angular velocity ($R_0 = 2$, $\dot{\theta} = \tau$).

and the Mach envelope (we take $0 \leq \tau \leq \pi$). We see from Figure 6.22(b) that now also the right-pointing boomrays form a fold caustic. The Mach envelope is now a closed curve featuring two Tricomi cusps, and it looks like a distorted version of the envelope of the accelerating motion in a straight line.

Thirdly, we consider a motion on the parabolic trajectory $x_0(t) = t, z_0(t) = -t^2$. This motion is an example for a motion that decelerates and then accelerates. The Mach number is $M_0 = \sqrt{1 + 4t^2}$. For $t < 0$ the source moves supersonically while decelerating, at $t = 0$ it touches the sound speed and for $t > 0$ it accelerates.

In Figure 6.23(a) we plot the wavefront pattern and the Mach envelope for for $t = 1$ and launch times $-1 \leq \tau \leq t = 1$. In Figure 6.23(b) we plot the boomrays and the Mach envelope. The boomray pattern has now some additional features. One of the two boomrays is always in the x-direction because $\dot{x}_0 = 1 =$ sound speed. When $-1 < \tau < 0$ (deceleration) the boomrays trace the light blue part of the envelope. The horizontal boomrays in this case are right-pointing. At time $\tau = 0$, the two boomrays are emitted from the origin and coincide, giving the *sonic* point of the envelope. The tangent to the envelope at this sonic point is normal to the x-axis. Subsequently, for $0 < \tau \leq 1$ the horizontal left-pointing boomrays from the acceleration phase trace *again* the part of the light blue envelope in $z \leq 0$. Therefore the $x > 0, z < 0$ region

[8] We have not seen the plot of Figure 6.20 somewhere though.

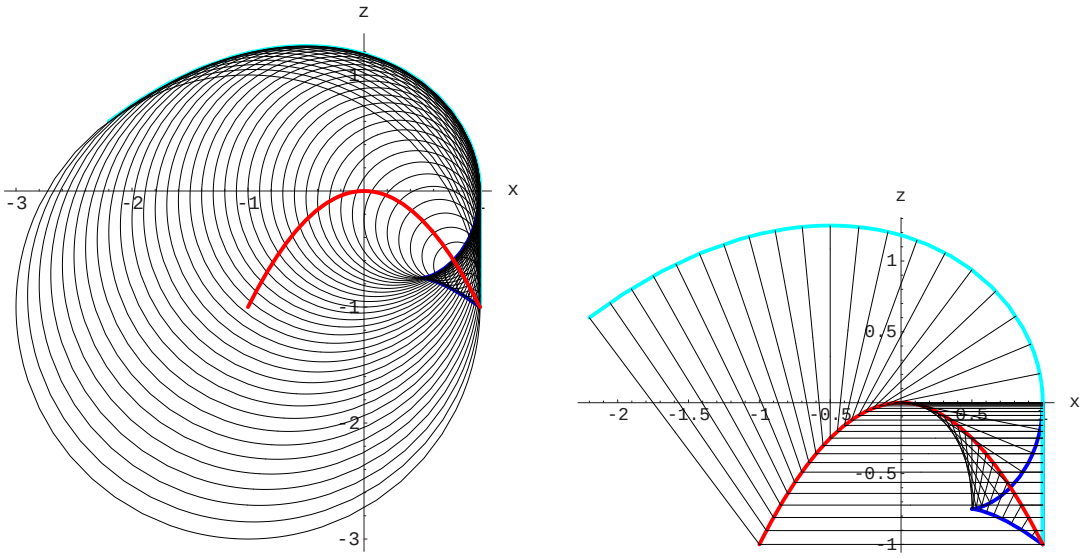

(a) The wavefront pattern and envelope ($t = 1$).

(b) The boomrays and envelope ($t = 1$).

Figure 6.23: Motion in a parabolic trajectory $x_0(\tau) = \tau, z_0(\tau) = \tau^2$: we take $t = 1$ and $-1 \leq \tau \leq t = 1$.

between the source trajectory and the Mach envelope is doubly traced; this is a direct consequence of there being always a horizontal boomray.

The right-pointing boomrays, for $0 < \tau \leq \tau^\star$ trace a darker blue envelope part which is qualitatively similar to the acceleration caustic. At $\tau = \tau^\star$ a right boomray passes through a cusp and for $\tau^\star < \tau \leq t$ the boomrays trace the part of the darker blue envelope part in a way which is qualitatively similar to that in a steady supersonic flight. We find $\tau^\star$ by setting $\dfrac{\partial^2 Q}{\partial \tau^2} = 0$:

$$\tau^\star = \frac{1}{2}\left((2t + \sqrt{1+4t^2})^{1/3} - \frac{1}{(2t+\sqrt{1+4t^2})^{1/3}} \right). \tag{6.134}$$

(Note that $\tau = 0$ is also a root of $\dfrac{\partial^2 Q}{\partial \tau^2} = 0$.)

6.2.6 Higher-order focusing

We have also investigated the possibility of identifying a motion where a focus of higher order than a fold caustic arises. Such a motion would be highly undesirable when manoeuvring a supersonic aircraft because it may lead to a very strong boom on the ground.

For cusp caustics of boomrays associated amplitudes at the ground are generally quoted to be ten times those of primary booms. (A cusp caustic of boomrays has been detected in the flight tests of [123].) After an exhaustive search, we have not been able to find in the literature an analytical example of a cusp caustic of boomrays. We subsequently achieved to pinpoint such an example and we present it in the next section. We note that when trying to construct a cusp caustic of boomrays geometrically a certain difficulty arises because the boomrays are always emitted at the angle fixed by the boomray condition. Such a constraint does not exist in a cusp caustic of ordinary rays: for, example, in the coffee-cup caustic, discussed in Chapter 3, the ray passing through the cusp is the one reflecting from the cup at right angles; however a boomray emitted at right angles to the direction of motion corresponds to an infinite source speed.

6.2.7 Accelerating motion in a stratified atmosphere

It is of practical interest to present also analytical examples for unsteady motions in nonuniform media, which would provide paradigm problems for secondary boom formation due to an unsteady motion. We studied the example for a motion with constant acceleration through the sound speed, in the stratified medium with sound speed profile $c = 1/\sqrt{1-z}$. Steady supersonic motion in this medium has been already discussed in detail in Chapter 3, and the boomray equations were derived there. We have, as in the previous parts of this chapter, $x_0(t) = -\dfrac{t^2}{2}, z_0 = 0$. As before, the motion is supersonic when $t \geq 1$. In Figure 6.24 we plot boomrays emitted at consecutive times τ and take $t = 3$, giving a finer spacing in Figure 6.25 in order to show in more detail the formation of the Mach envelope. The Mach envelope part formed by boomrays launched upwards is shown with green and the part formed by boomrays launched downwards is shown with red. Note that the Mach envelope is determined analytically as the locus of the tips of boomrays, as described in Chapter 3—see equations (3.114)–(3.116).

Comparing now Figure 6.25, Figure 3.27 in Chapter 3 (steady supersonic motion in the same atmosphere), and Figure 6.5 we observe similarities and differences. In all figures the boomrays form fold caustics; in Figure 3.27 one caustic is formed, and in Figures 6.25 and 6.5 two caustics are formed.

In Figure 6.25 the caustic is on the line $z = 1/2$ and this corresponds to one Tricomi cusp on the envelope; in Figure 3.27 the two caustics are formed symmetrically placed with respect to the line of motion, and two Tricomi cusps are formed on the envelope;

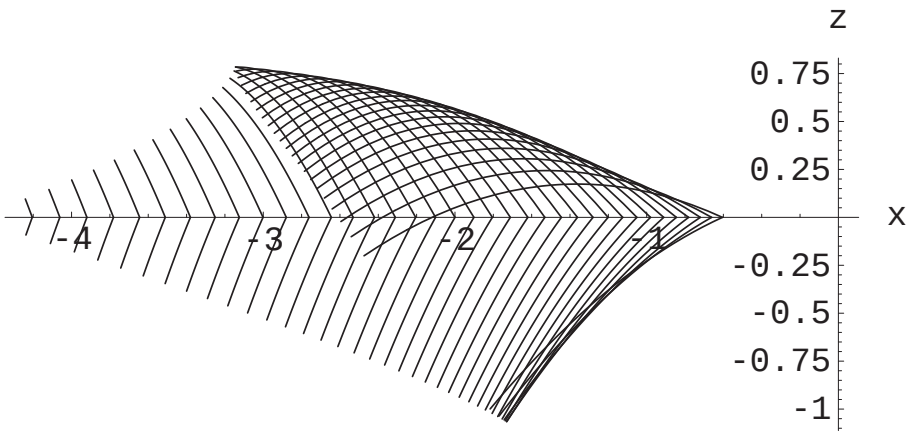

Figure 6.24: Constant acceleration in the stratified medium with sound speed profile $c = 1/\sqrt{1-z}$: Boomrays for $t = 3$, $\tau = 1.1$ to $\tau = 2.9$, in increments of 0.05.

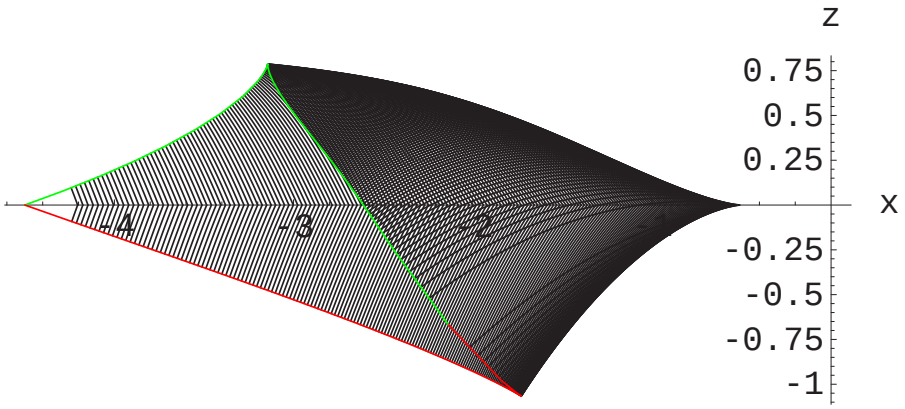

Figure 6.25: Constant acceleration in the stratified medium with sound speed profile $c = 1/\sqrt{1-z}$. The boomrays are ilustrated for $t = 3$, $\tau = 1.01$ to $\tau = 2.9$ (in increments of 0.01). The Mach envelope formed by the boomrays launched upwards is drawn with green and the Mach envelope formed by the boomrays launched downwards is drawn with red.

in Figure 6.25 this symmetry is destroyed due to the medium stratification: one caustic starts at $z = 0$ and goes up to approximately $z = 0.75$, and the other one starts at $z = 0$ and goes down to approximately $z = -1$. (Note that it is possible to find these caustics analytically.) The Tricomi cusps are not symmetric with respect to the line of flight. The Mach envelope is an open curve in Figure 3.27 and a closed curve in Figures 3.27 and 6.25, consisting of "incident" and "reflected" parts as we defined them in Chapter 3 and earlier in this chapter.

In Figure 6.26 we show the wavefronts for τ ranging from 1.1, to 2.9 in increments of 0.1. This figure is the analogue of Figure 6.7 in the current chapter and of Figure 3.25 in Chapter 3. Again, the wavefront patterns related to the incident parts of

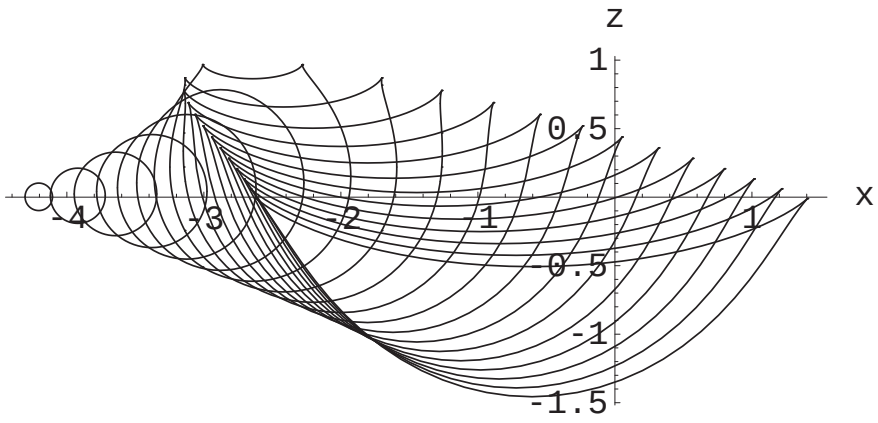

Figure 6.26: Wavefronts for $t = 3$: only supersonic part of the motion.

the envelope and to the reflected part of the envelope differ as illustrated in the schematic of Figure 6.8. Note that, as in Figure 3.25, the wavefront cusps will form a locus that is very close to the "reflected" envelope; this is still an artifact of the medium stratification and is not related to the formation of the reflected envelope.

However a novel behaviour is in store here. As seen in Figure 6.27, the analogue of Figure 6.4 for the current scenario, by time $t = 5$ the back envelope has changed curvature and at about $t = 8$ it develops a curvature discontinuity. For subsequent times, as the Mach envelope propagates further it folds on itself and this curvature discontinuity gives way to two *new* cusps. These cusps correspond to the formation of a *cusp caustic* of boomrays. In Figure 6.28 we show a magnified version of these cusps at times $t = 20$ and $t = 21$; the latter figure is qualitatively the same as Figure 3.43 in Chapter 3.

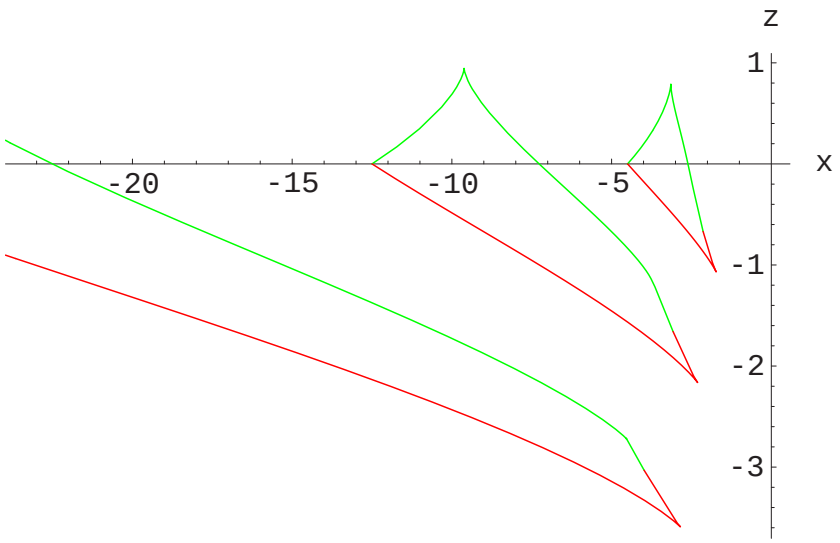

Figure 6.27: The Mach envelope for $t = 3$, $t = 5$, $t = 8$. (The envelope for $t = 8$ is very elongated in the x-direction and not all of it shown.)

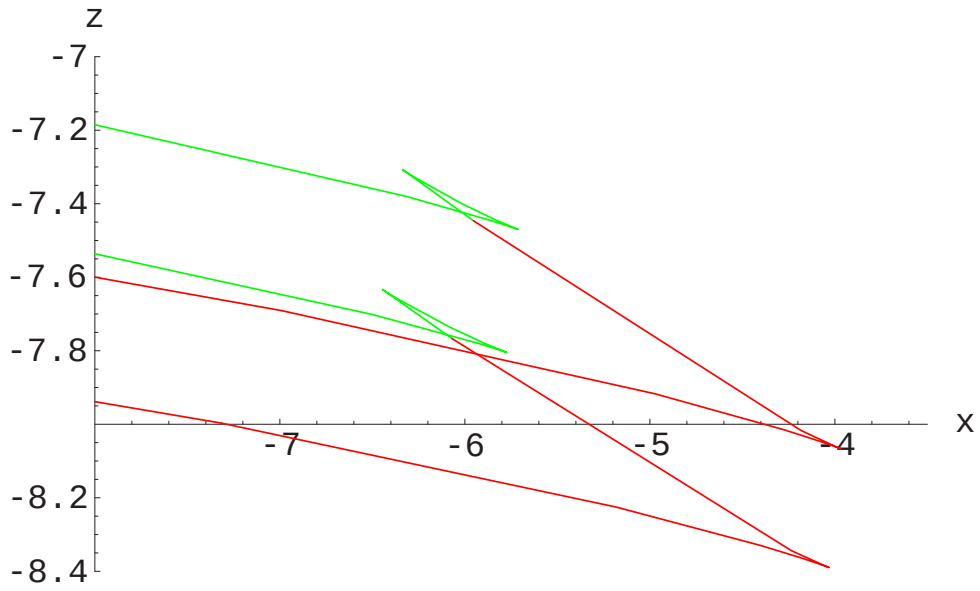

Figure 6.28: The Mach envelope for $t = 20$ and $t = 21$: magnified view near the new cusps which correspond to the formation of a cusp caustic of boomrays. The lower Tricomi cusps are also shown on each of the two envelope.

6.2.8 Perfect focus of boomrays

Dempsey [32] pinpointed two examples of perfect focusing, where all boomrays pass through the same point. We have reworked and plotted these examples below. The important point to make here is that for perfect focusing to occur at a point F, a "sound speed condition" should hold: the component of the source velocity towards F should equal the sound speed (which here is taken equal to 1). We consider the source moving from left to right, with $z_0 = 0$ and

$$x_0(\tau) = -\sqrt{\tau^2 - 1}, \quad \tau \leq -1. \tag{6.135}$$

Then the speed of the source is

$$x_0'(\tau) = -\frac{\tau}{\sqrt{\tau^2 - 1}}, \tag{6.136}$$

which is monotonically increasing with τ. The boomray angle θ_b satisfies

$$\cos\theta_b(\tau) = \frac{1}{|x_0'(\tau)|} = \frac{\sqrt{\tau^2 - 1}}{|\tau|}. \tag{6.137}$$

We consider only the left-pointing boomrays and look at the right angled triangle POF in Figure 6.29, where O is the origin. The side OF has the value 1 for all τ

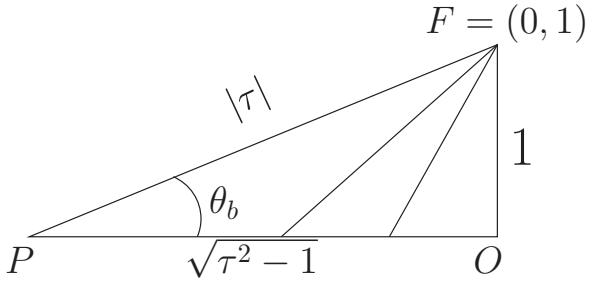

Figure 6.29: A perfect focus of boomrays (motion in a straight line).

and at $t = 1$ all boomrays pass through the perfect focus $F = (0, 1)$. The boomray pattern is of course symmetric with respect to the x-axis, and another focal point exists at $(0, -1)$.

Perfect focusing also occurs due to motion in an equiangular spiral, provided that the sound speed condition holds. We take the motion to be anticlockwise. All left-pointing boomrays pass through the origin (the right-pointing boomrays do not focus). In Figure 6.30(a) we display the source trajectory, wavefronts, and the Mach envelope (at $t = 2$). In Figure 6.30(b) we display the source trajectory, boomrays, and the Mach envelope.

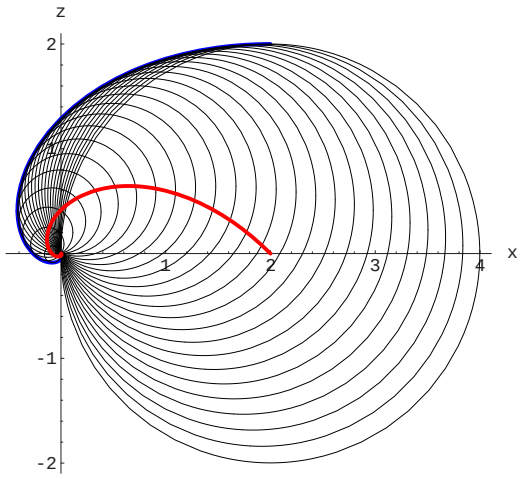

(a) The wavefront pattern and envelope for an equiangular spiral trajectory ($t = 2$).

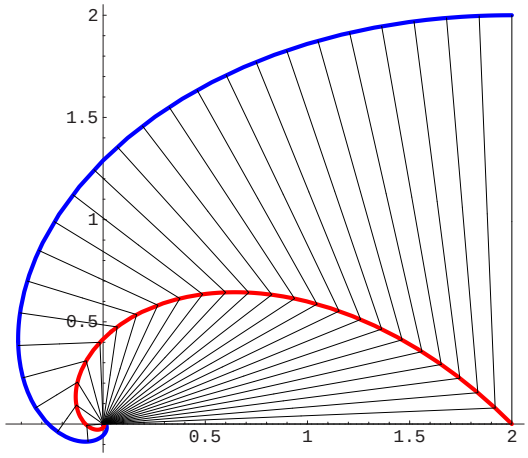

(b) The boomrays and envelope for an equiangular spiral trajectory ($t = 2$).

Figure 6.30: A perfect focus of boomrays: motion in an equiangular spiral.

6.3 Three-dimensional problems

When a supersonic source moves on a straight line, the Mach envelope in three dimensions is simply the surface of revolution of the Mach envelope in two dimensions. However, the pressure due to a point source is now given by

$$p(x, y, z, t; x_0(\tau)) = \frac{1}{4\pi} \int_{-\infty}^{\infty} \frac{\delta(g(\tau))d\tau}{f(\tau)}, \tag{6.138}$$

where $f(\tau) = |\mathbf{x} - \mathbf{x}_0(\tau)| = \sqrt{(x - x_0)^2 + y^2 + z^2}$ and $g(\tau) = t - \tau - |\mathbf{x} - \mathbf{x}_0(\tau)|$. The integral (6.138), by the integration property of the delta function, evaluates to

$$p = \frac{1}{4\pi} \sum_{i=1}^{n} \frac{1}{f(\tau_i)|g'(\tau_i)|}, \tag{6.139}$$

where n is the number of *distinct*, simple, real roots τ_i of the equation $g = 0$. Anywhere on the Mach envelope, g has coincident roots so p is not defined. Note that also in the two-dimensional analysis p was not defined on the envelope.

6.3.1 Steady motion

For steady supersonic motion $x_0(t) = -Ut$ for all t, $g = 0$ is equivalent to the same quadratic equation $Q = 0$ in Section 6.2.2.1, where Q is given by (6.24). The roots

of g are therefore given by (6.25). Therefore, the expression (6.139) evaluates to

$$p = \begin{cases} \frac{1}{2\pi} \frac{1}{\sqrt{(x+Ut)^2 - B_0^2(y^2+z^2)}} & \text{inside the Mach cone,} \\ 0 & \text{outside the Mach cone.,} \end{cases}$$

which is of course the Riemann function for $B_0^2 p_{XX} = p_{yy} + p_{zz}$. As expected, p tends to infinity as the Mach cone $(x + Ut)^2 - B_0^2(y^2 + z^2) = 0$ is approached from the inside. This constitutes a difference with the two-dimensional analysis where there is a *finite* jump in the wavefield across the Mach wedge.

6.3.2 Acceleration through the sound speed

For the uniformly accelerating motion $x_0(t) = -t^2/2$, the equation $g(\tau) = 0$ is equivalent to the quartic equation $Q = 0$, where Q is the quartic given in (6.54). The roots of g can thus be determined exactly and an exact expression for the wavefield can be obtained. However we will simplify things and get a better grasp of the qualitative behaviour if we approximate g near the Mach envelope with a lower-order polynomial as we did for the two-dimensional analysis; we undertake this below. To our knowledge, this is a new result.

Near any envelope point, excluding the cusp points, only two roots are in play when determining the sonic boom part of the wavefield, and we will thus approximate g with a quadratic:

$$g \approx g_a = \frac{1}{\tau_E}(x - x_E) + \frac{1}{2} g''(\tau_E)(\tau - \tau_E)^2 \tag{6.140}$$

where $g''(\tau_E) = \dfrac{t - \tau_E^3}{\tau_E(t - \tau_E)}$; therefore $g''(\tau_E) < 0$ on the front envelope (where $\tau_E > \tau_c = t^{1/3}$), $g''(\tau_E) > 0$ on the back envelope (where $1 < \tau_E < \tau_c$), and $g''(\tau_E) = 0$ at the cusp (where $\tau = \tau_c$). Note that $g_a(\tau) = \dfrac{-Q_a(\tau)}{2(t - \tau_E)}$ where Q_a was the quadratic approximation of Q in the two-dimensional analysis; this relation provides a clear link of the approximation method here with the approximation method of the two-dimensional analysis.

The roots of g_a are real when $x - x_E$ has opposite sign to $g''_E = g''(\tau_E)$ and are given by

$$\tau_{a\pm} = \tau_E \pm \sqrt{-\frac{2}{g''_E} \frac{(x - x_E)}{\tau_E}}. \tag{6.141}$$

The derivative of g_a, evaluated at these two roots is

$$g_a'(\tau_{a\pm}) = g_E''(\tau_{a\pm} - \tau_E) = \pm \text{sign}(g_E'') \sqrt{-2g_E'' \frac{(x - x_E)}{\tau_E}}. \tag{6.142}$$

Also

$$f = t - \tau_i \approx f_a = t - \tau_E \tag{6.143}$$

Therefore from (6.139), (6.142) and (6.143) we obtain

$$p \sim \frac{1}{4\pi} \left(-2g_E'' \frac{(t - \tau_E)^2}{\tau_E} (x - x_E) \right)^{-1/2}. \tag{6.144}$$

Expression (6.144) constitutes the sonic boom part of the wavefield; p tends to infinity with an $(x - x_E)^{-1/2}$ power law as the Mach envelope is approached from inside. The latter result is different from the analogous two-dimensional analysis where there is a *finite* jump in the wavefield across the front envelope, and there is a logarithmic singularity on both sides of the back envelope.

Just outside the envelope and inside the IW g has one real root. As a point (x, y, z) approaches the Mach envelope this root tends to $\tau_4 = -\tau_E + 2\sqrt{t/\tau_E}$ (see (6.59) in the two-dimensional analysis) and the corresponding limit of p is given by

$$p_l = \frac{1}{4\pi} \left(\frac{1}{f(\tau_4)|g'(\tau_4)|} \right). \tag{6.145}$$

Since $f(\tau_4) = t - \tau_4$ and $|g'(\tau_4)| = 1 + \dfrac{\tau_4(x_E + \tau_4^2/2)}{t - \tau_4}$, (6.145) yields

$$p_l = \frac{1}{4\pi} \left(\frac{\tau_E^{3/2}}{2t^{1/2}(t^{1/2} - \tau_E^{3/2})^2} \right). \tag{6.146}$$

The denominator in (6.146) becomes zero at the cusps. At the cusp the wavefield is more singular as $g_E'' = 0$. Three of the roots of g coalesce and we need to approximate g with a cubic:

$$g \approx g_c = \frac{1}{\tau_c}(x - x_c) + g'''(\tau_c) \frac{(\tau - \tau_c)^3}{6}, \tag{6.147}$$

where $g'''(\tau_c) = g_c''' = \dfrac{-3}{(t^{2/3} - 1)} < 0$. The triple root of g_c is

$$\tau_{\text{cusp}} = \tau_c + \left(-\frac{6(x - x_c)}{g_c''' \tau_c} \right)^{1/3}. \tag{6.148}$$

Therefore on either side of the cusp, at leading order, p is given by

$$p_c \sim \frac{1}{2\pi} \frac{6^{-2/3}\tau_c^{2/3}}{(t-\tau_c)|g_c'''|^{1/3}} |x - x_c|^{-2/3}. \tag{6.149}$$

From (6.149) we conclude that at the cusp p goes to infinity with the power law $|x - x_c|^{-2/3}$.

We close this section by plotting the trace of the fold caustic with a horizontal plane, which models the ground. The fold caustic is the surface

$$y_c^2 + z_c^2 = -\left(\frac{2}{3}x_c + \frac{1}{3}\right)^3, \tag{6.150}$$

obtained by revolution of (6.47) around the x-axis. The intersection of (6.150) with the ground, which is represented here by $z = z_g$, is thus

$$y_c^2 = -\left(\frac{2}{3}x_c + \frac{1}{3}\right)^3 - z_g^2. \tag{6.151}$$

It is on this curve that the boom is loudest. In Figure 6.31 we plot (6.151), taking $z_g = -8$. We also plot the (x, y)-cut of (6.151) at the horizontal plane of motion (dashed line). This curve is what we had arrowed as the "caustic" in Figure 1.3.

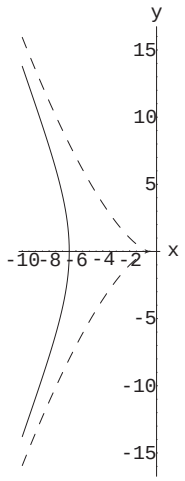

Figure 6.31: The trace of the fold caustic at the ground. The (x, y)-cut of the fold caustic at the height of the source ($z = 0$) is also plotted (with a dashed line).

6.4 The link between Chapter 6 and Chapter 7

In this chapter when we evaluated the wavefield near the Mach envelope for constant-acceleration motions in two and three dimensions we identified singularities that were incompatible with the small-amplitude assumption of linear theory. However, solving corresponding nonlinear problems is a formidable task. Therefore in the next chapter we will solve a simpler one-dimensional nonlinear problem. This will be itself a demanding task and will reveal an unexpectedly rich structure. We will see that nonlinearities, however small they may be, regularise the sonic singularities.

Chapter 7

Solution of the Kinematic Wave Equation with an accelerating point source

7.1 Introduction

In this chapter we solve, mainly analytically, the inhomogeneous Kinematic Wave Equation

$$u_t + \left(\frac{u^2}{2}\right)_x = A\delta\left(x - \frac{t^2}{2}\right), \text{ with the initial condition } u(x,0) = 1, \tag{7.1}$$

where A is any real number. Here, δ stands for the Dirac delta function and the equation is interpreted in the sense of distributions. Letting $u = 1 + Av$ we obtain the equivalent form

$$v_t + (1 + Av)v_x = \delta\left(x - \frac{t^2}{2}\right), \text{ with the initial condition } v(x,0) = 0. \tag{7.2}$$

This is a model equation for the interaction of nonlinearity with a point force that accelerates through the sound speed. The point force is represented here by the singular source term $\delta(x - t^2/2)$ and the sound speed by the initial value $u = 1$ in (7.1), or by the undisturbed characteristic speed 1 in (7.2). The displacement of the source is $x(t) = t^2/2$ (uniform acceleration) and therefore its velocity at time t is $\dot{x}(t) = t$. Consequently, for $0 < t < 1$ the source is subsonic, it passes through a sonic point at $t = 1$, and it is supersonic for $t > 1$.

Problem (7.1) is interesting because it constitutes an analytically tractable paradigm for the inclusion of nonlinearities in higher-order problems that involve accelerating motion, such as the rocket propulsion of carriages with the aim of achieving a certain

speed [107] and the pantograph problem [42, 61] related to an accelerating electric locomotive. It is also a paradigm for problems in more space dimensions such as the accelerating flight of a supersonic aircraft [73, 103]. In these and many other examples nonlinearity is important for determining the amplitudes correctly, but usually this cannot be tackled analytically. Therefore, any insight provided from paradigm problems is very valuable.

There is limited literature devoted to one-dimensional problems related to the nonlinear problem (7.1). H. Huang has performed direct numerical simulations for the related problem with small diffusion and with the source replaced by a narrow Gaussian [58]. The simpler problem of a point source moving with constant velocity has been considered by Hoffman [57] in the context of MHD, and by Whitham in [126]. Numerical simulations in the case of a stationary point source have been presented by LeVeque [69] for modelling nonlinear traffic flow with on-ramps or exits. An abbreviated version of the results in this chapter appears in the article [64].

The outline of the chapter is as follows: in Section 7.2 we show that a singularity arises at the sonic point from the linear approximation of (7.2) when A is small. To investigate whether the inclusion of nonlinearity converts the singularity into a finite value, in Section 7.3.1 we solve the nonlinear problem when A is positive and in Section 7.3.2 when A is negative. We summarise our results and draw conclusions in Section 7.4.

7.2 Linear problem

In order to demonstrate the appearance of the sonic singularity, we will solve below the linear approximation of problem (7.1). We linearise equation (7.2) around the state $u = 1$ by neglecting the quadratic term Avv_x, under the assumption of small A. We thus obtain[1]

$$v_t + v_x = \delta\left(x - \frac{t^2}{2}\right), \qquad v(x,0) = 0. \tag{7.3}$$

The characteristic projections are the straight lines $x = t + x_0$. A characteristic diagram with the characteristics $-1 < x_0 < 1/2$ is shown in Figure 7.1. The parabola $x = t^2/2$, representing the source path is also shown. The left dashed line is the characteristic tangent at the sonic point, called the sonic tangent from now on. The right dashed line is the characteristic carrying the disturbance emitted by the source initially (called the origin characteristic from now on) and this meets the source again at the time $t = 2$. The characteristics can be classified into three types, according to

[1]The problem appears in [86], exercise 4.6, p. 143.

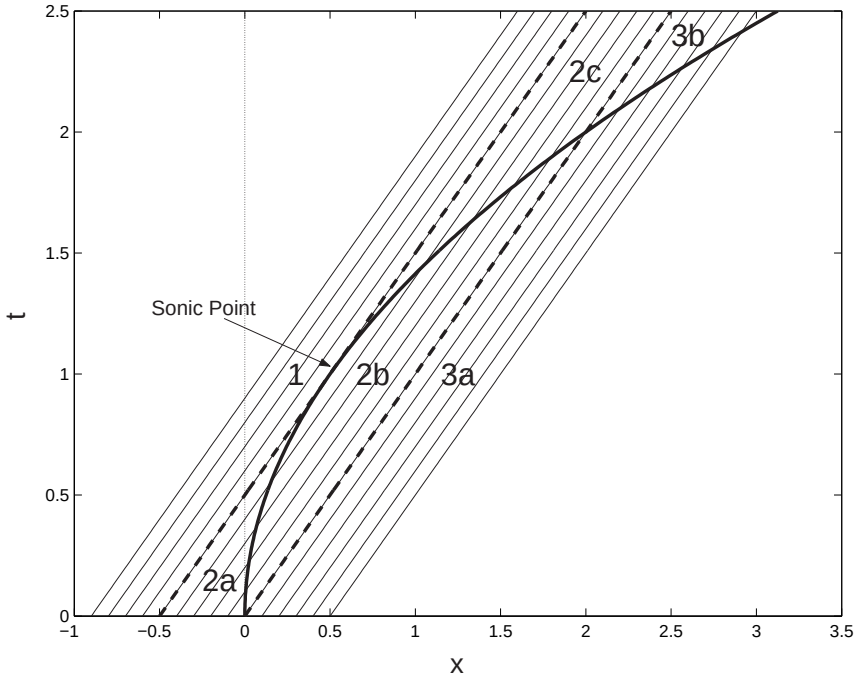

Figure 7.1: Characteristics for the linear problem. The various regions marked correspond to values of u as explained in the text.

the number of times they cross the source path. Those of Type1, on the left of the sonic characteristic ($x_0 < -1/2$), do *not* cross the source; those of Type2, between the sonic characteristic and the origin characteristic ($-1/2 < x_0 < 0$) cross *twice*, and those of Type3 on the right of the origin characteristic ($x_0 > 0$) cross *once*. The ordinary differential equation

$$\frac{dv}{dt} = \delta\left(t + x_0 - \frac{t^2}{2}\right) \tag{7.4}$$

holds on each characteristic. The *real* roots of the argument of the delta function $g(t; x_0) = t - t^2/2 + x_0$, are exactly the crossing times. To integrate (7.4) along the characteristic, we use the fact that

$$\int_a^b \delta(g(t))dt = \sum_i \frac{1}{|g'(T_i)|} \tag{7.5}$$

if g has simple zeros T_i in (a, b).

Therefore $v = 0$ before a crossing has occurred, $v = \dfrac{1}{|g'(t_1)|} = \dfrac{1}{\sqrt{1+2x_0}}$ after one crossing at $t = t_1$, and $v = \dfrac{1}{|g'(t_1)|} + \dfrac{1}{|g'(t_2)|} = \dfrac{2}{\sqrt{1+2x_0}}$ after two crossings at $t = t_1$ and $t = t_2$.

Therefore $v = 0$ in the regions 1, $2a$ and $3a$, $v = v(x,t) = \dfrac{1}{\sqrt{1+2(x-t)}}$ in regions $2b$ and $3b$ and $v = v(x,t) = \dfrac{2}{\sqrt{1+2(x-t)}}$ in region $2c$.

When $t < 1$ the jump in v at the source is $\dfrac{1}{1-t}$. This jump becomes infinite at the sonic point (arrowed in Figure 7.1). After the sonic point, an infinite jump continues on the sonic tangent $x = t - 1/2$ and a finite jump continues with the source and has value $\dfrac{1}{t-1}$. A jump of fixed value 1 *propagates* along the characteristic $x = t$ undisturbed from the origin to infinity.

We have presented the exact solution of the linearised problem and deduced that a sonic singularity emerges. Such a singularity violates the assumption of small disturbances tied to the linear problem. We will solve below the nonlinear problem (7.1), and show that nonlinearity converts the sonic singularity into a finite value.

7.3 Nonlinear problem

Returning to the problem (7.1), the characteristic projections have velocity $dx/dt = u$. Since the variation of u along the characteristics is governed by

$$\frac{du}{dt} = A\delta(x - t^2/2), \tag{7.6}$$

u is constant along characteristics except for jumps when crossing the source. Therefore before the characteristics cross the source, they are still the straight lines $x = t + x_0$. We still classify the characteristics by Type1, Type2 and Type3 *before* they cross the source. Type1 characteristics never cross the source as in the linear problem. If a Type2 characteristic crosses the source at time τ, u will change to a new value we call $u_{2R}(\tau)$, and the new characteristic, called Type2R, is

$$x = \frac{\tau^2}{2} + u(t - \tau). \tag{7.7}$$

We shall show below that for any characteristic crossing the source *from left to right* at time τ, the relation between u_L and u_R, is

$$u_R = \tau + \sqrt{(u_L - \tau)^2 + 2A}. \tag{7.8}$$

Therefore, applying (7.8) to the Type2R characteristics we find that

$$u_{2R} = \tau + \sqrt{(1 - \tau)^2 + 2A} \tag{7.9}$$

Finally Type3 characteristics always cross the source. After crossing, they are called Type3L and their velocity is $u_{3L} = \tau - \sqrt{(1-\tau)^2 - 2A}$, found according to the general relation

$$u_L = \tau - \sqrt{(u_R - \tau)^2 - 2A}, \tag{7.10}$$

satisfied by any characteristic crossing the source *from right to left* at time τ. We now derive (7.8) and (7.10). Let us define the new variable

$$\xi = x - t^2/2 \tag{7.11}$$

so that, in the (ξ, t)-plane, the source path transforms to the straight line $\xi = 0$ and the characteristics have velocity

$$\dot{\xi} = \dot{x} - t = u - t \text{ with } u \text{ varying on them as } \dot{u} = A\delta(\xi). \tag{7.12}$$

Differentiating $\dot{\xi}$ with respect to t, we obtain

$$\ddot{\xi} = \dot{u} - 1 = A\delta(\xi) - 1. \tag{7.13}$$

Multiplying (7.13) by $\dot{\xi}$, integrating over t, and applying the initial conditions, we have

$$\frac{\dot{\xi}^2}{2} = A(H(\xi) - H(x_0)) - \xi + x_0 + 1/2 \tag{7.14}$$

If a characteristic crosses the source, then applying (7.14) just on the left of the source ($\xi = 0^-$) and just on the right ($\xi = 0^+$), and taking the difference, we obtain

$$\frac{\dot{\xi}_R^2}{2} - \frac{\dot{\xi}_L^2}{2} = A \tag{7.15}$$

and using (7.12) we rewrite (7.15) as

$$(u_R - t)^2 - (u_L - t)^2 = 2A, \tag{7.16}$$

where t is the crossing time. This can also be obtained by a Rankine-Hugoniot type argument using the conservation law (7.1). We therefore have

$$u_R = t \pm \sqrt{(u_L - t)^2 + 2A} \quad \text{and} \quad u_L = t \pm \sqrt{(u_R - t)^2 - 2A}. \tag{7.17}$$

For characteristics crossing the source from left to right the velocity both on the left and on the right is *larger* than the source velocity. To satisfy this we must select the *positive* roots in (7.17). The first one of these equations is precisely relation (7.8), where $t = \tau$. However, for characteristics crossing the source from right to left the velocity at both sides is *smaller* than the source velocity. Therefore in (7.17) we have

to pick instead the negative roots and the second equation is precisely (7.10), where $t = \tau$.

We finally note that relation (7.10) is also to be applied if the Type2R characteristics cross the source from right to left; they would then be called Type2RL characteristics.

As we expect from (7.6), if $A > 0$ the characteristics become faster on crossing the source, but if $A < 0$ they become slower. We also deduce from the above discussion that whereas all Type2 characteristics cross the source for any $A > 0$, for negative A only characteristics with $\tau < \tau_m = 1 - \sqrt{2|A|}$ cross, since u_{2R} becomes complex if τ_m is exceeded. These first differences between the $A > 0$ and $A < 0$ cases indicate that the respective solutions will differ significantly. Therefore we first develop the case $A > 0$ in Section 7.3.1 and later the case $A < 0$ in Section 7.3.2.

7.3.1 Positive force ($A > 0$)

In addition to the characteristic families of Type 1, 2 and 3 (and the deflected families Type3L, Type2R and Type2RL), another family of characteristics appears in the nonlinear problem for $A > 0$. These characteristics all start from $x_0 = -1/2$, reach the source at $t = 1$ and then travel for some time along the source[2]. If they emerge out on the left where $\xi = 0^-$, and at time $\tau \geq 1$, then (7.14) implies $\dot{\xi} = 0$, i.e. $u = u_4(\tau) = \tau$, i.e. the characteristics emerge tangent to the source. We will call these characteristics Type4. If they emerge on the right, where $\xi = 0^+$, then (7.14) implies $\dot{\xi} = u - \tau = \pm\sqrt{2A}$ and since $u > \tau$ we have $u = u_{4R}(\tau) = \tau + \sqrt{2A}$ and the characteristics emerge at an angle to the source. We will call the latter characteristics Type4R.

Type2R and Type4R characteristics become faster as τ increases and each family, if not prohibited, would focus into an envelope in a finite time. The solution would become multi-valued beyond the envelopes and therefore the envelopes' formation has to be prevented by the introduction of shocks as we elaborate below. As an example, we show the focusing of the Type2R family (for $A = 1$) in Figure 7.2.

◇ Shock from the origin

Since the Type2R characteristics are faster than Type3, these families intersect and a multi-valued region is formed which is resolved by the introduction of a shock starting at the origin. We will call this ShockI from now on. We shall parametrise the path

[2]these characteristics will therefore fill what initially appears as an empty region between the sonic tangent and the $\tau = 1$ characteristic which has velocity $u_{2R}(\tau = 1) = 1 + \sqrt{2A}$

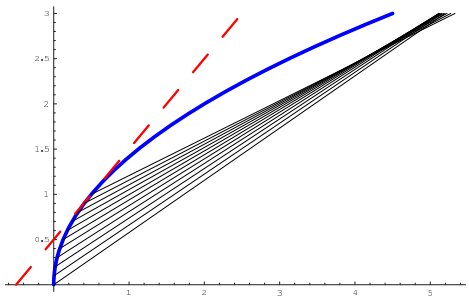

Figure 7.2: Focusing of the Type2R characteristics ($A = 1$)

(x_s, t_s) of ShockI by the value of τ parametrising the Type2R characteristics. The velocity of ShockI obeys the Rankine-Hugoniot condition,

$$\frac{dx_s}{dt_s} = \frac{1}{2}(1 + u_{2R}(\tau, A)) \tag{7.18}$$

which arises from the conservation law (7.1). In (7.18) we rewrite $dx_s/dt_s = x_s'/t_s'$, where $'$ denotes differentation with respect to τ, and this leads to an expression for x_s'. Furthermore, the characteristic expression (7.7) relates x_s and t_s, where $u = u_{2R}(\tau, A)$, and differentiating it we obtain a second expression for x_s',

$$x_s' = \tau + (t_s' - 1)u(\tau) + u'(\tau)(t_s - \tau). \tag{7.19}$$

Equating the two expressions we found above for x_s' we obtain obtain the linear first-order ordinary differential equation for t_s

$$t_s' + \frac{2u'}{u-1}t_s = 2(u - \tau + u'\tau) \tag{7.20}$$

which, upon using the integrating factor, is rearranged into

$$\frac{d}{d\tau}((u-1)^2 t_s) = 2(u-1)(u - \tau + u'\tau) \tag{7.21}$$

and integrated easily to give

$$t_s(\tau; A) = \frac{2\tau\sqrt{(1-\tau)^2 + 2A}}{\tau - 1 + \sqrt{(1-\tau)^2 + 2A}} = \frac{2\tau(u-\tau)}{u-1}. \tag{7.22}$$

Equation (7.21) is valid for any shock with $u = 1$ on one side and will also be of use later. The parametric expression (7.22) is potentially valid for $0 \leq \tau \leq 1$. However,

it may cease to be valid when ShockI hits the source or an envelope attempts to form on ShockI. We examine these two possibilities and we find that the first is realised for $0 < A < 0.27551$ and the second for $0.27551 < A < 1/2$. We will label with τ_{SI} the characteristic entering ShockI on the source; τ_{SI} is determined by solving algebraically the equation $x_s = t_s^2/2$. (This leads to a quartic in τ and care must be applied to select the root that is real and less than 1.) The point on ShockI where an envelope attempts to form on the shock is also determined algebraically by solving $dt_s/d\tau = 0$ (this also leads to a quartic for τ and again the chosen τ has to be the one that is real and less than 1).

Therefore it is for $A \geq 1/2$ that expression (7.22) is valid for all $0 < \tau \leq 1$. The endpoint of ShockI in this case is always at time $t = 2$ (and corresponds to $x = 3/2 + \sqrt{2A} \geq 5/2$ with equality at $A = 1/2$). It is useful to compare this with the linear problem; $t = 2$ was the time that the initial disturbance $x = t$ was intersecting the source path. Therefore we can think of ShockI as the path of the initial disturbance, modified by the nonlinearity. ShockI velocity is always greater than 1 and increases pointwise with A.

◇ Second shock

From our findings above it is obvious that for any $A < 1/2$ not all Type2R characteristics enter ShockI; the remaining ones would cross Type4R characteristics leading to a multi-valued region. To resolve this a second shock has to be introduced with Type4R entering it from the left and Type2R characteristics entering it from the right. Renaming $u_{4R} = u_1$ and $u_{2R} = u_2$, the Rankine-Hugoniot condition for ShockII is

$$\frac{dx_s}{dt_s} = \frac{1}{2}(u_1(\tau_1, A) + u_2(\tau_2, A)) \tag{7.23}$$

where (x_s, t_s) now labels a general point on ShockII. To decide where to start ShockII, we find the earliest time of singularity; for both families this is at time $t = 1 + \sqrt{2A}$, on the $\tau = 1$ characteristic. Therefore ShockII has to start at $x = 1 + \sqrt{2A} + 2A, t = 1 + \sqrt{2A}$. We note that it starts with zero strength as $u_{2R}(1) = u_{4R}(1) = 1 + \sqrt{2A}$. ShockII can be analytically calculated only in the vicinity of its starting point by using the parametric expressions for u_{4R} and u_{2R}: the relevant analysis is at the end of this section. For all later times it can only be determined numerically and for this we use the following method. From the Type4R and Type2R characteristics the

following two relations hold respectively on ShockII,

$$x_s = \frac{\tau_1^2}{2} + u_1(\tau_1, A)(t_s - \tau_1), \tag{7.24}$$

$$x_s = \frac{\tau_2^2}{2} + u_2(\tau_2, A)(t_s - \tau_2). \tag{7.25}$$

Differentiating (7.24) and (7.25) with respect to t_s, then combining in turn with the Rankine-Hugoniot condition (7.23) and solving for $d\tau_1/dt_s$ and $d\tau_2/dt_s$ we obtain the following system of ordinary differential equations for τ_1 and τ_2:

$$\frac{d\tau_1}{dt_s} = \frac{u_1(\tau_1) - u_2(\tau_2)}{2(u_1(\tau_1) - \tau_1 - u_1'(\tau_1)(t_s - \tau_1))}, \tag{7.26}$$

$$\frac{d\tau_2}{dt_s} = -\frac{u_1(\tau_1) - u_2(\tau_2)}{2(u_2(\tau_2) - \tau_2 - u_2'(\tau_2)(t_s - \tau_2))}. \tag{7.27}$$

The system (7.26)–(7.27) determines any shock that joins two non-constant u states, u_1 and u_2. It is therefore the only other tool we need, further to equation (7.21), for completing the solution. This system is easily solved numerically by using the Matlab ODE solver ode45.

To solve the system we also have to provide initial conditions for τ_1 and τ_2; for ShockII these are supplied by the starting point data, i.e. $\tau_1 = \tau_2 = 1$ at $t_s = 1+\sqrt{2A}$. We need to be careful when imposing the initial condition on ShockII numerically, because the denominator of (7.26) is zero at the starting point of the shock and (7.26) has a singularity there. By the geometry of the characteristic families it is clear that τ_1 should be increasing with t_s, whereas τ_2 should be decreasing. Therefore, we ensure this by selecting an initial value for τ_1 slightly larger than 1 and an initial value for τ_2 slightly smaller than 1 (below we find that near the shock starting point $\tau_1 \sim 1+c_2\sqrt{\epsilon}$, $\tau_2 \sim 1 - \left(\frac{2}{3}c_2\right)^{1/2}\epsilon^{3/4}$ where c_2 is a function of A. Using the latter expressions, with a fixed value of ϵ, would provide a more detailed way to choose τ_1 and τ_2). When the integration of the system is completed we plot τ_1 and τ_2 versus t_s in order to check that the former is monotonically increasing whereas the latter is monotonically decreasing with t_s. As a further quality control on the integration we also check that (7.24) and (7.25) agree (within tolerance).

◇ Analytical calculations in the vicinity of ShockII at starting point
Calculating the derivatives of

$$u_1(\tau_1) = u_{4R}(\tau_1) = \tau_1 + \sqrt{2A} \quad (\tau_1 \geq 1)$$

$$\text{and } u_2(\tau_2) = u_{2R}(\tau_2) = \tau_2 + \sqrt{(1-\tau_2)^2 + 2A} \quad (\tau_2 \leq 1)$$

we find that the first derivative $u_1'(1) = u_2'(1) = 1$ is equal at both sides at the starting point of ShockII. However, u'' jumps from $u_1''(1_+) = 0$ to $u_2''(1_-) = 1/\sqrt{2A}$. This discontinuity tends to zero as $A \to \infty$.

To investigate the vicinity of the starting point, we define $\epsilon > 0$ through the relation

$$t_s = 1 + \sqrt{2A} + \epsilon. \tag{7.28}$$

As we remarked above when we discuss the initial condition for ShockII, we expect τ_1 to change by some small positive amount dependent on ϵ and τ_2 by some small negative amount. Therefore set

$$\tau_1 = 1 + \delta_1, \tag{7.29}$$

$$\tau_2 = 1 - \delta_2, \tag{7.30}$$

where $\delta_1 \ll 1$ and $\delta_2 \ll 1$ are functions of ϵ. To determine δ_1 and δ_2 we will insert (7.28), (7.29) and (7.30) in the system (7.26)–(7.27). To facilitate this we will first expand the numerator of the system

$$\begin{aligned} u_1(\tau_1) - u_2(\tau_2) &= u_1(1) - u_2(1) + u_1'(1)\delta_1 + u_2'(1)\delta_2 - u_2''(1)\frac{\delta_2^2}{2} + O(\delta_2^4) \\ &= \delta_1 + \delta_2 - \frac{\delta_2^2}{2\sqrt{2A}} + O(\delta_2^4) \end{aligned} \tag{7.31}$$

Note that the errors in (7.31) are $O(\delta_2^4)$ because $u_2'''(1) = 0$.

Secondly, we consider the denominator of (7.26):

$$2(u_1(\tau_1) - \tau_1 - u_1'(\tau_1)(t_s - \tau_1)) = 2(\sqrt{2A} - t_s + \tau_1) = 2(\delta_1 - \epsilon). \tag{7.32}$$

Since τ_1 is increasing with t_s and $u_1(\tau_1) > u_2(\tau_2)$, the denominator (7.26) is positive and we thus deduce that $\delta_1 > \epsilon$.

The denominator of (7.27) similarly gives

$$-2(u_2(\tau_2) - \tau_2 - u_2'(\tau_2)(t_s - \tau_2)) = -2\left(\frac{3}{2}\frac{\delta_2^2}{\sqrt{2A}} - \epsilon + \frac{\epsilon\delta_2}{\sqrt{2A}} + O(\delta_2^3)\right). \tag{7.33}$$

Now, since τ_2 is decreasing with t_s, $\frac{3}{2}\frac{\delta_2^2}{\sqrt{2A}} - \epsilon + \frac{\epsilon\delta_2}{\sqrt{2A}} + O(\delta_2^3) > 0$. Since $\delta_2 \ll 1$ implies $\epsilon\delta_2 \ll \epsilon$, as $\epsilon \to 0$, we must have

$$\frac{3}{2}\frac{\delta_2^2}{\sqrt{2A}} > \epsilon \Rightarrow \delta_2 \geq O(\sqrt{\epsilon}). \tag{7.34}$$

Substituting the expressions we obtained for the denominators in the system (7.26)–(7.27) and using (7.28), (7.29) and (7.30) we obtain

$$\frac{d\delta_1}{d\epsilon} = \frac{1}{2}\left(\frac{\delta_1+\delta_2+\frac{\delta_2^2}{2\sqrt{2A}}+O(\delta_2^4)}{\delta_1-\epsilon}\right) \tag{7.35}$$

$$\frac{d\delta_2}{d\epsilon} = \frac{1}{2}\left(\frac{\delta_1+\delta_2+\frac{\delta_2^2}{2\sqrt{2A}}+O(\delta_2^4)}{\frac{3}{2}\frac{\delta_2^2}{\sqrt{2A}}-\epsilon+\frac{\epsilon\delta_2}{\sqrt{2A}}+O(\delta_2^3)}\right) \tag{7.36}$$

Conclusion (7.34) leads us to assume $\delta_2 \sim c_2\sqrt{\epsilon}$. Combining this with the guess that $\delta_1 \ll \delta_2$, (7.36) simplifies to

$$\frac{1}{2}c_2\epsilon^{-1/2} \sim \frac{1}{2}c_2\epsilon^{1/2}/\left(\left(\frac{3}{2}\frac{c_2^2}{\sqrt{2A}}-1\right)\epsilon\right), \tag{7.37}$$

in which both sides are proportional to $\epsilon^{-1/2}$. Equating the coefficients we find

$$c_2^2 = \frac{4}{3}\sqrt{2A}. \tag{7.38}$$

In order to proceed further with (7.35) since we have concluded already that $\delta_1 > \epsilon$ it is reasonable to make the guess $\epsilon \ll \delta_1$. Therefore we obtain

$$\frac{d\delta_1}{d\epsilon} \sim \frac{1}{2}\frac{\delta_2}{\delta_1} \sim \frac{c_2\sqrt{\epsilon}}{2\delta_1} \tag{7.39}$$

and this leads to

$$\delta_1 \sim \left(\frac{2}{3}c_2\right)^{1/2}\epsilon^{3/4}. \tag{7.40}$$

The scalings for δ_1 and δ_2 are therefore fully consistent. The jump at the shock is exactly the numerator (7.31) calculated above and to this order is approximated by $c_2\sqrt{\epsilon}$.

◇ Interaction of shocks

In Figure 7.3 we plot ShockI and ShockII for $A = 0.05$. ShockII has to be computed differently when it meets the source, on the characteristic $\tau = \tau_{SII}$ say, or when ShockII meets ShockI. For $A = 0.05$, the next change in behaviour is when the source catches up with ShockII. Therefore the subfamily of Type2R characteristics satisfying $\tau_{SI} \le \tau \le \tau_{SII}$ do not enter either ShockI or ShockII but cross the source instead, emerging on the left of the source as Type2RL characteristics. Applying the jump condition (7.10), at this second crossing time τ', we find that their velocity is

$$u_{2RL} = \frac{1}{3}+\frac{2}{3}(\tau'-\sqrt{(1-\tau')^2-6A}). \tag{7.41}$$

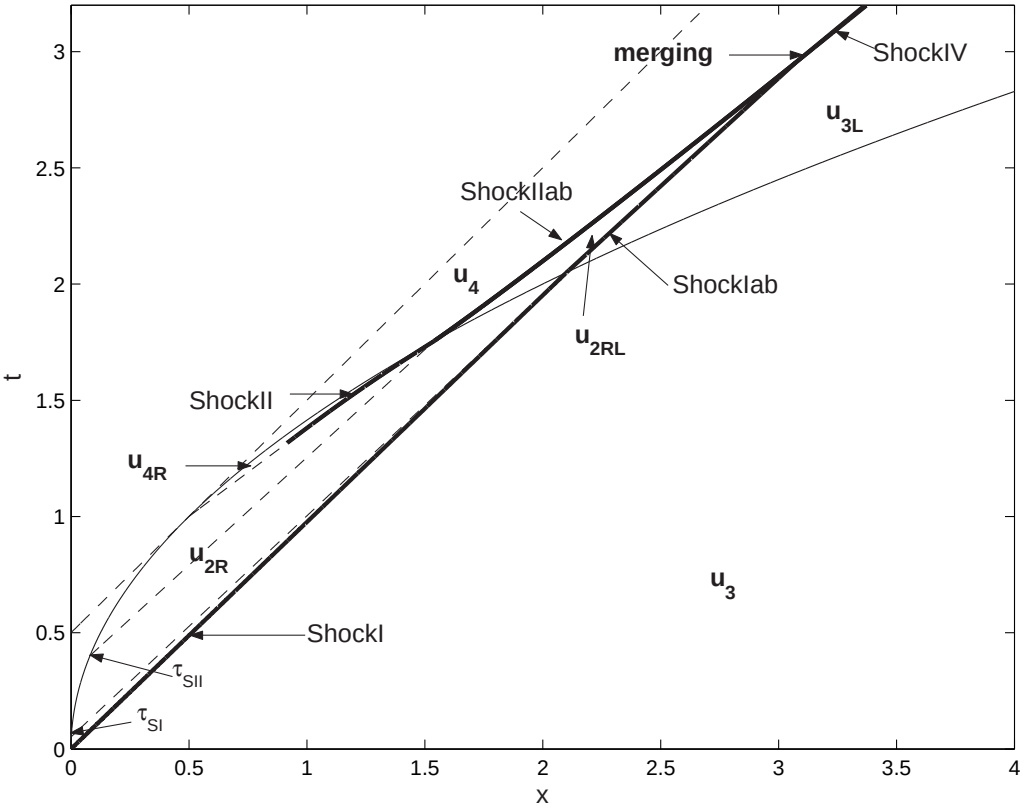

Figure 7.3: $A = 0.05$: the shocks and some important characteristics are plotted here. The value of u as parametrised by τ (or τ' as appropriate) is also noted in the various regions. The merging of the shocks occurs above the source path.

Below we derive the relation (7.41), which is valid for both positive and negative A. However for $A > 0$ (7.41) holds only for the restricted range of $\tau' \geq 1 + \sqrt{6A}$.

From the jump relation (7.17) we have the following relation between u_{2RL} and u_{2R}

$$u_{2RL} = \tau' - \sqrt{(\tau' - u_{2R})^2 - 2A}. \tag{7.42}$$

Since any Type2R characteristic is a chord of the parabola $x = t^2/2$, it satisfies the relation

$$\frac{\tau'^2}{2} = \frac{\tau^2}{2} + u_{2R}(\tau)(t - \tau) \tag{7.43}$$

which gives the relation

$$\tau' = 2u_{2R}(\tau) - \tau = \tau + 2\sqrt{(1-\tau)^2 - 2A}. \tag{7.44}$$

Inserting (7.44) in (7.42) we obtain

$$u_{2RL}(\tau', \tau) = 2u_{2R}(\tau) - 1 = \tau' + \tau - 1. \tag{7.45}$$

Therefore to express u_{2RL} in terms of τ' only we need to find τ as a function of τ' by solving (7.44) for τ. Rearranging (7.44) we obtain the quadratic

$$3(1-\tau)^2 + 2(1-\tau')(1-\tau) + 8A - (\tau' - 1)^2 = 0 \tag{7.46}$$

which gives

$$(1-\tau) = \frac{\tau' - 1}{3} \pm \frac{2}{3}\sqrt{(1-\tau')^2 - 6A} \tag{7.47}$$

and selecting the positive root and inserting in (7.45) we obtain (7.41). The positive root is selected by checking that when $A = 0$ (7.47) gives $\tau' = 2 - \tau$ as in (7.44).

ShockII will continue above the source; its continuation, called ShockIIab from now on, will have on the left Type4 characteristics and on the right Type2RL characteristics. The system (7.26)–(7.27) holds again for ShockIIab, but with u_1 replaced by u_4 and u_2 replaced by u_{2RL} (as indicated in Figure 7.3). Similarly, for the continuation of ShockI above the source, to be called ShockIab, the system (7.26)–(7.27) is to be solved again, but with u_1 replaced by u_{2RL} and u_2 replaced by u_{3L} (as indicated in Figure7.3). ShockIab and ShockIIab are shown in Figure 7.3.

ShockIab and ShockIIab merge at some time t_{merge}, and the resulting shock, called ShockIV, has on the left Type4 characteristics and on the right Type3L characteristics, and obeys again the system (7.26)–(7.27), with u_1 replaced by u_4 and u_2 replaced by u_{3L}. The merging point and ShockIV are indicated in Figure 7.3. Summarising, we used the ordinary differential equation (7.21) for determining ShockI and the system (7.26)–(7.27) for determining ShockII, ShockIIab, ShockIab and ShockIV.

When defining the initial conditions for each shock numerically, a careful procedure similar to that for ShockII was followed for ShockIab and ShockIIab, since (7.26) has a singularity at the starting point for these. Below we list the initial conditions for the shocks.

• For ShockIab: $\tau_1 = \tau_2 = t_s = \tau_{SI} + 2\sqrt{(1-\tau_{SI})^2 + 2A}$.

• For ShockIIab: $\tau_1 = \tau_2 = t_s = \tau_{SII} + 2\sqrt{(1-\tau_{SII})^2 + 2A}$.

Note that τ_1 and τ_2 and t_s stand for different quantities according to the shock we are considering.

• For ShockIV the initial conditions on τ_1 and τ_2 are determined by identifying the τ_c' that parametrises the common Type2RL characteristic entering the merging point of ShockIab and ShockIIab. Then for this τ_c' we identify the corresponding τ that parametrises the Type4 characteristic entering the merging point from the left and this provides the initial condition for τ_1 for ShockIV. We also use τ_c' to identify the τ of the Type3L characteristic entering the merging point from the right, and the latter value provides the initial condition for τ_2 for ShockIV.

As A increases we expect the merging of ShockIab and ShockIIab to occur at an earlier time. We find numerically that for $A \approx 0.109$ the merging happens on the source path, and for values of A larger than 0.109 the merging occurs below the source. (Therefore the threshold value $A = 0.27551$, mentioned earlier, proves to be irrelevant.)

As an example of this we present the case $A = 0.2$ in Figure 7.4. The shock formed when ShockI merges with ShockII, called ShockIII, can now be calculated analytically using (7.21) since it has on the left Type4R characteristics and on the right Type3 characteristics that have velocity 1. Integrating (7.21) with $u = u_{4R}$ we find

$$t_s(u) = \frac{\frac{2}{3}u^3 - u^2 + C}{(u-1)^2} \tag{7.48}$$

where the constant C is calculated numerically as a function of the merging point. ShockIV now starts where ShockIII meets the source and (7.26) has a singularity there. The initial conditions for ShockIV are $\tau_1 = \tau_2 = t_{sIII}$ where t_{sIII} is the time of crossing of ShockIII and the source (and can be determined analytically). In Figure 7.4 we also plot the sonic tangent and the $\tau = 1$ characteristic and label the various regions of u.

Finally, for values of $A \geq 1/2$, Type2R characteristics have all entered ShockI so ShockII is absent and ShockIII is formed as the continuation of ShockI. ShockIV starts at the source where ShockIII crosses. We display ShockI, ShockIII and ShockIV in Figure 7.5.

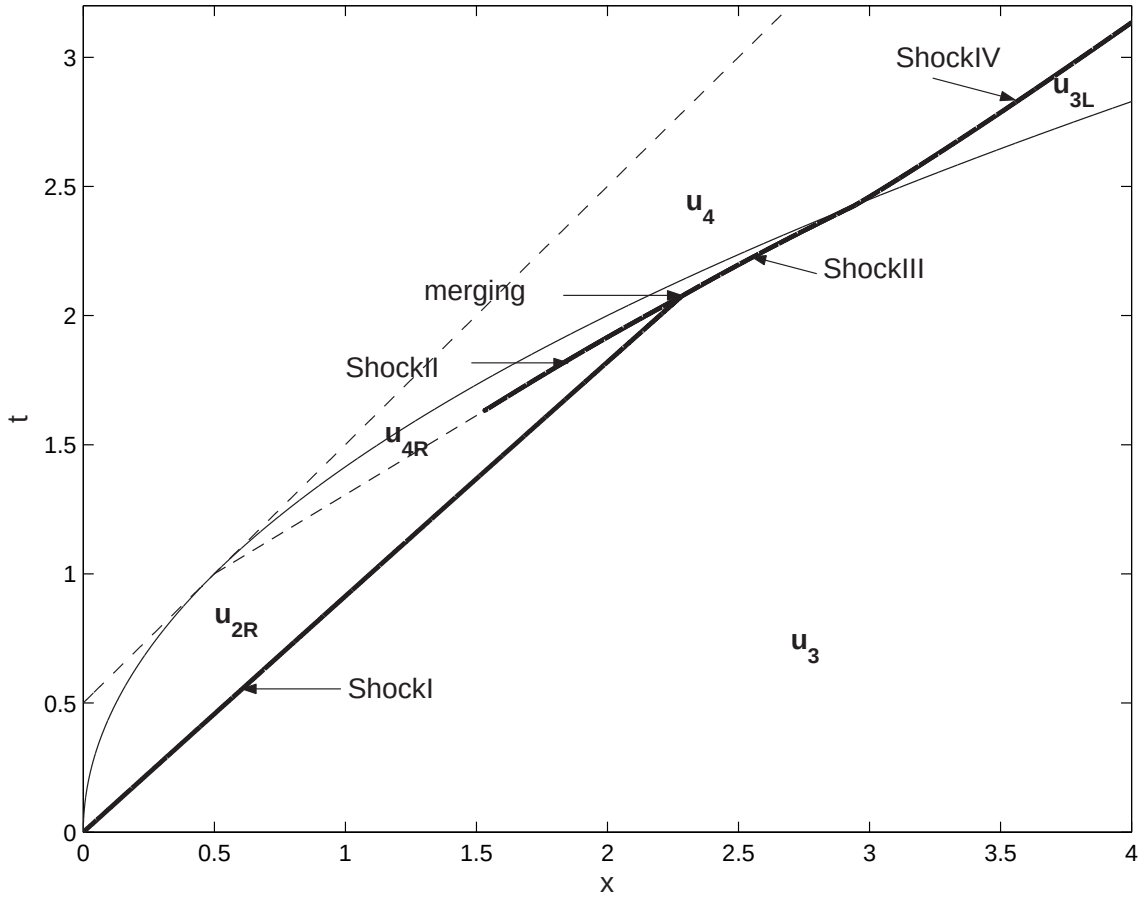

Figure 7.4: $A = 0.2$: the shocks are shown. Now the merging happens before the source path. The sonic tangent and the $\tau = 1$ characteristics are shown with dotted lines. The various regions of u values are indicated.

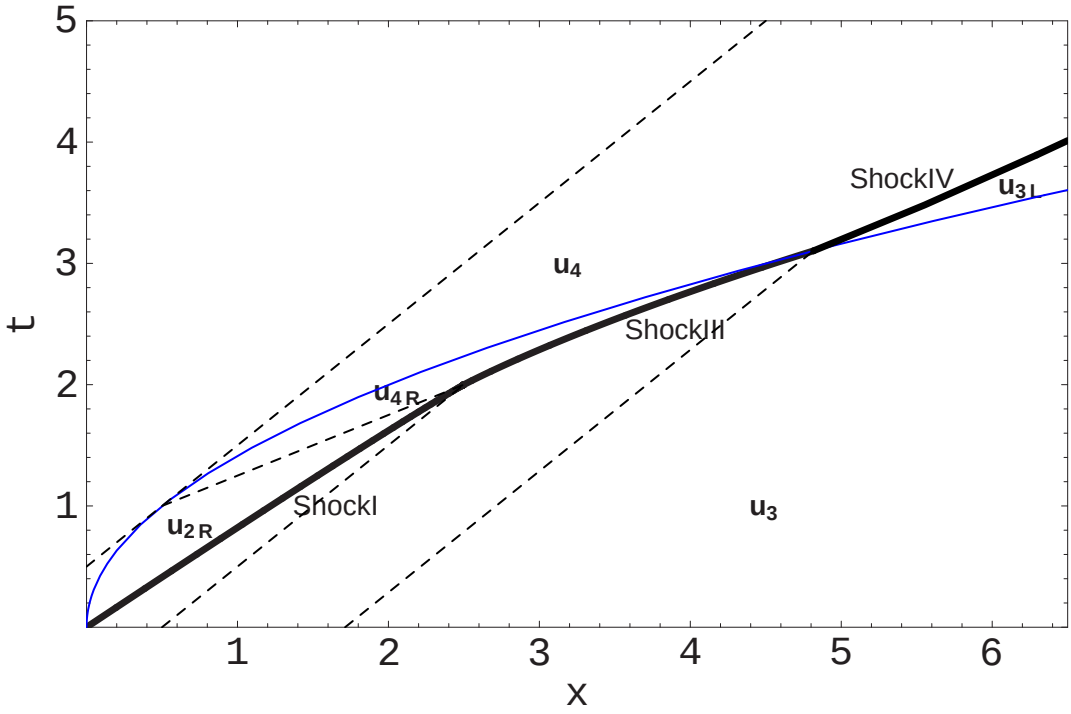

Figure 7.5: $A = 1/2$: the shocks, the characteristics entering the common point of ShockI and ShockIII, the sonic tangent and the $\tau = 1$ characteristic are shown. The various regions of u values are indicated.

◇ **Wavefield**

Having determined the characteristic geometry for all values of A we have also essentially determined the wavefield, since u is constant on each characteristic, and we have shown which family of characteristics covers each part of the (x,t)-plane. For $A = 0.05$, we plot a snapshot of the wavefield at the sonic time $t = 1$, $u(x,1)$, in Figure 7.6. We also plot $v(x,1) = (u(x,1) - 1)/A$. For any A, v is the solution of $v_t + (1 + Av)v_x = \delta(x - t^2/2)$ with initial condition $v(x,0) = 0$. We had shown in Section 7.2 that v becomes singular at the sonic point for the linearised problem for small A. Our plot in Figure 7.6 clearly shows that v at the sonic point has been made finite by the nonlinearity. Furthermore, v attains a peak value there. This peak value, attained at $x = (1/2)^+$, is $\sqrt{2/A} \to \infty$ as $A \to 0^+$. For more explicit calculations on

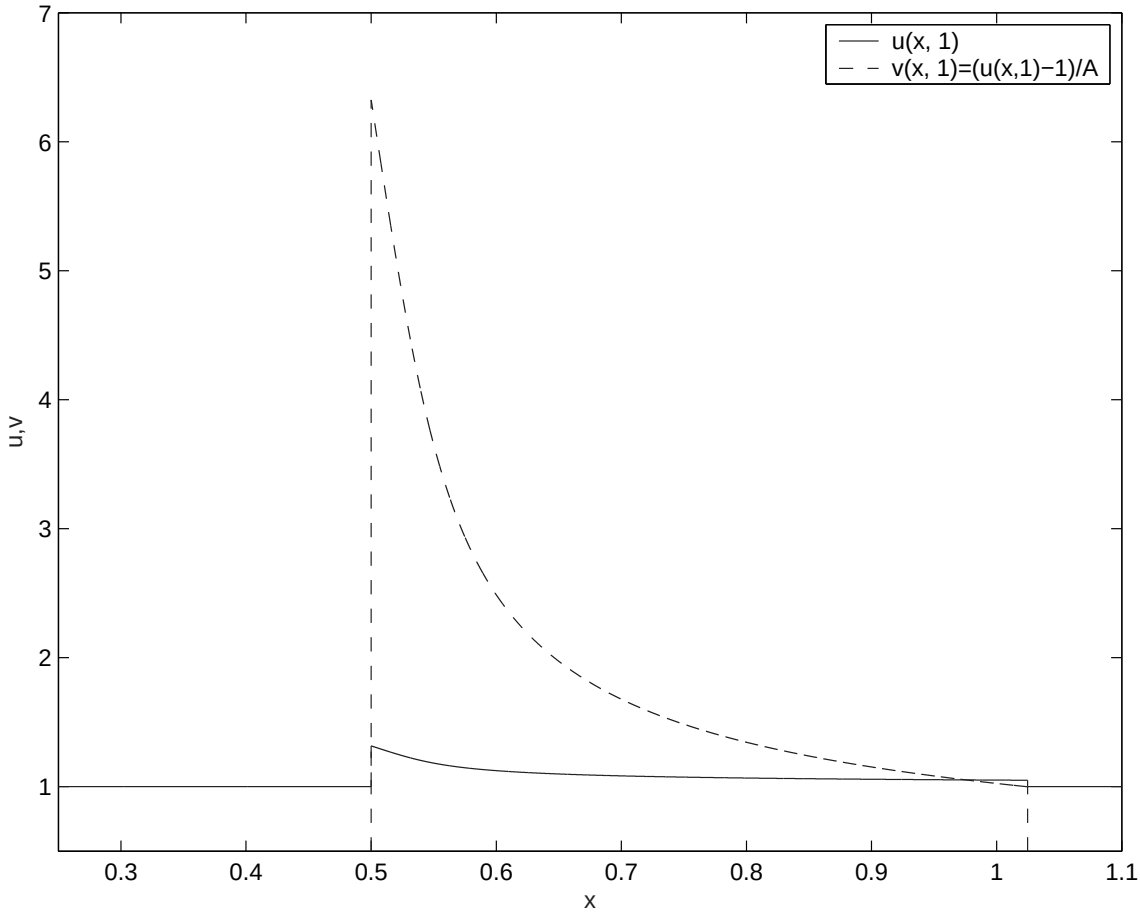

Figure 7.6: A=0.05: snapshot of the wavefield at the sonic time $t = 1$: $u(x,1)$ and the perturbation $v(x,1) = \dfrac{u(x,1) - 1}{A}$.

the wavefield and snapshots at other times see Appendix C.

7.3.2 Negative force ($A < 0$)

$\diamond$ Characteristic diagram and the shock

We now consider the $A < 0$ problem. In this case, we already noted that Type2R characteristics are slower than Type3 characteristics and therefore an empty region is formed between them. To resolve this, we introduce the expansion fan characteristics $x = \lambda t$, with $\sqrt{1-2|A|} \leq \lambda \leq 1$. We will call the expansion fan characteristics Type5. Clearly, $|A| = 1/2$ is a threshold value, and we start with the case $|A| < 1/2$. A characteristic in the expansion fan continues up to the source, crosses it at time τ, and then deflects with velocity

$$u_{5L}(\tau) = \tau - \sqrt{\frac{\tau^2}{4} + 2|A|}. \tag{7.49}$$

A Type3 characteristic crosses the source once at time τ and slows down afterwards with velocity $u_{3L} = \tau - \sqrt{(\tau-1)^2 + 2|A|}$. The Type2R characteristics cross the source again and emerge on the left of the source with a smaller velocity u_{2RL} (as given by (7.41) with $A = -|A|$). They therefore cross the Type1 characteristics coming from the left. Hence, we have to fit a shock on the left of the source. This shock starts on the source at the time $t = 1 - \sqrt{2|A|}$ when the leftmost Type2R characteristic becomes tangent to the source. This corresponds to a Type2RL characteristic with velocity $1 - 2\sqrt{2|A|}$ which crosses a Type1 characteristic at the source. Using this fact we calculate the initial velocity of the shock there, using the Rankine-Hugoniot condition,

$$dx/dt = (1 + (1 - 2\sqrt{2|A|}))/2 = 1 - \sqrt{2|A|}, \tag{7.50}$$

and we conclude that the shock starts off tangentially to the source. Since the Type1 characteristics have constant velocity equal to 1, this shock can be calculated analytically, by integrating (7.21). We find

$$\begin{aligned}(u_{2RL}(\tau') - 1)^2 t_s = \; & \tfrac{4}{27}(\sqrt{(\tau'-1)^2 + 6|A|}(1 + 6|A| + (4 - 5\tau')\tau') + \\ & \tau'(3 + 36|A| + \tau'(5\tau' - 9))) + \tfrac{4}{27} - \tfrac{8|A|}{3}.\end{aligned} \tag{7.51}$$

where the constant of integration is determined by imposing the initial condition, $t_s = 1 - \sqrt{2|A|}$ at $\tau' = 1 - \sqrt{2|A|}$.

The shock moves subsequently into the region of the Type5L characteristics, and then into the region of the Type3L characteristics, while having always Type1 characteristics on the left. The analytical expression for the shock, corresponding to the

above regions, in succession is

$$(u_{5L}(\tau)-1)^2 t_s = \tau(4|A|+(1-\tau)(-\tau+\sqrt{8|A|+\tau^2})) \quad (7.52)$$

$$(u_{3L}(\tau)-1)^2 t_s = 2(\tau-1)\,(2|A|+\tau(u_{3L}-1))+4|A| \quad (7.53)$$

where the constants in the right-hand sides are determined by joining smoothly together the three parts of the shock. In Figure 7.7, we display the (x,t)-plane for $A=-0.2$.

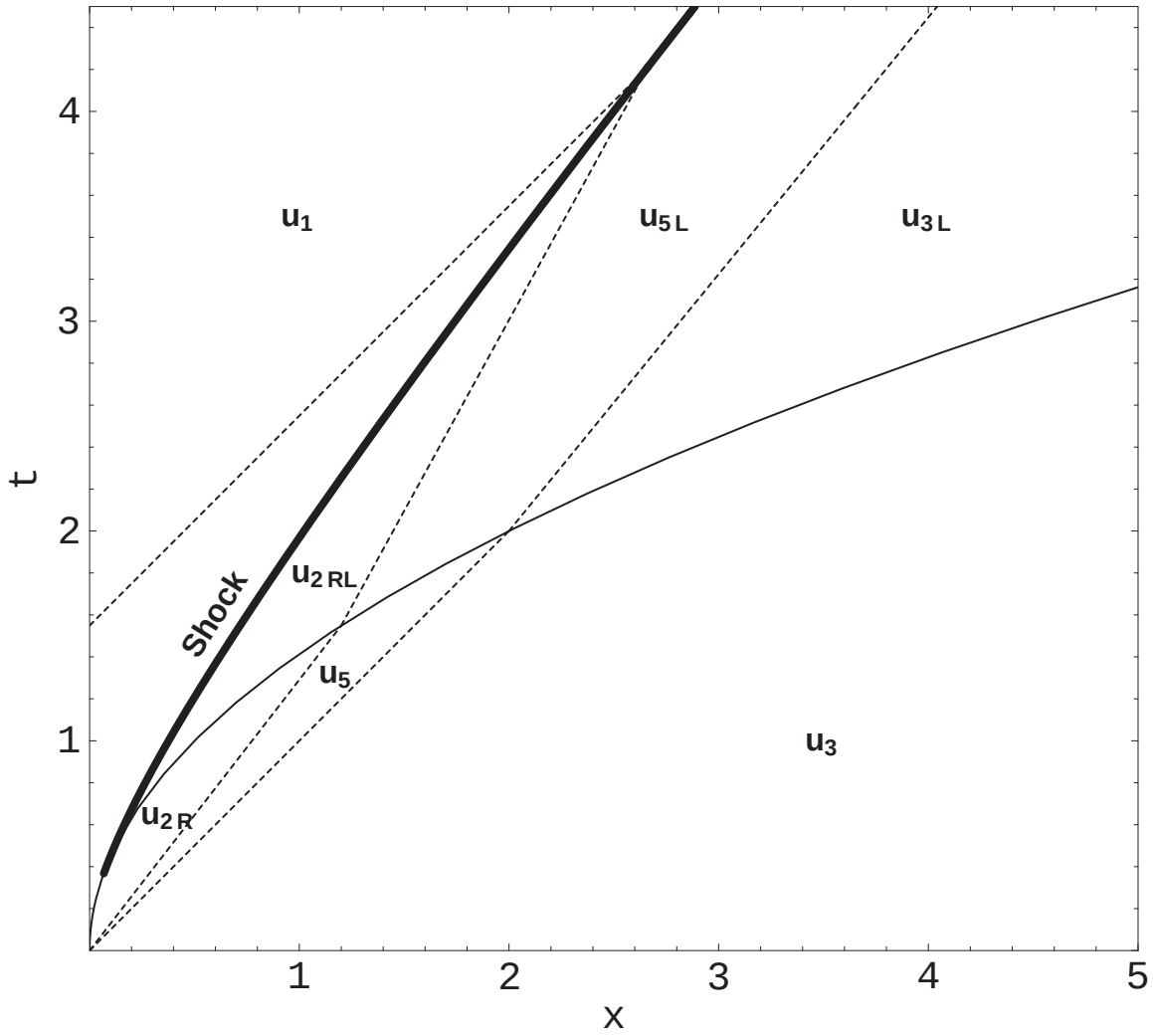

Figure 7.7: $A=-0.2$: the shock and the expansion fan (region inside the dashed lines on the right of the shock). The characteristics entering the point joining the first and second part of the shock are also shown. The various regions of u are indicated.

As $|A|$ increases from 0 to $1/2$ the starting point of the shock moves from the source point $x=(1-\sqrt{2|A|})^2/2$, $t=1-\sqrt{2|A|}$ down to the origin. For values of $|A|\geq 1/2$,

no Type2 characteristic enters the source (because u_{2R} would become complex). An empty region therefore forms between the source and the origin characteristic and to resolve this we need to extend the expansion fan so that it fills the whole of this region. The shock now starts at the origin but at a definite angle to the source that increases with A. The Type5L characteristic there has velocity $-\sqrt{2|A|}$ and therefore the initial velocity of the shock is $(1-\sqrt{2|A|})/2$, which is always negative for $|A| > 1/2$. However, u_{5L} increases with τ always attaining the value -1, and therefore the shock velocity will become zero at a certain point corresponding to $\tau_{\rm TP} = \frac{2}{3}(-2+\sqrt{1+6|A|})$. This point is a turning point for the shock (hence the use of the subscript TP). After turning, the shock velocity is positive and increasing, and the diagram is similar, in general terms, to Fig 7.7. The analytical expression for the shock is now given only by (7.52) and (7.53) (there is no Type2RL region). In Figure 7.8 we display an enlargement of the region near the origin, for $A = -1$, showing the shock with its turning point and the associated characteristics.

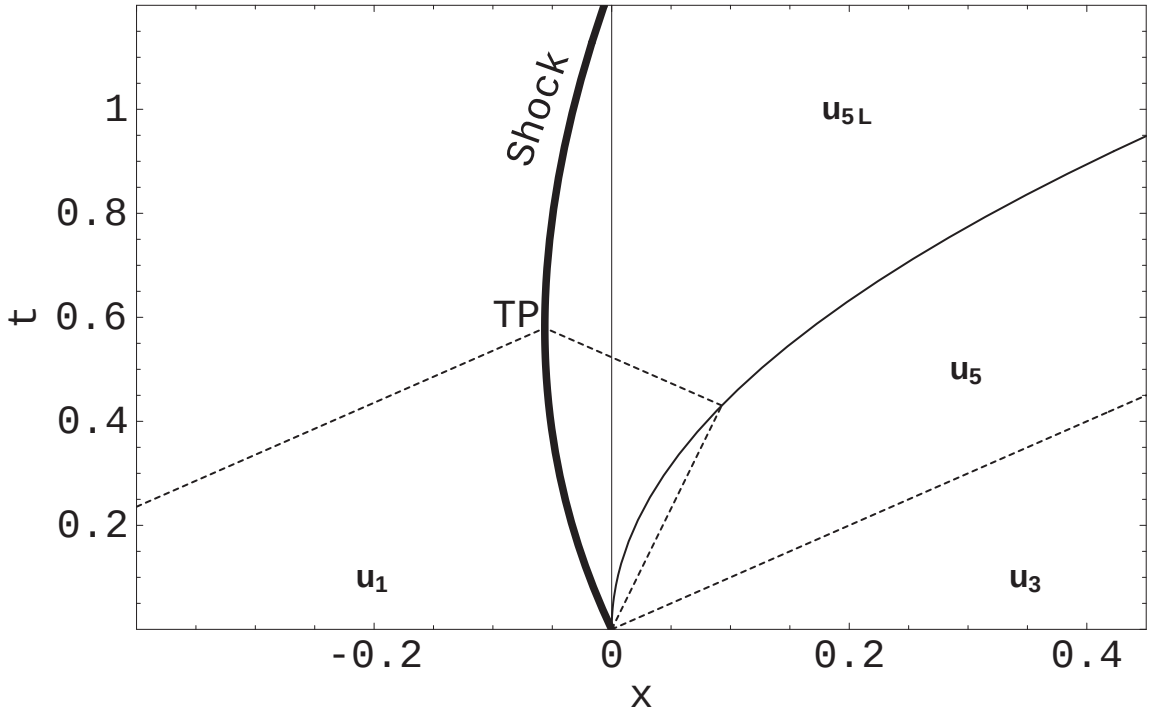

Figure 7.8: $A = -1$: details of the behaviour near the origin. The shock has a turning point corresponding to $\tau_{\rm TP} = 2/3(-2+\sqrt{7}) = 0.43$. We plot the characteristics entering this turning point from the left and from the right.

◇ Wavefield

Snapshot of the wavefield at the sonic time $t = 1$.

In Figure 7.9, for $A = -0.2$, we plot the snapshot of the wavefield for $t = 1$, $u(x, 1)$, and the corresponding $v(x, 1)$. Comparing Figure 7.6 and Figure 7.9 we find important

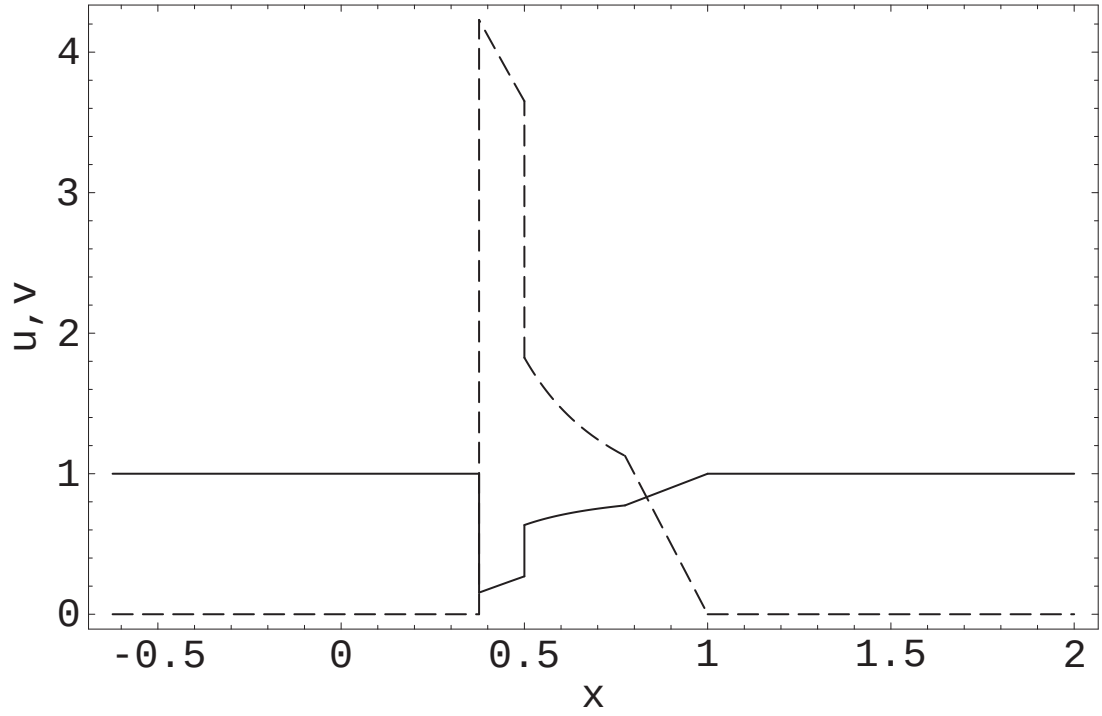

Figure 7.9: $A = -0.2$: snapshot of the wavefield at the sonic time $t = 1$. The snapshot $u(x, 1)$ is plotted with a solid line and the snapshot $v(x, 1) = (u - 1)/A$ is plotted with a dotted line.

qualitative differences. In the former Figure the peak value of v is attained at the sonic point but in the latter Figure it is attained at the shock. Furthermore, there are two jumps: a positive one at the shock and a negative one at the sonic point. These features are valid for any value of $A < 0$. It is of interest to investigate how the peak value varies with A. It is the peak value that tends to ∞ as $A \to 0$; the value of v at the sonic point does not do so and it is therefore less interesting.

There turn out to be four different cases depending on the value the parameter A takes:

Case a : $-3/8 < A < 0$

Case b : $5/4 - 3\sqrt{5}/4 < A < -3/8$

Case c : $-1/2 < A < 5/4 - 3\sqrt{5}/4$

Case d : $A < -1/2$

For cases a and b the peak of v is defined by a Type2RL characteristic; for cases c and d it is defined by a Type5L characteristic. The threshold value $A = 5/4 - 3\sqrt{5}/4$

holds when the leftmost Type5L characteristic enters the shock at time $t = 1$.

Examining in detail the cases a and b, to find the peak of v at the shock we employ the parametric shock expression (7.51). We reexpress (7.51) in terms of u by using the relation

$$\tau'(u) = 1 - \frac{2|A|}{u-1} + \frac{3}{4}(u-1), \tag{7.54}$$

(obtained by solving for τ' the expression for u_{2RL} and dropping the subscript) and set $t_s = 1$ to end up with the simple quartic equation

$$5(u-1)^4 - 64A^2 = 0, \tag{7.55}$$

which gives

$$u = 1 - \left(\frac{64}{5}\right)^{1/4} \sqrt{|A|} = 1 - \frac{2\sqrt{2}}{\sqrt[4]{5}}\sqrt{|A|}. \tag{7.56}$$

We have picked the root of (7.55) that is real and less than 1 as it should represent the velocity of characteristics that have crossed the source one or more times. (Also we check that from (7.56) and (7.54) we obtain

$$\tau' = 1 - \left(\frac{3-5^{1/2}}{2}\right) 5^{-1/4}\sqrt{2|A|} = 1 - 0.255\sqrt{2|A|}, \tag{7.57}$$

which is between the values $1 - \sqrt{2|A|}$ and 1 as expected.)

Therefore for these values of A, the peak in v is $\left(\frac{64}{5}\right)^{1/4} \frac{1}{\sqrt{|A|}}$. Comparing with the results for positive A (Section 7.3.1), we conclude that also for negative A, as $A \to 0$, the peak of v tends to ∞ with scaling $1/\sqrt{|A|}$ (except that the constants are different). The rate of change of the peak with A may change in cases c and d but we will not examine these cases here.

As an example of the calculation for obtaining the jump in v at the sonic point we examine case a: we evaluate $u_{2RL}(\tau' = 1) = 1 - 2\sqrt{\frac{2}{3}}\sqrt{|A|}$ to give the value just on the left, and using $u_{2RL} = 2u_{2R} - 1$ we find $u_{2R} = 1 - \sqrt{\frac{2}{3}}\sqrt{|A|}$, the value just on the right. Therefore the (negative) jump in v at the sonic point is $\sqrt{\frac{2}{3}}\frac{1}{\sqrt{|A|}}$. For snapshots at other times see Appendix C.

7.4 Conclusions and discussion

In this chapter, we have solved the one-dimensional, nonlinear, initial value problem (7.1) mostly analytically, for *all* values of the nonlinearity parameter A and for all

points in the (x,t)-plane. This problem constitutes a simple one-dimensional model for the interaction of nonlinearity with a point force accelerating through the sound speed. Our solution furnished us with the full details of this interaction. This understanding is useful for the various physical problems mentioned in the introduction of the chapter and which cannot be tackled by analytical means.

In Section 7.2 we have solved the linear approximation of problem (7.1), for small A in order to show that a singularity is formed at the sonic point $x = 1/2, t = 1$ which then *propagates* along the sonic tangent $x = t - 1/2$. In Section 7.3.1 we have solved the full problem (7.1) for all positive A, and in Section 7.3.2 for all negative A. We obtained the solution by constructing the characteristic diagram in the (x,t)-plane and resolving multi-valued regions with shocks and empty regions with expansion fans. For $0 < A < 1/2$, there are two shocks which merge later; for $A \geq 1/2$ and all negative A only one shock forms. The solution is entirely analytical for negative A. For positive A the solution is also analytical, except for some shocks that are calculated numerically by solving the second-order o.d.e. system (7.26)–(7.27).

Overall, the results are very different qualitatively for the different signs of A, reflecting the expected physical differences that would come about in the wavefield when a point force changes direction. However for any non-zero A our solution displays how the introduction of nonlinearity makes the sonic singularity finite. In order to show this clearly, for selected positive and negative A, we plotted snapshots of v at the sonic time $t = 1$. Furthermore, we found that the peak value of v tends to ∞ as $A \to 0$ with scaling $1/\sqrt{|A|}$.

We assumed uniform acceleration and were thus able to calculate most of the solution analytically. However, we expect this to be a very useful guide to any scenario where the source has a monotonically increasing velocity.

Chapter 8

Conclusions

We began the thesis with a brief history of sonic boom research and its current importance for a new SST. We subsequently gave a brief exposition of the established theory and the major open questions.

In Chapter 2 we presented the equations of gas dynamics, and explained when these equations simplify into the Euler equations, coupled with the appropriate Rankine-Hugoniot conditions for fitting shocks into the flow pattern. In this connection we also proved a new circulation theorem, closely related to Kelvin's circulation theorem, Bjerknes' theorem and Crocco's theorem, but one that is valid in the presence of shocks. We showed that the circulation Γ around a closed material curve in an inviscid gas flow evolves according to an equation that involves the entropy changes around this curve, excluding the entropy jumps at the shock. We thus proved, in a rigorous way, that if a uniform transonic or supersonic flow is incident on a thin wing or a slender rigid body, and the resulting flow contains only *weak* shocks with strength of order ϵ, then the vorticity produced after the shocks is of order ϵ^3. This result was subsequently needed in Chapter 4 for rigorously justifying the use of potential flow after a shock is crossed.

In Chapter 3 we started by laying out the basic definitions governing sonic boom geometry. The notions of a characteristic surface, wavefront, bicharacteristic, ray, boomray, Mach envelope, and the carpet were defined. Three ways to construct the Mach envelope were then presented and the relationships between them elucidated. We also outlined carefully the connection between the theory of characteristics and geometrical acoustics and showed that the equation for the characteristic surfaces of the wave equation is precisely the eikonal equation arising at the leading order in the geometrical acoustics framework. This is often not clear in the sonic boom literature.

We then applied the theoretical results to particular examples and illustrated them carefully in order to elucidate aspects of the long-range propagation of sound, and in

particular of sonic boom in *stationary media*. (The theory of Geometrical Acoustics in moving media was briefly presented in Section 3.10 and was used to explain how stratospheric SSBs may arise.)

We first studied the geometry of the ray surface in the model stratified atmosphere $c = 1/\sqrt{1-z}$. We found that the rays from a stationary source form a fold caustic. We subsequently calculated the amplitude due to a stationary, sinusoidal source in this atmosphere. Due to the nature of this particular sound speed profile we were able to use the full linear wave theory. We showed that inside the caustic there is an order 1 wavefield which is amplified on the caustic and decays exponentially outside. These results agreed nicely with the Geometrical Theory of Diffraction.

We then considered a source moving at constant supersonic speed in the same stratified medium. The governing linear PDE was of mixed type: in the vertical plane of motion, it was hyperbolic below the sonic height, parabolic at the sonic height, and elliptic above this height, and could be recast into the Tricomi equation. The boom reflects from the sonic line, the Mach envelope having the local shape of a Tricomi cusp there (as illustrated, for example, in Figure 3.27). This Tricomi cusp joins two qualitatively different parts of the Mach envelope, which we called respectively the *incident* part and the *reflected* part. It is a key fact that the presence of a Tricomi cusp on the Mach envelope is directly associated with the formation of a fold caustic of boomrays, and corresponds to focusing of the sonic boom. The fold caustic is precisely the sonic line (see Figure 3.27); the Tricomi cusp moves on the sonic line at the local sound speed. In Chapter 6, in a constant-acceleration motion through the sound speed in a uniform medium, we also saw a qualitatively similar behaviour (see Figure 6.5): boomrays again formed fold caustics[1], and this corresponded to Tricomi cusps that again moved at the sound speed on the "cusp-locus" curve (6.47).

The geometry of a fold caustic of ordinary rays and that of a fold caustic of boomrays is similar, and in terms of catastrophe theory they are essentially the same. This is generally the viewpoint found in the sonic boom literature. However, we emphasise two important differences:

- Boomrays are curves in $(\mathbf{x}, t)$-space emanating from the source, but for a stationary harmonic source one generally thinks of rays simply as curves in $\mathbf{x}$-space.

- Rays are emitted by a source in *all* directions, but boomrays are only emitted when the source is supersonic, and only at a certain angle to the direction of motion.

[1]Two caustics were formed which were symmetric with respect to the direction of motion.

Next, through a simple coordinate transformation we used the stationary source example $c = 1/\sqrt{1-z}$ to determine the Mach surface for steady motion in three dimensions in the medium with Prandtl-Glauert parameter $B^2 = 1 - z$. In this case the Tricomi cusp generalised to a focusing curve. The carpet was also determined analytically and possessed cusps, indicating the location of focusing regions on the ground.

We then extended the latter example to $B^2 = 1-|z|$, where the sound speed profile has a minimum, as in a typical (windless) atmosphere. We found that we could still treat this analytically. Some of the bicharacteristics launched downwards formed a primary boom carpet, some of those launched upwards formed a secondary carpet, whereas a third set of bicharacteristics was trapped in the atmosphere and never reached the ground, resulting in disjoint primary and secondary carpets. Again cusps were observed at the carpets corresponding to regions of focusing. This behaviour agreed qualitatively with the behaviour of bicharacteristics in a typical atmosphere, which was investigated numerically.

We discussed focusing of linear sound waves and weak shock waves at the end of the chapter in general and also in connection with specific examples. In Chapter 4 we mainly dealt with amplitude questions. We investigated the wavefield around thin aerofoils or slender axisymmetric bodies moving at constant supersonic speed in a uniform medium. The starting point was the nonlinear potential equation, derived exactly from the Euler equations under the assumption of potential flow (as justified by our results in Chapter 2). We used Matched Asymptotic Expansions (MAE) to derive consistent approximations of this potential equation in appropriately defined regions: in the inner region of the MAE (the near-field) we found that the pressure is governed by a linear wave equation at leading order. However, we showed that the linear approximation breaks down at a certain distance from the body, due to small nonlinearities that cumulatively become important. Thus a second region was introduced, the outer region (or the far-field). In this outer region, the consistent approximation of the potential equation at leading order is the nonlinear Kinematic Wave Equation (KWE). An N-wave signature was derived as a solution of this KWE, exactly for an aerofoil with parabolic shape in two dimensions, and asymptotically for any thin or slender shape in two or three dimensions. The work in this chapter formalises Whitham's rule [124, 125], and the work of Hayes in [51]. The latter studies accounted only for first-order corrections but our MAE framework allows for the calculation of the higher orders.

In Chapter 5 we extended the work of Chapter 4 in order to incorporate nonlinearities in a consistent way for the long-range propagation of weak shocks in a stratified atmosphere with wind. This work is new and can be thought of as the extension of the primary boom results in Chapter 4 (and other literature) to the case of secondary boom. We sought the wavefield due to a thin, two-dimensional aerofoil moving supersonically in a general weakly stratified medium with a horizontal wind, which itself was also weakly stratified. Two small nondimensional parameters were defined, namely the thickness ratio ϵ (as in Chapter 4), and the ratio of the aerofoil length to the scale height of the atmosphere, δ (as in Chapter 3). We have assumed that δ is much smaller than ϵ^2, an assumption which is reasonable for a typical atmosphere. We also abandoned the assumption of potential flow, since there is already vorticity in the incident stratified flow, so we worked with the full Euler equations. We again applied MAE to derive consistent approximations for these equations in three regions of interest:

- Near the aerofoil the wavefield was determined by linearised wave theory at leading order. This was the inner region of the MAE method.
- At distances of order L/ϵ nonlinear effects were important (but not stratification effects) and we found that the governing PDE at leading order was a KWE. This was the middle region of the MAE method.
- At distances of order L/δ stratification and nonlinear effects were both of order 1. This was the outer region of the MAE method. We found that the governing equation at leading order was an inhomogeneous KWE with non-constant coefficients. The derived KWE led to a very simple expression for the amplitude variation along the characteristics.

We noted that the approximations of the Euler equations in the inner region and the middle region turned out to be the same as those in Chapter 4, in the near-field and far-field respectively.

Our MAE method blows up near the sonic line where B is small. A fourth region needs to be introduced with B taken as a third small parameter. Pechuzal and Kevorkian [91] have undertaken this for the simpler scenario of a homogeneous medium that has a horizontal linearly stratified wind. They deduced that the consistent approximation of the Euler equations in this sonic region is a nonlinear Tricomi equation. It remains an open question as to what the analogous equation is for our scenario.

Another point we would like to stress here is that we retained the gravity term in the Euler momentum equation throughout Chapter 5, in contrast with Chapter 3 where it was neglected by arguing that acoustic and gravity waves were decoupled. We found that at the order we worked to there was no direct excitation of gravity waves, even though the motion took place in a gravitationally stratified atmosphere. This mathematically confirmed our approach in Chapter 3.

Finally, for this chapter it would be interesting to extend the work for studying a slender body in the same general ambient conditions.

In Chapter 6 we employed linear wave theory to determine the wavefield due to a point source in various unsteady motions, in two and three dimensions, in the *time domain*. In two dimensions we first considered uniform acceleration through the sound speed, in a uniform medium. We calculated analytically the Mach envelope; it has Tricomi cusps, qualitatively the same as those on the Mach envelopes for steady motions in the stratified atmospheres, as seen in Chapter 3. These cusps join two qualitatively different parts of the envelope. The so-called front, or incident, envelope is formed in a similar way to the usual Mach wedge of steady supersonic motion, with the wavefronts touching their envelope from inside. The so-called back or reflected envelope (also referred to as the acceleration caustic) is formed by wavefronts touching it from outside. This Tricomi cusp corresponded again to the formation of a fold caustic of boomrays and again the front envelope was formed by boomrays that have *not* touched this fold caustic and the back envelope by boomrays that *have* touched the caustic. This is a generic behaviour of all fold caustics and their associated Mach envelopes, and was illustrated in detail in all the scenarios we examined in this thesis, namely steady motion in a stratified medium (in Chapter 3), acceleration through the sound speed in a uniform medium (in Chapter 6) and manoeuvring in a uniform medium (in Chapter 6).

In order to determine the wavefield near the Mach envelope for the accelerating motion in two dimensions we devised a simple approximation method in the time domain: we found a finite jump at the front envelope and logarithmic singularities at the back envelope. The appearance of these singularities violates the assumption of small disturbances underlying the linear theory. This suggests that nonlinearity or damping have to be re-introduced into the equations. Experiments by Sturtevant and Kulkany have shown that in some circumstances, nonlinearity is the limiting factor. The link of our work with the existing literature is that the logarithmic singularities we identified correspond exactly to the infinite peaks of the U-wave formed when the N-wave reflects from the fold caustics. Our method was based on the fact that

for a uniform medium we can work with the wavefield integral rather than the wave equation itself, treating the time t as a parameter. This spared us the need to look for local approximations of the wave equation near the focusing regions, which is the current method in the literature.

We also considered a source that decelerates uniformly after initially travelling at a constant supersonic speed. We found that the geometry of the Mach envelope is very different from that of the accelerating motion. The Mach envelope does not have a Tricomi cusp (or equivalently no fold caustic is formed) and although focusing occurs when the source goes subsonic, it is restricted to a single point. We calculated the wavefield near the Mach envelope, using a similar simple approximation method as for the acceleration problem: we found that the wavefield is finite for all times except at the focusing point. This indicates that nonlinearity is likely to be far less crucial in the prediction of amplitudes in decelerating motion than in accelerating motion.

We then considered a point source accelerating uniformly through the sound speed, in three dimensions. The Mach envelope is just a conical generalisation of the Mach envelope in two dimensions but the wavefield exhibits a very different behaviour due to the difference between the two-dimensional and three-dimensional Riemann function. The wavefield tends to infinity on one side of the envelope and is finite on the other side. It would be interesting to investigate what these singularities become in the case of an extended source.

Moreover, at the end of Chapter 6 we looked at a uniformly accelerating motion through the sound speed in the stratified medium $c = 1/\sqrt{1-z}$: in Figure 6.25 we observed that the reflected envelope itself developed cusps which corresponded to a cusp caustic of boomrays.

The results of Chapter 6 for accelerating motion through the sound speed in two and three dimensions motivated us to investigate the effect of nonlinearity on singularities arising when a source goes through the sound speed. However, it is a formidable task to solve the nonlinear problem in two or three dimensions. What we have been able to achieve instead in Chapter 7 is to solve a related one-dimensional nonlinear problem. We considered $u_t + uu_x = A\delta(x - t^2/2)$, with the initial condition $u = 1$ at $t = 0$. This is a model for a locally forced kinematic wave in which the force accelerates through the sound speed at the sonic time $t = 1$. In the linear approximation, when the nonlinearity parameter A is small, there is a singularity at the sonic point, which propagates along the characteristic from that point. (The propagation of this sonic singularity is also a feature of higher-dimensional problems.)

However in such sonic singularities the amplitude may be limited by nonlinearity or damping. We thus produced a global solution of this PDE, valid for arbitrary A and which is in most regions analytical. As A varies, the qualitative features of the characteristic diagram change, but for all A we found that the introduction of nonlinearity leads to a *finite* amplitude at the sonic point. It still remains an interesting open question as to whether the introduction of nonlinearity regularises the singularities in two or three dimensions. It would also be interesting to pinpoint whether our one-dimensional problem could arise as a consistent approximation of the Euler equations. A possible scenario would be the forced acceleration of a body along a tube of gas, so that the drag would effectively exert a point force on the gas.

Appendix A

Transport Theorem for an open curve

A Transport Theorem for open curves with time-varying endpoints, was used in the derivation of the Circulation Theorem for a compressible flow that takes shocks into account, in Chapter 2. We called this theorem KCTS, where the S in the end is to signify that is valid in the presence of shocks.

The derivation was based in breaking up the closed curve (or circuit) of fluid elements $\mathcal{C}$ into open subcurves separated by shock fronts.

We consider one such subcurve and we parametrise it with s and t, where each s corresponds to a given fluid element in the gas and t is time. Such a parametric method is standard in the derivation of Kelvin's circulation theorem. With this parametrisation we have

$$\frac{\partial \mathbf{x}}{\partial t}(s,t) = \mathbf{u}(\mathbf{x}(s,t),t). \tag{A.1}$$

Let the endpoints of $\mathcal{C}$ be labelled by $\mathbf{P}$ and $\mathbf{Q}$. They correspond respectively to parameter values s_P and s_Q such that

$$\mathbf{P}(t) = \mathbf{x}(s_P(t),t), \quad \mathbf{Q}(t) = \mathbf{x}(s_Q(t),t). \tag{A.2}$$

For circulation theorems we are particularly interested in the rate of change of the circulation

$$\Gamma = \int_{\mathcal{C}} \mathbf{u}.d\mathbf{x}, \tag{A.3}$$

but here we will show a general result that is valid for any vector field, say $\mathbf{a}(\mathbf{x},t)$. We let

$$I = \int_{\mathbf{P}}^{\mathbf{Q}} \mathbf{a}(\mathbf{x},t).d\mathbf{x}, \tag{A.4}$$

and with the parametrisation introduced above, (A.4) becomes

$$I = \int_{s_P}^{s_Q} \mathbf{a}(\mathbf{x}(s,t),t).\frac{\partial \mathbf{x}}{\partial s} ds. \tag{A.5}$$

Therefore the total derivative of I

$$\frac{dI}{dt} = \frac{d}{dt}\int_{s_P}^{s_Q} \mathbf{a}(\mathbf{x}(s,t),t).\frac{\partial \mathbf{x}}{\partial s} ds; \tag{A.6}$$

applying the Fundamental Theorem of Calculus we have

$$\frac{dI}{dt} = \mathbf{a}(\mathbf{Q}).\frac{\partial \mathbf{x}}{\partial s}|_{s_Q}\dot{s}_Q - \mathbf{a}(\mathbf{P}).\frac{\partial \mathbf{x}}{\partial s}|_{s_P}\dot{s}_P + \int_{s_P}^{s_Q}\frac{\partial}{\partial t}\left(\mathbf{a}(\mathbf{x}(s,t),t).\frac{\partial \mathbf{x}}{\partial s}\right) ds. \tag{A.7}$$

We let the third term in (A.7) be

$$J = \int_{s_P}^{s_Q}\frac{\partial}{\partial t}\left(\mathbf{a}(\mathbf{x}(s,t),t).\frac{\partial \mathbf{x}}{\partial s}\right) ds. \tag{A.8}$$

and this, using $u_i = \dfrac{\partial x_i}{\partial t}$, is written in component form as

$$J = \int_{s_P}^{s_Q}\left(\frac{\partial a_i}{\partial t} + u_j\frac{\partial a_i}{\partial x_j}\right)\frac{\partial x_i}{\partial s} ds + \int_{s_P}^{s_Q} a_j\frac{\partial u_j}{\partial s} ds. \tag{A.9}$$

Integrating by parts the second integral in (A.9) we get

$$\begin{aligned}\int_{s_P}^{s_Q} a_j\frac{\partial u_j}{\partial s} ds &= [a_j u_j]_{s_P}^{s_Q} - \int_{s_P}^{s_Q} u_j\frac{\partial a_j}{\partial s} ds \\ &= \mathbf{a}(\mathbf{Q}).\mathbf{u}(\mathbf{Q}) - \mathbf{a}(\mathbf{P}).\mathbf{u}(\mathbf{P}) - \int_{\mathbf{P}}^{\mathbf{Q}} u_j\frac{\partial a_j}{\partial x_i} dx_i. \end{aligned}\tag{A.10}$$

Substituting (A.10) into (A.9) and returning to (A.7) we have

$$\begin{aligned}\frac{dI}{dt} = \mathbf{a}(\mathbf{Q}).\left(\mathbf{u}(\mathbf{Q}) + \frac{\partial \mathbf{x}}{\partial s}\dot{s}_Q\right) - \mathbf{a}(\mathbf{P}).\left(\mathbf{u}(\mathbf{P}) + \frac{\partial \mathbf{x}}{\partial s}\dot{s}_P\right) \\ + \int_{\mathbf{P}}^{\mathbf{Q}}\left(\frac{\partial a_i}{\partial t} + u_j\frac{\partial a_i}{\partial x_j} - u_j\frac{\partial a_j}{\partial x_i}\right) dx_i. \end{aligned}\tag{A.11}$$

Rewriting the first two terms using (A.2) and using

$$u_j\left(\frac{\partial a_i}{\partial x_j} - \frac{\partial a_j}{\partial x_i}\right) = ((\boldsymbol{\nabla}\times\mathbf{a})\times\mathbf{u})_i, \tag{A.12}$$

we finally have that the total derivative of the line integral I, for any vector field $\mathbf{a}$ is

$$\frac{dI}{dt} = \mathbf{a}(\mathbf{Q}).\dot{\mathbf{Q}} - \mathbf{a}(\mathbf{P}).\dot{\mathbf{P}} + \int_{\mathbf{P}}^{\mathbf{Q}}\left(\frac{\partial \mathbf{a}}{\partial t} + (\boldsymbol{\nabla}\times\mathbf{a})\times\mathbf{u}\right).d\mathbf{x}. \tag{A.13}$$

Note that another, more geometrical, way to derive the above Transport Theorem exists (see [8]) but we are not going to give it here.

Appendix B

Stationary-phase method for sonic boom problems

In this appendix we will present an alternative way for deriving the Mach envelope, in two dimensions for any unsteady supersonic motion in a straight line. The method also provides a classification of the Mach envelope points, according to the sign of the eigenvalues of an appropriately defined matrix and thus gives a clear link of the frequency domain to the time domain.

We consider a point source moving horizontally on the trajectory $(x_0(t), 0)$. A small disturbance due to this point source is governed by the linear wave equation and initial conditions

$$u_{tt} - \boldsymbol{\nabla}^2 u = \delta(x - x_0(t))\delta(z), \tag{B.1}$$

$$u = u_t = 0 \text{ at } t = 0. \tag{B.2}$$

(We have taken $c_0 = 1$.) Taking the Fourier Transform of (B.1)–(B.2) with respect to x and z we have

$$\bar{u}_{tt} + k^2\bar{u} = \exp(ik_1 x_0(t)), \tag{B.3}$$

$$\bar{u} = \bar{u}_t = 0 \text{ at } t = 0., \tag{B.4}$$

where $k = \sqrt{k_1^2 + k_2^2}$. Solving the ODE problem (B.3)–(B.4) we have

$$\bar{u}(k_1, k_2, t) = \int_0^t e^{ik_1 x_0(\tau)} \frac{\sin k(t-\tau)}{k} d\tau. \tag{B.5}$$

Taking the inverse Fourier transform of (B.5) we obtain

$$u(x_1, z, t) = \frac{1}{4\pi^2} \int_{-\infty}^{\infty} \int_{-\infty}^{\infty} \int_0^t e^{ik_1(x_0(\tau)-x)} e^{-ik_2 z} \frac{\sin k(t-\tau)}{k} d\tau dk_1 dk_2, \tag{B.6}$$

which can also be written as

$$u(x_1,z,t)=-\frac{i}{8\pi^2}\int_{-\infty}^{\infty}\int_{-\infty}^{\infty}\int_0^t \frac{e^{ik_1(x_0(\tau)-x_1)}e^{-ik_2z}\big(e^{ik(t-\tau)}-e^{-ik(t-\tau)}\big)}{k}d\tau dk_1dk_2. \tag{B.7}$$

From now on we will let

$$J_A=\iiint \frac{e^{it\phi}}{k}d\tau dk_1dk_2,\quad J_B=\iiint \frac{e^{it\psi}}{k}d\tau dk_1dk_2, \tag{B.8}$$

where the phase functions for J_A and J_B are respectively

$$\phi=\frac{k_1(x_0(\tau)-x_1)-k_2z+k(t-\tau)}{t},\quad \psi=\frac{k_1(x_0(\tau)-x_1)-k_2z-k(t-\tau)}{t}. \tag{B.9}$$

Therefore we have

$$8\pi^2u=-i(J_A-J_B). \tag{B.10}$$

Below we determine the stationary points of ϕ and ψ as a first step towards developing stationary-phase approximations to the integrals J_A and J_B (with t considered to be a large parameter) and show that the classical stationary-phase method cannot be used to calculate wavefields. However, the method is still very useful because even though it eventually breaks down, it provides the geometry of the Mach envelope.

Since $\psi(-\mathbf{k})=-\phi(\mathbf{k})$ there is a 1-1 correspondence between the stationary points of ϕ and ψ, and it is sufficient to calculate only the quantities associated with the phase ϕ. In order to determine the stationary point(s) of J_A, $\mathbf{s}_A$ say, we set respectively

$$\boldsymbol{\nabla}\,\phi|_{\mathbf{s}_A}=0. \tag{B.11}$$

We will make a convenient change of notation from (k_1,k_2,τ) to $\mathbf{s}=(s_1,s_2,s_3)$ so that the stationary points are denoted by $\mathbf{s}_A=(s_{A1},s_{A2},s_{A3})$. Writing (B.11) as a system of three equations in the three unknowns s_{A1},s_{A2},s_{A3} we have

$$\frac{\partial\phi}{ds_1}=0\Rightarrow\frac{x_0(s_{A3})-x}{t}+\frac{s_{A1}}{k_A}\left(1-\frac{s_{A3}}{t}\right)=0, \tag{B.12}$$

$$\frac{\partial\phi}{ds_2}=0\Rightarrow-\frac{z}{t}+\frac{s_{A2}}{k_A}\left(1-\frac{s_{A3}}{t}\right)=0, \tag{B.13}$$

$$\frac{\partial\phi}{ds_3}=0\Rightarrow\frac{s_{A1}x_0'(s_{A3})-k_A}{t}=0, \tag{B.14}$$

where $k_A=\sqrt{s_{A1}^2+s_{A2}^2}$. From (B.14) we have

$$x_0'(s_{A3})=\frac{k_A}{s_{A1}}. \tag{B.15}$$

Reverting to the original notation (B.15) gives

$$x_0'(\tau_0) = \frac{k_0}{k_{10}}. \tag{B.16}$$

Letting $k_{10} = k_0 \cos\theta$, $k_{20} = k_0 \sin\theta$ in (B.16) we recover the *boomray condition*

$$\cos\theta = \frac{1}{x_0'(\tau_0)}, \tag{B.17}$$

which has been discussed in detail in Chapter 3, p. 37. The boomray condition cannot hold if $|x_0'(\tau_0)| < 1$, which simply means that when the source motion is subsonic there are no boomrays. Also combining (B.12) and (B.13) we obtain

$$(x_0(\tau_0) - x)^2 + z^2 = (t - \tau_0)^2, \tag{B.18}$$

the circular wavefronts evaluated at the stationary point. The points defined by the relations (B.17) and (B.18) are precisely the Mach envelope points. Therefore the current method leads to expressions equivalent to the Mach envelope equations for any general motion on the horizontal line (see expressions (6.22) and (6.23)). For any τ such that the boomray passes through (x, z) at t, there is a corresponding half-line of (k_{10}, k_{20}) vectors. The stationary points are therefore not isolated and we now investigate this degeneracy.

B.1 Classification of the Mach envelope points

We proceed to determine the Hessian matrix of ϕ, which we will call A:

$$A_{jk} = \frac{\partial^2 \phi}{ds_j ds_k}|_{\mathbf{s}_A}, \quad . \tag{B.19}$$

A is a symmetric matrix and thus only six entries need to be calculated:

$$A_{11} = \frac{k_{20}^2}{k_0^3}\left(1 - \frac{\tau_0}{t}\right), \; A_{12} = -\frac{k_{10}k_{20}}{k_0^3}\left(1 - \frac{\tau_0}{t}\right), \; A_{13} = \frac{x_0'(\tau_0)}{t} - \frac{k_{10}}{k_0 t}$$
$$A_{22} = \frac{k_{10}^2}{k_0^3}\left(1 - \frac{\tau_0}{t}\right), \; A_{23} = -\frac{k_{20}}{k_0 t}, \qquad\qquad A_{33} = \frac{k_{10}}{t}x_0''(\tau_0).$$

The determinant is

$$\det A = -\frac{(t - \tau_0)(-x_0'(\tau_0)k_{10} + k_0)^2}{k_0^3 t^3} = 0, \tag{B.20}$$

having used the boomray condition (B.16). Therefore A is singular, and one of its three eigenvalues is zero, for *any* two-dimensional supersonic motion. The eigenvalues are

$$\lambda_1 = 0, \quad \lambda_{2,3} = \frac{C_2}{2} \pm \frac{1}{2}\sqrt{C_2^2 + 4C_1}, \tag{B.21}$$

$$\text{where } C_1 = -\lambda_2\lambda_3 = \frac{x_0'(\tau_0)^2 - 1}{t^2} - \frac{x_0''(\tau_0)}{x_0'(\tau_0)}\frac{t-\tau_0}{t^2}, \tag{B.22}$$

$$\text{and } C_2 = \lambda_2 + \lambda_3 = \frac{x_0''(\tau_0)}{x_0'(\tau_0)}\frac{k_0}{t} + \frac{t-\tau_0}{k_0 t}. \tag{B.23}$$

The subscripts "2" and "3" refer respectively to the positive and negative signs in front of the square root in (B.21). We expect a *qualitative change* in a Mach envelope point when an eigenvalue changes sign. We recall that the Mach envelope equations are determined by $Q = 0$, $\dfrac{\partial Q}{\partial \tau} = 0$ where

$$Q = (t-\tau)^2 - (x - x_0(\tau))^2 - z^2 = 0. \tag{B.24}$$

Taking the second derivative of Q with respect to τ we have

$$\frac{\partial^2 Q}{\partial \tau^2} = -2({x_0'}^2 - 1) + 2(x - x_0(\tau))x_0''. \tag{B.25}$$

Using the first envelope equation (6.22) we have

$$\frac{\partial^2 Q}{\partial \tau^2} = -2({x_0'}^2 - 1) - 2(t-\tau)\frac{x_0''}{x_0'}, \tag{B.26}$$

and from (B.26) and (B.22) we conclude that

$$\frac{\partial^2 Q}{\partial \tau^2} = 2t^2\lambda_2\lambda_3. \tag{B.27}$$

Relation (B.27) gives a very useful classification of the Mach envelope points. Before stating this classification criterion for the general case of a source moving with arbitrary velocity on a straight line, we will present the paradigm problem of a constant-acceleration motion through the sound speed. In this case

$$\frac{\partial^2 Q}{\partial \tau^2} = 2t^2\lambda_2\lambda_3 = -2\frac{\tau^3 - t}{\tau}. \tag{B.28}$$

We have already studied and plotted the Mach envelope for this in Chapter 6. There we found that it consists of a front envelope which the wavefronts envelope from inside, and a back envelope which the wavefronts envelope from outside. For the

back envelope we had identified that $\frac{\partial^2 Q}{\partial \tau^2} > 0$ and therefore $1 < \tau < t^{1/3}$, and for the front envelope we had identified that $\frac{\partial^2 Q}{\partial \tau^2} < 0$ and therefore $t^{1/3} < \tau < t$. This consistuted the algebraic criterion of p. 156. Now this criterion can be reinterpreted more lucidly in terms of the product of the eigenvalues of the Hessian matrix A: since $\lambda_2 \lambda_3 = -\frac{\tau^3 - t}{\tau t^2}$ we conclude that on the

- front envelope: $t^{1/3} < \tau < t \Leftrightarrow \lambda_2 \lambda_3 < 0 \Leftrightarrow \frac{\partial^2 Q}{\partial \tau^2} < 0$,
- back envelope: $1 < \tau < t^{1/3} \Leftrightarrow \lambda_2 \lambda_3 > 0 \Leftrightarrow \frac{\partial^2 Q}{\partial \tau^2} > 0$.

The front and back envelope join when $\lambda_2 \lambda_3 = 0$, $\frac{\partial^2 Q}{\partial \tau^2} = 0$, and Q has a point of inflexion there. We already know that this common point is a cusp. Having established these resuts we can proceed to state the following general assertion "For a general two-dimensional supersonic motion of a point source in a straight line (and with a uniform ambient medium) a Mach envelope point can only be one of the following three types:

Type a. $\frac{\partial^2 Q}{\partial \tau^2} < 0 \Leftrightarrow \lambda_2 \lambda_3 < 0$: the envelope point belongs to an envelope part that is formed by wavefronts enveloping it from inside (such as the Mach wedge in steady motion and the front envelope of the constant-acceleration motion).

Type b. $\frac{\partial^2 Q}{\partial \tau^2} = 0 \Leftrightarrow \lambda_2 \lambda_3 = 0$: cusp

Type c. $\frac{\partial^2 Q}{\partial \tau^2} > 0 \Leftrightarrow \lambda_2 \lambda_3 > 0$: the envelope point belongs to an envelope part which wavefronts envelope from outside (such as the back envelope of the constant-acceleration motion)."

Note that it is λ_3 that changes sign when going from the front to the back envelope.

This assertion gives consisely the relation of the frequency domain to the time domain in sonic boom problems.

B.2 Wavefield

We have established above a general method to classify the Mach envelope points. This method was set up as a stationary-phase method and the next question, after determining the stationary points, is whether it can be employed to determine

amplitudes, for two-dimensional sonic boom problems. Note that we have already calculated such amplitudes for steady flight, a uniformly accelerating flight, and a uniformly decelerating flight through a time-domain method in Chapter 6.

The task is to determine a consistent approximation of the integral (B.6). Letting

$$(k_1, k_2) = (k\cos\theta, k\sin\theta), \tag{B.29}$$

we have from (B.6) that

$$u(x,z,t) = \frac{1}{4\pi^2}\int_{k=0}^{\infty}\int_{\theta=0}^{\theta=2\pi}\int_0^t e^{ik((x_0(\tau)-x)\cos\theta - z\sin\theta)}\sin k(t-\tau)d\tau d\theta dk. \tag{B.30}$$

The k integral is not (classically or Lebesgue) convergent so it can only be interpreted in terms of distribution theory. The classical stationary-phase approximation breaks down because the contributions from *all* wavenumbers are important (instead of a certain interval of k dominating the integral). This arises because sound is not dispersive (in this approximation). Note that if we evaluate the integral over k as a distribution by

$$\int_0^{\infty} e^{ikp}dk = \pi\delta(p) + \frac{i}{p}, \tag{B.31}$$

then we recover exactly the usual integral representation of u, as cited on p. 143. (Noting that u here is the pressure p in the notation of Chapter 6).

Appendix C

Details of the wavefield features in Chapter 7

• **Case** $A > 0$

Below we will discuss in more detail the qualitative features of the wavefield discussed in Chapter 7 and show additional snapshots, for times other than $t = 1$. For $A < 1/2$ (and concentrating without loss of generality on values of $A < 0.109$) there are six types of qualitatively different behaviour, separated by the five events: the sonic time, the formation of ShockII, ShockII crossing the source, ShockI crossing the source, and shocks I and II merging.

In Figure C.1 (for $A = 0.05$) we show the characteristic diagram and separate these six regions with horizontal lines. We also mark the regions with WF1, WF2, WF3 and so on, in the direction of increasing time. Overall, the wavefield is not constant (not equal to 1) when the point (x, t) is in any of the five regions Type2R, Type2RL, Type3L, Type4 and Type4R. The wavefield can be calculated explicitly in the Type4 and Type4R regions: to obtain $u_4(x, t_0)$ we solve for $\tau(x, t_0)$ the characteristic expression

$$x = \frac{\tau^2}{2} + u_4(t_0 - \tau), \tag{C.1}$$

and this leads to

$$\tau(x, t_0) = u_4(x, t_0) = t_0 - \sqrt{t_0^2 - 2x}. \tag{C.2}$$

(We picked the negative root so that $u = 1$ at $x = t_0 - 1/2$.) In the same way, we find

$$u_{4R}(x, t_0) = t_0 + \sqrt{t_0^2 - 2x + 2A}, \tag{C.3}$$

(where the positive root has been picked so that $u > 1$).

An implicit expression is obtained for u_{2R} if we rearrange $u_{2R}(\tau) = \tau + \sqrt{(1-\tau)^2 + 2A}$ into $\tau(u_{2R}) = \dfrac{1 - u_{2R}^2 + 2A}{2(1-u_{2R})}$, and we substitute the latter relation into the Type2R characteristics. We obtain

$$x = \frac{1}{2}\left(\frac{1-u_{2R}^2+2A}{2(1-u_{2R})}\right)^2 + u_{2R}\left(t_0 - \frac{1-u_{2R}^2+2A}{2(1-u_{2R})}\right), \tag{C.4}$$

Similarly, to obtain $u_{3L}(x, t_0)$ we rearrange $u_{3L}(\tau)$ into $\tau(u_{3L}) = \dfrac{1 - u_{3L}^2 - 2A}{2(1-u_{3L})}$ and substitute into the Type3L characteristics; to obtain $u_{2RL}(x, t_0)$ we invert $u_{2RL}(\tau')$, get $\tau'(u_{2RL}) = \dfrac{3}{4}\dfrac{(u_{2RL} - \frac{1}{3})^2 - \frac{4}{9} + \frac{8A}{3}}{(u_{2RL} - 1)}$ and substitute into the Type2RL characteristics.

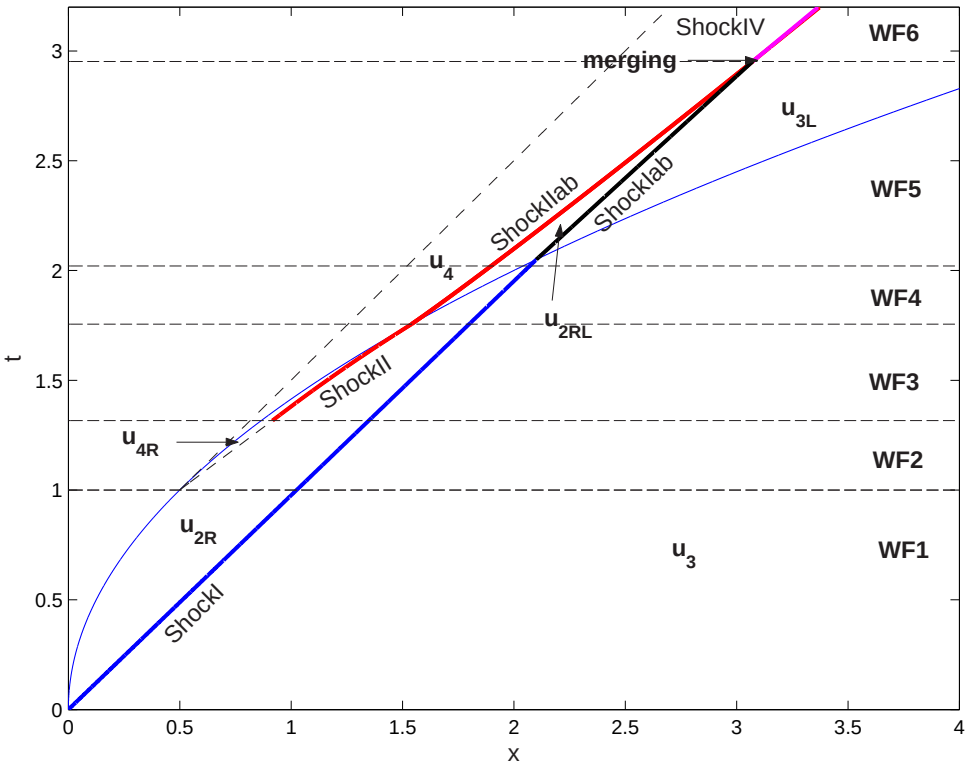

Figure C.1: $A = 0.05$: characteristic diagram that shows the six different types of behaviour a snapshot of the wavefield may have. The regions are separated with horizontal dotted lines and each region is marked with WF1, WF2, WF3 and so on.

We examine the features of a snapshot at fixed time t_0 as we are moving from small to large x.

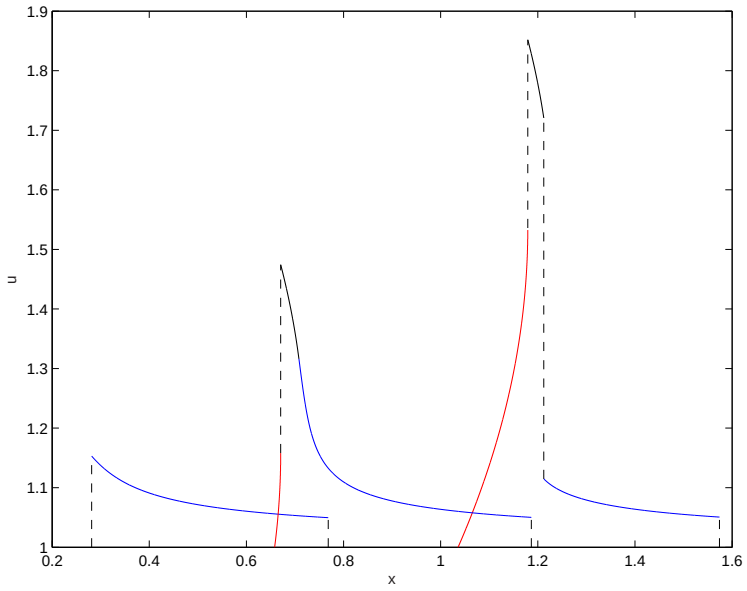

Figure C.2: Snapshots for $A = 0.05$ for times $t = 0.75, 1 + 0.5\sqrt{2A} = 1.158, 1.5$.

- $t_0 \leq 1$ (WF1, *see Figure C.2, first curve from the left)*: on the left of the source, $u = 1$ and u jumps to the value $u_{2R}(t_0) = t_0 + \sqrt{(1-t_0)^2 + 2A} > 1$ at the source. On the right of the source and left of ShockI, a Type2R region exists where $u = u_{2R}(x, t_0)$. Note that this decreases monotonically with x; for fixed t_0, and tracing back along the straight characteristics, larger values of x correspond to smaller values of u, since $u_{2R}(\tau)$ increases monotonically with τ.

  The value of u just on the left of ShockI, is found by obtaining τ numerically from the equation $t_{ShockI}(\tau) = t_0$, where t_{ShockI} is given by expression (7.22), and substituting into $u_{2R}(\tau)$.

- $1 \leq t_0 \leq 1+\sqrt{2A}$ (WF2, *see Figure C.2, second curve from the left)*. Type4 and Type 4R regions appear. Just on the left of the source we have $u = u_4(t_0) = t_0$. At the source, u jumps up to $u_{4R}(t_0) = t_0 + \sqrt{2A}$, decreases monotonically and joins with the Type2R region on the $\tau = 1$ characteristic. We note that the jump at the source from the Type4 to the Type4R regions has the constant value $\sqrt{2A}$.

- $1 + \sqrt{2A} \leq t_0 < t_{II}$ where t_{II} is the time at which ShockII intersects the source (WF3, *see Figure C.2, third curve from the left)*. The new feature is the presence of ShockII, which separates a Type4R from a Type2R region.

There are still three more cases to consider: $t_{II} < t_0 < t_I$ (WF4) where t_I is the time at which ShockI intersects the source path, $t_I < t_0 < t_{\text{merge}}$ (WF5) and $t_0 > t_{\text{merge}}$ (WF6). These transitions simply involve the shocks crossing the source, and merging, and are not illustrated.

For $A > 1/2$ the behaviour is slightly simpler as there are just four types of qualitatively different behaviour. For $A = 1$, in Figure C.3, we separate these regions with horizontal lines, corresponding to times $t = 1$, $t = 2$ and the time where ShockIII crosses the source ($t = 3.85$). Note that the snapshots C.4 given for the $A > 1/2$ case are also for $A = 1$.

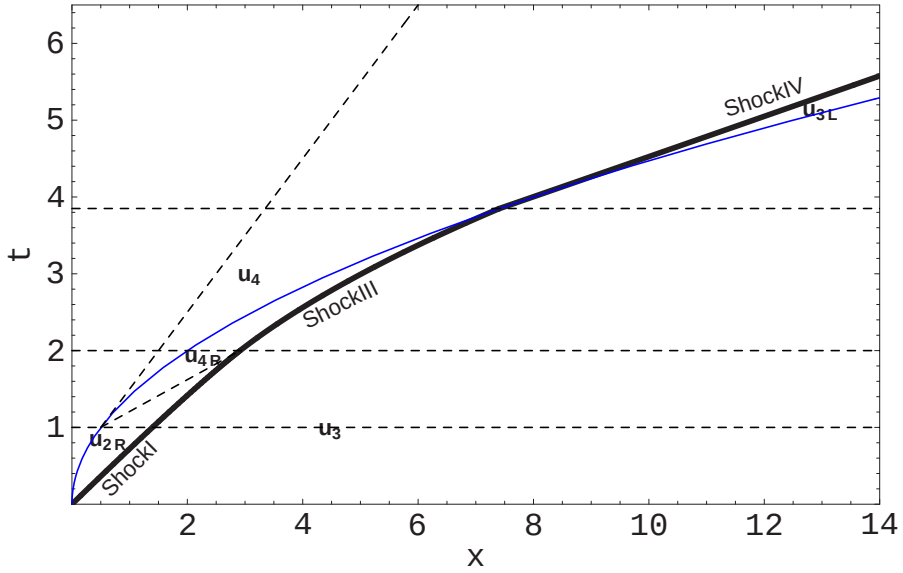

Figure C.3: $A = 1$: characteristic diagram showing the four cases of different wavefield behaviour.

- $t_0 < 1$: only ShockI is present. In Figure C.4, *first curve from the left*, we plot the $t_0 = 1/2$ snapshot.
- $1 < t_0 < 2$: the regions Type4 and Type4R appear. The Type4R region is separated from the Type2R region by the $\tau = 1$ characteristic. (For clarity the Type2R part is plotted with a thicker line.) In Figure C.4, *second curve from the left*, we plot the $t_0 = 3/2$ snapshot.
- $2 < t_0 < t_{III}$ where t_{III} is the time that ShockIII crosses the source path. The difference with the snapshots at earlier times is that the Type2R region vanishes and ShockIII takes over ShockI. In Figure C.4, *third curve from the left*, we plot the $t_0 = (1 + t_{III})/2 = 2.924$ snapshot.

- $t_0 > t_{III}$ ShockIV takes over from ShockIII, and the Type3L region appears on the right of it. In Figure C.4, *fourth curve from the left*, we plot the $t_0 = 4$ snapshot.

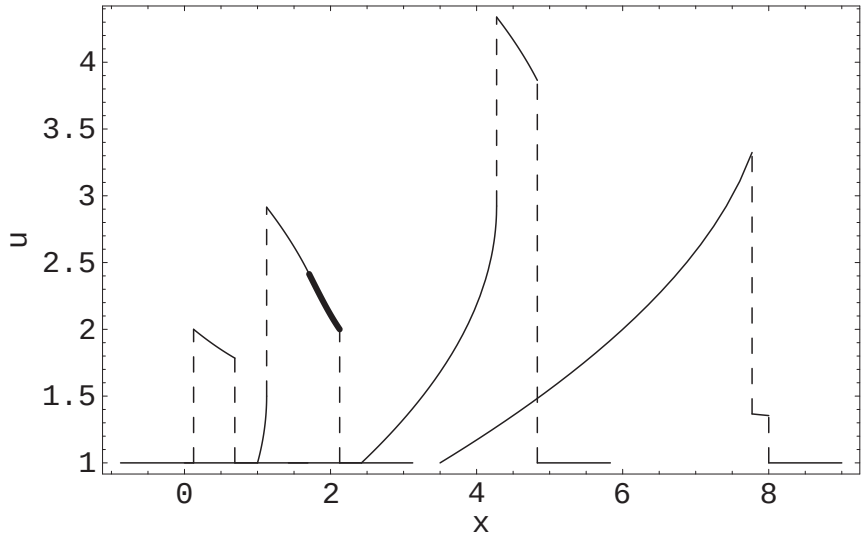

Figure C.4: $A = 1$: snapshots at times $t_0 = 0.5, 1.5, 2.924, 4$. Each snapshot belongs to a different time regime as explained in the text.

• Case $A < 0$

Assuming $-1/2 < A < 0$, without loss of generality, the wavefield has five cases of qualitatively different behaviour. In Figure (C.6), we show the characteristic diagram for $A = -0.2$ and separate the five regions with horizontal lines for the times $t = 1-\sqrt{2|A|} = 0.367, t = \sqrt{1-2|A|} = 0.774, t = 2$ and the time where the u_{2RL} and u_{5L} regions meet on the shock ($t = t_{\text{shock}} = 4.211$). The wavefield is not constant when the point (x, t) is in either of the five regions Type2R, Type2RL, Type3L, Type5 and Type5L. The wavefield in the first three regions is obtained in the same way as for the $A > 0$ case. In the Type5 region $u = u_5(x, t_0) = x/t_0$. To obtain $u_{5L}(x, t_0)$ we rearrange $u_{5L}(\tau')$ into $\tau'(u_{5L}) = \frac{4}{3}u_{5L} + \frac{2}{3}\sqrt{u_{5L}^2 + 6|A|}$ and we substitute into the Type5L characteristics.

- $t < 1 - \sqrt{2|A|}$ (see Figure C.6, *first curve from the left)*): this corresponds to times before the shock is formed. On the left of the source, u equals 1 and u drops to $u_{2R}(t_0^2/2, t_0) < 1$ on the right of the source. It then increases monotonically up to the leftmost characteristic of the expansion fan, $x = \sqrt{1-2|A|}t$. In the expansion fan (Type5 region) $u = u_5(x, t_0) = x/t_0$, which becomes 1 on the characteristic $x = t$.

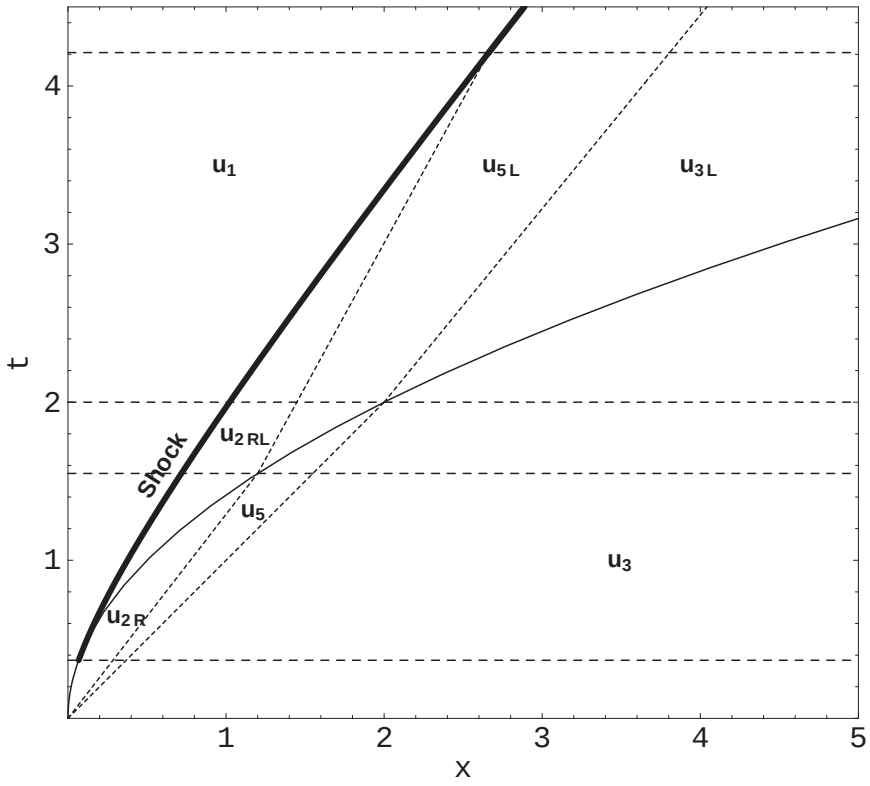

Figure C.5: $A = -0.2$: characteristic diagram with horizontal lines marking the times $t = 1 - \sqrt{2|A|} = 0.367$, $t = \sqrt{1 - 2|A|} = 0.774$, $t = 2$, $t_{\text{shock}} = 4.211$ dividing the five cases of different wavefield behaviour.

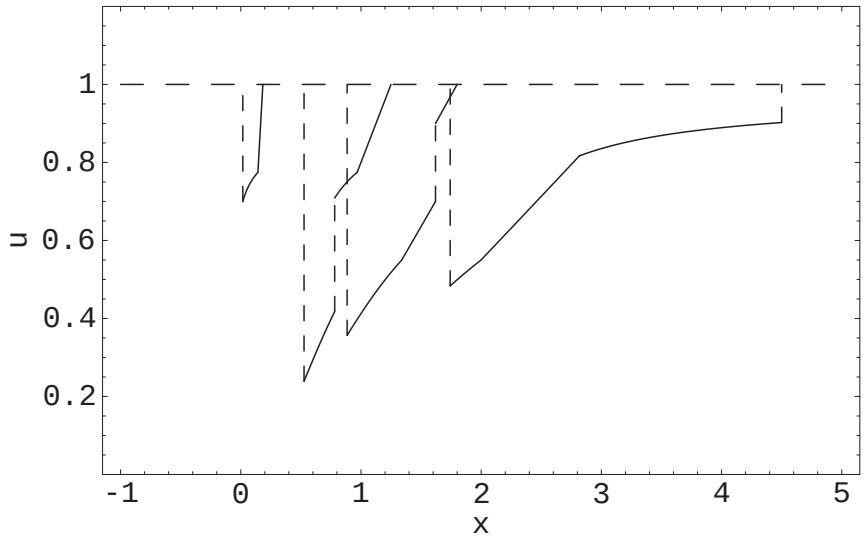

Figure C.6: $A = -0.2$: wavefield snapshots for $t = (1 - \sqrt{2|A|})/2 = 0.184, 1.25, 1.8, 3$. These correspond respectively to the first four cases.

- $1-\sqrt{2|A|} < t < 2\sqrt{1-2|A|}$ (see Figure C.6, *second curve from the left)*): The shock now appears. On the left of it u equals 1; this value drops to $u_{2RL}(x,t_0)$ if $A > -3/8$ and to $u_{5L}(x,t_0)$ if $A < -3/8$. We are primarily interested in small A so we are going to pursue only the $A > -3/8$ case. At the source, u jumps up to $u_{2R}(x,t_0)$ and from then on the features are the same as for the first 3 cases.

- $2\sqrt{1-2|A|} < t < 2$ (see Figure C.6, *third curve from the left)*): a Type5L region appears.

- $2 < t < t_{\text{shock}}$ where t_{shock} is evaluated at $\tau = 2\sqrt{1-2|A|}$ (see Figure C.6, *fourth curve from the left)*) : the new feature is the appearance of the Type3L region on the right of the Type5L region. At the source u jumps from $u_{3L}(x,t_0)$ up to 1.

- $t > t_{\text{shock}}$: the Type2RL region vanishes but otherwise all the features are the same as in the preceding snapshot.

References

[1] M. Abramowitz and I.A. Stegun. *Handbook of Mathematical Functions.* Wiley, New York, 1971.

[2] D.J. Acheson. *Elementary Fluid Dynamics.* Clarendon Press, Oxford, 1990.

[3] Federal Aviation Adminstration. Civil aircraft sonic boom. Aeronautics and Space, Code of Federal Regulations, Title 14, Part 91, January 1987. pp. 169–170.

[4] G.B. Airy. On the intensity of light in the neighbourhood of a caustic. *Trans. Camb. Phil. Soc.*, **6**:379–401, 1838.

[5] D.J. Allwright, L. Dallois, and K. Kaouri. SOBER report D9: Secondary sonic boom. Technical report, University of Oxford, July 2002.

[6] D.J. Allwright, L. Dallois, K. Kaouri, P. Blanc-Benon, J. Scott, and U. Berger. SOBER report D14: Report and software code for simulating secondary boom in a three-dimensionally inhomogeneous atmosphere and comparison with observations. Technical report, University of Oxford, Ecole Centrale de Lyon, Leibniz-Institute of Atmospheric Physics, March 2004.

[7] D.J. Allwright, L. Dallois, K. Kaouri, P. Blanc-Benon, J. Scott, and U. Berger. SOBER report D18: Guideline on the environmental impact of secondary boom. Technical report, University of Oxford, Ecole Centrale de Lyon, Leibniz-Institute of Atmospheric Physics, April 2004.

[8] D.J. Allwright and K. Kaouri. Circulation in inviscid gas flows with shocks. *Appl. Math. Let.*, **17**:767–770, July 2004.

[9] T. Aubin and F. Coulouvrat. Nonlinear acoustic waves in a relaxing fluid. *J. Math. Pure Appl.*, **77**(4):387, 1998.

[10] T. Auger. *Modélisation et simulation numérique de la focalisation d'ondes de chocs acoustiques en milieu en mouvement. Application à la focalisation du bang sonique en accélération.* PhD thesis, Université Paris VI, 2001.

[11] Th. Auger and F. Coulouvrat. Numerical simulation of sonic boom focusing. *AIAA Journal*, **40**(9):1726–1734, 2002.

[12] H.E. Bass, J. Ezell, and R. Raspet. Effect of vibrational relaxation on rise times of shock waves in the atmosphere. *J. Acoust. Soc. Am.*, **74**(5):1514–17, 1983.

[13] H.E. Bass, B.A. Layton, L.N. Bolen, and R. Raspet. Propagation of medium strength shock waves through the atmosphere. *J. Acoust. Soc. Am.*, **82**:306–310, 1987.

[14] G.K. Batchelor. *An Introduction to Fluid Dynamics.* Cambridge University Press, 3rd edition, 2000.

[15] M.V. Berry. Waves and Thom's theorem. *Adv. Phys.*, **25**:1–26, 1976.

[16] V. Bjerknes. On a fundamental theorem of hydrodynamics and its applications particularly to the mechanics of the atmosphere and the world's oceans. (in German). *Proc. Roy. Swed. Acam. Sci.*, 1898.

[17] D.I. Blokhintsev. The propagation of sound in an inhomogeneous and moving medium I. *J. Acoust. Soc. Am.*, **18**:322–328, 1946.

[18] M. Born and E. Wolf. *Principles of Optics.* Cambridge University Press, Cambridge, 7th edition, 2002.

[19] R.B. Buchal and Keller J.B. Boundary layer problems in diffraction theory. *Comm. Pur. Appl. Math.*, **13**:85–144, 1960.

[20] L. Cambier. "The elsA project". In *First ONERA/DLR Aerospace Symposium*, Paris, June 1999.

[21] C. J Chapman. *High Speed Flow.* Cambridge University Press, 2000.

[22] C.J. Chapman. Time-domain asymptotics and the method of stationary phase. *Proc. Roy. Soc. Lon.*, **437**(1899):25–40, 1992.

[23] H.K. Cheng and M.M. Hafez. The superboom as a Tricomi problem: application. In *IUTAM Symposium Transsonicum*, Gottingen, Germany, September 2002.

[24] R. Cleveland. *Propagation of sonic booms through a real, stratified atmosphere.* PhD thesis, Univ. Texas at Austin., 1995.

[25] F. Coulouvrat. Focusing of weak acoustic shock waves at a caustic cusp. *Wave Motion*, **32**(3):233–45, 2000.

[26] F. Coulouvrat. Sonic boom in the shadow zone: a geometrical theory of diffraction. *J. Acoust. Soc. Am.*, **111**(1):499–508, 2001.

[27] F. Coulouvrat. Numerical simulation of shock wave focusing at fold caustics with application to sonic boom. *J. Acoust. Soc. Am.*, **114**(4):1758–1771, 2003.

[28] M.S. Cramer. Focusing of weak three-dimensional shock waves. *AIAA Journal*, **19**(10):1363–1365, 1981.

[29] M.S. Cramer and A.R. Seebass. Focusing of weak shock waves at an arête. *J. Fluid Mech.*, **110**:249–253, 1981.

[30] S.C. Crow. Distortion of sonic bangs by atmospheric turbulence. *J. Fluid Mech.*, **37**:529–563, 1969.

[31] L. Dallois, P. Blanc-Benon, J. Scott, U. Berger, D.J. Allwright, and K. Kaouri. Secondary sonic boom modelling for realistic atmospheric conditions. In *Proceedings of the CFA-DAGA Meeting*, Strasburg, 2004.

[32] D.F. Dempsey. Focusing conditions for sonic booms. *J. Acoust. Soc. Am.*, **61**(3), March 1977.

[33] W.L. Donn. Exploring the atmosphere with sonic booms. *American Scientist*, **66**:724–733, 1978.

[34] M. Downing, N. Zamot, C. Moss, D. Morin, Ed. Wolski, S. Chung, K. Plotkin, and D. Maglieri. Controlled focused sonic booms from maneuveuring aircraft. *J. Acoust. Soc. Am.*, **104**(1), 1998.

[35] J.W.M. DuMond, E.R. Cohen, W.K.H. Panofksy, and E. Deeds. A determination of the wave forms and laws of propagation and dissipation of ballistic shock waves. *J. Acoust. Soc. Am.*, **18**(1):97–118, 1946.

[36] Effects of aircraft noise and sonic boom on domestic animals and wildlife: A literature synthesis. Engineering and Services Centre, Fish and Wildlife Service, U.S. Air Force, June 1988.

[37] T.P. Evans and J.J. Doherty. The aerodynamic design of EUROSUP configuration. DERA/AS/ASD/CR97620/1.0, 1997.

[38] A. Ferri, L. Ting, and R.W. Lo. Nonlinear sonic boom propagation including the asymmetric effects. *AIAA Journal*, **15**(5):653–658, 1977.

[39] F.I. Frankl and E.A. Karpovich. *Gas Dynamics of Thin Bodies.* Interscience Publishers Ltd., 1953.

[40] F. G. Friedlander. *Sound Pulses.* Cambridge University Press, 1958.

[41] K.Y. Fung. Shock wave formation at a caustic. *SIAM J. Appl. Math.*, **39**:355–371, 1980.

[42] G. Gilbert and H.E.H. Davies. Pantograph motion on a nearly uniform railway overhead line. *Proc. IEE*, **113**(3):485–492, 1966.

[43] P.M. Gill and A.R. Seebass. Nonlinear acoustic behavior at a caustic: an approximate analytical solution. In *AIAA Aeroacoustics Conference*, Cambridge, MA, U.S.A., 1973. MIT Press.

[44] M.E. Goldstein. *Aeroacoustics.* McGraw-Hill International Book Co, New York, 1976.

[45] J.-P. Guiraud. Acoustique géométrique, bruit balistique des avions supersoniques et focalisation. *J. Mec.*, **4**:215–267, 1965.

[46] J. Hadamard. *Leçons sur la Propagation de Ondes.* Hermann, Paris, 1903.

[47] G.T. Haglund and E.J. Kane. Analysis of sonic boom measurements near shock wave extremities for flight near Mach 1.0 and for airplane accelerations. *NASA CR*, **2417**, 1974.

[48] G.T. Haglund and H.W. Poling. HSCT sonic boom impact at the Earth's surface due to secondary booms. Technical report, Boeing Commercial Airplane Company, Seattle, WA, 1995. Prepared for Nasa Langley Research Center, contract NAS1-20220.

[49] P.W. Hammerton. Effect of molecular relaxation on the propagation of sonic booms through a stratified atmosphere. *Wave Motion*, **33**(4):359–377, April 2001.

[50] W.D. Hayes. *Linearised Supersonic Flow*. PhD thesis, California Institute of Technology, 1947.

[51] W.D. Hayes. Pseudotransonic similitude and first-order wave structure. *J. Aero. Sci.*, **21**:721–730, 1954.

[52] W.D. Hayes. Brief review of the basic theory: sonic boom research. *NASA SP*, **147**:3–7, 1967.

[53] W.D. Hayes. Similarity rules for nonlinear acoustic propagation through a caustic. (Proceedings of the second conference on sonic boom research). *NASA SP*, **180**:165–171, 1967.

[54] W.D. Hayes, R.C. Haefeli, and H.E. Kulsrud. Sonic boom propagation in a stratified atmosphere, with computer program. *NASA CR*, **1299**, 1969.

[55] H.M. Helfand. *An application of the method of Multiple Scales to problems arising in supersonic aerodynamics and stratified fluid mechanics*. PhD thesis, Cornell University, 1974.

[56] G.S. Heller. Propagation of acoustic discontinuities in an inhomogeneous moving liquid medium. *J. Acoust. Soc. Am.*, **25**:950–951, 1953.

[57] A.L. Hoffman. A single fluid model for shock formation in MHD shock tubes. *J. Plasma Phys.*, **1**:193–207, 1967.

[58] H. Huang. Private communication. York University, Toronto, Canada.

[59] J.K. Hunter and J.B. Keller. Caustics of nonlinear waves. *Wave Motion*, **9**(5):429–443, 1987.

[60] J Jena and V.D. Sharma. Far-field behaviour of waves in a relaxing gas. *Acta Astronautica*, **40**(10):713–718, 1996.

[61] C.N. Jensen. *Nonlinear systems with discrete and continuous elements*. PhD thesis, Technical University of Denmark, 1997.

[62] M.E. Johnson and P.W. Hammerton. Effect of molecular relaxation processes on travelling wave solutions of sonic boom waveforms. *Wave Motion*, **38**(3):229–240, September 2003.

[63] K. Kaouri. Effects of the earth's curvature and rotation on sound ray propagation. Technical report, OCIAM, Mathematical Institute, Oxford., 2002.

[64] K. Kaouri. Solution of the kinematic wave equation with an accelerating point source. *Wave Motion*, 2004. (in press).

[65] J.B. Keller. Geometrical acoustics I: the theory of weak shock waves. *J. Appl. Phys.*, **25**(8):938–947, 1954.

[66] J.B. Keller. A geometrical theory of diffraction. In *Proc. Symposia Appl. Math.*, **8**, pages 27–32. McGraw-Hill, 1958.

[67] L.D. Landau. On shock waves at large distances from the place of their origin. *Journal of Physics of the Academy of Sciences of the U.S.S.R.*, **9**:496, 1945.

[68] J.M. Lawry. *Some results on diffraction theory.* Master's thesis, Oxford University, 1993.

[69] R.J. LeVeque. *Finite Volume Methods for Hyperbolic Problems.* Cambridge University Press, Cambridge, 2002.

[70] H.W. Liepmann and A. Roshko. *Elements of Gasdynamics.* John Wiley, Inc., 1956.

[71] M.J. Lighthill. The conditions behind the trailing edge of the supersonic aerofoil. *Rep. Memor. Aero. Res. Comm. Lond.*, **1930**, 1944.

[72] M.J. Lighthill. *Waves in Fluids.* Cambridge University Press, 1978.

[73] G.M. Lilley, R. Westley, A.H. Yates, and J.R. Busing. Some aspects of noise from supersonic aircraft. *J. Roy. Aero Soc.*, **57**:396–414, 1953.

[74] H. Lomax. The wave drag of arbitrary configurations in linearised flow as determined by areas and forces in oblique planes. *NACA RM*, **A55 A18**, 1955.

[75] D. Ludwig. Uniform asymptotic expansions at a caustic. *Comm. Pur. Appl. Math.*, **19**:215–250, 1966.

[76] D.J. Maglieri and K.J. Plotkin. *Sonic Boom*, chapter 10, pages 519–561. NASA, USA, 1991.

[77] R. Marchiano, F. Coulouvrat, and Grenon R. Numerical simulation of shock wave focusing at fold caustics, with application to sonic boom. *J. Acoust. Soc. Am.*, **114**(4):1–14, 2003.

[78] R. Marchiano, F. Coulouvrat, and J.-L. Thomas. Focusing of finite amplitude waves at caustics. Moscow (Russia), August 2002. 16th Int. Sump. Nonlinear Acoustics.

[79] D.A. McCurdy, S.A. Brown, and R.D. Hilliard. The effects of simulated sonic booms on people in their homes. In 33*rd Aerospace Sciences Meeting, AIAA*, **95-0834**, 1995.

[80] C.B. Moler and L.P. Solomon. Use of splines and numerical integration in Geometrical Acoustics. *J. Acoust. Soc. Am.*, **48**:739–734, 1970.

[81] J.F. Nye. *Natural focusing and fine structure of light: caustics and wave dislocations.* Institute of Physics Publishing, Bristol, 1999.

[82] H. Ockendon and J.R. Ockendon. *Waves and Compressible Flow.* Springer-Verlag, New York; London, 2004.

[83] H. Ockendon and D.A. Spence. Nonlinear wave propagation in a relaxing gas. *J. Fluid Mech.*, **39**:329–345, 1969.

[84] H. Ockendon and A.B. Tayler. *Inviscid Fluid Flows.* Springer-Verlag, New York, 1983.

[85] J. Ockendon, S. Howison, A. Lacey, and A. Movchan. *Applied Partial Differential Equations.* Oxford University Press, 1st edition, 1999.

[86] J. Ockendon, S. Howison, A. Lacey, and A. Movchan. *Applied Partial Differential Equations.* Oxford University Press, 2nd edition, 2003.

[87] C. B. Officer. *Introduction to the Theory of Sound Transmission: With Application to the Ocean.* McGraw-Hill series in the geological sciences. McGraw-Hill, 1958.

[88] R.O. Onyeowu. Diffraction of sonic boom past the nominal edge of the corridor. *J. Acoust. Soc. Am.*, **58**:326–330, 1975.

[89] N.W. Page and K.J. Plotkin. An efficient method for incorporating Computational Fluid Dynamics into sonic boom prediction. **AIAA-1991**, page 3275. AIAA Aeroacoustics conference, 1991.

[90] T. Pearcey. The structure of an electromagnetic field in the neighbourhood of a cusp of a caustic. *Phil. Mag.*, **37**:311–7, 1946.

[91] W.R. Pechuzal and J. Kevorkian. Supersonic-transonic flow generated by a thin airfoil in a stratified atmosphere. *SIAM J. Appl. Math.*, **33**(1):8–33, 1977.

[92] A.D. Pierce. Maximum overpressures of sonic boom near the cusp of caustic. In M.J. Crocker, editor, *Noise and Vibration Control Engineering.*, pages 478–487. Purdue University Press, 1971.

[93] A.D. Pierce. Statistical theory of atmospheric turbulence on sonic boom rise times. *J. Acoust. Soc. Am.*, **49**:906–924, 1971.

[94] A.D. Pierce. *Acoustics, an Introduction to its Physical Principles and Applications.* Acoustical Society of America, 1994.

[95] A.D. Pierce. Dispersion relation influence on rise times of sonic boom propagation through turbulence. *J. Acoust. Soc. Am.*, **99**(4):2488–2500, 1996.

[96] A.D. Pierce and D.J. Maglieri. Effects of atmospheric irregularities on sonic boom propagation. *J. Acoust. Soc. Am.*, **51**(2):702–721, 1972.

[97] K.J. Plotkin. Sonic boom focal zones from tactical aircraft maneuvers. *J. Aircraft*, **30**(1):75–80, 1993. interlibrary.

[98] K.J. Plotkin. State of the art of sonic boom modeling. *J. Acoust. Soc. Am.*, **104**:1830, 1998.

[99] K.J. Plotkin. State of the art of sonic boom modeling. *J. Acoust. Soc. Am.*, **111**(1):530–536, 2002.

[100] K.J. Plotkin and N.W. Page. Extrapolation of sonic boom signatures from CFD solutions. **AIAA-0922**, pages 1–6. AIAA Aeroacoustics conference, 2002.

[101] A.L. Polyakova, S.I. Soluyan, and R.V. Khokhlov. Propagation of finite disturbances in a relaxing medium. *Soviet Phys. Acoust.*, **8**:78–82, 1962.

[102] P.S. Rao. Supersonic bangs I. *Aero Q.*, **7**:21–44, 1956.

[103] P.S. Rao. Supersonic bangs II. *Aero Q.*, **7**:135–155, 1956.

[104] E. Rickley and A. Pierce. Detection and assessment of secondary sonic booms in New England. *J. Acoust. Soc. Am.*, **67**(1), 1980.

[105] R. A. Riehle and R.C. Newman, editors. *Principles of Extracorporeal Shock Wave Lithotripsy.* Churchill Livingstone, New York, 1987.

[106] L.D. Robinson. *Sonic boom propagation through an inhomogeneous, windy atmosphere.* PhD thesis, University of Texas at Austin., 1991.

[107] R Rodeman, D.B. Longcope, and L.F Shampine. Response of a string to an accelerating mass. *J. Applied Mech.*, **98**(4):675–680, 1976.

[108] P.H. Rogers and J.H. Gardner. Propagation of sonic booms in the thermosphere. *J. Acoust. Soc. Am.*, **67**(1):79–91, 1980.

[109] R.R. Rosales and E.G. Tabak. Caustics of weak shock waves. *Phys. Fluids*, **10**(1):206–222, 1998.

[110] C. Schar. Infrasonic wave propagation in the atmosphere (in German)., 1993.

[111] J. Scott. personal communication.

[112] W.R. Sears, editor. *General Theory of High Speed Aerodynamics.* Princeton University Press, 1954.

[113] A.R. Seebass. Nonlinear acoustic behavior at a caustic. (Proceedings of the third conference on sonic boom research.). *NASA SP*, **255**:87–120, 1971.

[114] K.P. Shepherd, S.A. Brown, J.D. Leatherwood, and D.A. McCurdy. Human response to sonic booms-recent NASA research. NASA Langley Research Center, Hampton, VA 23681, USA.

[115] Y.L. Sinai and J.F. Clarke. The wave system attached to a finite slender body in a supersonic relaxing gas stream. *J. Fluid Mech.*, **84**:717–741, 1978.

[116] M.J.T. Smith. *Aircraft Noise.* Cambridge University Press, 1989.

[117] V. Sparrow. Review and status of sonic boom penetration into the ocean. *J. Acoust. Soc. Am.*, **111**(1):537–543, 2002.

[118] B. Sturtevant and V.A. Kulkarny. The focusing of weak shock waves. *J. Fluid Mech.*, **73**(4):651–671, 1976.

[119] A.D. Taylor. The TRAPS sonic boom program. Technical report, U.S. Dept. of Commerce, 1980.

[120] C.L. Thomas. Extrapolation of sonic boom pressure signatures by the waveform parameter method. *NASA TN*, **D-6832**, 1972.

[121] M.D. Van Dyke. *Perturbation Methods in Fluid Mechanics.* Stanford: Parabolic Press, 1975.

[122] F. Walkden. The shock pattern of a wing-body combination, far from the flight path. *Aeronautical Q.*, **IX**:164–194, 1958.

[123] J.-C.L. Wanner, J. Vallee, C. Vivier, and C. Thery. Theoretical and experimental studies of the focus of sonic booms. *J. Acoust. Soc. Am.*, **52**(1):13–32, 1972.

[124] G.B. Whitham. The flow pattern of a supersonic projectile. *Comm. Pur. Appl. Math.*, **5**:301–348, 1952.

[125] G.B. Whitham. On the propagation of weak shocks. *J. Fluid Mech.*, **1**:290–318, 1956.

[126] G.B. Whitham. *Linear and Nonlinear Waves.* Wiley, New York, 1974.